Source field reconstruction based on virtual acoustic volume concept : Regularization strategies and blind reconstruction and separation

Emmanuel Manu Dabankah

N° d'ordre NNT : 2022LYSEI057

THESE de DOCTORAT DE L'UNIVERSITE DE LYON
opérée au sein de
l'INSA Lyon

École Doctorale ED 162
MEGA (Mécanique, Energétique, Génie Civil, Acoustique)

Spécialité/ discipline de doctorat : Acoustique

Soutenue publiquement le 22/06/2022, par :
Emmanuel Manu Dabankah

Source field reconstruction based on virtual acoustic volume concept:
Regularization strategies and blind reconstruction and separation

---

Devant le jury composé de :

THOMAS, Jean-Hugh, Professeur des Universités, LAUM, Le Mans Université	Président
THOMAS, Jean-Hugh, Professeur des Universités, LAUM, Le Mans Université	Rapporteur
AUCEJO, Mathieu, Maître de Conférences HDR, LMSSC, CNAM	Rapporteur
FORGET, Sandra, Docteure, Renault	Examinatrice
COLANGELI, Claudio, Docteur, Siemens	Examinateur
TOTARO, Nicolas, Professeur des Universités, LVA, INSA-Lyon	Directeur de thèse
ANTONI, Jérôme, Professeur des Universités, LVA, INSA-Lyon	Co-encadrant de thèse

Département FEDORA – INSA Lyon - Ecoles Doctorales

SIGLE	ECOLE DOCTORALE	NOM ET COORDONNEES DU RESPONSABLE
CHIMIE	**CHIMIE DE LYON** **https://www.edchimie-lyon.fr** Sec. : Renée EL MELHEM Bât. Blaise PASCAL, 3e étage secretariat@edchimie-lyon.fr	**M. Stéphane DANIELE** C2P2-CPE LYON-UMR 5265 Bâtiment F308, BP 2077 43 Boulevard du 11 novembre 1918 69616 Villeurbanne **directeur@edchimie-lyon.fr**
E.E.A.	**ÉLECTRONIQUE, ÉLECTROTECHNIQUE, AUTOMATIQUE** **https://edeea.universite-lyon.fr** Sec. : Stéphanie CAUVIN Bâtiment Direction INSA Lyon Tél : 04.72.43.71.70 secretariat.edeea@insa-lyon.fr	**M. Philippe DELACHARTRE** INSA LYON Laboratoire CREATIS Bâtiment Blaise Pascal, 7 avenue Jean Capelle 69621 Villeurbanne CEDEX Tél : 04.72.43.88.63 **philippe.delachartre@insa-lyon.fr**
E2M2	**ÉVOLUTION, ÉCOSYSTÈME, MICROBIOLOGIE, MODÉLISATION** **http://e2m2.universite-lyon.fr** Sec. : Bénédicte LANZA Bât. Atrium, UCB Lyon 1 Tél : 04.72.44.83.62 secretariat.e2m2@univ-lyon1.fr	**Mme Sandrine CHARLES** Université Claude Bernard Lyon 1 UFR Biosciences Bâtiment Mendel 43, boulevard du 11 Novembre 1918 69622 Villeurbanne CEDEX **sandrine.charles@univ-lyon1.fr**
EDISS	**INTERDISCIPLINAIRE SCIENCES-SANTÉ** **http://ediss.universite-lyon.fr** Sec. : Bénédicte LANZA Bât. Atrium, UCB Lyon 1 Tél : 04.72.44.83.62 secretariat.ediss@univ-lyon1.fr	**Mme Sylvie RICARD-BLUM** Institut de Chimie et Biochimie Moléculaires et Supramoléculaires (ICBMS) - UMR 5246 CNRS - Université Lyon 1 Bâtiment Raulin - 2ème étage Nord 43 Boulevard du 11 novembre 1918 69622 Villeurbanne Cedex Tél : +33(0)4 72 44 82 32 **sylvie.ricard-blum@univ-lyon1.fr**
INFOMATHS	**INFORMATIQUE ET MATHÉMATIQUES** **http://edinfomaths.universite-lyon.fr** Sec. : Renée EL MELHEM Bât. Blaise PASCAL, 3e étage Tél : 04.72.43.80.46 infomaths@univ-lyon1.fr	**M. Hamamache KHEDDOUCI** Université Claude Bernard Lyon 1 Bât. Nautibus 43, Boulevard du 11 novembre 1918 69 622 Villeurbanne Cedex France Tél : 04.72.44.83.69 **hamamache.kheddouci@univ-lyon1.fr**
Matériaux	**MATÉRIAUX DE LYON** **http://ed34.universite-lyon.fr** Sec. : Yann DE ORDENANA Tél : 04.72.18.62.44 yann.de-ordenana@ec-lyon.fr	**M. Stéphane BENAYOUN** Ecole Centrale de Lyon Laboratoire LTDS 36 avenue Guy de Collongue 69134 Ecully CEDEX Tél : 04.72.18.64.37 **stephane.benayoun@ec-lyon.fr**
MEGA	**MÉCANIQUE, ÉNERGÉTIQUE, GÉNIE CIVIL, ACOUSTIQUE** **http://edmega.universite-lyon.fr** Sec. : Stéphanie CAUVIN Tél : 04.72.43.71.70 Bâtiment Direction INSA Lyon mega@insa-lyon.fr	**M. Jocelyn BONJOUR** INSA Lyon Laboratoire CETHIL Bâtiment Sadi-Carnot 9, rue de la Physique 69621 Villeurbanne CEDEX **jocelyn.bonjour@insa-lyon.fr**
ScSo	**ScSo*** **https://edsciencessociales.universite-lyon.fr** Sec. : Mélina FAVETON INSA : J.Y. TOUSSAINT Tél : 04.78.69.77.79 melina.faveton@univ-lyon2.fr	**M. Bruno MILLY** Université Lumière Lyon 2 86 Rue Pasteur 69365 Lyon CEDEX 07 **bruno.milly@univ-lyon2.fr**

*ScSo : Histoire, Géographie, Aménagement, Urbanisme, Archéologie, Science politique, Sociologie, Anthropologie

Acknowledgments

This work was carried out as part of the Pass-By Noise second version (PBNv2) project, which focuses on "next generation Pass-By Noise techniques for new powertrain vehicles": It is made up of ten beneficiaries from renowned educational institutions, research institutes, and industries, as well as seven partner organizations with roots in European automotive research and development. The partnership brings together a wide range of disciplines and industries in vibroacoustics and beyond, fostering intersectoral, multidisciplinary, and creative training and mobility for the project's fourteen early-stage researchers. Under grant agreement No 721615, this project was funded by the European Union's Horizon 2020 research and innovation initiative.

This work was performed within the framework of the Labex CeLyA of Université de Lyon, operated by the French National Research Agency (ANR-10-LABX-0060/ANR-11-IDEX-0007).

To my PBNv2 project collaborators. Friendships created during the course of our trip together will surely be with me for many years. It was a privilege to share this voyage with you all. Not to mention my INSA LVA Lab colleagues, who assisted me in settling in Lyon and making the city seem like home.

Also, I would like to thank karl Janssens, Claudio Colangeli and Bart Forrier for their tremendous help and support throughout my secondment with Siemens in Leuven. Not to mention the significant role they had in carrying out the experiments during the peak of the COVID19 pandemic.

Nicolas Totaro and Jerome Antoni, my supervisors, who gave me with crucial direction, support, and numerous resources that I required to finish critical areas of my research. Words can't express how much of an influence you had on my professional life.

To Silvia Dabankah, the love of my life, for always being supportive of my decision and showering me with immeasurable love. To my two amazing children, Samuel Nana-Yaw Dabankah and Kobi Manu Dabankah, who fill me with joy and provide me with motivation to strive forward in life.

Finally, I give thanks to God for my life and the strength to finish my PhD thesis work.

Résumé

La pollution sonore générée par les moyens de transports en général et les automobiles en particulier est un problème de société qui a un impact considérable sur la vie et la santé des personnes vivant dans les villes ou près d'infrastructures bruyantes. Pour minimiser ces nuisances sonores, les pouvoirs publics imposent des normes et réglementations exigeantes en termes de bruit émis, notamment par les automobiles. Pour pouvoir relever ce challenge, les industriels du transport doivent intégrer ces critères dès la conception des véhicules car les solutions palliatives ne sont plus suffisantes. De nos jours, la conception des systèmes est principalement réalisée via des simulations numériques mais les campagnes de mesures expérimentales sont toujours précieuses pour à la fois améliorer la compréhension des phénomènes à l'origine des sources de bruit et permettre de corréler les résultats des simulations numériques aux données expérimentales.
De ce fait, les méthodes de caractérisation expérimentale des sources de bruit ont suscité un grand intérêt de la part des industriels. Ces méthodes sont soit des méthodes de mesures directes soit des méthodes dites inverses. Dans ce cas, l'objectif est d'observer la conséquence pour identifier la cause. On distingue généralement deux catégories de méthodes inverses de caractérisation de sources en acoustique : les méthodes de localisation de sources acoustiques et les méthodes de reconstruction de champs. Malgré les nombreuses recherches menées au fil des ans, les acousticiens et les ingénieurs NVH (Noise Vibrations Harshness) continuent de rencontrer des difficultés notamment à cause du contexte industriel des mesures expérimentales qui s'éloigne nettement des conditions de laboratoire dans lesquelles les méthodes sont généralement développées. Lorsque l'objectif est la reconstruction des champs acoustiques (vitesse, pression, intensité) à la surface de l'objet d'étude, plusieurs difficultés, spécifiques au contexte industriel, peuvent se poser :

- Le système étudié est généralement un assemblage de pièces et de composants formant une géométrie complexe et tri-dimensionnelle. Une grande partie des méthodes de reconstruction de champ telles que la méthode Nearfield Acoustic Holography (NAH) ne permettent de reconstruire les champs acoustiques que sur une surface de géométrie simple (le plus souvent plane) proche du système réel. Or cela rend l'interprétation de résultats et leur exploitation (pour alimenter un modèle numérique par exemple) particulièrement difficile dans le cas de systèmes à géométrie complexe.

- Le champ acoustique du local de mesure ne respecte que très rarement les conditions que l'on retrouve dans une salle anéchoïque de laboratoire. Le banc d'essai est généralement placé dans un espace calme (parois traitées acoustiquement mais non parfaitement anéchoïques) mais des sources perturbatrices peuvent aussi devoir y être présentes. C'est le cas par exemple d'armoires électriques, de moteurs d'entraînement ou de freins. Les méthodes de caractérisation de sources utilisées doivent pouvoir s'affranchir de cet environnement acoustique mal maîtrisé en intégrant par exemple des techniques de séparation de champs, isolant le bruit provenant du système étudié des nuisances sonores provenant de l'environnement.

- Le système étudié est la plupart du temps maintenu ou suspendu sur des cadres ou des structures porteuses. De même, d'autres objets peuvent être placés à proximité immédiate du système étudié. Enfin, le système étudié peut lui-même être fixé sur une structure massique. Toutes ces situations ont en commun la présence d'objets masquants dans l'environnement immédiat du système étudié générant des réflexions des ondes rayonnées et limitant les possibilités d'accès par un moyen de mesure (typiquement une antenne de microphones) dans certaines zones autour de l'objet. Une solution palliative est de recouvrir les objets avec des matériaux absorbants pour limiter les réflexions. Cette solution ne répond que partiellement à la problématique dans la mesure où elle n'améliore pas les possibilités de placement des antennes, voir même elle peut les limiter encore plus.

- Dans le cas très courant dans l'industrie d'un assemblage de composants, les champs

reconstruits peuvent être complexes et être eux-mêmes le résultat de la combinaison de plusieurs phénomènes (plusieurs sources de vibrations typiquement) qu'il serait intéressant de séparer pour améliorer la compréhension du processus de génération du bruit rayonné. Certaines méthodes, dites de séparation de sources existent et peuvent, sous certaines conditions, permettre d'extraire des informations pertinentes des champs reconstruits.

L'objectif de cette thèse est de montrer que la méthode de reconstruction de champs appelée inverse Patch Transfer Function (iPTF) permet de réponse à l'ensemble de ces problématiques industrielles. La méthode, développée depuis une dizaine d'années au Laboratoire Vibrations Acoustique, est basée sur le concept de volume acoustique virtuel entourant le système à étudier. Ce volume est délimité par l'enveloppe du système à étudier, par d'éventuelles surfaces rigides et par une surface virtuelle entourant l'objet d'étude. En fonction de la variante de la méthode iPTF utilisée (u-iPTF ou m-iPTF), la vitesse des particules d'air ou la pression acoustique seront mesurées sur la surface virtuelle, discrétisées en éléments de surface appelés « patchs ». Enfin, des mesures de pression acoustique seront également nécessaires à l'intérieur du volume virtuel. Ces mesures, combinées à une modélisation numérique du volume virtuel, permettent, en inversant le problème, de reconstruire les champs acoustiques directement sur l'enveloppe du système étudié, même si celle-ci est de forme complexe. Le volume acoustique modélisé numériquement (par éléments finis) est considéré « virtuel » car des conditions aux limites qui ne représentent pas la réalité du problème étudié sont imposées sur la surface elle-même également qualifiée de virtuelle. Les conditions aux limites virtuelles à imposer peuvent être de deux types : de Neumann (u-iPTF) ou de Dirichlet (m-iPTF). Le choix de la condition à la limite virtuelle conditionne la quantité qui devra être mesurée sur la surface virtuelle : vitesse des particules d'air pour u-iPTF et pression acoustique pour m-iPTF.
La méthode iPTF a déjà été appliquée avec succès pour reconstruire des champs acoustiques à la surface d'objets complexes tels qu'un bloc moteur d'automobile. Ses capacités de séparation de champs ont également été démontrées, lui conférant la possibilité d'être utilisée dans un environnement acoustique mal maîtrisé. Les travaux menés dans la présente thèse ont trois principaux objectifs :

- Etudier les problèmes liés à l'inversion du problème posé. En effet, comme presque toutes les méthodes inverses en acoustique, la méthode iPTF est mal posée et nécessite l'emploi d'une technique de régularisation lors du processus d'inversion de l'opérateur. De nombreuses méthodes sont étudiées et une nouvelle approche, basée sur une description Bayésienne du problème est proposée.

- Démontrer que la méthode iPTF peut être employée même en présence d'objets masquants. Une étude paramétrique est préposée : elle consiste en la reconstruction des champs acoustique à la surface d'une plaque appuyée masquée par un objet parallélépipédique, plus ou moins large et placé plus ou moins loin de la plaque. Cette capacité à gérer les objets masquants est également démontrée par une étude expérimentale portant sur la reconstruction des champs acoustiques à la surface d'un moteur électrique.

- Adapter le concept de séparation de sources dans la cadre de la méthode iPTF. L'objectif est ici d'obtenir non pas une seule cartographie pour les champs reconstruits mais N cartographies provenant des N sources ou phénomènes à l'origine du bruit rayonné. L'applicabilité de cette approche est démontrée sur une expérience numérique.

Le mémoire de thèse est organisé de la manière suivante :
Le chapitre 1 présente le contexte scientifique et technique des travaux menés. Il précise ainsi que les travaux de thèse ont été menés dans le cadre du projet Européen PBNv2 (Next Generation Pass-By Noise Approaches for modern powertrain vehicles) qui s'articulait autour de trois grands axes définissant le bruit de passage des véhicules : les sources, les chemins de transfert et la personne soumise au bruit. Les travaux de la thèse présentés ici s'intègrent dans la partie

« sources » du projet. Dans ce chapitre sont ensuite détaillées les principales méthodes de caractérisation de sources, qu'elles soient directes (mesure la puissance rayonnée par exemple) ou inverses (localisation ou reconstruction de champs).
Le chapitre 2 synthétise les principaux développements de la méthode iPTF qui sera utilisée tout au long des travaux de thèse présentés. Ainsi, le cadre théorique des deux variantes de la méthode est rappelé pour permettre au lecteur une meilleure compréhension des développements menés par la suite.
Le chapitre 3 traite de la problématique de régularisation d'un problème inverse mal posé dans le cadre de la méthode iPTF. Des nombreuses approches, toutes reformulées dans le cadre de la méthode iPTF sont proposées. Ainsi, des approches de type Tikhonov, des approches itératives et des approches statistiques sont détaillées. Dans les travaux menés précédemment, une régularisation Bayésienne, uniquement applicable à la méthode m-iPTF, avait été proposée. Dans le chapitre 3, une nouvelle approche statistique est proposée, permettant d'être appliquée dans le cadre des deux variantes.
Le chapitre 4 évalue les méthodes de régularisation présentées au chapitre 3 sur trois cas d'application différents, issus d'expériences numériques. Le premier est un cas idéal dans lequel les « mesures » ne sont pas entachées par un bruit perturbateur et le problème comporte autant d'inconnues que d'équations. Dans ce cas, seules les erreurs de méthodes et/ou de discrétisation peuvent être à l'origine de problèmes d'inversion. Le second cas porte sur l'introduction d'un bruit perturbateur ajouté aux mesures. Le rapport signal à bruit imposé varie de manière à évaluer l'impact de mesures bruitées sur la qualité des reconstructions de champs. Dans le dernier cas, le problème est sous-déterminé ce qui a un effet sur la qualité des reconstructions, notamment par les approches de Tikhonov.
Le chapitre 5 démontre que la méthode iPTF permet de gérer très facilement la présence d'objets masquants immobiles et rigides. Dans ce cas, le modèle numérique du volume acoustique virtuel doit intégrer l'empreinte de l'objet. Il suffit ensuite simplement d'imposer des conditions de murs rigides sur les surfaces de l'empreinte. Ainsi, grâce à l'équivalence entre les conditions aux limites réelles et virtuelles, la présence de l'objet masquant est intégrée dans le modèle numérique et ne nécessite aucune mesure spécifique. Dans ce chapitre, une étude paramétrique est menée pour étudier l'influence du pourcentage de la surface de la structure masquée (de 0 à 100%) et de la distance entre le système à étudier (ici une plaque plane) et l'objet masquant (de 1 cm à 15 cm). Dans les deux cas, la méthode iPTF démontre une robustesse très encourageante. Il est démontré également que la méthode iPTF permettait aussi de caractériser la directivité du système étudié comme s'il était placé dans un environnement anéchoïque alors que les mesures ont été réalisées dans un environnement non anéchoïque avec la présence de surfaces réfléchissantes ou d'objets masquants.
Le chapitre 6 est l'occasion d'appliquer la méthode iPTF sur un cas d'application industriel : un moteur électrique monté sur un banc d'essai. Les mesures ont été réalisées sur le banc de Siemens à Leuven en Belgique. Deux campagnes identiques ont été réalisées : elles diffèrent simplement par la présence ou non d'un panneau épais de bois faisant office d'objet masquant. Les résultats comparés entre eux et par rapport à une méthode (Bayesian focusing approach) reconstruisant les champs sur un plan démontrent que la méthode iPTF donnent des résultats très précis et indépendants de la présence d'objets masquants.
Enfin, dans le chapitre 7 une méthode de séparation de sources (blind separation) est développée pour la méthode iPTF. Elle permet, grâce à des critères de « décorrélation », d' « orthogonalité » ou de « séparation spatiale » (spatial disjointness) de séparer les contributions de sources décorrélées pour ensuite reconstruire les champs correspondants. Cette approche est évaluée sur une expérience numérique pour laquelle une procédure pour générer un champ acoustique dû au rayonnement de deux plaques excitées par des efforts ponctuels décorrélés est proposée. Après application de la méthode BSS-iPTF (Blind Source Separation) les champs reconstruits permettent de séparer les contributions des deux plaques, démontrant l'applicabilité de la

méthode.

Mots clés : inverse Patch Transfer Function, Méthode inverse, Reconstruction de champs acoustiques, régularisation, objet masquant, séparation de sources.

Abstract

Noise pollution generated by means of transport in general and cars in particular is a social problem which has a considerable impact on the life and health of people living in cities or near noisy infrastructures. To minimize this noise pollution, the public authorities impose demanding standards and regulations in terms of noise emitted, in particular by cars. To be able to meet this challenge, transport manufacturers must integrate these criteria from the design of vehicles because palliative solutions are no longer sufficient. Nowadays, the design of systems is mainly carried out via numerical simulations, but experimental measurement campaigns are always valuable for both improving the understanding of the phenomena at the origin of noise sources and allowing the results of numerical simulations to be correlated to experimental data. As a result, the methods of experimental characterization of noise sources have revealed great interest on the part of industrialists. These methods are either direct measurement methods or so-called inverse methods. In this case, the objective is to observe the consequence to identify the cause. There are generally two categories of inverse methods for characterizing sources in acoustics: methods for localizing acoustic sources and methods for reconstructing fields. Despite the extensive research expected over the years, acousticians and NVH (Noise Vibration Harshness) engineers will continue to encounter difficulties, in particular because of the industrial context of the experimental measurements, which differ from the laboratory conditions in which the methods are generally developed. When the objective is the reconstruction of the acoustic fields (velocity, pressure, intensity) at the surface of the object of study, several difficulties, specific to the industrial context, may arise:

- The designed system is generally an assembly of parts and components forming a complex and three-dimensional geometry. A large part of field reconstruction methods such as the Nearfield Acoustic Holography (NAH) method does not allow the acoustic fields to be reconstructed except on a surface of simple geometry (most often flat) close to the real system. However, this makes the interpretation of results and their use (to feed a numerical model for example) particularly difficult in the case of systems with complex geometry.

- The acoustic field of the measurement room only very rarely meets the conditions found in an anechoic laboratory room. The test bench is generally placed in a quiet space (walls treated acoustically but not perfectly anechoic) but disturbing sources may also have to be present there. This is the case, for example, of electrical cabinets, drive motors or brakes. The source characterization methods used must be able to overcome this poorly controlled acoustic environment by integrating, for example, field separation techniques, isolating the noise coming from the system to the one coming from the environment.

- The studied system is most of the time maintained or suspended on frames or load-bearing structures. Similarly, other objects can be placed in the immediate vicinity of the system considered. Finally, the studied system can itself be fixed on a massive structure. All these situations have in common the presence of masking objects in the immediate environment of the system generating reflections of the radiated waves and limiting the possibilities of access by a means of measurement (typically a microphone antenna) in certain zones around the object. A palliative solution is to cover objects with absorbent materials to limit reflections. This solution only partially solves the problem insofar as it does not improve the possibilities of placement of the antennas, or even it can limit them even more.

- In the very common case in industry of an assembly of components, the reconstructed fields can be complex and themselves be the result of the combination of several phenomena (several sources of vibrations typically) that it would be interesting to separate to improve understanding of the radiated noise generation process. Certain methods, known as source

separation methods exist and can, under certain conditions, make it possible to extract relevant information from the reconstructed fields.

The objective of this thesis is to show that the field reconstruction method called inverse Patch Transfer Function (iPTF) provides an answer to all of these industrial issues. The method, developed over the past ten years at the Laboratoire Vibrations Acoustique, is based on the concept of virtual acoustic volume surrounding the system to be studied. This volume is delimited by the envelope of the system to be studied, by any rigid surfaces and by a virtual surface surrounding the object of study. Depending on the variant of the iPTF method used (u-iPTF or m-iPTF), the particle velocity or the acoustic pressure will be measured on the virtual surface, discretized into surface elements called “patches”. Finally, sound pressure measurements will also be necessary inside the virtual volume. These measurements, combined with a numerical modeling of the virtual volume, make it possible, by reversing the problem, to reconstruct the acoustic fields directly on the envelope of the system studied, even if it is of complex shape. The acoustic volume modeled numerically (by finite elements) is considered "virtual" because boundary conditions which do not represent the reality of the problem studied are imposed on the surface itself, also qualified as virtual. The virtual boundary conditions to be imposed can be of two types: Neumann (u-iPTF) or Dirichlet (m-iPTF). The choice of the virtual boundary condition determines the quantity that must be measured on the virtual surface: air particle velocity for u-iPTF and acoustic pressure for m-iPTF.
The iPTF method has already been successfully applied to reconstruct acoustic fields on the surface of complex objects such as an automobile engine block. Its field separation capabilities have also been demonstrated, giving it the possibility of being used in a poorly controlled acoustic environment.
The work carried out in this thesis has three main objectives:

- Study the issues related to the inversion of the problem posed. Indeed, like almost all inverse methods in acoustics, the iPTF method is ill-posed and requires the use of a regularization technique during the operator inversion process. Many methods are studied and a new approach, based on a Bayesian description of the problem is proposed.

- Demonstrate that the iPTF method can be used even in the presence of masking objects. A parametric study is required: it consists of the reconstruction of the acoustic fields on the surface of a supported plate masked by a parallelepipedal object, more or less wide and placed more or less far from the plate. This ability to manage masking objects is also demonstrated by an experimental study on the reconstruction of acoustic fields on the surface of an electric motor.

- Adapt the concept of source separation within the framework of the iPTF method. The objective here is to obtain not a single map for the reconstructed fields but N maps from the N sources or phenomena at the origin of the radiated noise. The applicability of this approach is demonstrated on a numerical experiment.

The thesis is organized as follows:
Chapter 1 presents the scientific and technical context of the work carried out. It thus specifies that the thesis work was carried out within the framework of the European project PBNv2 (Next Generation Pass-By Noise Approaches for modern powertrain vehicles) which was articulated around three main axes defining the noise of passing vehicles: the sources, the transfer paths and the person subjected to the noise. The work of the thesis presented here is the aspect of the “sources” section of the project. This chapter then details the main source characterization methods, whether direct (measurement of radiated power, for example) or inverse (localization or reconstruction of fields).
Chapter 2 summarizes the main developments of the iPTF method that will be used throughout the thesis work presented. Thus, the theoretical framework of the two variants of the method are

recalled to allow the reader a better understanding of the developments carried out thereafter.
Chapter 3 deals with the problem of regularizing an ill-posed inverse problem within the framework of the iPTF method. Numerous approaches, all reformulated within the framework of the iPTF method, are proposed. Thus, Tikhonov-type approaches, iterative approaches and statistical approaches are detailed. In previous work, a Bayesian regularization, only applicable to the m-iPTF method, was proposed. In chapter 3, a new statistical approach is proposed, allowing to be applied within the framework of the two variants.
Chapter 4 evaluates the regularization methods presented in Chapter 3 on three different application cases, resulting from numerical experiments. The first is an ideal case in which the "measurements" are not marred by disturbing noise and the problem has as many unknowns as there are equations. In this case, only the errors of methods and/or discretization can be at the origin of problem of inversion. The second case concerns the introduction of a disturbing noise added to the measurements. The imposed signal-to-noise ratio varies so as to assess the impact of noisy measurements on the quality of field reconstructions. In the last case, the problem is under-determined which has an effect on the quality of the reconstructions, in particular by Tikhonov's approaches.
Chapter 5 demonstrates that the iPTF method makes it very easy to manage the presence of immobile and rigid masking objects. In this case, the numerical model of the virtual acoustic volume must integrate the "footprint" of the object. Then simply impose rigid wall conditions on the surfaces of the footprint. Thus, thanks to the equivalence between the real and virtual boundary conditions, the presence of the masking object is integrated into the numerical model and does not require any specific measurement. In this chapter, a parametric study is carried out to study the influence of the percentage of the masked surface of the structure (from 0 to 100%) and the distance between the system to be studied (here a flat plate) and the masking object (from 1 cm to 15 cm). In both cases, the iPTF method demonstrates a very encouraging robustness. It is also demonstrated that the iPTF method thus made it possible to characterize the directivity of the system studied as if it were placed in an anechoic environment whereas the measurements were carried out in a non-anechoic environment with the presence of reflecting surfaces or masking objects.
Chapter 6 is an opportunity to apply the iPTF method to an industrial application case: an electric motor mounted on a test bench. The measurements were carried out on the Siemens bench in Leuven, Belgium. Two identical campaigns were carried out: they differ simply by the presence or not of a thick wooden panel acting as a masking object. The results compared with each other and with a method (Bayesian focusing approach) reconstructing the fields on a plane demonstrate that the iPTF method gives very precise results independent of the presence of masking objects.
Finally, in chapter 7 a source separation method (blind separation) is developed for the iPTF method. It allows, thanks to criteria of "decorrelation", "orthogonality" or "spatial separation" (spatial disjointness) to separate the contributions of decorrelated sources in order to then reconstruct the corresponding fields. This approach is evaluated on a numerical experiment for which a procedure to generate an acoustic field due to the radiation of two plates excited by decorrelated point forces is proposed. After application of the BSS-iPTF (Blind Source Separation) method, the reconstructed fields make it possible to separate the contributions of the two plates, demonstrating the applicability of the proposed method.

Keywords: inverse acoustics, regularization, iPTF method, blind identification, blind separation.

Contents

1 Scientific and technological context

1.1 Societal challenges

It is generally accepted that noise is not only an immense ecological challenge but also an unpredictable risk to human health. Since the development of big cities and the increasing number of motor vehicles on the streets and roads, this issue persists [1].

1.1.1 Human health effects

Exposure to noise pollution is a major problem more now than before. As urban sprawl continues, with more than half of the world's population and three quarters of the European Union (EU) now living in urban areas [2, 3], even more people are subjected to noise pollution.

Exposure to night-time noise triggers sleep disruption [2, 4], which has many negative health effects [5, 6, 7]. Noise exposure in the evening hours and during the night period has important health effects as it impacts sleep and thus stress. Sleep is also an essential mediator of cardiovascular function [2, 8]. Noise exposure has also been associated with reduced cognitive performance, hormonal abnormalities, diabetes, stroke and mental disorder [9, 10, 11, 12, 13]. The health implications of noise is widely acknowledged, particularly in relation to cardiovascular effects. Research demonstrates that ambient noise is linked to an increased risk of high blood pressure, heart attack and stroke [2, 14].

For World Health Organization (WHO) [15], ample evidence is now available that connects human exposure from environment noise to adverse health effects, rendering environmental noise a significant environmental health issue, next only to air pollution [2, 15].

1.1.2 Noise mitigation

The intricate and persistent problem of noise pollution does not have a concrete answer; it needs a mix of short-, medium- and long-term methods and critical analysis of the existence of the noise source [2]. There are several causes of noise pollution, each requiring personalized mitigation steps.

For example, in cars, fuel engine is a dynamic source of vibrations and noise emissions. Passengers in vehicles hear the amount of airborne noise and structure borne transfer noise to the interior of the vehicle and the contribution of aerodynamic and tire rolling noises. However, in most situations, passenger can not discriminate between various types of noise inside the car. Therefore, drivers and passengers are not merely prone to their own car noise but from all other road vehicles as well [1].

Many parts in a vehicle contribute to the cumulative emission of the noise of a car radiating between 60 and 70 dBA (see Figure 1.1) [16]. The major source of environment noise is road

traffic noise [17], the pollution is far beyond those associated with rail and aviation emissions [18], as seen in Figure 1.2.

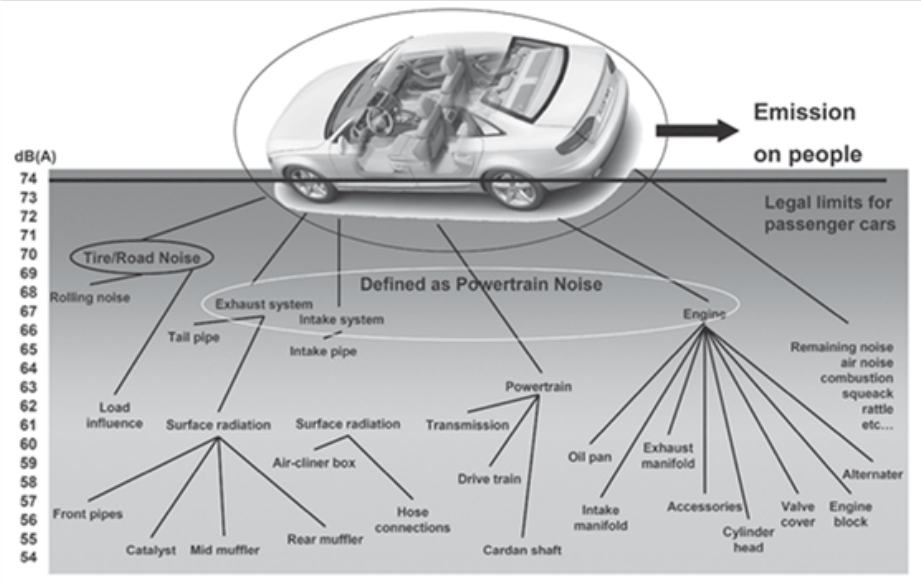

Figure 1.1: Components with Influence on noise [16]

In urban areas, 80% of the noise pollution is caused by road traffic [19]. It is projected that, in general, about 24% of the population of Europe is subjected to noise in and outside urban areas. The noise of road traffic produces a combination of rolling noise (due to vibrations and contacts between the vehicle's tyre and the road's surface) and noise of combustion (emanating from the motor). The rolling noise predominates as vehicles drive more than around 30 km/h, while combustion noise is the principal noise source below this point.

Noise from vehicles may be cut at source by interventions related to cars, tyres, road

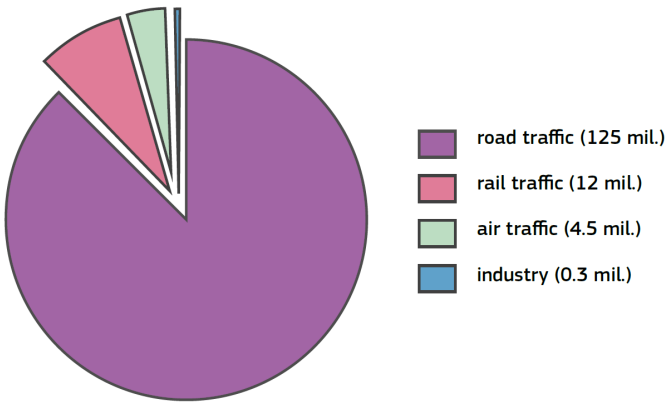

Figure 1.2: Sound-level distribution of the European population above 55 dB L_{den} by a noise source (millions). It includes people live in big cities (> 100,000 inhabitants) and near major facilities [2, 17, 20]

conditions and traffic control and infrastructure or by anti-propagative or insulation steps to decrease people's exposure. Some EU rules concentrate on reducing source noise, such as setting restrictions on vehicles encouraging less noisy pneumatic tyres, and designing low-rise road surfaces. Silent motors and hybrid cars also offer more options. Low-noise road surfaces have substantial potential for noise control which supplement approaches that minimise engine combustion and pneumatic noise in passenger cars and larger vehicles [1, 21].

1.1.3 Noise policies and regulations

The acoustics in the passenger cabin today is one of the vehicles' most significant characteristics. Noise in the car is important and reduces the impact of other car functions. Thus, the feeling of a high-quality car is missed because the noise is irritating. For this reason, automotive manufacturers pay careful attention to automotive noise control. Over the years, in response to consumer demands, the interior noise of the car has decreased dramatically. In the last 40 years, there have been significant improvements in reducing differences in interior noise levels among family and luxury vehicles.

However, sometimes, the acoustic issue is the opposite. For instance, new luxury, battery and autonomous cars have now slipped below the optimal noise levels. They are then too silent [1] which can increase the danger of vehicles, especially for the visually impaired.

The ISO and its 43 Technical Committee (ISO/TC 43) [1, 22] are investigating in global acoustic issues, some of which apply to the sound problems in the car. The United Nations Economic Commission for Europe (UNECE) has already issued a range of automotive noise laws beginning with Directive 70/157/ altogether in 1970 [1]. In recent years, standards for automotive acoustics have grown, due to growth in consumer demand and health concern. In compliance with the Environmental Noise Directive (END) 2002/49/EC, nearly 125 million residents are usually subject to unacceptable levels of traffic noise. The limit level of noise monitoring and action planning standard of END are 55 dB for the day-evening-night noise predictor, L_{den}, and 50 dB for the night-time noise predictor, L_{night} [23, 21]. As a result, innovations and changes often comes along with it. This raises the value of reducing vehicle weight and costs. However, because more engine capacity, price factor and vehicle recycling regulations are required, a balance must be found, particularly between weight and acoustic comfort, strength and price and regulation [1].

1.1.4 PBNv2 Project

The modern cars represent a dynamic balance between conflicting safety, exhaust emissions, noise, efficiency and price specifications. However, as already said, it is commonly accepted that the quality of life are highly affected by air and noise emissions from road transport, especially in the urban environments [16]. In this context, a number of stakeholders, including leading academics, research institutes and leading car-related manufacturers, have collectively decided to follow a coordinated solution in order to better address the traffic pollution challenges facing our community. The PBNv2 project [24, 25] came into being.

The proposed PBNv2 project (Next Generation Pass-By Noise Approaches for modern power-train vehicles) is based on the above-mentioned social challenges related to traffic noise and aims to optimally overcome this issue. The ultimate goal of the PBNv2 project is to develop pass-by noise technologies for silent and safe vehicles in the next decade. As a result the project aims to build scalable, interconnected technologies, taking into consideration renewable technology advances as well as reducing noise and vibration on modern vehicles fitted with a next-generation highly fuel/energy efficient power drives. The project lays out a number of basic strategic goals focused on this submission, which include:

- Development of improved pass-by noise measurement techniques.
- Improvement of automobile model manufacturing strategies and innovations to reduce the noise effect of single cars more efficiently than changes in traffic.
- Build noise and vibration control methods to tackle the evolving challenges in lightweight electrification.

- Describe the acoustic criteria for secure electric vehicles in urban traffic in terms of auditory perception by pedestrians with hearing disabilities, in particular visually disabled persons and elderly people.

The project trains early stage researchers in creative subjects in the field of noise engineering through theoretical and practical education. The project discusses the different facets of pass-by noise: the 'source', the 'transfer path' and the 'receiver'.

This doctoral thesis is part of PBNv2 project and focuses specifically on the source aspect of the pass-by noise. The overarching aim of this PhD work is to develop experimental methods to enhance understanding origins of vehicle noise. This addresses the industrial problem in the identification, localization, ranking and classification of simultaneous noise sources of diverse origins.

1.2 Direct characterization of sources

A means of characterizing a source is the description of all the properties and quantities that characterize the behaviour of a source. Experimental characterization of acoustic sources can be divided into two distinct categories: direct (forward) and indirect problems (inverse) [26]. The direct approach of the source characterization is discussed in this section. The solution process involves the direct measurement of the radiated field due to the vibrations of the source (see Figure 1.3).

Different metrics exist to characterize the acoustic source behavior. One can cite the radiated

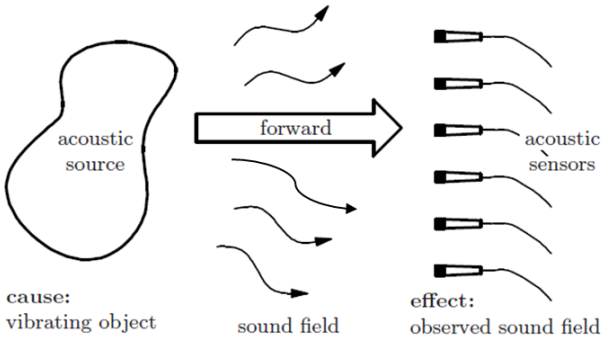

Figure 1.3: Illustration of the forward acoustic problem [26].

power, the intensity field, the wall pressure and velocity fields or the radiation efficiency. Thus, measuring directly involves performing experiments. This section addresses the questions: which quantities to measure? How are they measured? And which sensors are to be used?. Some traditional and current methods for direct source measurement are also described in this section.

1.2.1 Acoustic quantities usually measured

In order to optimize the vibro-acoustic behaviour of a source, the first step consists in characterizing it by using different metrics. For a source delimited by a vibrating surface and placed in the air (weak coupling hypothesis), the following information ensures the complete characterization of the source [27]:

- The normal acoustic velocity field at the surface of the source. This is local information often used as input for numerical vibro-acoustic simulations.
- The surface pressure field is the "complementary" acoustic quantity of the velocity field. Combined, they determine the surface impedance of the source and its intensity field, two local characteristics of acoustic radiation.

- The active sound intensity field normal to the source surface is the main information, which characterizes the source. This indicates the regions on the source surface radiating in the far field.

- The radiated sound power is the integral of the intensity on the surface of the source. This scalar globally quantifies the power level emitted by the source. It allows to easily compare different configurations or parts between them and to prioritize them according to their respective influence.

- The radiation efficiency assesses the ability of the source to transform its vibrations into noise radiated in the far field. This overall amount thus reflects the effectiveness of the radiation.

Knowledge of these quantities makes it possible to completely characterize the vibro-acoustic behavior of a source. Access to these quantities is possible by numerical simulation, but the modeling and predictability of numerical models are still today limited. The experimental characterization of the sources therefore remains relevant, both in the development and optimization process of physical structures and in the validation of numerical models.

1.2.2 Measurement techniques

The sound pressure that we hear or measure with a microphone depends on the distance from the source and the acoustic environment (or sound field) in which the sound waves are present. This depends on the size of the space and the sound absorption of the surfaces. So, by measuring sound pressure, it is not possible to characterize the source independently from its environment. In addition, in case of noise emitted by a machinery with different components, it is difficult using pressure measurement to rank the contribution of each part of the system. For this aim, the sound power of the individual component has to be measured and listed in the order of the highest sound power. This ranking paves the way of optimizing the design of the components that are responsible of the radiated noise.

Sound power can be associated with sound pressure only under carefully controlled conditions where special assumptions are made about the sound field. Specially constructed rooms, such as anechoic or reverberant chambers, meet these requirements. Traditionally, in order to measure sound power, the noise source had to be mounted in these rooms [28]. However, the sound intensity can be determined in any sound area. This property allows all measurements to be performed directly in situ. And measurements may be made on individual machines or components, even though all others are radiating noise. Since sound intensity provides a measure of both direction and amplitude, it is also very useful when identifying sound sources. The radiation patterns of complex vibrating machines can therefore be investigated in situ [28].
Methods for evaluating the source of sound power to ensure different grades of quality are set out in a sequence of international standards [29, 30, 31]. Sound intensity measurements can be used as a general diagnostic tool to determine the distribution of sound power to separate components of extended sound sources, such as industrial equipment, as aids in the specification of noise control procedures [32, 33].

1.2.2.1 Measurement Surfaces

To measure a sound source, a measurement surface is often built around that source. The measurement surface is a hypothetical surface on which acoustic measurements are made, and which either completely encloses the source under test, or in conjunction with an acoustically rigid, continuous surface, encloses the noise source under test. The measurement surface is usually subdivided into a set of smaller areas known as segments [34], elements or patches. The

measurement surface could be hemisphere, rectangular or conformal as shown in Figure 1.4 [28, 35].

The measurement surface is chosen as long as no other sources or sinks (absorbers of sound)

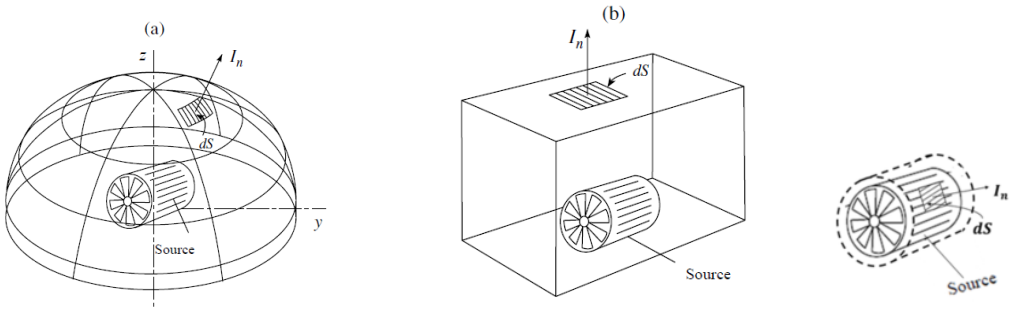

(a) (b) (c)

Figure 1.4: Measurement surfaces and Sound intensity measured on a segment of (a) a hemispherical measurement surface and (b) a rectangular measurement surface and (c) conformal measurement surface (I_n is the intensity vector normal to the elemental surface dS).

are present within the surface. The surface may, in theory, be at any distance from the source. According to ECMA [34], one can define the shortest distance between the physical sound source surface under test and measurement surface as measurement distance. The three often used examples are described in the next paragraph.

First, the rectangular measurement as seen in Figure 1.4(b). This surface is easy to define and the planar surfaces make averaging the acoustic quantities such as intensity over the surface a simple matter. The partial sound powers can be found from each side and added. Second, the hemisphere as seen in Figure 1.4(a). This shape is most likely to give the least number of measuring points. International Standard ISO 3745 (sound power from pressure measurements) [28] recommends starting with ten measurement positions; three microphone positions on three radii and one on the top of the hemisphere. If the intensity varies too much over this surface, the number of positions should be increased. Third, the conformal shape as seen in Figure 1.4(c). This allows near field measurements which will improve the signal-to-noise ratio. The measured sound intensity can also be related back to the specific source locations [28].

Another important source quantity to consider is the radiation efficiency or radiation ratio [36] of a vibrating structure. This is a dimensionless quantity that indicates how much sound power a given structure radiates compared with an ideal case of a piston of the same surface area radiating plane waves and vibrating with a mean-square velocity equal to the spatially-averaged mean-square velocity of the structure. Thus to determine the radiation efficiency, two measurements are required: an acoustic measurement, namely the radiated sound power as described above, and a mechanical measurement, namely the spatially-averaged squared velocity using vibration transducer such as Laser Doppler Vibrometers (LDV) [36, 37] or accelerometers. These must be measured for the same excitation conditions.

1.2.2.2 Measurement procedures

Over time, several techniques and apparatus have been suggested in order to characterize the source. Notwithstanding the post-processing methods used, the existing measurement procedures for characterizing sound fields can be divided into three key categories: point-by-point, simultaneous and scanning measurements.

Point-by-point (discrete point) measurement [28, 38, 34, 37] is one of the most common techniques for generating spatial representations of stationary sound fields. The measurement method involves the formation of a measuring surface with a grid on it. The grid may be a string

or wire frame [28]. Measurement is then performed for each noise component to be identified at each grid location as shown in Figure 1.5(a). Output is a data vector for each grid point. The approach is therefore based on the collection of data at a set of discrete positions. Flexibility of this approach is one of its key benefits, as the number of transducers and their spatial distribution are adjustable. The number of sensors used is directly related to the cost of the experiment, but inversely proportional to the time required to perform the measurements. In the event that all locations are found at the same time, a large multi-channel device must be used and, thus, simultaneous measurements must be carried out.

Simultaneous measurement [38, 37] is used to produce spatial representations of stationary and transient noise. The measurement method includes the identification of a measuring surface with a grid on it and the assignment of a sensor at each grid position to form a sensor array as shown in Figure 1.5(b). The data acquisition system must have the necessary channels to accommodate all the sensors used. Usually, a colormap of the time-domain noise distribution is generated. Pressure, particle velocity and intensity can be measured using this process. Conventionally, sensor-based systems are expensive and have low versatility due to their complexity. Alternatively, scanning methods can be used to reduce the time of measurement and the cost of providing a time-stationary sound field.

The *Scanning measurement* technique of scanned metrics [28, 35, 34] differs fundamentally from the above: data are no longer gathered at distinct spatial sites, as sensors or set of sensors are pushed in each segment of the selected area of measurement along the defined paths as shown in Figure 1.5(c) during the acquisition process. The reported acoustic signal has an associated scanning path defining the sensor position during the measurement. The short interval of time when the sensor passes over the region of interest (segment) will estimate the spectral content at the specific position. In other words, through the motion of the probe on the scan line, the temporal average is equal to the spatial average. The scanning process should be conducted such that the indicated scanning path is precisely followed, the sample axis is always perpendicular to the surface measurement and the movement speed of the measuring transducer is consistent. Manually or mechanically, scanning may be performed. To limit the error to an acceptable limit, a scanning speed of more than 0.3 m/s or less than 0.1 m/s should be performed [34]. In the case of machined scanning, these criteria may be technically met carefully on any surface measurement type (as illustrated in Figure 1.4(c)). These criteria are almost impossible to achieve with manual scanning. Therefore, as shown in Figure 1.4(b), normal surface shapes are favored. The basic element of a scan is a straight line. The scan path comprises a number of parallel straight lines that cover each section. The distances between the adjacent lines shall not be more than half the average distance from the source surface of the section. Adjacent lines are linked by semicircular paths between their extremities or may be suspended temporarily by signal acquisition as the sample passes between adjacent lines [28]. Scan-based techniques typically require costly and complex tracking systems. Despite their capacities, scan-based measurement techniques have earned far too little recognition. Several attempts have been made to increase their ability by using microphone scan arrays with acoustic holography algorithms [39, 40, 41, 42, 43, 44]. The high costs of the scanning systems and the complex experimental set-up have nevertheless limited the application of this efficient measurement technique.

The above-mentioned techniques can also be used to collect data across a sound field, depending on how the phase data is collected. Firstly, to get the phase information completely characterized, it is necessary for sensors to be placed at each point to be evaluated (simultaneous measurement). For most applications, this is a costly and impractical strategy. The use of relative phase information is sufficient in some situations. A single or collection of fixed reference sensors may therefore be used to maintain a relative phase connected to a certain location on the field. In this case, scanning or point-by-point measurements may be carried out. Third, if phase information can be considered negligible, point by point or scan-based measurements can then be used to acquire data in an asynchronous manner, thus collecting only variations in magnitude

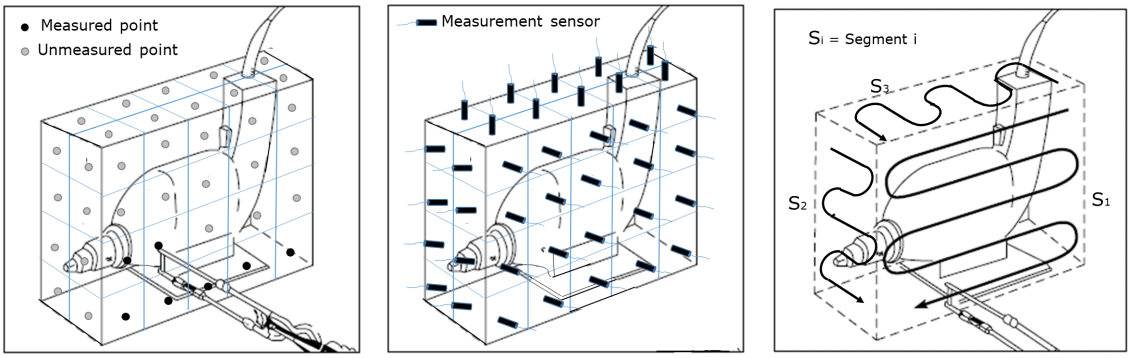

(a) (b) (c)

Figure 1.5: Measurement procedures: (a) discrete point measurement, (b) simultaneous measurement and (c) scanning measurement [28, 35, 34, 45].

across the region of measurement [37].

1.2.3 Limitations and challenges of direct measurements

In brief, direct experimental methods for characterizing a source are appealing, as they do not require a propagation model or base functions to imitate the measuring environment. They are often less reliant on theoretical models and are therefore the best way to achieve accurate and consistent source characterization. Also, they provide direct measurements of specific acoustic quantities such as sound pressure level, particle velocity level, sound intensity and sound power level. Their limitations are [27]:

- They provide specific acoustic quantities at the measurement locations only.
- It is difficult to pinpoint the location of a noise source, which is especially true when there are other sources or reflecting surfaces nearby.
- It is not possible to identify the structural waves that are traveling along the surface or to visualize the out-of-plane vibration pattern, which may have a direct impact on the resultant structure-borne sound.
- These direct experimental measurements can become tedious or even impossible to achieve for complex source geometry and a potentially congested environment (obstacle, wiring, etc.).
- In certain instances the direct approaches can be costly, inapplicable or difficult to use.

Due to the above concern, it has prompted scientists to research alternate solutions of resolving these issues. The indirect acoustic methods introduced and discussed in the next section 1.3 form part of the solution techniques.

1.3 Source localization, identification and mapping methods

The process of characterizing the source involves one or a combination of the following process: source localization (find the source spatial position), source identification (retrieving source field quantities) and source field visualization (map images of source quantities). The toughest challenge facing any acoustics engineer is figuring out where the sound originates – especially when there is considerable interference and reverberation flying around. Thus the acoustic source characterization is an increasingly important aspect in acoustic [46].

In general, the methods fall into two categories depending on the position of the acoustic array with respect to the test object: far-field array technology and near-field array technology. This is illustrated in Figure 1.6. The former usually takes place far from the source(s) providing directional information of the surrounding field, whereas the latter is based on the measurement in the proximity of the source and the following reconstruction of the acoustic quantities on its surface [47]. The farfield methods are usually used for source localization whilst the nearfield methods are for source identification. Although various configurations of the measurement array (planar, cylindrical, spherical,...) are usable for both techniques, the subsequent signal processing usually differs [47].

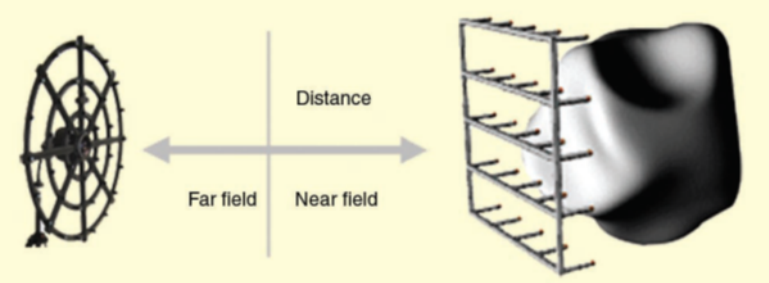

Figure 1.6: Technique relies on distance to object [46].

Microphone signal processing techniques using far-field and near-field arrays, as detailed in this section, have a different purpose than their known usage of speech enhancement in telecommunications. Instead, this section primarily aims at noise source localization, identification and sound field visualization for noise analysis and control engineering. The techniques mentioned in this section are the most utilized methods currently. This section reviews available techniques and explains how the methods have evolved over the years.

1.3.1 Far-field localization methods

Acoustic source localization (ASL) [48] methods determine the location and strength of the sources which are the cause of sound based on measurements of the sound field. This section reviews many facets of the acoustic source localization technique, its problem as well as the development and implementation. The aim of a far-field ASL system is to estimate the position of sound sources in space by analyzing the sound field with a microphone array, a set of microphones arranged to capture the spatial information of sound. From a conceptual point of view, the localization of acoustic sources is simple. However, the performance of these systems involves considerable complexity and still remains an open field of research [49]. Multi-channel signal processing for sound localization can be divided into two categories: Time Delay Estimation (TDE) and Steered Response Power (SRP) beamforming.

1.3.1.1 Time Delay Estimation

Time difference of arrival (TDOA) is a technique that involves using two or more receivers to locate a signal source from the different arrival times at the receivers. Popular techniques used to estimate TDOA are the classic Cross-Correlation, the Generalized Cross-Correlation (GCC) [50] and its derivatives, such as Generalized Cross-Correlation using Phase Transform (GCC-PHAT) and the Cross Power Spectrum Phase (CSP) and the Adaptive Eigenvalue Decomposition (AED) [51] based on the Blind System Identification (BSI), which focuses on the impulse responses between the source and the microphones. However, these methods are defined for an anechoic environment, so they do not help localize reverberated sound sources.

There has been development made to show that for any array containing M microphones (M $>$ 2), the Steered Response Power Phase Transform (SRP-PHAT) [52] provides the sum of the

GCC-PHAT from all of the microphone pairs. The Multichannel Cross-Correlation Coefficient (MCCC) [53, 54] uses the spatial prediction error to measure the correlation among multiple signals and uses the redundant information between microphones to estimate the TDOA in a more robust manner under a reverberant and noisy condition. The extension of the AED in the case of multiple microphones was proposed in Huang and Benesty [55], and it is called Adaptive Blind Multichannel Identification (ABMCI). In contrast, the SRP is based on maximizing the power output of a beamformer. Recently, more sophisticated algorithms have been proposed for time delay estimation that use Minimum Entropy [56, 57] and broadband Independent Component Analysis (ICA) [58]. Salvati [49] demonstrated in his thesis work that the ICA-based methods are more robust against high background noise levels compared with the conventional GCC-PHAT approach.

A widely used approach, called the indirect method, is used to estimate source positions and consists of two steps. In the first step, a set of Time Difference Of Arrivals (TDOAs) are estimated using measurements across various combinations of microphones. In the second step, when the position of the sensors and the speed of sound are known, the source positions can be estimated using geometric considerations and approximate estimators. These are closed-formed estimators [59] based on a least squares solution [60, 61, 62, 63, 64, 65] and iterative maximum likelihood estimators [66, 67, 68, 69].

However, the direct method yields an acoustic map of the area, from which the position of the sources can be estimated directly and spatial likelihood functions can be defined [70, 71, 72, 73, 74].

Both of these procedures have been tested in many single source scenarios; however, in multiple sources cases, they require new considerations. Several works address the problem of multiple sources using a Bayesian approach based on the tracking of the sources and using Kalman filter [75, 76, 77, 78, 79, 80, 81] and particle filter [82, 73, 83, 84, 85, 86].

1.3.1.2 Beamforming

Acoustic source localization techniques in combination with microphone array measurements have become an important tool in the development of new products. Moreover, these techniques can be used for failure diagnosis and monitoring as well as for sound design or noise reduction tasks. One well known technique in this area is the Beamforming method. Beamforming first introduced by Billingsey et al. [87] is based on evaluating simultaneously collected sound pressure data from microphone array measurements in far field taking into account the phase differences between the microphones and their known locations. The sound pressure obtained at different microphone positions are mapped to an image of the acoustic source field. This obtained source map is referred to as beamform map which indicates the location and strength of acoustic sources [88]. The beamform map is usually an amplitude of the pressure recorded, the higher levels indicate the presence of a source. As a rule of thumb, the far field is defined as being further away from the source than the array dimensions or diameter [89].

Beamforming is a widely applied method for imaging noise sources [87, 90]. It is used to determine source locations and distributions, measure acoustic spectra for complete models and sub-components, and project results from the array to far field points [88]. The method is based on the phase differences between the microphones and their known locations. In other words, beamforming is considered as a combination of the delayed signals from each microphone in a manner in which an expected pattern of radiation is preferentially observed. The conventional beamformer is the Delay and Sum (DS) [91]; it consists of the synchronization of signals that steer the array in a certain direction, and it sums the signals to estimate the power of the spatial filter. The high-resolution SRP has been developed to improve the performance of the spatial filter, and the adaptive beamformer is called the Minimum Variance Distortionless Response (MVDR) according to Capon [92]. The MUltiple Signal Classification (MUSIC) algorithm is based on an eigen subspace decomposition method [93, 94], and the Estimation of Signal Parameters via Rotational Invariance Techniques (ESPRIT) is based on subspace decomposition exploits the

rotational invariance [95, 96, 97].

Beamforming has been applied effectively for localizing and identifying acoustic sources on moving objects [98], high-speed trains and civil aircrafts in aeroacoustics [99, 100, 101]. At present, beamforming methods employing microphone arrays combined with signal processing technology have been widely used for both two-dimensional (2D) and three-dimensional (3D) acoustic source localization in numerous fields [102, 103, 104]. In the work of Ding et al. [89], layer-by-layer scanning of the sound source field is achieved and thus realizes 3D acoustic-source localization and 3D sound source image output.

Beamforming methods have been extensively applied for 2D localization using planar microphone arrays, which can locate an acoustic source in the XY plane parallel to the array, but cannot identify the distance between the source and the array in the Z direction, denoted as the source depth. For example, generalized cross-correlation (GCC) beamforming has obtained precise 2D acoustic-source localization results in the time-domain [105]. Similarly, chirp Z transform (CZT) digital beamforming has been proposed for far-field acoustic-source localization in the frequency domain [106]. This method was demonstrated to overcome typical problems affecting other frequency-domain beamforming techniques such as zero-padded fast fourier transform beamforming. In particular, the accelerated proximal gradient singular value thresholding-based linearly constrained singular canceler (APG-LCSC) algorithm [107] has been demonstrated to provide highly accurate 2D beamforming using a sparse array.

In 3D beamforming methods based on 3D microphone arrays, the concept of spherical harmonics has been employed with a spherical microphone array [108], and GCC has been employed with a polyhedral microphone array [109] for near-field reconstruction. Deconvolution based on spherical harmonics [110] and functional delay and sum (FDAS) [111] beamforming methods with spherical arrays have been shown to provide good spatial resolution and low sidelobes in the near-field. Moreover, FDAS with ridge detection (RD) and FDAS with RD and a deconvolution approach for the mapping of acoustic sources (DAMAS) [112] realized rapid acoustic-source localization as well as high resolution. Similarly, both generalized inverse beamforming (GIB) [113] and functional GIB (FGIB) [114] exhibited these characteristics using a double-layer microphone array.

According to the above discussion, previous beamforming methods employing planar microphone arrays have mainly focused on acoustic-source localization on a 2D surface. While these methods provide an acoustic field hologram, they cannot determine the source depth, so they are inappropriate for 3D source localization [87, 115, 116, 117, 118, 119, 120, 121]. However, present applications are increasingly concerned with acoustic sources located on the surfaces of complex objects or on complicated structures in 3D space. Yet, research regarding 3D acoustic-source localization remains relatively rare, and beamforming methods employing 3D microphone arrays remain limited to near-field reconstruction. And also compared with the 3D microphone array [122], using the 2D planar can also achieve three-dimensional recognition ability with greater adaptability. Furthermore, quantitative analyses of localization error and the influence of frequency have been rarely investigated [123, 124].

In summary, the beamforming relies upon the farfield assumption that the sources are far away and the waves become spherical or planar at the array position. It is essentially a remote localization technique of the sound source, which ensures that the evanescent sound field is not recorded. For this reason, beamforming therefore cannot be seen as sound field reconstruction techniques and offers only an estimated relative map 'source strength' and not a quantitative reconstruction. As a results beamforming does not really provide information on acoustical variables of the noise sources and their radiated sound field [125, 37, 47].

1.3.2 Near-field identification methods

Apart from the prior farfield array technologies, acousticians also developed nearfield arrays in the 1980s. These nearfield array techniques were given the name "nearfield acoustical holography"

(NAH) when they were first introduced [125].

Sound source localization by Nearfield Acoustical Holography (NAH) [126, 127, 128, 129] is an approach that has been continuously developing since the 1980s. The principle of this technique in acoustics is computation of the sound field everywhere in the space based on the measurement of both an amplitude and a spatial phase of an acoustic quantity in several points in the space (measured data must be spatially correlated). However, the main application of this method is the localization of the sound source(s) in sense to compute (reconstruct) acoustic quantities on the vibrating surface(s) of the source based on the (non-contact) measurement of the sound field above the surface. This technique differs from other sound source localization techniques (i.e. beamforming described above) mainly in capturing the evanescent components in the near field of a sought source – thus, the nearfield attribute [47]. The near field can be described as the area that is closer to the sound source than one or two wavelengths of the highest frequency [46].

Development of nearfield acoustical holography (NAH) brought the possibility of enhancing the efficiency of diagnosing the sources of sound radiation from a vibrating structure by visualizing the entire radiated sound field [130]. Thus NAH is regarded as an effective tool to visualize a sound field and to analyze vibro-acoustic responses of a vibrating structure [131, 130].

Near-field acoustic holography (NAH) is by now a well known technique that has fundamentally changed noise diagnostics. This is because it enables one to get all acoustic quantities such as the acoustic pressure, particle velocity, acoustic intensity, sound power, normal surface velocity in space as well as on structural surface based on measurements of radiated acoustic pressures in the near field [132]. The insight into the acoustic characteristics of a sound source that one can get from NAH cannot be matched by any conventional method described in section 1.2. For this reason we dive into the various techniques and the state of the art approaches used to implement NAH for reconstructing acoustic quantities.

1.3.2.1 Fourier-based NAH

The approaches to solve the inverse problem of NAH described in this section are based on the spatial Fourier transform.

Fourier NAH, a celebrated technique for noise source identification [125] was pioneered by Maynard and Williams in the early 1980s [133, 134, 135, 136]. The technique enables reconstructing a three-dimensional (3D) sound field from the two-dimensional (2D) hologram data scanned above the source surface. Bruel and Kjael commercialized the Fourier NAH with a new name, spatial transformation of sound field (STSF) [137, 138, 139]. A comprehensive treatment of Fourier NAH for Cartesian, cylindrical, and spherical coordinates can be found in the monograph by Williams [140].

In the original NAH technique, the acoustic pressure was obtained by taking an inverse Fourier transform of the angular spectrum of the acoustic pressure measured on a hologram plane multiplied by a propagator, where the angular spectrum is a spatial Fourier transform of the measured acoustic pressure into the wave number domain and the propagator represents a phase shift from the hologram plane to any parallel plane in a source-free region. Once the acoustic pressure is reconstructed, the particle velocity can be obtained by Euler's equation and acoustic intensity is retrieved by multiplying the acoustic pressure and particle velocity. Therefore, all the acoustic quantities are determined once the acoustic pressure on a hologram plane is measured. This is the essence and power of NAH.

The Fourier-transform-based NAH is suitable for a surface containing a level of constant coordinates such as an infinite plane, infinite circular cylinder, and a sphere. Theoretically, a hologram plane must be infinite so as to facilitate the Fourier transform. If the acoustic pressures on this hologram plane could be measured continuously and exactly, the spatial resolution of a reconstructed acoustic image would be infinitely high. In practice, however, such a scenario is nonexistent, because the measurement space is limited, and input data contain errors or are

insufficient. As a result, the reconstructed acoustic images may be distorted. Also, in practice, few structures have a level of constant coordinates. Therefore, the Fourier-transform-based NAH is limited in its applications. For example, when planar or cylindrical NAH is used to reconstruct an acoustic field from a nonplanar or noncylindrical source, one can back propagate the acoustic field to a surface conformal to the hologram surface tangential to the source surface. This is because extrapolation of an acoustic field from one surface to another is valid in a source-free region, beyond which it is no longer source free, and back propagation becomes invalid. Thus the limitations stem from the fact that the Fourier NAH relies heavily on the two-dimensional Fourier transform between the physical space and the wave number space. For example, the planar NAH requires that frequency-domain complex phasors of a stationary sound signal must be available and the scanned grid points must be equally spaced on a planar rectangular area [141]. Numerical artifacts such as aliasing arising in Fourier transform may adversely affect the imaging quality. This situation is further aggravated in practical applications, where the number of sensors is often limited due to cost consideration. In Fourier NAH, microphone spacing must be kept less than half of the wavelength at the interested frequency to prevent the spatial aliasing problem from happening. Many microphones and important processing power are required to fully cover the source area. In addition, latency becomes more of a problem when one has to measure a transient noise such as pass-by noise in real time [125].

Inspite of the advantages of Fourier NAH (ease of implementation and low computational requirements) and the elegant solution it provides for most acoustical computation problems it is impractical in most cases due to the aforementioned limitations described. Other techniques have been develop to tackle these limitations. These techniques are grouped into two kinds, namely: the patch-based NAH and inverse-based NAH.

1.3.2.2 Patch-based NAH

The two methods described in this section have been developed to overcome the aperture size limitations encountered in the Fourier-based NAH. They fall under the category of Least square NAH. These methods use the elementary wave model (EWM) to approximate the measured acoustic quantity. The EWM could be composed of any functions and its definition usually corresponds with the geometry of the sound source(s) as well as the geometry of the measurement aperture (to be able to represent any acoustic field, the EWM should constitute a complete basis) [47]. The two known methods under this technique are Statistically Optimized NAH (SONAH) and Helmholtz Equation Least-Squares (HELS).

Statistically Optimized NAH

Statistically Optimized NAH has been developed by Steiner and Hald [142] to overcome the limitations that are caused by the use of the Fourier transform (it completely avoids this spatial-wavenumber transform). In this method, the acoustic quantities on a mapping surface near the measurement surface are calculated by using a transfer matrix defined in such a way that all propagating waves and a weighted set of evanescent waves are projected with optimal average accuracy. It considers a series of propagating plane and evanescent waves as eigen-functions, that represent separable solution of Helmholtz equation [47].

SONAH is an approximate method and the reconstruction may diverge even without noise. A discretization of k-space must be performed carefully to ensure correct approximation. Jacobsen and Hald extend this method for the pressure-velocity sensors measurement, which shows better results for the normal surface velocity reconstruction from particle velocity measurement and provides some possibilities to control the sound waves coming from other directions [143]. For this purpose, several papers also deal with the two-layer arrays [144].

Helmholtz Equation Least Squares

An alternative to Fourier transform is the Helmholtz Equation Least Squares (HELS) method [145, 146]. Unlike the Fourier transform, this method attempts to find approximate solutions to all acoustic quantities produced by a vibrating structure using an expansion of the admissible basis functions with errors minimized by least squares. This approach simplifies the problem, yet still enables one to tackle complex situations with relatively few measurements. The Helmholtz-equation least-squares (HELS) method, has shown a great promise in reconstructing acoustic fields in both exterior and interior regions from an object of arbitrary shape [145, 147, 146, 148, 149, 130].

It is vital to emphasized that HELS has no restrictions whatsoever on the use of the coordinate systems and the corresponding wave functions. Use of the spherical coordinates leads to an approximate solution in terms of the spherical wave functions. Similarly, use of the cylindrical coordinates yields an approximate solution in terms of cylindrical wave functions. The coefficients in any expansion are determined by matching an assumed-form solution to the measured acoustic pressures and the errors are minimized by the least-squares method. Since HELS solves the Helmholtz equation directly, its solution is always unique at any frequency. However, it should be noted that there is no single set of coordinate system that can provide good approximations for all surface geometry. For example, the spherical wave functions are natural choice for a blunt or convex surface, and the cylindrical wave functions will be ideal for a slender object. If the spherical wave functions are used to approximate acoustic quantities on the surface of highly non-spherical geometry, convergence of an HELS expansion will be greatly reduced. Theoretically, different coordinate systems should be used in HELS expansions for different geometry. However, in practice we have to strike a balance between simplicity in numerical implementations and accuracy in reconstruction, for example, by sticking to one set of coordinates and the corresponding wave functions that are easy to use and readily available in any software library [132]. The HELS can be executed through a conformal array of microphones at a very close distance to a vibrating object and allows for patch reconstruction. For example, it enables one to reconstruct the acoustic quantities on a portion of a source surface, which can be very convenient in practice [132].

The main advantages of the HELS method are its simplicity in mathematical formulation, efficiency in numerical computations, and flexibility in applications. Moreover, the HELS method is immune to the non-uniqueness difficulty inherent in inverse-based NAH such as the inverse boundary-element method (BEM). The HELS method also allows for piece-wise reconstruction which can be very handy in engineering applications. Thus, it can become a potentially powerful diagnostic tool for practicing noise-control engineers to visualize sources of sound and vibration and their transmission paths [130].

The disadvantage of HELS is that it proves effective in imaging blunt and convex sources, but not for a highly elongated and planar sources. The cylindrical coordinate system is ideal for imaging a slender body, but not for a flat surface [125].

1.3.2.3 BEM-based approaches

Nearfield Acoustic Holography has proven to be a powerful tool for source identification. Nevertheless, the approach is limited to simple sources and measurement surfaces. To overcome this limitation, inverse approach is used. The numerical solutions offered by this approach is the boundary-element method (BEM) and because it is an inverse problem, this technique is known as inverse boundary element method (IBEM) [150].

The sound field at a spatial domain is determined from the source, scatterer, and boundaries inside or around the region of interest. The source would be a vibrating object. The scatterer might be an irregular body having rigid or flexible surfaces, and the reflecting boundary would change the phase of incident sound, absorbing some amount of sound and reflecting the rest. The

Kirchhoff–Helmholtz integral equation [125] provides the general solution of the sound radiation and scattering problems, which represents the sound field constructed by the monopole and dipole source distributions on a vibrating surface. The acoustic boundary element method (BEM) based on the Kirchhoff–Helmholtz integral formulation has been widely used to solve the radiation and scattering problems with irregularly shaped geometry, which has no closed form solutions in separable coordinates. Because the Kirchhoff–Helmholtz integral equation is solved on the boundary of the domain, there is a reduction in spatial dimensions by one compared with other numerical modal methods, such as finite element method (FEM) and finite difference method (FDM). This means that, for a three dimensional sound radiation and propagation problem, boundary element modeling can be carried out only on the two-dimensional boundaries of the domain. Furthermore, for exterior problems of infinite extent, the discretization can be limited to the finite boundary surface of a radiator by imposing the Sommerfeld radiation condition. Generally, it can be said that the BEM gives relatively more accurate results on the boundary surface than the other numerical methods. It is also capable of modeling the acoustic problems in relatively low frequency regions with high certainty [125].

There are two types of boundary element formulations: direct BEM (dBEM) and indirect BEM (iBEM). In case of dBEM, variables of pressure and velocity are solved directly at collocating points on the boundary surface. This corresponds to the numerical computation of the Kirchhoff–Helmholtz integral equation. Meanwhile, iBEM solves for a distribution of fictitious sources on or very near to the boundary. Although the concept of the collocation method has been well known in fluid mechanics for a long time, the basic formulation of acoustical iBEM was firstly proposed by Chen and Schweikert [125, 151].

Surface monopole strengths are calculated for expressing the acoustic field equivalent to that generated by the actual vibration surface. This superposition integral is based on the idea that an array of monopole sources can be arranged to reproduce a velocity profile on the surface of the radiator [152, 153, 154, 155, 156]. Therefore, it can be considered as a numerical implementation of the Huygens' principle in acoustics. However, if one would solve the interior and exterior sound radiation and scattering problems simultaneously, the distributed sources must include the single layer and double layer potentials, which are the differences between the outside and inside values of pressure and its gradients, respectively. Unfortunately, the integral has the hyper-singularity term, which raises difficulties in the numerical calculation and is integrable only in the finite-part sense. Then, the evaluation of this singularity can be proceeded by adopting a variational formulation [157, 158]. The resulting coefficient matrix obtained from the variational formulation is symmetric, but the double surface integral should be carried out. Because iBEM has been known as consuming much time in formulation and calculation for most practically small-sized problems, dBEM has been used popularly because of its simplicity and acceptable accuracy for most acoustic problems, which are not large and do not involve a very high frequency calculation [125].

The basic concept of the BEM-based inverse approaches was first explicitly studied by Gardner and Bernhard [159], who introduced the source identification method in the highly reactive field by utilizing direct BEM. Veronesi and Maynard [160] utilized the singular value decomposition of the discretized direct boundary integral equation, in order to decompose the field and source properties into the wave-vector domain. They demonstrated that the suppression of the amplification effect of the measurement noise via the rejection of higher wave-vector mode components led to an improved resolution. Bai [161] formulated the generalized holography equation based on direct BEM. He represented all possible combinations of the transfer matrix, in order to correlate the particle velocity and field pressure on the source surface and the field plane. Kim and Ih [162] described a resolution enhancement technique using the optimal selection of measurement points and regularization of the transfer matrix for the interior problem. By utilizing a trade-off relationship between variance and bias errors, the optimal rank, which produces the minimum mean square error could be determined. Zhang, et al. [163] employed

the indirect formulation for the BEM-based NAH. Valdivia and Williams [164] suggested the iterative technique, which can avoid using the singular value decomposition technique that may be beneficial in dealing with a large transfer matrix [165].

As aforementioned, the BEM-based inverse approaches thus provide a good opportunity for restoring the vibro-acoustic field of many practical arbitrarily shaped sources. Its optimal feature is that only the measured field pressure is required for determining pressure, particle velocity, surface admittance, intensity, and power flow of the source and the domain of interest as well. This type of conformal inverse technique has the following advantages compared with conventional NAH based on the spatial Fourier transform. One can deal with the complex shaped sources that cannot be described by separable coordinates; the pressure need not be measured in separable coordinates, thus a reduced number of measurements with uneven spacing is possible; reflections from all directions can be considered; concave regions of the source can be reconstructed; and wrap-around error due to the finite aperture size is not involved. However, this method has some inconvenient aspects as well. The acoustic and geometric relation of the source surface and the hologram plane should be modelled via the use of the BEM and this causes problems. A considerable number of boundary elements and nodes are ultimately required for modelling the actual source surfaces involved in a practical noise problem and the amount of field pressure data increases in parallel with that of the surface nodes. The applicable frequency range can be limited by the characteristic length of the typical element. In addition, care should be taken with respect to the inversion of the fully populated vibro-acoustic transfer matrix that has a high singularity. However, if such difficulties are somehow overcome with some technical labour, the drawback of additional BEM modelling may not be a big loss after all because one needs the BEM model of the irregular 'source' for the eventual forward prediction of the sound field, anyway [165].

Another shortcoming of IBEM-based approach is that it fails to yield a unique solution when an excitation frequency is near one of the eigenfrequencies of the corresponding interior boundary value problem. While the non-uniqueness can be overcome by combining the exterior and interior integral formulations, known as a CHIEF method [166] or by combining the single- and double-layer potentials, [167, 168] numerical computations can become even more complicated and time consuming.

1.3.2.4 Other techniques

Principles are applied to above methods to handle their shortcormings and through the process, new forms of techniques are emerged. Three noteworthy alternatives are briefly describe below.

The Combined (HELS and IBEM) method: CHELS

A combined Helmholtz equation–least squares (CHELS) [149] method is developed for reconstructing acoustic radiation from an arbitrary object. This method combines the advantages of both the HELS method and the Helmholtz integral theory based near-field acoustic holography (NAH). As such it allows for reconstruction of the acoustic field radiated from an arbitrary object with relatively few measurements, thus significantly enhancing the reconstruction efficiency.

The first step in the CHELS method is to establish the HELS formulations based on a finite number of acoustic pressure measurements taken on or beyond a hypothetical spherical surface that encloses the object under consideration. Next enough field acoustic pressures are generated using the HELS formulations and taken as the input to the Helmholtz integral formulations implemented through the boundary element method (BEM). The acoustic pressure and normal component of the velocity at the discretized nodes on the surface are then determined by solving two matrix equations using singular value decomposition (SVD) and regularization techniques.

For the same amount of measurements taken on or beyond a spherical surface that encloses the object, the CHELS method may give a more accurate reconstruction by increasing the number

of discrete nodes and the necessary input data than the BEM-based NAH does. Since these input data are calculated but not measured, the reconstruction efficiency is greatly enhanced. However, since the measurements are taken over a spherical surface rather than a conformal surface, the accuracy of reconstruction of the surface acoustic quantities may be limited because some evanescent waves may be lost. On the other hand, if reconstruction of acoustic radiation in the far field is desired where the evanescent waves are negligibly small, the CHELS method can be straightforward and much more efficient than BEM [149].

Equivalent Source Model (ESM)-based NAH

The equivalent source method (ESM), also known as wave superposition method [169, 170, 171], used in sound field calculation has gained much attention in recent years and has been widely used for solving the inverse problems of NAH. The ESM is a truly meshless collocation technique for discretizing integral equations [172]. It approximates the solution of a partial differential equation by a linear combination of fundamental solutions with singularities, where no complicated mesh construction and integration process are required. In other words, it represents the sound field of interest with a distribution of discrete simple sources and hence no numerical integration is required. These simple sources are only in a virtual sense for representation purposes and are solutions of the acoustic wave equation. These virtual sources can be monopoles, dipoles, or even higher order of simple sources placed inside the vibrating structure.

By representing the sound field using simple sources, one obtains a matrix system of equations with source strengths as the unknowns. The source strengths calculated, with the aid of the regularization techniques detailed previously, serve as the basis for predicting the sound field at any point including the source surface. However, how to distribute the virtual simple sources in terms of location and retreat distance is not as straightforward and deserves some investigation [125].

The low numerical complexity makes ESM an appealing approach for computational acoustics, as compared to the direct IBEM approach. While ESM was generally used as a benchmark for BEM, it has been shown by numerous studies that, with careful choice of parameters, ESM is capable of achieving comparable accuracy to other methods such as FDM, FEM and BEM [173, 174]. A hybrid method that combines single and double layer potentials was proposed to overcome the non-uniqueness problems of ESM [175]. Like IBEM, the use of ESM is not restricted to sources with regular geometries and can be applied to arbitrarily shaped vibrating structures. ESM forms the heart of many microphone techniques as presented in [125].

Transient Near-Field Acoustical Holography

Analyses of transient acoustic radiation are often encountered in engineering applications because most vibrating structures are subject to impulsive or transient force excitations. In many cases, the transient excitations are unspecified and therefore the structural vibration responses are unknown, which makes the analysis of resultant acoustic field difficult.

Transient near-field acoustical holography (NAH) [176, 177] formulation is derived from the Helmholtz equation least squares (HELS) method to reconstruct acoustic radiation from a spherical surface subject to transient excitations in a free field. According to Wu et al. [177], the temporal solutions, make use of the Laplace transform and expansion in terms of the spherical Hankel functions and spherical harmonics, with their coefficients settled by solving a system of equations obtained by matching an assumed-form solution to the measured acoustic pressure. The derive general form of solution for a temporal kernel is obtain first through substituting the spherical Hankel functions and their derivatives with polynomials, followed by recasting the infinite integrals in the inverse Laplace transform as contour integrals in a complex s-plane and then evaluate it via the residue theorem. The transient acoustic quantities anywhere including

the source surface are then obtained by convoluting the temporal kernels with respect to the measured acoustic pressure.

Wu et. al [177], extended HELS formulations to the reconstruction of transient acoustic radiation from a spherical source subject to arbitrarily time-dependent excitations in a free field. It is shown that HELS enables one to obtain the satisfactory reconstruction of 3-D images of transient acoustic waves as they travel in space and time based on a few measurements taken along a finite line segment. Since HELS imposes no restrictions whatsoever on measurement locations and since the nature of HELS formulations is naturally suited for transient NAH, it can become the method of choice for visualizing transient acoustic quantities.

Inverse Patch Transfer Function (iPTF) method

Aucejo *et al.* [178], Vigoureux [179] and Forget [180] developed the iPTF (inverse Patch Transfer Functions) method. It corresponds to the inverse formulation of the PTF method, initiated by Ouisse *et al.* [181] for calculating vibro-acoustics problems by a substructuring technique. The iPTF method is based on an integral formulation of a "virtual" interior Green problem. The bounded domain is indeed delimited by the surface of the source, possibly a rigid wall and a virtual surface defined arbitrarily around the source so as to theoretically isolate it (controlled environment) from its external environment. All of these surfaces are discretized into elementary surfaces which are named patches, hence the name of the method. Its particularity is that it uses modal behavior of this virtual acoustic volume as the basis for the decomposition of the field. The transfer matrices governing the problem are impedance matrices and can be computed numerically by a solver FE (modal extraction) and independently of the measurements (linked to the geometry of the domain). The reconstruction of the acoustic fields is therefore done directly on the real geometry of the source. The method requires combined measurements of pressure and particle velocity of air produced on the virtual surface to identify the velocity field of the source. The direct PTF formulation then makes it possible to retrieve all the other acoustic quantities (pressure, intensity, power, etc.), thus ensuring the complete characterization of the source on its surface. Therefore, a simpler and automated measuring system is possible, because this virtual measurement surface is arbitrary and thus independent of the source surface. In addition, it surrounds completely the source to be identified, thus its combined measurement of particle velocity and pressure allows the measurement to be independent of the uncontrolled external environment. Also, the iPTF formula intrinsically takes into account any rigid surface boundary or included in the virtual acoustic field. The method is capable of handling equally inhomogeneous environment around the source. A wide variety of validation applications have been carried out with the method iPTF, in particular on an L-shaped plate [182], on baffled pistons in the presence of secondary correlated sources, on a diesel engine pre-catalyst [183], on a gearbox at reduced speed [184] and on a baffled oil pan [185].

With regard to the industrial specifications, the iPTF method therefore has the potentiality to meet all of the expectations set. It allows indeed an identification on the actual surface of the source and from a flexible measurement device that can be implemented in a complex environment, i.e. potentially noisy and cluttered.

1.4 Research objective

When looking through the scientific literature, one realises that a great deal of research has been carried out to develop more advanced ”source identification” methods. There are many categories of methods, all of which have theoretical bases and different objectives due to the variety of applications. In particular, a distinction is made between the methods of ”source location” and the methods of ”field reconstruction” (of velocity, pressure and/or intensity) which, in turn, enable the source to be fully characterized. The thesis work falls into the category of

"field reconstruction" methods.

It should be noted that even though these techniques have undergone constant improvement, the problem remains that there is no "magical" sound source characterization technique that prevails over the others. Depending on the test object, the nature of the sound and the actual environment, engineers have to select one method or the other. Among the existing methods of identifying sources as described above there remains some problems which are still unsolved in characterising the source in specific condition and environment. In an industrial environment as complex as that of an engine test bench, some of these methods suffer from certain constraints that limit their use. In particular,

- most of these methods can only reconstruct sound fields on simple surfaces (planes, cylinders, spheres),
- they must be carried out in a controlled acoustic environment (anechoic room),
- they must be carried out facing the object without the presence of obstacles or masking object between the source and the means of measurement (usually microphone sensors).

In order to overcome all these limitations, this thesis work used a methodology, which has been developed at the "Laboratoire Vibrations Acoustique" of INSA-Lyon. This identification method is known as the inverse Patch Transfer Function (iPTF) as briefly introduced above. The principle is based on the concept of closed virtual acoustic volume defined around the source and on the application of Green's identity. This volume can be defined arbitrarily and the method allows for the effective handling of rigid obstacles. This even makes it feasible for the method to be used in congested source environment. The discrete acoustic measurements are performed at accessible positions around the source and are feasible in a non-controlled acoustic environment thanks to Green's identity, which acts as a field separation method. The measurements made are then coupled with numerical modelling, which enables the source geometry to be managed whatever its complexity. Thus, from a double formulation, direct and inverse of the acoustic problem, the source is fully characterised and the reconstruction of the entire acoustic field is carried out directly on its geometry.

The main objective of this thesis work is to demonstrate how to use the iPTF method in the blind identification of a vibratory fields. The term "blindness" here has two meanings:

- the reconstruction of the velocity field of a vibrating structure can be blind if objects mask parts of the structure to characterize.
- the identification can be blind if the velocity field is the result of the combination of several unknown sources and if one wants to separate the contribution of each source.

In this thesis work numerical and experimental results are shown to illustrate both aspects of the blind identification.

1.5 Thesis Outline

This chapter has given an overview of the societal problem, introduced PBNv2 project and discussed source characterisation methods using the conventional techniques and indirect means with the state-of-art technologies.

The thesis is structured based on the objectives defined above. Thus the thesis work has been divided into two parts. The first part deals with the aspect of blind reconstruction in presence of masking object whilst the second part deals with the source separation aspect.

Firstly, chapter 2 reviews the theory and concept of iPTF approaches. In this section the concept of the virtual acoustic volume which forms the theoretical basis of the iPTF will be

reviewed. Secondly, the choice of the virtual boundary conditions and implication on measurement setup will be presented. The two iPTF variant forms, u-IPTF and m-IPTF, will therefore be introduced.

As an inverse approach, the IPTF is often faced with issues associated with ill-posed problems and therefore requires proper regularization. The regularization methods are covered in Chapter 3 of the thesis. The chapter 3 looks at how to deal with inverse problems from a theoretical standpoint. Specifically, the iPTF problem of determining the particle velocity of an acoustic source utilizing field measurements of acoustic pressures and/or particle velocities and FEM impedance transfer matrices. Regularization is one of the methods for obtaining an accurate identification in such an inverse problem. Regularization, in general, may be thought of as a type of optimization process that entails the generation of several solutions from which the optimum one is selected, and the criteria for selecting the best one are a must. Chapter 3 focuses only on the theoretical aspects of numerical approaches for inverse problems. The implementation of all of these techniques is discussed in Chapter 4.

The major goal of chapter 4 is to select one of the regularization strategies described in chapter 3 that is most suited for both the m-iPTF and u-iPTF methods presented in chapter 2. The technique entails conducting numerical experiments using a variety of situations to generate a collection of test cases that characterize the iPTF problems. It includes a description of the numerical experiments performed for the various test scenarios under consideration. Two separate numerical experiments were performed to give input data for both the u-iPTF and m-iPTF problems. The idealistic inverse problem was used as the initial test case, and all the considered regularization techniques were used. A set of correlation measurements is used to validate the identified results from each of the techniques. The technique that emerged as the best appropriate technique is investigated further using realistic inverse problems as the other test cases. Then the influence of noisy measurements on the quality of the iPTF results is evaluated. Lastly, the under-determined situation where the number of equations is much lower than the number of unknowns is investigated.

Chapter 5 presents how the presence of masking objects can be handled. The specific interesting characteristics are deduced from the theory of iPTF in relation to the presence of the masking object. Some numerical experiments will be carried out when dealing with masking objects to serve as an iPTF method validation. The approach, methodology and the results identified are also presented and discussed.

Chapter 6 presents the industrial application of the iPTF method in relation to the handling of the presence of masking objects as another means of validating the method. The chapter describes the functionality of the system under test and how the experiments are carried out. It presents the pre-processing and processing of experimental data, including modelling and signal analysis. The approach, methodology and the identified results are discussed.

Blind Source Seperation in IPTF (BSS-iPTF) context is described and presented in Chapter 7. A brief overview of the source separation techniques is presented. The theory and concept of the developed BSS-iPTF algorithm is introduced and presented. Various numerical experiments are carried out to serve as a validation of BSS-iPTF algorithm. The approach, methodology and the evaluated results are equally presented.

2

Theory and concept of inverse Patch Transfer Function method (iPTF)

As already briefly explained in Chapter 1, the iPTF approaches are a set of field reconstruction methods based on the virtual acoustic volume concept thoroughly explained in the following sections. The theoretical background of the virtual acoustic volume concept has been developed by Aucejo *et al.* [178], Vigoureux *et al.* [179], Totaro *et al.* [185] and Forget *et al.* [180] and the so-called u-iPTF (iPTF with uniform boundary conditions) and m-iPTF (iPTF with mixed boundary conditions) have been derived. This chapter provides an overview of the virtual acoustic volume concept and of the derivation of u-iPTF and m-iPTF.

It should be noted that the theory and concept offered in this chapter is a revised translation from French to English of an extract from Section 1.1 and Section 2.1 of Forget [27] PhD thesis.

2.1 Concept of virtual acoustic volume

Let's consider a vibrating structure radiating noise in an unbounded environment. For sake of simplicity, the example of a flat plate radiating noise in semi-infinite free field will be used, as presented in Figure 2.1. Let's consider now that one wants to compute the acoustic pressure $p(M)$ at a point M. A way to do that is to use the properties of the Green's identity that stipulates that the acoustic field in a closed volume is completely defined if the normal velocity is known on its boundaries (envelope surface). Let's define then a zone of the unbounded semi-infinite free field, called virtual acoustic volume Ω, delimited by surfaces. In the general case, these surfaces are composed by the source surface itself Γ_S, an arbitrarily chosen virtual surface Γ_V and a rigid surface Γ_R as shown in Fgure 2.1.

The virtual acoustic volume as well as the virtual surface Γ_V have no physical reality as they simply serve to theoretically define a closed and controlled acoustic volume around the source in the unbounded space. In the case of Figure 2.1 this virtual surface is chosen rectangular, but any other choice remains admissible (arbitrary volume).

In this acoustic volume Ω, provided that there is no any other source inside, the pressure $p(M)$ at all points M satisfies the Helmholtz-Kirchhoff homogeneous equation (the time dependence e^{iwt} of the acoustic pressure is omitted in the following description):

$$\Delta p(M) + k^{*2} p(M) = 0, \quad \forall M \in \Omega, \tag{2.1}$$

with $k^* = \omega / c^*$ denoting the complex wavenumber, ω the angular frequency and $c^* = c(1 + i\eta)$ the complex speed of sound in the air with η being the damping loss factor and c the real speed of sound.

To solve this volume problem, Green's identity is applied. It makes it possible to treat a

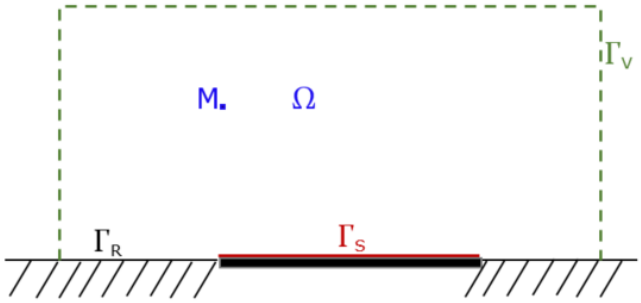

Figure 2.1: Definition of the virtual acoustic volume Ω and its boundaries: the source surface Γ_S, the rigid baffle Γ_R and the virtual surface Γ_V.

volume problem by using known conditions applied on its boundaries. The general formulation involves two functions Ψ and Φ, twice continuously differentiable on the domain Ω and its boundaries Γ:

$$\iiint_{\Omega}[\Psi\Delta\Phi - \Phi\Delta\Psi]\mathrm{d}\Omega = \iint_{\Gamma}\left[\Psi\frac{\partial\Phi}{\partial n} - \Phi\frac{\partial\Psi}{\partial n}\right]\mathrm{d}\Gamma. \tag{2.2}$$

These two functions can be arbitrarily chosen. As detailed in [27, 180, 186], the pressure at any point M in the virtual volume (the bounded domain Ω) can be derived from Equation (2.2) and expressed as

$$p(M) = \sum_{n=1}^{\infty}\frac{\phi_n(M)}{(k^{*2} - k_n^2)\,\Lambda_n}C_n, \tag{2.3}$$

where $\phi_n(M)$ is the pressure mode shape of the virtual volume, which also satisfies the Helmholtz equation

$$\Delta\phi_n(M) + k_n^2\phi_n(M) = 0, \quad \forall M \in \Omega, \tag{2.4}$$

where k_n is the acoustic wavenumber of mode n at the eigen angular frequency ω_n, and where Λ_n is the norm of the n^{th} mode shape and C_n corresponds to the right-hand side of Green's identity as seen in [27, 180, 186]

$$C_n = \iint_{\Gamma} p(M)\frac{\partial\phi_n(M)}{\partial n} - \phi_n(M)\frac{\partial p(M)}{\partial n}\ \mathrm{d}\Gamma. \tag{2.5}$$

By detailing the three boundaries of the bounded domain Ω presented in Fig. 2.1, C_n is written:

$$\begin{aligned} C_n = &\iint_{\Gamma_S} p(Q_S)\frac{\partial\phi_n(Q_S)}{\partial n} - \phi_n(Q_S)\frac{\partial p(Q_S)}{\partial n}\ \mathrm{d}\Gamma_S \\ &+ \iint_{\Gamma_V} p(Q_V)\frac{\partial\phi_n(Q_V)}{\partial n} - \phi_n(Q_V)\frac{\partial p(Q_V)}{\partial n}\ \mathrm{d}\Gamma_V \\ &+ \iint_{\Gamma_R} p(Q_R)\frac{\partial\phi_n(Q_R)}{\partial n} - \phi_n(Q_R)\frac{\partial p(Q_R)}{\partial n}\ \mathrm{d}\Gamma_R. \end{aligned} \tag{2.6}$$

To calculate C_n, the boundary conditions of the problem must be applied. By detailing the surfaces of the acoustic domain Ω, the boundary conditions given by the Euler relation are then written

$$\frac{\partial p(Q_S)}{\partial n} = -\mathrm{i}\omega\rho_0 v(Q_S), \quad \forall Q_S \in \Gamma_S \tag{2.7}$$

$$\frac{\partial p(Q_V)}{\partial n} = -\mathrm{i}\omega\rho_0 v^{\mathrm{rad}}(Q_V), \quad \forall Q_V \in \Gamma_V \tag{2.8}$$

$$\frac{\partial p(Q_R)}{\partial n} = 0, \quad \forall Q_R \in \Gamma_R \tag{2.9}$$

where $v^{\text{rad}}(Q_V)$ denotes the outgoing normal particle velocity of any point Q_V of the virtual surface, $v(Q_S)$ is the structural velocity of any point Q_S of the surface of the plate. The partial derivative of the pressure is null in Equation (2.9) because it is assumed here that the surface Γ_R is perfectly rigid. By applying these boundary conditions 2.7, 2.8 and 2.9, C_n is simplified

$$\begin{aligned} C_n = &\iint_{\Gamma_S} p(Q_S)\frac{\partial\phi_n(Q_S)}{\partial n} + \mathrm{i}\omega\rho_0 v(Q_S)\phi_n(Q_S)\ \mathrm{d}\Gamma_S \\ &+ \iint_{\Gamma_V} p(Q_V)\frac{\partial\phi_n(Q_V)}{\partial n} + \mathrm{i}\omega\rho_0 v^{\text{rad}}(Q_V)\phi_n(Q_V)\ \mathrm{d}\Gamma_V \\ &+ \iint_{\Gamma_R} p(Q_R)\frac{\partial\phi_n(Q_R)}{\partial n}\ \mathrm{d}\Gamma_R. \end{aligned} \tag{2.10}$$

At this step, no boundary condition has yet been defined for the virtual volume to determine the eigenmodes in pressure ϕ_n and in velocity, $\frac{\partial\phi_n}{\partial n}$. Thus, the Equations (2.3) and (2.10) are valid whatever the boundary conditions imposed [27, 180, 186]. It is therefore possible to define the boundary conditions of the virtual problem without having a correspondence with the real problem. However these conditions which one will qualify as virtual govern a modal behaviour and therefore cannot meet a Robin type condition with damping [27]. Several choices are therefore possible. Two possibilities as detailed in [27, 180, 186] are in the rest of the section:

- The case of a uniformly rigid virtual volume at it's the boundaries surfaces (homogeneous Neumann condition) is presented in section 2.1.1.
- The case of a virtual volume made up of mixed boundary conditions (of the homogeneous Neumann and Dirichlet types) is detailed in section 2.1.2.

2.1.1 Uniform virtual boundary conditions (homogeneous Neumann BC)

Uniformly rigid virtual boundary conditions are the basis of the method initially called PTF [181] which will be designated as the u-PTF (uniform-PTF) method. They result in a homogeneous Neumann condition on all the surfaces of the virtual domain Ω:

$$\frac{\partial\phi_n(Q)}{\partial n} = 0, \quad \forall Q \in \Gamma_S, \Gamma_V, \Gamma_R \tag{2.11}$$

Under these conditions, C_n of Equation (2.10) is simplified

$$C_n = \iint_{\Gamma_S} \mathrm{i}\omega\rho_0 v(Q_S)\phi_n(Q_S)\ \mathrm{d}\Gamma_S + \iint_{\Gamma_V} \mathrm{i}\omega\rho_0 v^{\text{rad}}(Q_V)\phi_n(Q_V)\ \mathrm{d}\Gamma_V. \tag{2.12}$$

The integral formulation is an exact formulation of the acoustic problem since it represents the continuity on the virtual acoustic volume and on its boundaries. From the resolution point of view, the surface integrals are discretized and approximated by summing elementary surfaces called "patches". The first consequence is that the data must be averaged over these patches and that the approximation of the solution will depend both on the type of averaging carried out (central value, arithmetic mean, ...) and the choice of discretization (more or less coarse). In the same way, the modal series must be truncated to a certain mode N. After discretization of the problem, the pressure field at any point M of the domain Ω is expressed through:

$$p(M) = \sum_{n=1}^{N} \mathrm{i}\rho_0 \frac{\phi_n(M)}{(k^{*2} - k_n^2)\Lambda_n} \left[\sum_{j=1}^{N_S} \omega A_j \langle\phi_n\rangle_j \langle v\rangle_j + \sum_{k=1}^{N_V} \omega A_k \langle\phi_n\rangle_k \langle v\rangle_k \right], \tag{2.13}$$

where the indices j and k correspond to elementary patches surfaces belonging respectively to surfaces Γ_S (source surface) and Γ_V (virtual surface). The notation $\langle X\rangle_l$ indicates the spatial

mean of variable X on patch l of area A_l.

It is important to note that the physically rigid surface Γ_R no longer appears in the final expression of the calculation of the radiated field as noted in Equation (2.13). This peculiarity comes from the equivalence between the real boundary conditions and the virtual boundary condition on that surface.

The radiated pressure field in unbounded environment is thus accessible throughout the field Ω by knowing the normal particle velocity at the source surface Γ_S, the air particle velocity normal to the virtual surface Γ_V and the modal behaviour of the virtual acoustic volume expressed in terms of pressure mode shapes. No condition of non-reflection at infinity is here translated: the influence of the external acoustic environment to the virtual volume is intrinsically taken into account by the velocities on the surface Γ_V which translate the coupling between the virtual volume and the external acoustic environment. One of the well-known properties of Green's identity is exploited here to separate the acoustic volume Ω from its external environment by knowing the velocity on all of its boundaries.

2.1.2 Mixed virtual boundary conditions (homogeneous Neumann and Dirichlet BC)

For the second possibility in the choice of the virtual boundary conditions, the condition of Homogeneous Neumann applied to the virtual surface is replaced by a homogeneous Dirichlet condition of Equation (2.15). The homogeneous Neumann condition is preserved for the source surfaces and physically rigid (Equation (2.14)) to respectively keep the normal vibratory velocity data at the source and remove the contribution from any rigid surface delimiting the virtual domain (Equation (2.16)).

$$\frac{\partial \phi_n(Q)}{\partial n} = 0, \quad \forall Q \in \Gamma_S, \Gamma_R \tag{2.14}$$

$$\phi_n(Q_V) = 0, \quad \forall Q_V \in \Gamma_V. \tag{2.15}$$

Under these conditions, C_n of Equation (2.10) is simplified as:

$$C_n = \iint_{\Gamma_S} \mathrm{i}\omega\rho_0 v(Q_S)\phi_n(Q_S)\ \mathrm{d}\Gamma_S - \iint_{\Gamma_V} \mathrm{i}\omega\rho_0 p(Q_V)\chi_n(Q_V)\ \mathrm{d}\Gamma_V, \tag{2.16}$$

where χ_n represents the n-th eigen-mode shape of the virtual acoustic volume expressed in terms of normal velocity as given by Euler's relation:

$$\frac{\partial \phi_n(Q_V)}{\partial n} = -\mathrm{i}\omega_n\rho_0\chi_n(Q_V). \tag{2.17}$$

After discretization of the problem, the pressure field inside the virtual volume is finally expressed through:

$$p(M) = \sum_{n=1}^{N} \mathrm{i}\rho_0 \frac{\phi_n(M)}{(k^{*2} - k_n^2)\,\Lambda_n} \left[\sum_{j=1}^{N_j} \omega A_j \left\langle \phi_n \right\rangle_j \left\langle v \right\rangle_j - \sum_{k=1}^{N_k} \omega_n A_k \left\langle \chi_n \right\rangle_k \left\langle p \right\rangle_k \right]. \tag{2.18}$$

This formulation, known as m-PTF for mixed virtual boundary conditions on which it is based, differs from the u-PTF method on the type of data evaluated at the level of virtual surface. Indeed, the particle air velocity necessary for the u-PTF method is replaced in this formulation by a data of acoustic pressure on this surface. In return, the m-PTF method requires knowledge of the mode shapes in velocity and pressure against those expressed only in pressure initially. The m-PTF method therefore also allows the calculation of the pressure field radiated by a source in unbounded environment. It requires the normal vibratory velocity at the source, the acoustic pressure at the level of the virtual surface and the modal behavior of the virtual volume expressed in terms of acoustic pressure and velocity. No condition of non-reflection at infinity

also appears in this formulation. In addition, as previously observed for the u-PTF method, the contribution of the physically rigid surface Γ_R no longer appears in Equation (2.18) thanks to the equivalence between real and virtual boundary conditions on this surface.

In conclusion, this section thus made it possible to establish the PTF formulations for the calculation of the radiation from any source in its external environment, whatever it is, based on the concept of volume virtual acoustics. Its principle is based on the definition of an arbitrary virtual air volume around the source, the use of Green's identity, and an arbitrary choice of boundary conditions. Thus, for the calculation of radiation in this area, the PTF methods require only the knowledge of the normal vibration velocity at the source, one of the two acoustic quantities on the virtual surface border to the domain (either speed for u-PTF, or pressure for m-PTF) which materializes the external environment as complex as it is, and the modal behavior of the virtual acoustic volume.

2.2 Formulations of iPTF methods

As presented in Section 2.1, PTF methods are used to calculate the pressure field around vibrating structure placed in any acoustic environment. For this, an arbitrary virtual volume Ω is defined around the source as shown in Figure 2.1 and Green's identity is applied to this area. Thanks to this identity, the pressure field inside the virtual volume is expressed by the sum of two contributions. On the one hand, the contribution of the source, taking into account the normal vibration velocity of the surface Γs and, on the other hand, the contribution of its environment, taken into account by means of a known acoustic quantity on the virtual surface Γ_V (pressure for m-PTF and particle velocity for u-PTF). The unknown is therefore the sound pressure in the virtual volume and the particle velocity data and / or sound pressure on the surfaces of the virtual volume are considered to be known. This resolution is called "direct" because it makes it possible to solve the radiation problem from a source taking into account its external environment. Now suppose that the velocity is unknown on the surface of the source Γs but that the pressure in the virtual volume is known at a certain number of points M. It is then possible to deduce the velocity field from the source surface Γ_S by reversing the problem. This so-called "inverse" approach is the subject of the next two parts which respectively present the two possibilities offered by the formulations u-PTF and m-PTF presented in the previous section 2.1.

2.2.1 Uniform virtual boundary conditions (u-iPTF)

The u-PTF method is based on the arbitrary definition of a virtual volume whose virtual boundaries conditions are uniformly rigid. It allows, as shown in Figure 2.2, to calculate the pressure field radiated by a source and its environment inside this virtual volume in knowing:

- the normal vibration speed of the patches j of the source surface Γ_S,
- the air particle velocity normal to the patches k of the virtual surface Γ_V,
- and of the modal behavior of the virtual acoustic volume Ω expressed in terms of pressure modes ϕ_n.

The u-PTF formulation is thus given by Equation (2.13).

To evaluate this pressure at several points m of the virtual volume, it is possible to write a matrix formulation of the problem (the vectors are considered as column vectors):

$$\mathbf{p}_m = \mathbf{Z}_{mj}\mathbf{v}_j + \mathbf{Z}_{mk}\mathbf{v}_k \tag{2.19}$$

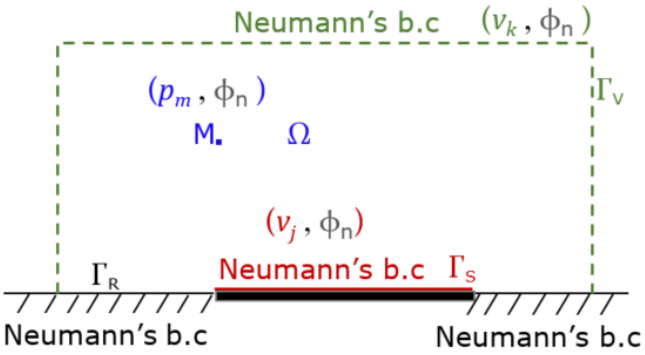

Figure 2.2: Simple supported excited plate radiating in a free field environment. Indication of the boundary conditions (b.c) and of the evaluated data (real data, modal data) for u-PTF and u-iPTF formulations.

With

$$\mathbf{Z}_{mj} = \sum_{n=1}^{N} \mathrm{i}\omega\rho_0 \frac{(\phi_n)_m \langle\phi_n\rangle_j A_j}{(k^{*2} - k_n^2)\Lambda_n} \quad \text{and} \quad \mathbf{Z}_{mk} = \sum_{n=1}^{N} \mathrm{i}\omega\rho_0 \frac{(\phi_n)_m \langle\phi_n\rangle_k A_k}{(k^{*2} - k_n^2)\Lambda_n}. \tag{2.20}$$

As a reminder, the notation $\langle X\rangle_l$ designates the spatial mean of the variable X on the patch l of area A_l, while that the notation $(X)_m$ denotes the value of the variable X at point m. The two matrices $\mathbf{Z}_{mj}$ and $\mathbf{Z}_{mk}$ at Equation (2.19) represent the transfer matrices between the vibration of the patches j of the source surface Γ_S and the pressure evaluated at the points m in the virtual volume and between the vibration of the patches k of the virtual surface Γ_V and the pressure at points m of the virtual volume respectively. They are therefore defined as matrices of acoustic impedance $\mathbf{Z}_{mj}$ and $\mathbf{Z}_{mk}$. They can be computed by numerical methods as soon as the geometry of the virtual volume is defined. The matrix formulation with Equation (2.20) highlights the separation of the term relating to the source ($\mathbf{Z}_{mj}\mathbf{v}_j$) and the term taking into account the outside environment ($\mathbf{Z}_{mk}\mathbf{v}_k$). By manipulating this equation, the term relating to the source can be isolated

$$\mathbf{Z}_{mj}\mathbf{v}_j = \mathbf{p}_m - \mathbf{Z}_{mk}\mathbf{v}_k. \tag{2.21}$$

Equation (2.21) thus represents a linear system of the general form $\mathbf{Ax} = \mathbf{y}$. The modal matrix $\mathbf{Z}_{mj}$ being known, its inversion then makes it possible to solve this linear problem and finally to find the normal vibration velocity on the source surface

$$\mathbf{v}_j = \mathbf{Z}_{mj}^{-1}(\mathbf{p}_m - \mathbf{Z}_{mk}\mathbf{v}_k). \tag{2.22}$$

In reality, the resolution of such a linear problem poses a certain number of difficulties which will be detailed and thoroughly analyzed in Chapter 3. For this chapter, we will omit these constraints and consider that the inversion of the $\mathbf{Z}_{mj}$ matrix is optimal. It is therefore finally possible to reconstruct the normal velocity field on the surface of the source by knowing both the acoustic pressure at points m of the virtual acoustic volume and the particle velocity of air from all the patches k of the virtual surface.

The surface of the source being discretized in patches (elementary surfaces), the velocity $\mathbf{v}_j$ obtained are the velocities normal to the source surface patches and averaged over their respective surface. With the vector $\mathbf{v}_j$ of the normal velocities to the source surface patches being now identified, it is possible to calculate the pressure field at source surface using the direct formulation of Equation (2.19), expressed averagely on the patches

$$\mathbf{p}_i = \mathbf{Z}_{ij}\mathbf{v}_j + \mathbf{Z}_{ik}\mathbf{v}_k, \tag{2.23}$$

where the index $i \neq j$ denotes a patch of the surface of the source.

The two complementary quantities of sound pressure and particle velocity now being known on the surface of the source, the source intensity field $\mathbf{i}_i$ is deduced by

$$\mathbf{i}_i = \frac{1}{2}\Re(\mathbf{p}_i \circ \mathbf{v}_i^*), \tag{2.24}$$

where the notations $\Re(\mathbf{r})$ and $\mathbf{r}^*$ denote respectively the real part and the conjugate complex of a complex vector $\mathbf{r}$. The operator $\circ$ corresponds to Hadamard's term-to-term product.

The global indicators such as the sound power radiated by the source W (Equation (2.25)) and the radiation efficiency σ_{rad} (Equation (2.26)) are then accessible

$$W = \mathbf{a}_i^T \mathbf{i}_i \tag{2.25}$$

and

$$\sigma_{rad} = \frac{\mathrm{W}}{\frac{1}{2}\rho_0 c \mathbf{a}_i^T (\mathbf{v}_i \circ \mathbf{v}_i^*)}, \tag{2.26}$$

where the operator $\mathbf{r}^T$ designates the transpose of a vector r and $\mathbf{a}_i$ is the vector of the source patch areas.

The source is then completely characterized conjointly by the inverse (Equation (2.22)) and direct formulation (Equation (2.23)) of the problem of acoustic radiation. It is the basis of the method of identifying source referred to as u-iPTF, which is based on a uniformly rigid virtual volume.

2.2.2 Mixed virtual boundary conditions (m-iPTF)

The m-PTF method presented in Section 2.1.2 is based on the arbitrary definition of a virtual volume whose virtual boundary conditions are chosen mixed. It allows, as shown schematically to Figure 2.3, to calculate the sound pressure field radiated by a source and its environment inside this volume knowing:

- the normal vibration velocity of the patches j of the source surface Γ_S,
- the sound pressure evaluated at the level of the patches k of the virtual surface Γ_V,
- and the modal behavior of the virtual acoustic volume Ω, expressed in terms of deformations of pressure ϕ_n and normal particle speed of air χ_n.

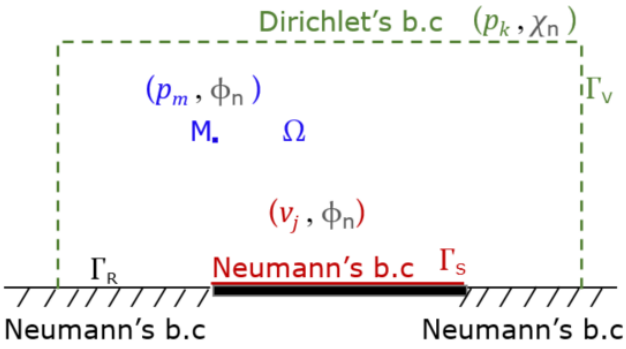

Figure 2.3: Complex baffled vibro-acoustic structure radiating in an a free field environment. Indication of the boundary conditions (b.c) and of the evaluated data (real data, modal data) for m-PTF and m-iPTF formulations.

The m-PTF formulation is thus given by the relation is given by Equation (2.18). To calculate the pressure at several points m in the virtual acoustic volume, the Equation (2.18) can be in the following matrix form

$$\mathbf{p}_m = \mathbf{Z}_{mj}\mathbf{v}_j - \mathbf{Y}_{mk}\mathbf{p}_k, \tag{2.27}$$

with

$$\mathbf{Z}_{mj} = \sum_{n=1}^{N} \mathrm{i}\omega\rho_0 \frac{(\phi_n)_m \langle\phi_n\rangle_j A_j}{(k^{*2} - k_n^2)\Lambda_n} \quad \text{and} \quad \mathbf{Y}_{mk} = \sum_{n=1}^{N} \mathrm{i}\omega_n\rho_0 \frac{(\phi_n)_m \langle\chi_n\rangle_k A_k}{(k^{*2} - k_n^2)\Lambda_n}. \tag{2.28}$$

In Equation (2.27), unlike the u-iPTF method (Equation (2.20)), only the transfer matrix $\mathbf{Z}_{mj}$ denotes an acoustic impedance matrix. However, each of the two matrices $\mathbf{Z}_{mj}$ and $\mathbf{Y}_{mk}$ are matrices which can be calculated purely numerically. The m-PTF method being based on Green's identity, the separation of the fields in Equation (2.27) allows to separate the term $(\mathbf{Z}_{mj}\mathbf{v}_j)$ relating to the source

$$\mathbf{Z}_{mj}\mathbf{v}_j = \mathbf{p}_m + \mathbf{Y}_{mk}\mathbf{p}_k. \tag{2.29}$$

As with the u-iPTF method, Equation (2.27) represents a linear system whose solution is obtained by inverting the $\mathbf{Z}_{mj}$ matrix

$$\mathbf{v}_j = \mathbf{Z}_{mj}^{-1}\left(\mathbf{p}_m + \mathbf{Y}_{mk}\mathbf{p}_k\right). \tag{2.30}$$

As mentioned earlier, this Equation (2.30) inversion process is not without repercussions and the problems relating to this step will be explained in Chapter 3.

Finally, considering Equation (2.30), the normal vibration velocity of the patch j of the source is accessible by knowing the sound pressure both of the patch k of the virtual surface and at points m in the virtual acoustic volume (Figure 2.3). Also, once the velocity field is identified, the surface pressure field of the source is known by extending the direct formulation of m-PTF (Equation (2.30)) on the source surface patches

$$\mathbf{p}_i = \mathbf{Z}_{ij}\mathbf{v}_j - \mathbf{Y}_{ik}\mathbf{p}_k. \tag{2.31}$$

Thus, the intensity field (Equation (2.24)), the radiated acoustic power (Equation (2.25)) and the radiation efficiency (Equation (2.26)) can be deduced from the identification of these two fields. The source is then completely characterized. The conjoint inverse (Equation (2.30)) and direct (Equation (2.31)) formulations of the radiation problem forms the basis theory of the source identification method called m-iPTF. It is based on a virtual volume arbitrary with mixed boundary virtual type conditions.

2.3 Interests and comparison of iPTF identification methods

Based on an inverse and direct formulation of the radiation problem, the two iPTF methods both allow the complete characterization of a vibro-acoustic source. For this, they require the pressure data taken at several points around the source inside the virtual volume and an acoustic quantity (pressure for m-iPTF and particle velocity for u-iPTF) evaluated on a virtual surface surrounding it completely. As these data are measurable, the iPTF methods constitute experimental identification methods of acoustic sources. They were formulated from the arbitrary definition of a defined acoustic volume around a source placed in any environment and on Green's identity application. Thus, they combine a number of experimental advantages:

- The arbitrary nature of the virtual acoustic volume (and of the virtual surface) makes it possible to manage the source environment by adapting the measurement process accordingly. Also, the position of the points inside the volume not being imposed, the measurements can be made by positions only accessible around the source.

- Green's identity acts as a field separation technique to achieve measurements regardless of the external source environment,

- The transfer matrices are defined with the geometry of the virtual volume and are therefore independent of measurements. This feature makes it possible to test different test conditions with a unique modal extraction calculation.

- Any rigid surface is no longer involved in the final formulation of iPTF methods due to the equivalence between the real and virtual boundary condition for this surface. This is a way to reduce the measurement surface (of the virtual surface) using rigid walls. Also, any rigid object can be included in the volume (in the case of a congested source for example) to work around it and therefore simplify the measurement. This unique feature in the field of acoustic inverse approaches will be the subject of Chapter 5.

In addition, the fact of having initially used a modal decomposition of the pressure field induced modal transfer matrices which are solvable with a finite element type solver. This is a departure from other methods of identifying sources based most of the time on an expansion in plane, spherical waves or on BEM type formulations. Such a choice is accomplished by the use of finite element (FE) solvers which are now standard in companies. This makes it possible to handle the geometric complexity of any problem. Indeed, it is then possible by iPTF methods to reconstruct all the source sound fields directly on the surface of the structure, thereby solving a major industrial challenge.

The two methods u-iPTF and m-iPTF are based on different virtual boundary conditions, which modifies both the measures and the modal data necessary for their calculation. Experimentally, the u-iPTF method requires pressure measurement inside the virtual acoustic volume and measuring the normal air particle velocity at the virtual surface which requires some dedicated sensors. Conversely, the m-iPTF method needs only pressure measurements and thus only requires the use of classical microphones. In return, while the u-iPTF method only uses the modes of the virtual volume expressed in terms of acoustic pressure, the m-iPTF method also requires those expressed in terms of acoustic velocity. We thus have two distinct identification methods, the choice of which will essentially depend on the measurement means available (microphone for sound pressure and particle velocity sensors for air velocity) and the FE solver used.

2.4 Originalities of the conducted work

On the basis of the u-iPTF and m-iPTF, the present work has three main objectives:

- As mentioned in this chapter, both methods are ill-posed problems (as most of the inverse approaches). This means that the inversion process of Equations (2.22) and (2.30) needs to be regularized to minimize errors due to noisy measurements. The most common regularization technique is the so-called Tikhonov regularization. The method is based on a regularization parameter that must be carefully chosen to obtain the optimal solution. To select the best value for the regularization parameter, one has to define a criterion on a cost function. Apart from Tikhonov regularization, several other approaches have been developed along with several different criteria. In Chapter 3 some statistical, deterministic and iterative regularization methods and a collection of selection criteria are expressed in the framework of both iPTF methods. An in-depth analysis of the regularization strategies is performed to fully understand advantages and drawbacks of the considered regularization approaches. They are then bench-marked in Chapter 4 on several numerical test cases.

- One of the promising features of the iPTF approaches is the possibility to handle rigid surfaces around the source without any need to measure a quantity (pressure) on them. In Chapter 5 this property is exploited to handle the presence of a masking object. This

term is used for a rigid structure, placed more or less close to the source to identify, which makes impossible to place sensors in the acoustic space in between the source and the object. At our knowledge, this feature is unique for a field reconstruction method. In this thesis, this feature will be referred as "blind reconstruction". In Chapter 6, this feature will be evaluated on a real industrial application: the field reconstruction applied on a electric motor partially masked by a rigid object.

- Chapter 7 is devoted to a completely new development in iPTF context: the so-called "blind separation" of fields. The objective is here to reconstruct not only the fields on the surface of a vibrating structure but also to separate fields due to uncorrelated sources responsible of the structure vibration. The term "blind" comes here from the fact that no prior information on the sources is necessary. This approach is be validated on a numerical test case.

3

Regularization techniques

The preceding chapter demonstrated how, based on the concept of a virtual acoustic volume created around a vibro-acoustic source, two methods of determining acoustic source particle velocity that are particularly promising for industrial applications might be formulated. The two iPTF approaches (m-iPTF and u-IPTF) both rely on the inversion of a direct radiation problem, specifically on the inversion of a transfer matrix. The goal of this chapter is to discuss matrix inversion and regularization of iPTF problems. In the first section, we demonstrate that iPTF problems are ill-posed and that their poor conditioning causes difficulties in the inverse process. A regularization of the inverse problem is required to obtain a correct identification. The latter will then arrive at an optimal solution based on a set of criteria. We first discuss the causes of poor iPTF method conditioning, specifically the measurement and discretization of the integral problem, as well as the various parameters involved in the stability of the inverse process. We then discuss how to regularize the iPTF problem and which regularization techniques are accessible and suited for use.

3.1 Introduction

In general, inverse problems are concerned with determining the causes of an observed or desired effect. In this regard, one usually divides them in terms of [187]: Identification or reconstruction (if one looks for the cause for an observed effect) and control or design (if one looks for a possible cause of a desired effect). Both problems are related, but there are also several mathematical consequences due to the different aims. For instance, in an identification problem a desirable property is uniqueness of a solution (identifiability), because there is probably a specific cause for the observed effect, which one would like to obtain. In a control or design problem, uniqueness is not really of importance, since non-uniqueness only means that the design goal can be reached by different strategies and hence, one has additional freedom (e.g. to incorporate further design goals).

A common property of a vast majority of inverse problems is their ill-posedness. In the sense of Hadamard [188], a mathematical problem is well-posed if it satisfies the following properties:

- *Existence* : for all (suitable) data, there exists a solution of the problem (in an appropriate sense).
- *Uniqueness*: for all (suitable) data, the solution is unique.
- *Stability*: the solution depends continuously on the data.

According to this definition, a problem is ill-posed if one of these three conditions is violated. An important consequence of non-uniqueness and ill-posedness is that the reconstructed source

velocity $\mathbf{v}_j$ can be far from the true source field. This indicates that, regardless of how effectively a regularized solution is reconstructed, there will be still error when compared to the forward solution counterpart. As a consequence, trying to invert the forward solution directly (or solve for the "best-fit-to-data" solution) leads to the amplification of high-frequency components. Thus, any noise in the measurements and any error in the forward model will contain such high-frequency components which will then dominate unconstrained solutions. The effects of these components on the solution must be constrained if the result is to be useful.

In very broad terms, the inverse problem of iPTF as seen in Equations (2.22) and (2.30) may be defined as the determination of the acoustic source indicators (especially velocity) from a number of remote recordings of either pressure and/or velocity in an acoustic field and corresponding transfer matrices. Unfortunately, unless this problem is appropriately constrained, in all likelihood it will be ill-posed in the sense of Hadamard [188] – the solution will not depend continuously on the data, meaning that small perturbations in the input data will result in disproportionately large changes in the computed solution. The principal matter of this chapter is to provide a description of the important techniques used for the analysis, regularization, and various forms of numerical solution of the iPTF problems.

3.2 Inverse Problem Formulation

In this section we describe in general terms a formulation of the inverse problem that encompasses all the variants we will then describe in more detail. We will then discuss, again in general terms, solution strategies that address the ill-posedness explained in the introduction section 3.1. The prototype of inverse problem will be an equation of the form

$$y = A(x) \tag{3.1}$$

where A is a forward operator which incorporates a parameterized model of the sources and produces a prediction of the measured pressure or velocity. x holds input parameters (the solution of interest), y holds the output parameters (noisy measurements). The noisy measurements are modeled as $y = \overline{y} + \mathbf{e}_y$, where e_y represents the measurement noise and $\overline{y}$ is the noiseless part of y.

For linear forward operators, A becomes a matrix $\mathbf{A}$ and measurements, solution and noise can be denoted as column vectors: $\mathbf{y}$, $\mathbf{x}$, and $\mathbf{e_y}$ respectively. In this situation the forward model becomes

$$\mathbf{y} = \mathbf{A}\mathbf{x} \tag{3.2}$$

such that $\mathbf{y}$ is a noisy signal such that $\mathbf{y} = \overline{\mathbf{y}} + \mathbf{e_y}$.

Although we have written the forward operator A above as free of error, it is important to recognize that generally, none of the components of Equation (3.2) are exact – in addition to measurement noise the forward operator is corrupted to some degree by the modelling errors arising from many sources: inaccuracies in developing the geometric model, errors associated with the numerical solution of the forward problem.

Moreover, the measured signals from the acoustic sensors have errors due to background noise, calibration and geometrical positions in space. Errors may be considered small after proper calibration but such errors can and do become greatly amplified in an inverse calculation, especially without careful treatment, due to the ill-posed nature of the problem.

3.2.1 Discrete ill-posed and ill-conditioned problems

In regularization theory the problem, like Equation (3.3),

$$\mathbf{Z}_{mj}\mathbf{v}_j = \hat{\mathbf{p}}_m \quad \text{with} \begin{cases} \hat{\mathbf{p}}_m = \mathbf{p}_m - \mathbf{Z}_{mk}\mathbf{v}_k & \text{for u-iPTF} \\ \hat{\mathbf{p}}_m = \mathbf{p}_m + \mathbf{Y}_{mk}\mathbf{p}_k & \text{for m-iPTF} \end{cases} \tag{3.3}$$

is commonly written in the discrete matrix form:

$$\mathbf{A}\mathbf{x} = \mathbf{y} \quad \text{with} \quad \mathbf{A} \in \mathbb{C}^{m\times n}, \quad \mathbf{y} \in \mathbb{C}^{m\times 1} \quad \text{and} \quad \mathbf{x} \in \mathbb{C}^{n\times 1} \tag{3.4}$$

or as a minimization of the residual norm:

$$\min_{\mathbf{x}} \|\mathbf{A}\mathbf{x} - \mathbf{y}\|_2^2 \tag{3.5}$$

where $\|\mathbf{r}\|_2$ represents the Euclidian norm of $\mathbf{r}$ and $\mathbf{A}$ represents the transfer matrix that relates an input vector $\mathbf{x}$ (cause) to an output vector $\mathbf{y}$ (effect) of dimensions n and m, respectively. Essentially, the matrix forms a discrete representation of the system under consideration.

For the sake of simplicity in the formulations to come, $\mathbf{Z}_{mj}$ will be replaced with $\mathbf{A}$, $\mathbf{v}_j$ with $\mathbf{x}$ and $\hat{\mathbf{p}}_m$ with $\mathbf{y}$.

In a forward problem the input vector $\mathbf{x}$ is known and a solution to the output $\mathbf{y}$ in the field is sought. In inverse problems the challenge is to obtain a meaningful estimate of the unknown original input $\mathbf{x}$ of the system given the output vector $\mathbf{y}$. This data vector $\mathbf{y}$ is commonly obtained from a measurement and the transfer matrix, $\mathbf{A}$ can either be measured or computed (in the case of iPTF method).

When the system Equation (3.4) or (3.5) arises from a discretization of an ill-posed problem,

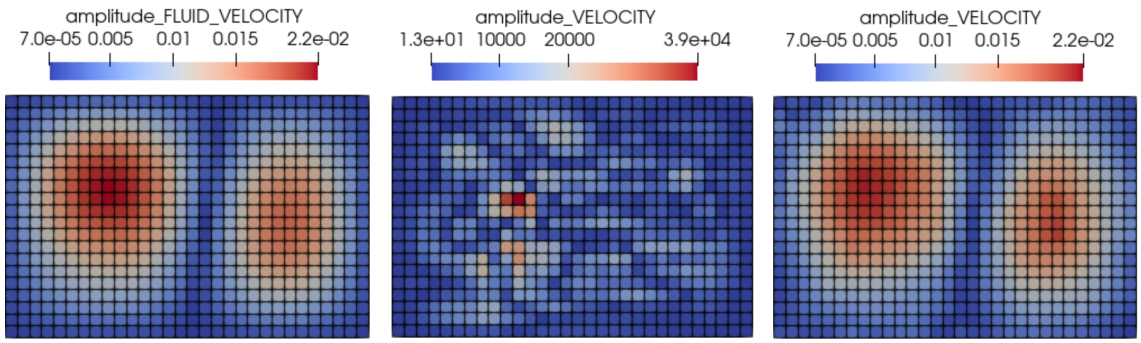

(a) (b) (c)

Figure 3.1: Comparison of the source velocity field maps (m/s) at 100 Hz obtained (a) by the reference calculation (b) without regularization of the m-iPTF problem and (c) with regularization of the m-iPTF problem.

the transfer matrix is ill-conditioned and hence standard inversion techniques fail to obtain a physically meaningful approximation to $\mathbf{x}$. For the iPTF problem such ill-behaviour is illustrated in Figure 3.1, which shows the useless identification of the source velocity field. It should be noticed that Figure 3.1 depicts identification findings from one of the idealized case studies described in Section 4.3 (which basically entails exciting a simply supported plate with a unit point force).

On the other hand, things get more complicated in a practical situation where the measured components of $\mathbf{y}$ are contaminated with some level of noise, in such a way that the actual measured data contains not only components of the true field data but also a noisy component. In the worst case if the levels of noise are larger than the actual field data, the reconstructed

parameters will be dominated only by errors.

For these reasons acoustic parameter estimation by iPTF, and in general inverse problems in the form of Equation (3.4), requires a special treatment known as regularization. As stated by Martin [187]:

> *Without regularization and without further information, the error between the exact and noisy solution can be arbitrarily large, even if the noise is arbitrarily small.*
>
> — Martin

As mentioned earlier, despite the system being ill-conditioned, meaningful approximate solutions can still be obtained by the application of more sophisticated so-called regularization methods rather than naive standard solution techniques.

3.2.2 Ill-conditioning of the acoustic transfer matrix

Before passing to review some of the existing regularization techniques, two aspects regarding the ill-conditioning of the matrix $\mathbf{Z}_{mj}$ represented now as matrix $\mathbf{A}$ will be discussed.

3.2.2.1 Singular Value Decomposition

In order to better appreciate the effects of the ill-conditioning of the acoustic transfer matrix, let us take hand of the Singular Value Decomposition (SVD) technique, which is a useful numerical tool that has been widely used in the analysis of linear systems due to its capability to provide detailed information of the linear system's behavior. In our current situation, it will help reveal all the difficulties associated with the ill-conditioning of matrix $\mathbf{A}$ [189, 190]. The theory of this useful technique is well established and it has been well documented in the literature [191]. This section is therefore devoted to show the application of the SVD to the acoustic transfer matrix rather than introducing the fundamentals of the SVD technique itself. Nevertheless the basic properties of the SVD are discussed next.

Considering the rectangular transfer matrix $\mathbf{A} \in \mathbb{C}^{m \times n}$ the SVD of this matrix is written as:

$$\mathbf{A} = \mathbf{U}\Sigma\mathbf{V}^{H} = \sum_{i=1} \mathbf{u}_i \sigma_i \mathbf{v}_i^{\mathrm{H}}. \tag{3.6}$$

In the case of an overdetermined system ($m > n$), matrix $\mathbf{U}$ is of dimensions $m \times n$, $\mathbf{V}$ is of $n \times n$. For an underdetermined system ($m < n$), $\mathbf{U}$ is of dimensions $m \times m$ and $\mathbf{V}$ of $n \times m$. In both cases, $\mathbf{U}$ and $\mathbf{V}$ are unitary matrices, $\mathbf{U}^{\mathrm{H}}\mathbf{U} = \mathbf{I}_m$ and $\mathbf{V}^{\mathrm{H}}\mathbf{V} = \mathbf{I}_n$, with their columns representing the left and right singular vectors $\mathbf{u}_i$ and $\mathbf{v}_i$, respectively:

$$\mathbf{U} = \begin{bmatrix} \mathbf{u}_1 & \mathbf{u}_2 & \cdots & \mathbf{u}_{\min(m,n)} \end{bmatrix} \text{ and } \mathbf{V} = \begin{bmatrix} \mathbf{v}_1 & \mathbf{v}_2 & \cdots & \mathbf{v}_{\min(m,n)} \end{bmatrix}. \tag{3.7}$$

The nonnegative and real singular values, σ_i, are collected on the diagonal of matrix $\mathbf{\Sigma} = \mathrm{diag}\begin{pmatrix} \sigma_1 & \sigma_2 & \cdots & \sigma_{\min(m,n)} \end{pmatrix}$ in descending order such that $\sigma_1 \geq \sigma_2 \geq \ldots \geq \sigma_{\min(m,n)} > 0$.

It is worth to introduce also the term condition number, which is another concept useful to quantify the ill-conditioning of a matrix, and is defined as

$$cond(\mathbf{A}) = \|\mathbf{A}\|_2 \left\|\mathbf{A}^{-1}\right\|_2 = \frac{\sigma_1}{\sigma_{\min(m,n)}}. \tag{3.8}$$

The condition number of $\mathbf{A}$ equals the ratio of the largest and smallest singular values as defined in equation (3.8). This ratio is a measure for the sensitivity of the solution to perturbation errors in matrix $\mathbf{A}$ or the right-hand side $\mathbf{y}$. It has to be remarked that the SVD presented in equation (3.6) is a so-called 'economy sized' type of decomposition, that is the singular values

and vectors associated with the null-space of matrix $\mathbf{A}$ are intentionally left out of consideration. In connection with discrete ill-posed problems, three characteristic features of the SVD of $\mathbf{A}$ are often found [192, 190, 193, 194]:

- The singular values σ_i decay gradually to zero with no particular gap in the spectrum.
- The condition number of $\mathbf{A}$ is large.
- The left and right singular vectors $\mathbf{u}_i$ and $\mathbf{v}_i$ tend to have more sign changes in their elements as index i increases. In other words, as σ_i decreases (index i increases) the singular vectors become more oscillatory.

These characteristics are confirmed by the decomposition of the $\mathbf{Z}_{mj}$ matrix in equation (2.30) for m-iPTF problem (same test case study as in Figure 3.1) performed at frequency of 100 Hz. For example, Figure 3.2 clearly illustrates the gradual decay of the singular values σ_i. Moreover, even for such a small problem (dimensions of $\mathbf{Z}_{mj}$ are 600×600), the condition number $\kappa(\mathbf{A}) = 2.06 \times 10^8$ already spans several orders of magnitude.

In Figure 3.3 it is confirmed that the left and right-hand singular vectors indeed contain

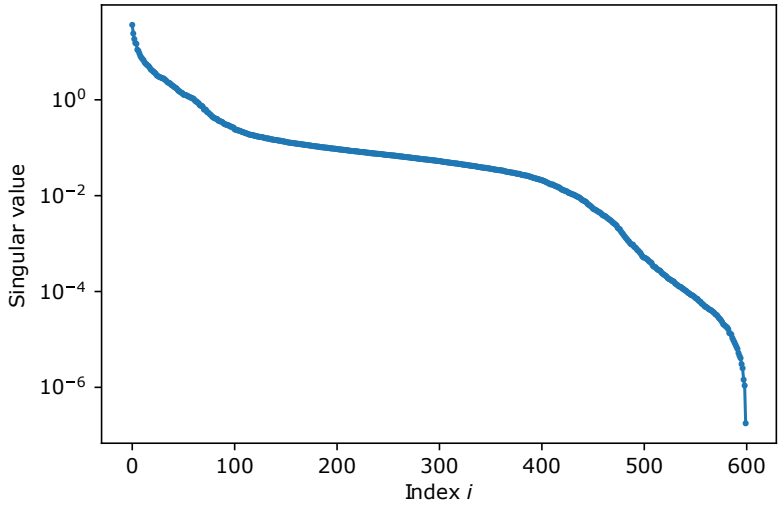

Figure 3.2: Singular value spectrum of the 600×600 impedance transfer matrix $\mathbf{Z}_{mj}$ in Equation (2.30) at 100Hz.

more oscillations as the index of the singular value increases. Figure 3.3 was created using the same test case study as Figure 3.1.

Borgiotti [195] and Photiadis [196] were amongst the first to employ the SVD algorithm to analyze the radiation from a vibrating structure into the farfield. They showed that the matrix decomposition provides a 'modal' representation of source strength distributions, the *source modes* $\mathbf{V}$, and distributions of an accompanying property in the field, *the field modes* $\mathbf{U}$. This can be easily understood by performing the SVD on the iPTF problem (2.30) presented in the previous subsection 2.1.2

$$\begin{aligned} \mathbf{y} &= \mathbf{A}\mathbf{x} \\ &= \mathbf{U}\Sigma\mathbf{V}^{\mathrm{H}}\mathbf{x}. \end{aligned} \tag{3.9}$$

Multiplying this expression by $\mathbf{U}^{\mathrm{H}}$ and accounting for the fact that $\mathbf{U}$ is unitary yields

$$\mathbf{U}^{\mathrm{H}}\mathbf{y} = \Sigma\mathbf{V}^{\mathrm{H}}\mathbf{x}. \tag{3.10}$$

Since the columns of both $\mathbf{U}$ and $\mathbf{V}$ are orthonormal, the pre-multiplication with the Hermitian of these matrices can be interpreted as a projection of $\mathbf{y}$ and $\mathbf{x}$ onto two linearly independent

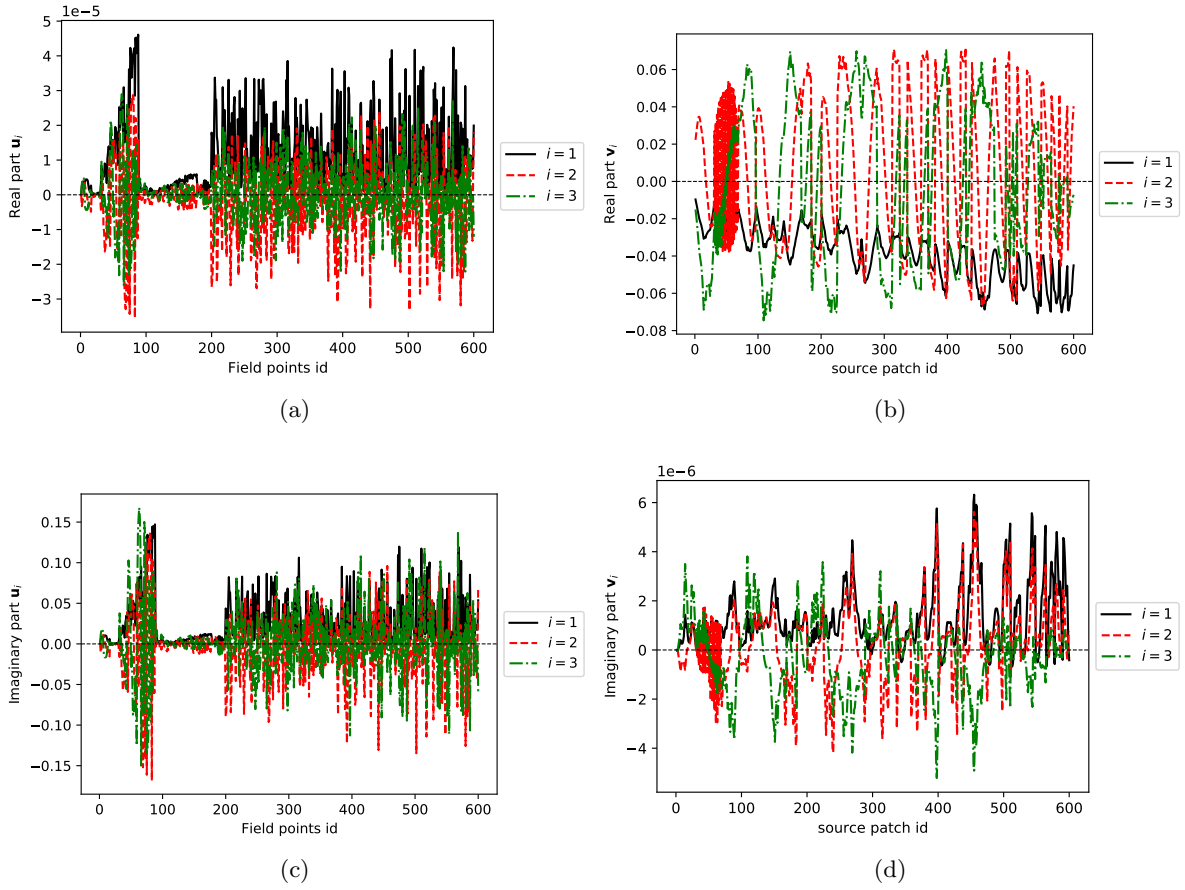

Figure 3.3: Singular vectors show more oscillations for higher index i. (a), (b) are the real part of $\mathbf{u}_i$ and $\mathbf{v}_i$ respectively. Likewise (c) and (d) are the imaginary part of vector $\mathbf{u}_i$ and $\mathbf{v}_i$ respectively. Vectors $\mathbf{u}_i$ can be interpreted as field modes whereas vectors $\mathbf{v}_i$ represent source modes.

bases. The participation coefficient of each left- and right-hand singular vector in the field distribution $\mathbf{y}$ and source quantity $\mathbf{x}$ are collected in vectors $\tilde{\mathbf{y}}$ and $\tilde{\mathbf{x}}$ defined as

$$\tilde{\mathbf{y}} = \mathbf{U}^{\mathrm{H}}\mathbf{y} \quad \text{and} \quad \tilde{\mathbf{x}} = \mathbf{V}^{\mathrm{H}}\mathbf{x}. \tag{3.11}$$

Substitution of equation (3.10) into (3.11) results in a decoupled system of equations that independently relates each participation factor of a source mode $\mathbf{v}_i$ by multiplication of the corresponding singular value σ_i to the participation of the field mode $\mathbf{u}_i$

$$\tilde{\mathbf{y}} = \mathbf{\Sigma}\tilde{\mathbf{x}}. \tag{3.12}$$

So, regarding the iPTF problem, the left-hand singular vectors $\mathbf{u}_i$ represent mode shapes describing pressure of field point distribution in the virtual volume whereas the right-hand singular values $\mathbf{v}_i$ are associated with spatial patterns of the particle velocity on the source surface. The coupling between a field and source mode is uniquely given by the corresponding singular value. Although it might be suggested in Figure 3.3, the field and source modes are generally not identical since the shapes of the virtual boundary and the field points distributions are not necessarily the same.

Finally, the SVD also gives important insight into another aspect of ill-conditioned problems, namely the smoothing effect. This is typically associated with integral kernels encountered in many physical problems [190, 193]. For example consider the mapping $\mathbf{y} = \mathbf{A}\mathbf{x}$ of an arbitrary vector $\mathbf{x}$. Application of the SVD yields

$$\mathbf{y} = \mathbf{U}\mathbf{\Sigma}\mathbf{V}^{\mathrm{H}}\mathbf{x}, \quad \text{or componentwise,} \quad \mathbf{y} = \sum \sigma_i \left(\mathbf{v}_i^{\mathrm{H}}\mathbf{x}\right)\mathbf{u}_i. \tag{3.13}$$

The product $\mathbf{v}_i^{\mathrm{H}}\mathbf{x}$ can be interpreted as a measure for the spatial matching (or participation factor) between singular vector $\mathbf{v}_i$ and vector $\mathbf{x}$. With this knowledge and recalling that the singular vectors $\mathbf{u}_i$ and $\mathbf{v}_i$ become more oscillatory as σ_i decreases, it is obvious that the multiplication with σ_i leads to more damping of the high wavenumber components of $\mathbf{x}$ and less damping of the low wavenumber components in mapping $\mathbf{A}\mathbf{x}$. As a consequence, in forward problems the solution $\mathbf{y}$ is generally smoother than the prescribed vector $\mathbf{x}$.

In contrast, the inverse problem will show the opposite effect, amplifying the components with high spatial oscillations in the right-hand side $\mathbf{y}$. Owing to the smoothing characteristics of the forward problem, noise often has a relatively strong contribution to the high-frequency oscillations in $\mathbf{y}$. Therefore, the noisy components especially are subjected to a large amplification in the inverse process.

Concluding, the forward operation of mapping input vector $\mathbf{x}$ onto output vector $\mathbf{y}$ has a smoothing effect on $\mathbf{x}$, whilst the opposite operation tends to amplify oscillations in vector $\mathbf{y}$. Hence, if a solution of $\mathbf{x}$ is required with a limited L_2 norm, then not all distributions $\mathbf{y}$ form a valid right-hand side. In fact, vector $\mathbf{y}$ must be sufficiently smooth to 'survive' the inversion back to a physically meaningful $\mathbf{x}$. The mathematical formulation of this smoothness criterion on $\mathbf{y}$, given a certain kernel or transfer matrix, is known as the *discrete Picard condition* [192, 197] as presented in the next section.

3.2.2.2 A mathematical criterion: Discrete Picard condition (DPC)

In the framework of regularization techniques, an important criterion exists to evaluate if the regularization process provides a reasonable solution: it's the so-called discrete Picard condition (DPC) [192, 197]. The DPC determines how well the regularized solution approximates the unknown exact solution.

For an ill-posed problem, the singular values σ_i of matrix $\mathbf{A}$ in Equation (3.4) decay gradually toward nearly zero and the condition number of $\mathbf{A}$, $\kappa(\mathbf{A})$, is very large. Thus Discrete ill-posed problems have an ill-determined rank, that is there does not exist a gap in the singular values

that could be used as a natural threshold. The DPC refers to whether the Fourier coefficients $\left|\mathbf{u}_i^{\mathrm{H}}\mathbf{y}\right|$ of the unperturbed right-hand side of Equation (3.4) decay to zero faster than the singular values σ_i do, with an increasing index i. If $\left|\mathbf{u}_i^{\mathrm{H}}\mathbf{y}\right|$ decay faster than σ_i, DPC is satisfied.
In the example shown in Figure 3.4, the DPC is fulfilled for an index lower than $i_{dpc} = 83$, represented by the vertical line. Above this index value, the data becomes dominated by errors and the DPC fails. The problem on which Figure 3.4 is generated is the noiseless setup of Section 4.4's test case study for m-iPTF at 370 Hz.

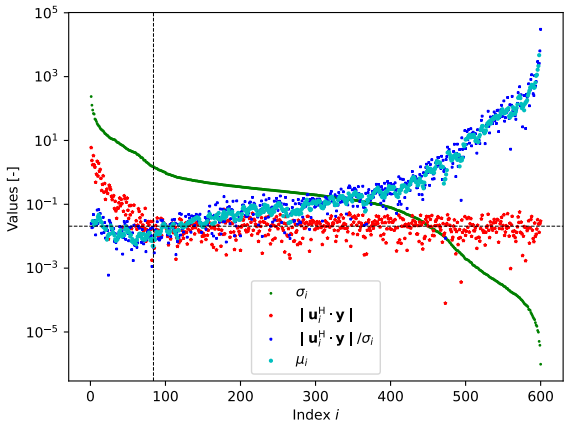

Figure 3.4: Picard plot for the m-iPTF problem carried out at 370 Hz where the vertical dashed line marks the beginning of $\left|\mathbf{u}_i^{\mathrm{H}}\mathbf{y}\right| < \sigma_i$ and the horizontal line represents the noise level μ_c. DPC is satisfied for $i_{dpc} < 83$.

Unfortunately, there exists no straightforward way to define the index value i_{dpc} numerically. Although the singular values are ordered so that $\sigma_i \geq \sigma_{i+1}$ (that is they monotonously decay to zero), the same is not true for the Fourier coefficients. Due to the noise in the measurements the property $\left|\mathbf{u}_i^{\mathrm{H}}\mathbf{y}\right| \geqslant \left|\mathbf{u}_{i+1}^{\mathrm{H}}\mathbf{y}\right|$ does not hold in general. Therefore, it is necessary to check for a trend in the coefficients to decay to zero faster than the singular values.
A practical solution to this problem was proposed by Hansen [192, 197] who suggested to evaluate the *moving geometric mean*

$$\mu_i = \frac{1}{\sigma_i}\left(\prod_{j=i-q}^{i+q}\left|\mathbf{u}_j^{\mathrm{H}}\mathbf{y}\right|\right)^{\frac{1}{2q+1}}, \quad i = q+1,\ldots,n-q \tag{3.14}$$

where q is a small integer (for instance 1, 2 or 3) ensuring the locality of μ_i. The i_{dpc} index is defined as $i_{dpc} = q + \operatorname{argmin}\mathcal{H}_q$ with $\mathcal{H}_q = [\mu_{q+1}, \mu_{q+2}\ldots,\mu_{n-q}]$.
Assuming a noise free $\mathbf{A}$ and a noisy $\mathbf{y} = \overline{\mathbf{y}} + \mathbf{e}_{\mathbf{y}}$, where $\overline{\mathbf{y}}$ is the true noiseless $\mathbf{y}$ the DPC can be mathematically formulated as

$$\left|\mathrm{u}_i^{\mathrm{H}}\mathbf{y}\right| = \left|\mathrm{u}_i^{\mathrm{H}}\overline{\mathbf{y}} + \mathrm{u}_i^{\mathrm{H}}\mathbf{e}_{\mathbf{y}}\right| \approx \left|\mathrm{u}_i^{\mathrm{H}}\mathbf{e}_{\mathbf{y}}\right| \approx \hat{c}_i \quad \text{for} \quad i > i_{dpc}, \tag{3.15}$$

The DPC is only partially met in real problems, as illustrated in Figure 3.4. Indeed, the sequence $\left\{\left|\mathbf{u}_i^{\mathrm{H}}\mathbf{y}\right|/\sigma_i\right\}$ declines for a time before increasing for $i > i_{dpc}$. This rise appears to be "noise" or "ill-posedness" caused by the iPTF's proceedings, such as the discretization or measurement processes, producing a $\mathbf{y}$ that does not totally fulfill the DPC. As a result, the iPTF problem's ill-posedness nature can be described by the distribution of the noise, which can

be quantified by the mean noise level μ_c

$$\mu_c = \frac{1}{n - i_{dpc}} \sum_{i=(i_{dpc}+1)}^{n} \left| \mathbf{u}_i^{\mathrm{H}} \mathbf{y} \right|. \tag{3.16}$$

Figure 3.5 plots the evolution of the mean noise level, denoted as ill-posedness level in the following chapters, as a function of frequency for different Signal-to-Noise Ratios (SNR) added on $\bar{\mathbf{y}}$ to simulate the noisy measurement $\mathbf{y}$. Figure 3.5 is built on the same problem as the m-iPTF test case study provided in Section 4.4.

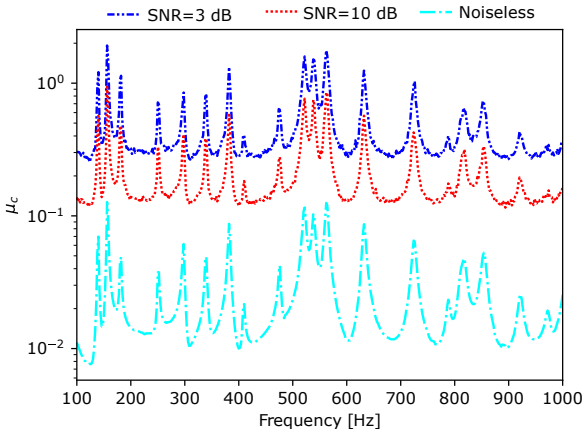

(a) μ_c spectra

Figure 3.5: Ill-posedness level spectra for m-iPTF problems with different levels of simulated noisified $\mathbf{y}$ for full frequency of study.

Figure 3.5 depicts clearly that the ill-posedness level of the iPTF increases as measurement data $\mathbf{y}$ become noisier (signal-to-noise ratio (SNR) value reduces) just as expected. DPC is a necessary condition for obtaining acceptable regularized solution. The reasons that a problem does not satisfy DPC are probably:

- the error in right hand side of Equation (3.4) is too large;
- insufficient collected data by $\mathbf{y}$ of Equation (3.4) for meaningful analysis;
- physical relation of the underlying exact problem is not reasonable.

Rather than the condition number of the matrix of a linear system, the rate of decrease of the singular values σ_i is a better indication of the conditioning of the problem 3.4 [198, 199]. Furthermore, the discrete Picard's condition (DPC) provides an objective assessment of the ill-posedness of the entire problem relating the matrix information $\mathbf{A}$ (by means of the singular values σ_i) with the measurements $\mathbf{y}$ [198]. The DPC ensures that the solution components related to small singular components are not over amplified, the percentage of useful σ_i, $((i_{dpc}/n) \times 100\%)$ can be used as a measure of posedness of an inverse problem.

In a nutshell, for real problems, measured data $\mathbf{y}$ are generally contaminated by different types of noise and it usually does not fully satisfy the condition. If the DPC holds partially, until a point where the data space coefficient levels off and becomes dominated by errors, a valid solution should be obtained by any regularisation method. On the other hand, if the DPC is violated for a given problem one should question the validity of the solution. See [192] for further information and how to implement a check for DPC satisfaction in practice.

3.2.2.3 Causes of ill-conditioned matrix $\mathbf{Z}_{mj}$

From the above discussion, it is noticed that when the acoustic transfer matrix $\mathbf{Z}_{mj}$ of Equation (3.3) is ill-conditioned, the singular values σ_i of the diagonal of $\mathbf{\Sigma}$ of Equation (3.6) tend to fall quickly to smaller values (and consequently a large condition number is obtained). This tendency has been observed by previous work, [200, 201, 180, 27] and in section 4.5 to be highly dependent on the place of the measurement points. The best situation that can be achieved is when the measurements are taken right on the source surface (taking into account enough evanescent waves). The condition number then increases drastically as the measurement points are moved out from the source surface (taking more propagating waves than the evanescent waves).

The condition number remains low as long as the measured data is not dominated by high levels of noise as seen in Section 4.4, and the geometry of the problem allows measurements at least as close as possible to the source surface patches. In practice this situation is hardly found, therefore acoustic engineers on inverse acoustic problems have to deal with highly ill-conditioned transfer matrices.

From the definition in Equation (3.8), it can be expected that transfer matrices with large condition numbers are nearly singular, implying that their inverse may not exists and that the solution of the linear system is not unique. Unfortunately, a general rule to specify limits on how much singular the transfer matrix is allowed to be in order to obtain meaningful solutions is still a research subject.

In addition to the problem of non-uniqueness of the solution of Equation (3.4) or (3.5), the ill-conditioning of the transfer matrix affects the accuracy of the reconstructed parameters in another way: as the transfer matrix gets more singular, the inverse linear system becomes more sensitive to the noise in the measured data.

The causes of the ill-conditioned nature of the acoustic transfer matrix $\mathbf{Z}_{mj}$ are manifold. For instance, while it has been observed by Forget *et al.* [180] that the ill-conditioning keeps a strong relationship with the geometric complexity of the problem, other factors such as the extracted modes of the virtual acoustic cavity and the quality of the modeling mesh have also influence over the condition number of the acoustic transfer matrix $\mathbf{Z}_{mj}$. These latter two factors are evident in the results shown in Section 5.3 and 5.4.

3.2.3 The Inverse Problem

3.2.3.1 General considerations

With the above notation, the inverse problem can be stated as finding a solution x which

1. matches the results that the model A would predict for that particular solution to the actual measurements y,

2. also is indeed a reasonable solution for parameters of iPTF problem.

One can think of this as "inverting" the operator in Equation (3.1) (although, as discussed below in Section 3.2.3.2, there are iterative approaches as described to finding x that do not explicitly compute an inverse, for either algorithmic or computational reasons). As we have stated above, even with a linear forward matrix $\mathbf{A}$ representing the impedance transfer matrix $\mathbf{Z}_{mj}$ and a vector $\mathbf{x}$ representing the source velocity vector $\mathbf{v}$, the inverse problem is ill-posed. This ill-posedness manifests itself in the severe ill-conditioning of the matrix $\mathbf{A}$. There is no reason to expect $\mathbf{A}$ to be square, and therefore, it is typically not invertible as in most cases. The usual solution in such cases, at least if the number of acoustic measurements is greater than the number of identification source patches (so that $\mathbf{A}$ is over-determined, that is, it has more rows than columns), is to solve the problem in a least-squares sense. This is the solution which minimizes the (Euclidean) magnitude of the residual error in Equation (3.5). The resulting

solution solves the square matrix equation

$$\mathbf{x}_{\mathrm{LSS}} = \left(\mathbf{A}^{\mathrm{H}}\mathbf{A}\right)^{-1}\mathbf{A}^{\mathrm{H}}\mathbf{y} = \mathbf{V}\Sigma^{-1}\mathbf{U}^{\mathrm{H}}\mathbf{y} = \sum_{i=1}^{\min(m,n)} \frac{\mathbf{u}_i^{\mathrm{H}}\mathbf{y}}{\sigma_i}\mathbf{v}_i. \tag{3.17}$$

This equation, in theory, has a unique solution if the columns of $\mathbf{A}$ are linearly independent (in effect, if the vectors which describe how each identification source patch j is related to all the measurement field locations in the virtual acoustic cavity are not redundant). However, even in this case, $\left(\mathbf{A}^{\mathrm{H}}\mathbf{A}\right)$ is even more poorly conditioned than $\mathbf{A}$, meaning that its inverse is even more challenging to obtain reliably. In the case that the number of acoustic field measurements, m is less than the number of identification source patch n at which one desires to estimate the relevant parameters (that is $m < n$, the matrix $\mathbf{A}$ is under-determined), there can be no unique solution. The most common strategy in this case is to find a solution which minimizes the Euclidean magnitude of the residual and is itself the shortest (in Euclidean length) of the infinite number of vectors which will achieve this minimum error. The "formula" for finding the solution is similar in spirit to Equation (3.17). It too requires solving a very badly conditioned system of equations, which leads to the same problem as discussed below in the framework of Equation (3.17).

From previous section, the forward operator A is ill-posed, a simple data fit by the minimization of the residual norm as given by Equation (3.5), for any of these formulations, leads to a (almost certainly) wildly erroneous inverse solution, with unrealistically large magnitudes, as illustrated in Figure 3.1(b). To obtain a reasonable inverse solution, prior knowledge about the solution needs to be added to the problem formulation as a constraint or set of constraints. The difficulties in accomplishing this goal include identification of physically useful descriptions of such prior knowledge, of mathematically tractable ways of including them into the inverse problem, and of practical algorithmic approaches to solving the resulting constrained optimization problem.

This section briefly introduces methods for the numerical treatment of discrete ill-posed problems. The problem of determining $\mathbf{x}$ in Equation (3.2) is an example of a rather general type of "inverse problem" that arises frequently in science and engineering (for a more general treatment of inverse problems the reader can refer to textbooks from Hansen [202] or Kaipio and Somersalo [203]). If the stability condition is violated, the numerical solution of the inverse problem by standard methods is difficult and often yields instability, even if the data are exact (since any numerical method has internal errors acting like noise) [187].

In inverse acoustics, as in other such inverse problems, there are special techniques that can be used to obtain a stable approximation of the solution. These techniques formulations fall into two categories. One is a deterministic framework, generally referred to as "regularization," in which an objective function to be minimized or a constraint function to be satisfied is composed of a combination of the norm of the residual error and some norm of a constraint function (or multiple constraint functions). Since the appropriate construction and analysis of regularization methods is the major issue in inverse problems, most of the section will be dedicated to this task. The other category of formulation is a statistical framework, in which the solution is treated as random with an appropriate probability model, and a probabilistic error measure is minimized to find a likely solution.

3.2.3.2 Deterministic regularization approaches

Conceptually, deterministic regularization approaches can be summarized by three different categories:

1. *Approximate the best-fit-to-data solution.* One or more spatial penalty functions acting on a candidate solution are defined, and then a weighted sum of these functions plus the

residual norm is minimized. This approach is generally called Tikhonov regularization [202, 204, 205]. The penalty functions generally used constrain the magnitude of the inverse solution or its high spatial frequency content (often formulated via a first or second order spatial derivative). One can summarize the resulting formulation as

$$\mathbf{x}_\lambda = \operatorname{argmin} \left\{ \|\mathbf{A}\mathbf{x} - \mathbf{y}\|_2^2 + \lambda^2 \|\mathbf{L}\mathbf{x}\|_2^2 \right\}, \tag{3.18}$$

where $\mathbf{L}$ represents a "regularization operator" and λ^2 is the regularization parameter whose value controls the level of regularization (that is the balance between the data fit and the amount of regularization). For a nonlinear operator $\mathbf{A}$ or nonlinear regularization operator $\mathbf{L}$, nonlinear optimization methods are used to obtain the solution. For the linear cases, $\mathbf{A}$ and $\mathbf{L}$ become matrices and the Tikhonov solution simplifies to:

$$\mathbf{x}_\lambda = \left(\mathbf{A}^{\mathrm{H}}\mathbf{A} + \lambda^2 \mathbf{L}^{\mathrm{H}}\mathbf{L} \right)^{-1} \mathbf{A}^{\mathrm{H}}\mathbf{y}, \tag{3.19}$$

(or equivalently solving $\left(\mathbf{A}^{\mathrm{H}}\mathbf{A} + \lambda^2 \mathbf{L}^{\mathrm{H}}\mathbf{L} \right) \mathbf{x}_\lambda = \mathbf{A}^{\mathrm{H}}\mathbf{y}$ by any appropriate algorithm).

2. *Approximate the forward operator.* In this approach, the forward operator $\mathbf{A}$ is approximated with an operator A_k that is "similar" to $\mathbf{A}$ in some well-defined sense, but much better conditioned. Formally, given $\mathbf{A}_k$ as some well-behaved approximation of $\mathbf{A}$, one solves

$$\mathbf{x}_k = \operatorname{argmin} \left\{ \|\mathbf{A}_k\mathbf{x} - \mathbf{y}\|_2^2 \right\}. \tag{3.20}$$

   In the discrete linear case, the most common version of this approach is called the Truncated Singular Value Decomposition (TSVD) [202] and $\mathbf{A}_k$ is a well-conditioned low-rank least squares approximation to $\mathbf{A}$.

3. *Iterative approach.* The iterative methods are another deterministic approach to solve the inverse problem. In these methods, a sequence of candidate solutions is produced and each one is evaluated according to a "goodness" criterion: if the solution meets some threshold of accuracy, the iterations stop, otherwise they continue with additional candidate solutions. These approaches draw on the standard techniques for solving large linear systems of equations [206, 26]. However, because such methods, like the unconstrained least-squares methods already described, will converge to unreliable solutions, the regularization approach is to truncate the iterations before convergence [202]. In this case, the number of iterations plays the role of a regularization parameter.
   Iterative methods are especially favorable for large-scale problems for which direct regularization methods are computationally expensive, and in problems in which a matrix representation of the forward operator or an explicit representation of the inverse solution are not available. However, their use is not limited to these cases; they can be used as an alternative approach to direct regularization approaches. Most iterative methods can be represented in terms of filter factors such as those already discussed for Tikhonov and TSVD approaches [202], which demonstrates the similarity between iterative methods and direct methods in their filtering of the small singular values of the forward matrix. In regularized iterative methods, the solution converges to the lower frequency modes of the right singular vectors of A in the earlier iterations, and thus stopping the iteration filters out the effect of the otherwise amplified higher frequency modes.
   The most commonly used iterative methods in this context are in the class of Krylov subspace methods, for which the connection between iteration number and modes of $\mathbf{A}$ is most clear. Brooks et al. [207] reported an early attempt to use this approach, in which the Conjugate Gradient (CG) iterative method was combined with regularization constraints. More recently, Ramanathan et al. [208] have reported using another Krylov subspace

method, the Generalized Minimum Residual (GMRes) method, with significant success. In this present study, a novel iterative conjugate gradient approach is investigated. This method is the Conjugate gradient for the normal equations (CGNE) via Lanczos bidiagonalization reorthogonalization algorithm proposed by Delillo [209].

It is noticed that under quite general conditions the linear versions of these three approaches can be shown to be closely related, somewhat surprising given the difference in their conceptual underpinnings [206].

3.2.3.3 Statistical regularization approaches

In *statistical approaches* $\mathbf{x}$ and $\mathbf{e_y}$ (the noise in $\mathbf{y}$) are considered as random vectors with given probability models. In particular, the probability model for $\mathbf{x}$ encodes our belief about how a reasonable, or physical, solution should behave. One Bayesian solution is the posterior mean of $\mathbf{x}$ [210], meaning that it is the statistical average, or expected value, of the probability distribution of the solution given the data. Applications of this approach to inverse acoustics to date have tended to use a simplified version of this general model with the following assumptions:

1. a linear forward matrix $\mathbf{A}$,
2. Gaussian statistical models for both $\mathbf{x}$ and $\mathbf{e_y}$.

Under these assumptions, the Bayesian solution becomes identical to the maximum of the posterior probability distribution of $\mathbf{x}$ given the measurements $\mathbf{y}$, and this solution is commonly called the Maximum a Posteriori (MAP) solution. With non-Gaussian models, the MAP solution is the best linear mean square error solution for $\mathbf{x}$ but not necessarily the posterior mean [210].

Independent of the assumption of probability models, there are a number of ways one can treat the temporal variation of $\mathbf{x}$ statistically. For simplicity, we discuss the possibilities in the context of Gaussian distributions for both the unknowns and the noise, which means that we need only to specify the mean and the covariance. The simplest and most widely used model assumes that each time instant is a vector drawn from a (second order) stationary distribution; in the case of a Gaussian model this means that a constant mean (almost always taken to be zero) and a fixed covariance matrix determine the model. One can also assume the covariance matrix to be fixed over time but let the mean be time-varying, or one can assume a constant mean but a general spatio-temporal covariance matrix, or one can let the mean vary in time and have a spatial-temporal covariance matrix as well. In any of the zero-mean cases, the MAP solution can be written as

$$\mathbf{x}_{\mathrm{MAP}} = \left(\mathbf{A}^{\mathrm{H}}\mathbf{C}_{e_y}^{-1}\mathbf{A} + \mathbf{C}_x^{-1}\right)^{-1}\mathbf{A}^{\mathrm{H}}\mathbf{C}_{e_y}^{-1}\mathbf{y}, \tag{3.21}$$

where $\mathbf{C}_x$ and $\mathbf{C}_{e_y}$ are appropriate solution and noise covariance matrices, respectively.

If $\mathbf{e_y}$ is assumed to be white noise ($\mathbf{C}_{e_y} = \sigma_{e_y}^2\mathbf{I}$, where σ_{e_y} is the noise variance), the solution becomes

$$\mathbf{x}_{\mathrm{MAP}} = \left(\mathbf{A}^{\mathrm{H}}\mathbf{A} + \sigma_{e_y}^2\mathbf{C}_x^{-1}\right)^{-1}\mathbf{A}^{\mathrm{H}}\mathbf{y}. \tag{3.22}$$

Comparing this result to Equation (3.19), we note a parallel structure; the inverse of the solution covariance matrix plays the role of the regularization term $\mathbf{L}^{\mathrm{H}}\mathbf{L}$ in the Tikhonov solution and the noise variance $\sigma_{e_y}^2$ plays the role of the regularization parameter.

Within the scope of the present study, two types of statistical approaches were investigated. The first method, proposed by Forget [27], concerns the use of Bayesian probability approach for the m-iPTF method. The other method called DBKH-iPTF algorithm 1 is new developed method we propose.

The relative strengths of the deterministic and statistical formulations lie in the ability to specify constraint functions $\mathbf{L}$ or statistical priors as determined by the covariance matrix $\mathbf{C}_x$.

It will be seen in subsequent subsections how each has been used to capture and formulate relevant assumptions about realistic solutions and to then solve the resulting version of the inverse problem.

3.3 Techniques for obtaining solutions for inverse problems

By posing the inverse problem in terms of reconstructing source surface velocity $\mathbf{x}$, the problem is linear and the resulting solution depends on dimension and rank of $\mathbf{A}$, as previously discussed. [211]. However, as already noted, because the inverse problem is ill-posed, such a formulation is inherently unstable; even extremely low levels of signal noise or very small geometric errors can result in an unbounded solution. Hence, in order to stabilize the problem and to obtain a reasonable solution, it is necessary to incorporate further constraints before attempting to solve the equations.

Considering each individual column of the matrix system in $\mathbf{A}$ are independent and solving for the vector $\mathbf{y}$, to obtain the regularized solution, $\mathbf{x}$ of Equation (3.17), that is the reconstructed source velocity

$$\mathbf{x}_{reg} = \mathbf{A}^{\dagger}_{reg}\mathbf{y} \tag{3.23}$$

where $\mathbf{A}^{\dagger}_{reg}$ is the regularized inverse matrix of $\mathbf{A}$. In terms of the singular value decomposition, the generalised inverse of $\mathbf{A}$, which is $\mathbf{A}^{\dagger}_{reg}$ can be defined as

$$\mathbf{A}^{\dagger}_{reg} = \sum_{i=1}^{\min(m,n)} f_i \mathbf{v}_i \sigma_i^{-1} \mathbf{u}_i^{\mathrm{H}} \tag{3.24}$$

where numbers f_i are known as the *filter factors*. Therefore, when solving the matrix Equation (3.4) in the "regularized" least squares sense by minimising the solution can be written as

$$\mathbf{x}_{reg} = \mathbf{A}^{\dagger}_{reg}\mathbf{y} = \sum_{i=1}^{\min(m,n)} f_i \frac{\mathbf{u}_i^{\mathrm{H}}\mathbf{y}}{\sigma_i}\mathbf{v}_i \tag{3.25}$$

These filter factors must have the important property that for decreasing values of σ_i, the corresponding factor f_i approaches zero in such a way that the contributions $\left(\mathbf{u}_i^{\mathrm{H}}\mathbf{y}/\sigma_i\right)\mathbf{v}_i$ to the solution from the smaller σ_i are effectively filtered out. In order to overcome the undesirable behavior associated with the ill-posed nature of the problem, Equation (3.4) and for $\mathbf{x}$ to represent a reasonable solution to Equation (3.4), the discrete Picard condition described in Section 3.2.2.2 must first be satisfied before applying any class of regularization technique. This condition requires on the average that, the absolute values of the coefficients $\mathbf{u}_i^{\mathrm{H}}\mathbf{y}$ decay to zero faster than the singular values.

The difference between the various regularization methods lies essentially in the way in which these filter factors are defined. Hence, the filter factors play an important role in connection with the regularization theory, and it is worth to characterize these factors for the regularization methods. One can noticed that by introducing the filter factors in Equation (3.24) the ill-conditioned problem is replaced by a well-conditioned problem whose solution approximates the desired unknown solution. The next section describes in detail the two of the most common specific approaches to generate $\mathbf{A}^{\dagger}_{reg}$ both of which are widely used in inverse acoustics.

3.3.1 Tikhonov Regularization (`Tikh` techniques)

The focus of this study will be zero-order Tikhonov regularization; thus objective function to minimize becomes

$$\mathbf{x}_{\lambda} = \min\left\{\|\mathbf{A}\mathbf{x}_{\lambda} - \mathbf{y}\|_2^2 + \lambda^2\|\mathbf{x}_{\lambda}\|_2^2\right\} \tag{3.26}$$

and the solution for zero-order Tikhonov regularization becomes

$$\mathbf{x}_\lambda = \mathbf{A}^\dagger \mathbf{y} = \left(\mathbf{A}^{\mathrm{H}}\mathbf{A} + \lambda^2 \mathbf{I}\right)^{-1} \mathbf{A}^{\mathrm{H}}\mathbf{y} = \sum_{i=1}^{n} \frac{\sigma_i^2}{\sigma_i^2 + \lambda^2} \frac{\alpha_i}{\sigma_i} \mathbf{v}_i \tag{3.27}$$

where $\alpha_i = \mathbf{u}_i^{\mathrm{H}}\mathbf{y}$.

It can be shown that the two terms in the zero-order Tikhonov functional (3.26) can be written as [202],

$$\rho^2(\lambda) := \|\mathbf{A}\mathbf{x}_\lambda - \mathbf{y}\|_2^2 = \sum_{i=1}^{n} \frac{\lambda^2 \alpha_i^2}{\left(\sigma_i^2 + \lambda^2\right)^2} + \|\mathbf{r}_\perp\|_2^2 \tag{3.28}$$

and

$$\eta^2(\lambda) := \|\mathbf{x}_\lambda\|_2^2 = \sum_{i=1}^{n} \frac{\sigma_i^2 \alpha_i^2}{\left(\sigma_i^2 + \lambda^2\right)^2} \tag{3.29}$$

where $\|\mathbf{r}_\perp\|_2^2 = \|\mathbf{A}\mathbf{x}_{\mathrm{LSS}} - \mathbf{y}\|_2^2$ is the residual from the least squares solution to Equation (3.4), (that is where $\lambda = 0$).

Furthermore, after transformation to the standard form, the zero-order Tikhonov regularized solution can be written conveniently in terms of filter factors in combination with the SVD of $\mathbf{A}$ [53]:

$$\mathbf{x}_\lambda = \sum_{i}^{\min(m,n)} f_i \frac{\mathbf{u}_i^{\mathrm{H}}\mathbf{y}}{\sigma_i} \mathbf{v}_i \tag{3.30}$$

where f_i are the Tikhonov filter factors given by

$$f_i = \frac{\sigma_i^2}{\sigma_i^2 + \lambda^2} \quad \begin{cases} 1 & \sigma_i \gg \lambda \\ \sigma_i^2/\lambda^2 & \sigma_i \ll \lambda \end{cases} \tag{3.31}$$

These factors have the effect of filtering out contributions to the reconstructed $\mathbf{x}_\lambda$ that correspond to the small singular values while leaving the SVD components corresponding to large singular values almost unaffected. The regularization parameter λ is usually chosen to lie between the largest and smallest singular values. Evidently, all regularization methods act as low-pass filters in the singular value spectrum [26].

The question remains how to select the optimum regularization parameter. The answer to this is the subject content for Section 3.4.

3.3.2 Iterative Approaches (`Itr` techniques)

All methods discussed so far can be classified as direct methods, because they are based on an explicit singular value decomposition. Although direct methods as described above are very accurate they have the disadvantage that their computational effort increases excessively with the number of unknowns N, typically proportional $\mathcal{O}\left(N^3\right)$. For this reason they are only applicable for models containing up to a few thousand unknowns [26].

Despite the fact that in practice the number of unknowns applied in acoustic source localization methods is sufficiently small to use the SVD based regularization methods, it still can be advantageous to apply an iterative approach [26]. As a result of the regularization process only a limited number of the singular values and singular vectors effectively contribute to the approximated solution. Moreover, as concluded in many studies [190, 212, 189], certain iterative methods possess the interesting property that the low-frequency components of the solution tend to converge faster than the high-frequency components. Hence, these iterative schemes have some sort of inherent regularization effect in which the number of iterations plays the role of the regularization parameter. A comprehensive explanation of this behaviour is given by Hansen [190].

Within the scope of the present study, an iterative conjugate gradient approach, namely conjugate gradient for the normal equations (CGNE) via Lanczos bidiagonalization reorthogonalization algorithm proposed by Delillo [209] is investigated. For the sake of completeness it is mentioned here that the minimization problem solved by the iterative approaches concerned with either the conjugate gradient (CG) algorithm applied to the normal equations $\mathbf{A}^{\mathrm{H}}\mathbf{A}\mathbf{x} = \mathbf{A}^{\mathrm{H}}\mathbf{y}$ and/or the other methods based on Lanczos bidiagonalization algorithm of Paige and Saunders [212] can be written as

$$\min_{\mathbf{x}} \|\mathbf{A}\mathbf{x} - \mathbf{y}\|_2 \quad \text{subject to} \quad \mathbf{L}\mathbf{x} \in \mathcal{K}\left(\mathbf{A}^{\mathrm{H}}\mathbf{A}, \mathbf{A}^{\mathrm{H}}\mathbf{y}\right), \tag{3.32}$$

where $\mathcal{K}\left(\mathbf{A}^{\mathrm{H}}\mathbf{A}, \mathbf{A}^{\mathrm{H}}\mathbf{y}\right)$ is the Krylov subspace (to be defined in Equation (3.35) associated with the normal equations).

Regarding the application of the iterative methods, it is interesting to realize that only a few iteration steps are required to obtain a physically meaningful regularized solution because the low frequency components of the solution vector converge faster then the high frequency ones. As a result, the iterative approaches are commonly faster than the regularization methods based on a direct solution procedure. Furthermore, the optimum number of iterations can be found with the same technique as employed to find optimum regularization parameters for the direct solution procedure [26].

The main idea of the modified Delillo algorithm presented below is derived from Delillo [209] algorithm based on Conjugate gradient for the normal equations via Lanczos bidiagonalization reothorgonalization (CGNE-LBR).

The conjugate gradient algorithm applied to the normal equations (CGNE)

$$\mathbf{A}^{\mathrm{H}}\mathbf{A}\mathbf{x} = \mathbf{A}^{\mathrm{H}}\mathbf{y}, \tag{3.33}$$

at the i^{th} iteration step minimizes the $\mathbf{A}^{\mathrm{H}}\mathbf{A}$–norm error

$$\|\mathbf{x} - \mathbf{x}_i\|_{\mathbf{A}^{\mathrm{H}}\mathbf{A}} = \|\mathbf{A}(\mathbf{x} - \mathbf{x}_i)\|_2^2 = \|\mathbf{y} - \mathbf{A}\mathbf{x}_i\|_2^2, \tag{3.34}$$

over the i^{th} Krylov subspace,

$$\mathcal{K}_i\left(\mathbf{A}^{\mathrm{H}}\mathbf{A}, \mathbf{A}^{\mathrm{H}}\mathbf{y}\right) = \operatorname{span}\left(\mathbf{A}^{\mathrm{H}}\mathbf{y}, \left(\mathbf{A}^{\mathrm{H}}\mathbf{A}\right)\mathbf{A}^{\mathrm{H}}\mathbf{y}, \ldots, \left(\mathbf{A}^{\mathrm{H}}\mathbf{A}\right)^{i-1}\mathbf{A}^{\mathrm{H}}\mathbf{y}\right), \tag{3.35}$$

where $i \in (1, 2, \ldots, r)$ and r is the *maximum iteration number*. It is well-known, that the CGNE algorithm can be implemented via the Lanczos bidiagonalization process, see [191] as shown in Appendix A.

The approach is to seek regularized solutions within the Krylov subspaces of $\mathbf{A}^{\mathrm{H}}\mathbf{A}$. It uses the SVD of the bidiagonal matrix $\mathbf{B}_i$ generated by the Lanczos process to construct a new basis for $\mathcal{K}_i\left(\mathbf{A}^{\mathrm{H}}\mathbf{A}, \mathbf{y}\right)$ which plays the role of the right singular vectors of $\mathbf{A}$. Next is to compute the expansion coefficients of $\mathbf{x}_i$ in this basis and apply the stopping method. Mostly i is chosen such as that it minimizes the magnitude of the i^{th} coefficient of $\mathbf{x}_i$. A formal description follows.

Considering the iPTF problem of Equation (3.4), the conjugate gradient algorithm to the normal equations $\mathbf{A}^{\mathrm{H}}\mathbf{A}\mathbf{x} = \mathbf{A}^{\mathrm{H}}\mathbf{y}$ is applied to it. As described in Delilo [209], the next step is to use the Lanczos bidiagonalization process to construct a lower bidiagonal matrix $\mathbf{B}_i$ and two rectangular matrices $\mathbf{U}_{i+1}$ and $\mathbf{V}_i$ with orthonormal columns such that

$$\mathbf{A}\mathbf{V}_i = \mathbf{U}_{i+1}\mathbf{B}_i, \tag{3.36}$$

and $\mathbf{y}/\|\mathbf{y}\|_2$ is the first column of $\mathbf{U}_{i+1}$. Let

$$\mathbf{B}_i = \hat{\mathbf{U}}_i \hat{\Sigma}_i \hat{\mathbf{V}}_i^{\mathrm{H}} \tag{3.37}$$

be the singular value decomposition of $\mathbf{B}_i$. The columns $\mathbf{u}_1^i, \mathbf{u}_2^i, \ldots, \mathbf{u}_i^i$ of $\mathbf{U}_i\hat{\mathbf{U}}_i$ form an orthonormal basis of the Krylov subspace $\mathcal{K}_i\left(\mathbf{A}^{\mathrm{H}}\mathbf{A}, \mathbf{y}\right)$ while the columns $\mathbf{v}_1^i, \mathbf{v}_2^i, \ldots, \mathbf{v}_i^i$ of $\mathbf{V}_i\hat{\mathbf{V}}_i$ an orthonormal basis of the Krylov subspace $\mathcal{K}_i\left(\mathbf{A}^{\mathrm{H}}\mathbf{A}, \mathbf{A}^{\mathrm{H}}\mathbf{y}\right)$. The parameter selection is finally described by computing the coefficients of the approximate solution $\mathbf{x}_i$ as represented in the basis $\mathbf{v}_1^i, \mathbf{v}_2^i, \ldots, \mathbf{v}_i^i$ of $\mathbf{V}_i\hat{\mathbf{V}}_i$. According to [209],

$$\mathbf{x}_i = \|\mathbf{y}\|_2 \mathbf{V}_i\hat{\mathbf{V}}_i\hat{\mathbf{\Sigma}}_i^{-1}\hat{\mathbf{U}}_i(1,:)^{\mathrm{H}} = \|\mathbf{y}\|_2 \sum_{j=1}^{i} \frac{\overline{\hat{\mathbf{U}}_i(1,j)}}{\hat{\mathbf{\Sigma}}_r(j,j)}\mathbf{v}_j^i \tag{3.38}$$

Up to a constant factor, the magnitude of the i^{th} coefficient is given by the formula

$$\psi_i = \frac{\left|\hat{\mathbf{U}}_i(1,i)\right|}{\hat{\mathbf{\Sigma}}_i(i,i)}. \tag{3.39}$$

the value of $i = i_{\text{opt}}$ where the sequence $\{\psi_i\}$ has a global minimum is then sought for and the vector $\mathbf{x}_{i_{\text{opt}}}$ is chosen as the approximation to $\mathbf{x}$. The algorithm 2 in Appendix A is used in generating the sequence for $\{\psi_i\}$ and $\{\mathbf{x}\}$.

In order to successfully apply the Dellilo algorithm to iPTF problem, the following should be taken into accounts:

- The conjugated gradient normal Equation (3.33) must be first be normalized with a weight of $\left\|\mathbf{A}^{\mathrm{H}}\mathbf{A}\right\|_2$ and $\left\|\mathbf{A}^{\mathrm{H}}\mathbf{y}\right\|_2$ and the obtained solution should be weighted (multiplied by a weighting factor) as seen in algorithm 2 of Appendix A. The purpose of the normalization is to avoid running into computational numeric difficulties such as precision and round-off errors associated with floating point representation.
- The choice of the optimum $\mathbf{x}_{i_{\text{opt}}}$ from the sequence $\mathbf{X}$ in Algorithm 2 can be obtained using either `Itr_ZERO` of Equation (A.3) or `Itr_MINP` of Equation (A.2).

3.3.3 Statistical Approaches (`Bay techniques`)

Although some of the original reports on inverse acoustics for source identification were based on the statistical model in Equation (3.21), the main challenge of this approach remains specifying the model (that is determining appropriate parameters of the mean and covariance of the desired solution and the noise). The simplest technique, which was adopted by these early investigators, is to assume that not only is the noise white and uncorrelated, as in Equation (3.21), but that the solution has the same structure, with zero mean and variance σ_x^2. In this case the relevant equation becomes

$$\mathbf{x}_{\text{MAP}} = \left(\mathbf{A}^{\mathrm{H}}\mathbf{A} + \frac{\sigma_{e_y}^2}{\sigma_x^2}\mathbf{I}\right)^{-1}\mathbf{A}^{\mathrm{H}}\mathbf{y}. \tag{3.40}$$

This is the same as Tikhonov regularization with an identity matrix as the regularizer (that is, zero-order Tikhonov) and with a statistical model for picking the regularization parameter. The challenge for this statistical approach is to find a good model for the variance of the unknown solution.

3.3.3.1 Bayesian framework for the m-iPTF method

This section offers a brief overview of how Bayesian concepts have been used in the m-iPTF context to produce regularization formulations that solely deal with m-iPTF-related inverse

problems. The technique is dubbed "Bayesian m-IPTF" in this thesis. It is to be reminded that the originality of this concept is by Forget [27].

The Bayesian m-IPTF method is developed by Forget [27] basically made use of the Bayesian formulation of Tikhonov regularization to solve m-iPTF problem.

Bayes' theorem states that if $p(\mathbf{y} \mid \mathbf{x})$ is the probability density function for the random variable $\mathbf{y}$ given $\mathbf{x}$, which is determined by the model Equation (3.2), and $p(\mathbf{x})$ is the assumed probability density function for the unknown $\mathbf{x}$, known as the prior probability density function, then for a particular realization of the data $\mathbf{y}$, the posterior probability density function $p(\mathbf{x} \mid \mathbf{y})$ can be written as

$$p(\mathbf{x} \mid \mathbf{y}) \propto p(\mathbf{y} \mid \mathbf{x}) p(\mathbf{x}) \tag{3.41}$$

According to Forget [27], the noise structure for the m-iPTF problem is $\mathbf{C}_{\mathbf{e}_y} = \mathbf{I} + \mathbf{Y}\mathbf{Y}^{\mathrm{H}}$ (the $\mathbf{Y}$ is the same as the $\mathbf{Y}_{mk}$ as seen in Equation (2.29)). The likelihood function $p(\mathbf{y} \mid \mathbf{x})$ is a probability which depends on the errors linked to the measurement noise and is given by

$$p(\mathbf{y} \mid \mathbf{x}) \propto \mathcal{N}_c\left(\mathbf{A}\mathbf{x}, \gamma_{\mathbf{e}_y}^2 \mathbf{C}_{\mathbf{e}_y}\right) = \frac{1}{\pi^m \gamma_{\mathbf{e}_y}^{2m} \det\left[\mathbf{C}_{\mathbf{e}_y}\right]} \exp\left(-\frac{\|\mathbf{y} - \mathbf{A}\mathbf{x}\|_{\mathbf{C}_{\mathbf{e}_y}}^2}{\gamma_{\mathbf{e}_y}^2}\right) \tag{3.42}$$

where the notation $\mathcal{N}_c$ stands for "complex Normal" with $\gamma_{\mathbf{e}_y}^2$ as the average noise power, $\det[\mathbf{B}]$ is the determinant of the matrix $\mathbf{B}$ and $\mathbf{C}_{\mathbf{e}_y}$ is the noise structure matrix (covariance matrix whose coefficients are correlation coefficients which define the nature of the noise). In addition, by notational convention $\|\mathbf{q}\|_{\mathbf{C}_\mathbf{q}}^2 = \mathbf{q}^{\mathrm{H}} \mathbf{C}_\mathbf{q}^{-1} \mathbf{q}$ represents the squared norm of vector $\mathbf{q}$ with metric $\mathbf{C}_{\mathbf{e}_y}$.

Also, Forget [27], assumed the sources to radiate like white noises of an acoustic power $\gamma_\mathbf{x}^2$ distributed according to a Gaussian complex law

$$p(\mathbf{x}) \propto \mathcal{N}_c\left(\mathbf{0}, \gamma_\mathbf{x}^2 \mathbf{C}_\mathbf{x}\right) = \frac{1}{\pi^n \gamma_\mathbf{x}^{2n} \det\left[\mathbf{C}_\mathbf{x}\right]} \exp\left(-\frac{\|\mathbf{x}\|_{\mathbf{C}_\mathbf{x}}^2}{\gamma_\mathbf{x}^2}\right), \tag{3.43}$$

with $\mathbf{C}_\mathbf{x} = \mathbf{I}$.

At this point, the conventional technique from previously discussed inverse issues is to compute the maximizer of $p(\mathbf{x} \mid \mathbf{y})$, which is aptly dubbed the maximum a posteriori (MAP) estimator. Alternatively, one may minimize "$-\ln p(\mathbf{x} \mid \mathbf{y})$", resulting in

$$\begin{aligned}
\mathbf{x}_{\mathrm{MAP}} &= \mathrm{Argmax}\left\{p(\mathbf{x} \mid \mathbf{y})\right\} \\
&= \mathrm{Argmax}\left\{\mathcal{N}_c\left(\mathbf{A}\mathbf{x}, \gamma_{\mathbf{e}_y}^2 \mathbf{C}_{\mathbf{e}_y}\right) \mathcal{N}_c\left(\mathbf{0}, \gamma_\mathbf{x}^2 \mathbf{C}_\mathbf{x}\right)\right\} \\
&= \mathrm{Argmin}\left\{-\ln\left(\mathcal{N}_c\left(\mathbf{A}\mathbf{x}, \gamma_{\mathbf{e}_y}^2 \mathbf{C}_{\mathbf{e}_y}\right) \mathcal{N}_c\left(\mathbf{0}, \gamma_\mathbf{x}^2 \mathbf{C}_\mathbf{x}\right)\right)\right\} \\
&= \mathrm{Argmin}\left\{m \ln\left(\gamma_{\mathbf{e}_y}^2\right) + n \ln\left(\gamma_\mathbf{x}^2\right) + \gamma_{\mathbf{e}_y}^{-2} \|\mathbf{y} - \mathbf{A}\mathbf{x}\|_{\mathbf{C}_{\mathbf{e}_y}}^2 + \gamma_\mathbf{x}^{-2} \|\mathbf{x}\|_{\mathbf{C}_\mathbf{x}}^2\right\} \\
&= \mathrm{Argmin}\left\{\|\mathbf{y} - \mathbf{A}\mathbf{x}\|_{\mathbf{C}_{\mathbf{e}_y}}^2 + \lambda^2 \|\mathbf{x}\|_2^2\right\} \quad \text{(ignore terms independent of } \mathbf{x}\text{)},
\end{aligned} \tag{3.44}$$

with $\lambda^2 = \gamma_{\mathbf{e}_y}^2 / \gamma_\mathbf{x}^2$.

By considering the m field point pressure measurements, the regularization parameter is therefore finally obtained by minimizing the following function `MAP` [213, 214]:

$$\mathtt{MAP}\left(\lambda^2\right) = m \ln\left(\mathbf{y}^{\mathrm{H}} \left(\mathbf{A}\mathbf{A}^{\mathrm{H}} + \lambda^2 \mathbf{C}_{\mathbf{e}_y}\right)^{-1} \mathbf{y}\right) + \ln\left(\left|\mathbf{A}\mathbf{A}^{\mathrm{H}} + \lambda^2 \mathbf{C}_{\mathbf{e}_y}\right|\right) \tag{3.45}$$

The reader should referred to Forget's PhD thesis [27] for further details on Bayesian m-iPTF method.

3.3.3.2 Proposed Algorithm to solve an inverse problem in iPTF context (DBKH-iPTF algorithm)

At this point, a novel approach based on stochastic inverse problem formulation technique is proposed to solve the iPTF problem of Equation (3.4). This approach is referred to as the DBKH-iPTF algorithm. The letters in 'DBKH' were drawn from the author's surname DaBanKaH.

The differences between the DBKH-iPTF algorithm and the Bayesian framework mentioned in section 3.3.3.1 are detailed in the following paragraphs.

With DBKH-iPTF algorithm, $\mathbf{C}_{\mathbf{e}_y}^{-1}$ is defined as $\mathbf{C}_{\mathbf{e}_y}^{-1} = \gamma_{\mathbf{e}_y}^2 \mathbf{I}$ and $\mathbf{C}_{\mathbf{x}}^{-1}$ as $\mathbf{C}_{\mathbf{x}}^{-1} = \gamma_{\mathbf{x}}^2 \mathbf{L}^{\mathrm{H}}\mathbf{L}$. $\gamma_{\mathbf{x}}^2$ and $\gamma_{\mathbf{e}_y}^2$ are a positive scale factors for tuning the degree of smoothness in $\mathbf{x}$ and determining the precision level in $\mathbf{y}$ respectively. $\mathbf{L} \in \mathbb{C}^{n \times n}$ can be seen as a regularization operator which act as the smoothing filter to lessen the effect of noise in the generated solution. $\mathbf{L}$ is obtained by implementation of algorithm 3 in Appendix B on $\mathbf{A}$, $\mathcal{TRM}(\mathbf{A})$.

The parameters $\gamma_{\mathbf{e}_y}^2$ and $\gamma_{\mathbf{x}}^2$ are usually tuned empirically. The next paragraph presents a way to determine them automatically.

The Bayesian inference approach

The data model of Equation (3.4) defines the likelihood function as

$$p\left(\mathbf{y} \mid \mathbf{x}, \gamma_{\mathbf{e}_y}^2\right) \propto \gamma_{\mathbf{e}_y}^{2n} \exp\left[-\gamma_{\mathbf{e}_y}^2 \left\|\mathbf{y} - \mathbf{A}\mathbf{x}\right\|_2^2\right]. \tag{3.46}$$

The uncertainty nature of the unknown $\mathbf{x}$ coupled with the prior information about some of its properties are formulated in the prior probability density function as:

$$p\left(\mathbf{x} \mid \gamma_{\mathbf{x}}^2\right) \propto \gamma_{\mathbf{x}}^{2n} \exp\left[-\gamma_{\mathbf{x}}^2 \left\|\mathbf{L}\mathbf{x}\right\|_2^2\right]. \tag{3.47}$$

The choice of a Gaussian prior $p\left(\mathbf{x} \mid \gamma_{\mathbf{x}}^2\right)$ results in a probability density $p\left(\mathbf{y} \mid \mathbf{x}, \gamma_{\mathbf{e}_y}^2\right) p\left(\mathbf{x} \mid \gamma_{\mathbf{x}}^2\right)$ that is Gaussian in $\mathbf{x}$, and hence $p\left(\mathbf{x} \mid \gamma_{\mathbf{x}}^2\right)$ is a conjugate prior [215, 216].

Furthermore, $p(\gamma_{\mathbf{e}_y}^2)$ and $p(\gamma_{\mathbf{x}}^2)$ are assumed to be Gamma distributions, thus $p\left(\mathbf{y} \mid \mathbf{x}, \gamma_{\mathbf{e}_y}^2\right) p(\gamma_{\mathbf{e}_y}^2)$ and $p\left(\mathbf{x} \mid \gamma_{\mathbf{x}}^2\right) p(\gamma_{\mathbf{x}}^2)$ are also Gamma distributions in $\gamma_{\mathbf{e}_y}^2$ and $\gamma_{\mathbf{x}}^2$, respectively. As a results $p(\gamma_{\mathbf{e}_y}^2)$ and $p(\gamma_{\mathbf{x}}^2)$ are define as

$$p(\gamma_{\mathbf{e}_y}^2) \propto {\gamma_{\mathbf{e}_y}^2}^{(\alpha_{\mathbf{e}_y}-1)} \exp\left(-\beta_{\mathbf{e}_y} \gamma_{\mathbf{e}_y}^2\right), \tag{3.48}$$

$$p(\gamma_{\mathbf{x}}^2) \propto \gamma_{\mathbf{x}}^{2(\alpha_{\mathbf{x}}-1)} \exp\left(-\beta_{\mathbf{x}} \gamma_{\mathbf{x}}^2\right), \tag{3.49}$$

where $\alpha_{\mathbf{e}_y} > 0$, $\alpha_{\mathbf{x}} > 0$, $\beta_{\mathbf{x}} > 0$ and $\beta_{\mathbf{e}_y} > 0$ and their values are assigned according to Higdon [217]. The hyper-priors might be considered "uninformative." These uninformative hyper-priors are chosen to have a minimal impact on the sampled values. Note that the many situations for which these parameter selections have been used required no adjusting at all [218]. Furthermore, no further parameters need to be set. However, if one has a decent a priori idea of what $\gamma_{\mathbf{e}_y}^2$ and/or $\gamma_{\mathbf{x}}^2$ should be, the hyper-prior parameter selections might be adjusted appropriately.

Combining Equation (3.46) - (3.49) in hand, the posterior probability density can be defined as

$$\begin{aligned} p(\mathbf{x}, \lambda, \delta \mid \mathbf{y}) &\propto p\left(\mathbf{y} \mid \mathbf{x}, \gamma_{\mathbf{e}_y}^2\right) p(\gamma_{\mathbf{e}_y}^2) p\left(\mathbf{x} \mid \gamma_{\mathbf{x}}^2\right) p(\gamma_{\mathbf{x}}^2) \\ &= {\gamma_{\mathbf{e}_y}^2}^{(n/2+\alpha_{\mathbf{e}_y}-1)} {\gamma_{\mathbf{x}}^2}^{(n/2+\alpha_{\mathbf{x}}-1)} \\ &\exp\left(-\gamma_{\mathbf{e}_y}^2 \left\|\mathbf{A}\mathbf{x} - \mathbf{y}\right\|^2 - \gamma_{\mathbf{x}}^2 \left\|\mathbf{L}\mathbf{x}\right\|_2^2 - \beta_{\mathbf{e}_y} \gamma_{\mathbf{e}_y}^2 - \beta_{\mathbf{x}} \gamma_{\mathbf{x}}^2\right) \end{aligned} \tag{3.50}$$

Samples from Equation 3.49 are computed taking into acccount the conjugacy relationships

mentioned above.

The use of a Gaussian prior for $\mathbf{x}$ and Gamma hyper-priors for $\gamma^2_{\mathbf{e}_y}$ and $\gamma^2_{\mathbf{x}}$ were formulated on the basis of conjugacy relationships [215, 216], so that the full conditional densities have the same form as the corresponding prior/hyper-prior. The full conditional densities are expressed as follows: have the form

$$p(\mathbf{x} \mid \gamma^2_{\mathbf{e}_y}, \gamma^2_{\mathbf{x}}, \mathbf{y}) \propto \exp\left(-\gamma^2_{\mathbf{e}_y} \|\mathbf{A}\mathbf{x}-\mathbf{y}\|_2^2 - \gamma^2_{\mathbf{x}} \|\mathbf{L}\mathbf{x}\|_2^2\right) \tag{3.51}$$

$$p(\gamma^2_{\mathbf{e}_y} \mid \mathbf{x}, \gamma^2_{\mathbf{x}}, \mathbf{y}) \propto \gamma^{2(n/2+\alpha_{\mathbf{e}_y}-1)}_{\mathbf{e}_y} \exp\left(\left[-\frac{1}{2}\|\mathbf{A}\mathbf{x}-\mathbf{y}\|_2^2 - \beta_{\mathbf{e}_y}\right]\gamma^2_{\mathbf{e}_y}\right), \tag{3.52}$$

$$p(\gamma^2_{\mathbf{x}} \mid \mathbf{x}, \gamma^2_{\mathbf{e}_y}, \mathbf{y}) \propto \gamma^{2(n/2+\alpha_{\mathbf{x}}-1)}_{\mathbf{x}} \exp\left(\left[-\frac{1}{2}\|\mathbf{L}\mathbf{x}\|_2^2 - \beta_{\mathbf{x}}\right]\gamma^2_{\mathbf{x}}\right), \tag{3.53}$$

and hence,

$$\gamma^2_{\mathbf{e}_y} \mid \mathbf{x}, \gamma^2_{\mathbf{x}}, \mathbf{y} \sim \Gamma\left(m/2+\alpha_{\mathbf{e}_y}, \frac{1}{2}\|\mathbf{A}\mathbf{x}-\mathbf{y}\|_2^2 + \beta_{\mathbf{e}_y}\right), \tag{3.54}$$

$$\gamma^2_{\mathbf{x}} \mid \mathbf{x}, \gamma^2_{\mathbf{e}_y}, \mathbf{y} \sim \Gamma\left(n/2+\alpha_{\mathbf{x}}, \frac{1}{2}\|\mathbf{L}\mathbf{x}\|_2^2 + \beta_{\mathbf{x}}\right) \tag{3.55}$$

where " Γ " denotes Gamma distribution

$$\mathbf{x} \mid \gamma^2_{\mathbf{e}_y}, \gamma^2_{\mathbf{x}}, \mathbf{y} \sim \mathscr{N}_c\left(\widehat{\mathbf{x}}, \widehat{\mathbf{C}}_{\mathbf{x}}\right), \tag{3.56}$$

Thus the conditional posterior law of x is Gaussian with mean as

$$\widehat{\mathbf{x}} = \widehat{\mathbf{C}}_{\mathbf{x}} \mathbf{A}^{\mathrm{H}} \mathbf{C}_{\mathbf{e}_y} \mathbf{y}, \tag{3.57}$$

and covariance as

$$\widehat{\mathbf{C}}_{\mathbf{x}} = (\mathbf{A}^{\mathrm{H}} \mathbf{C}^{-1}_{\mathbf{e}_y} \mathbf{A} + \gamma^2_{\mathbf{x}} \mathbf{L}^{\mathrm{H}} \mathbf{L})^{-1}. \tag{3.58}$$

By substitution

$$\begin{aligned} \widehat{\mathbf{x}} &= \gamma^2_{\mathbf{e}_y}\left(\gamma_{\mathbf{e}_y}\mathbf{A}^{\mathrm{H}}\mathbf{A} + \gamma^2_{\mathbf{x}}\mathbf{L}^{\mathrm{H}}\mathbf{L}\right)^{-1}\mathbf{A}^{\mathrm{H}}\mathbf{y} \\ &= \left(\mathbf{A}^{\mathrm{H}}\mathbf{A} + \lambda^2\mathbf{L}^{\mathrm{H}}\mathbf{L}\right)^{-1}\mathbf{A}^{\mathrm{H}}\mathbf{y}, \end{aligned} \tag{3.59}$$

where $\lambda^2 = \gamma^2_x/\gamma^2_{e_y}$.

At this point, it can be seen that the posterior mean estimator of Equation (3.59) is equivalent to the standard Tikhonov Regularization as seen in Equation (3.19), with the regularization parameter λ stochastically generated through hyperparameter simulation (iteratively sampling of $\gamma^2_{\mathbf{e}_y}$ and $\gamma^2_{\mathbf{x}}$ from their respective Gamma distribution).

Since $\widehat{\mathbf{x}}$ of Equation (3.59) is solution that occurs at particular λ^2, the challenge for selection of the optimum λ^2_{opt} is often encountered in this case. The `MINP` of Equation (3.81) is used for selecting the λ^2_{opt} as seen in Equation (3.62). An alternative approach is to use the `Bay_MAD` algorithm 4 in Appendix B to estimate the mean as seen in Equation (3.64).

Finally, a summarized version of the all above discussion is presented in the DBKH-iPTF algorithm 1.

Algorithm 1 DBKH-iPTF algorithm for iPTF

Inputs:
$\mathbf{A} \in \mathbb{C}^{m\times n}$ and $\mathbf{y} \in \mathbb{C}^{m\times 1}$ of Equation (3.4)
$\mathbf{L} = \mathcal{TRM}(\mathbf{A})$, $\mathbf{L} \in \mathbb{C}^{n\times n}$
Output: $\widehat{\mathbf{x}} \in \mathbb{C}^{n\times 1}$
Initialize:
$\alpha_{\mathbf{e}_y} = \alpha_{\mathbf{x}} \leftarrow 1$
$\beta_{\mathbf{e}_y} = \beta_{\mathbf{x}} \leftarrow 10^{-4}$
$\gamma_x^{2(0)} \leftarrow 1$
$\gamma_{e_y}^{2(0)} \leftarrow 1$
$\Lambda(:) \leftarrow \mathbf{0}, \quad \Lambda \in \mathbb{R}^r$
$\mathrm{J}(:) \leftarrow \mathbf{0}, \quad \mathrm{J} \in \mathbb{R}^r$
$\mathbf{X}(:,:) \leftarrow \mathbf{0}, \quad \mathbf{X} \in \mathbb{C}^{n\times r}$
for $i = 1, 2, \ldots, r$ **do**
$\mathbf{b} \leftarrow \gamma_{e_y}^{2(i-1)} \mathbf{A}^{\mathrm{H}}\mathbf{y}$
$\mathbf{Q} \leftarrow \gamma_{e_y}^{2(i-1)} \mathbf{A}^{\mathrm{H}}\mathbf{A} + \gamma_x^{2(i-1)} \mathbf{L}^{\mathrm{H}}\mathbf{L}$
$\mathbf{x}_i \leftarrow \mathbf{Q}^{-1}\mathbf{b}$ (Optimization)
$\mathbf{X}(:,i) \leftarrow \mathbf{x}_i$
$\gamma_{e_y}^{2(i)} \leftarrow \Gamma\left(m/2 + \alpha_{\mathbf{e}_y}, \frac{1}{2}\|\mathbf{A}\mathbf{x} - \mathbf{y}\|_2^2 + \beta_{\mathbf{e}_y}\right)$ (Hyperparameter simulation)
$\gamma_x^{2(i)} \leftarrow \Gamma\left(n/2 + \alpha_{\mathbf{x}}, \frac{1}{2}\|\mathbf{L}\mathbf{x}\|_2^2 + \beta_{\mathbf{x}}\right)$
$\lambda_i^2 \leftarrow \gamma_x^{2(i)} / \gamma_{e_y}^{2(i)}$
$\Lambda(i) \leftarrow \lambda_i^2$

$$\mathrm{J}(i) \leftarrow (\|\mathbf{A}\mathbf{x}_i - \mathbf{y}\|_2) \cdot (\|\mathbf{L}\mathbf{x}_i\|_2) \quad \text{(Bay\_MINP Objective function value)} \tag{3.60}$$

end for
Estimation of $\mathbf{x}$: $\widehat{\mathbf{x}}$
Bay_MINP Estimation: Find $\widehat{\mathbf{x}}$ as the $\mathbf{x}_i$ in $\mathbf{X}$ that yields the minimum value in J :

$$\widehat{\mathbf{x}} = \operatorname{argmin} \quad \mathrm{J} \tag{3.61}$$

Alternatively, use the robust mean estimator from the algorithm 4 as follows:

$$\mu_\lambda = \text{Bay\_MAD}(\Lambda) \tag{3.62}$$

$$\begin{aligned} \overline{\mathbf{X}} &= [\mathbf{x}_i : \lambda_i \leqslant \mu_\lambda \quad \text{for} \quad i = 1, \ldots, r] \\ &= [\mathbf{x}_1, \mathbf{x}_2 \ldots, \mathbf{x}_w], \quad k = 1, \ldots, w < r \end{aligned} \tag{3.63}$$

$$\begin{aligned} \widehat{\mathbf{x}} &= \left[x_j = \text{Bay\_MAD}(\overline{\mathbf{X}}(j,:)) \quad \text{for} \quad j = 1, \ldots, n\right] \\ &= [x_1, x_2 \ldots, x_n]^{\mathrm{T}} \end{aligned} \tag{3.64}$$

3.3.4 Regularization with 'expected solution' (`Twomey` technique)

Sometimes numerical simulation can provides an expected solution $\overline{\mathbf{x}}$ which can be used in the regularization process. In such situation, Equation (3.65) and (3.66) which represent a variant form of Tikhonov regularization often referred to as *Phillips-Twomey regularization method* [219, 220] can be used.

$$\min\left\{\|\mathbf{A}\mathbf{x}-\mathbf{y}\|_2^2+\lambda^2\|\mathbf{x}-\overline{\mathbf{x}}\|_2^2\right\},\quad \lambda>0, \tag{3.65}$$

and solution of Equation (3.65) reads

$$\widehat{\mathbf{x}}=\left(\mathbf{A}^{\mathrm{H}}\mathbf{A}+\lambda^2\mathbf{I}\right)^{-1}\left(\mathbf{A}^{\mathrm{H}}\mathbf{y}+\lambda^2\overline{\mathbf{x}}\right). \tag{3.66}$$

This regularization differs from the usual Tiknonov regularization in the sense that instead of imposing constraints on the magnitude of the solution or on its derivatives, this method minimizes the difference between the regularized solution $\widehat{\mathbf{x}}$ and an expected solution $\overline{\mathbf{x}}$ as the residual error in the least square sense.

It should be noted that the accuracy of the estimated solution is highly dependent on the authenticity of the prior information used. As a results the solution tends to be bias towards the available input prior information. Thus these techniques should be used only when one is sure of the prior information at hand. As stated by [219], the best choice of the regularization parameter with these regularization techniques is still an open question.

3.4 Selecting a regularization parameter

One of the main difficulties in properly solving a discrete ill-posed problem is how to determine a suitable regularization parameter. The choice of this parameter is a delicate subject: a small value of λ, equivalent to a large value of i at a stopped criteria in iterative case, gives a good approximation to the system of equations (low residual) but the influence of the data errors causes instabilities. Conversely, a large value of λ, or a low value of i, suppresses the data errors but increases the approximation error. This means that a trade-off between the two components in the error vector of solution $\mathbf{x}_\lambda$ has to be made

$$\begin{aligned}\mathbf{e}_{\mathbf{x}} &= \mathbf{x}_\lambda-\overline{\mathbf{x}}\\ &=\sum_i f_i\frac{\mathbf{u}_i^{\mathrm{H}}\cdot(\overline{\mathbf{y}}+\mathbf{e}_{\mathbf{y}})}{\sigma_i}\mathbf{v}_i-\sum_i\frac{\mathbf{u}_i^{\mathrm{H}}\overline{\mathbf{y}}}{\sigma_i}\mathbf{v}_i\\ &=\sum_i(f_i-1)\frac{\mathbf{u}_i^{\mathrm{H}}\overline{\mathbf{y}}}{\sigma_i}\mathbf{v}_i+\sum_i f_i\frac{\mathbf{u}_i^{\mathrm{H}}\mathbf{e}_{\mathbf{y}}}{\sigma_i}\mathbf{v}_i.\end{aligned} \tag{3.67}$$

Where $\overline{\mathbf{x}}$ is the true solution and $\overline{\mathbf{y}}$ is the unperturbed part of $\mathbf{y}$. The error component represented by the first summation in Equation (3.67) is solely caused by the regularization method and is called the regularization error. The second summation which finds its origin in the perturbation $\mathbf{e}_{\mathbf{y}}$ of the right-hand side vector $\mathbf{y}$, is denoted as the perturbation error. When no regularization is introduced, all filter factors equal unity and the error vector $\mathbf{e}_{\mathbf{x}}$ is fully dominated by the perturbation error. In this case, the solution $\mathbf{x}_\lambda$ is said to be under-regularized or under-smoothed as it appears to be completely random due to the many sign changes of the oscillatory singular vectors belonging to small singular values. On the other hand, a high degree of regularization implies that most filter factors are small $f_i\leqslant 1$ and the error in $\mathbf{x}_\lambda$ is dominated by the regularization process. Because regularization acts as a low-pass filter in the singular value spectrum, the oscillatory components are damped and hence an over-smoothed solution remains. Obviously a regularization parameter must be found that yields a fair balance between the regularization and the perturbation errors in the reconstructed solution.

3.4.1 Methods for selecting the regularization parameter

Over the years different techniques for choosing regularization parameters have been proposed in the literature. These methods can roughly be divided into two classes, based on the assumption made about the perturbation of the right-hand side vector $\|\mathbf{e_y}\|_2$ and/or $\overline{\mathbf{x}}$:

- The *a priori* methods which rely on knowledge of noise statistics (such as $\|\mathbf{e_y}\|_2$) as described in Section 3.3.3.1 or other prior knowledge (e.g. expected solution $\overline{\mathbf{x}}$) as presented in section 3.4.1.3.
- The *posteriori* methods do not require any either $\|\mathbf{e_y}\|_2$, or $\overline{\mathbf{x}}$ but instead try to extract the necessary information from the given right-hand side vector $\mathbf{y}$. Thus these methods try many regularization parameters, test the results of each trial, and then select one of the parameters based on some criteria as discussed in section 3.4.1.2.

Each of these regularization parameter estimation methods attempts to provide a balance between the solution and regularization norm. An important tool that is often used as a guide in the selection process of optimum regularization parameter is the *L-curve plot* [221].

3.4.1.1 The L-curve plot

The idea behind the L-curve is to plot the norm of the regularized solution:

$$\eta = \|\mathbf{x}_\lambda\|_2 , \tag{3.68}$$

versus the corresponding residual norm:

$$\rho = \|\mathbf{A}\mathbf{x}_\lambda - \mathbf{y}\|_2 , \tag{3.69}$$

for all valid regularization parameters. Such a plot, usually on a double logarithmic scaling, clearly visualizes the compromise between minimization of these two quantities, which according to Equation (3.67) is the essence of regularization. Under the assumption that the unperturbed right-hand side $\overline{\mathbf{y}}$ satisfies the discrete Picard condition of section 3.2.2.2, the noise $\mathbf{e_y}$ has a zero mean value and $\|\mathbf{e_y}\|_2 \ll \|\mathbf{y}\|_2$ the generic shape of the L-curve is similar to the curve depicted in the Figure 3.6(a).

For discrete ill-posed problems it turns out that the L-curve, hence its name, has a characteristic L-shaped appearance with a distinct corner separating the vertical and horizontal parts of the curve. Each of the regions can be connected with one of the two error components expressed in Equation (3.67).
The horizontal part of the L-curve corresponds to solutions where the regularization error dominates, that is at this level of filtering a very smooth solution is produced. In this region the solution is said to be over-regularized because not only noise but also useful information contained in the right-hand side vector $\mathbf{y}$ is suppressed.

In the vertical part of the curve insufficient filtering (under-regularization) is applied and $\mathbf{x}_\lambda$ is dominated by the effects of noise. Hence, in this region the solutions are characterized by many oscillations resulting from higher order singular vectors.
The optimum level of regularization is found in the corner region of the L-curve since it provides a value for the regularization parameter that minimizes both η and ρ. It is in this region that the best balance is found between fitting the solution to data (minimization of the residue) and the suppression of ill-conditioned behavior (minimization of the solution norm).

It is shown in references [26, 221, 222] that the location of the corner coincides with the crossing of two separate extreme L-curves as illustrated in Figure 3.6(b). The horizontal L-curve part is found for an exact, unperturbed right-hand side that satisfies the discrete Picard condition, whereas the vertical part of the curve is retrieved for a right-hand side consisting of spatially

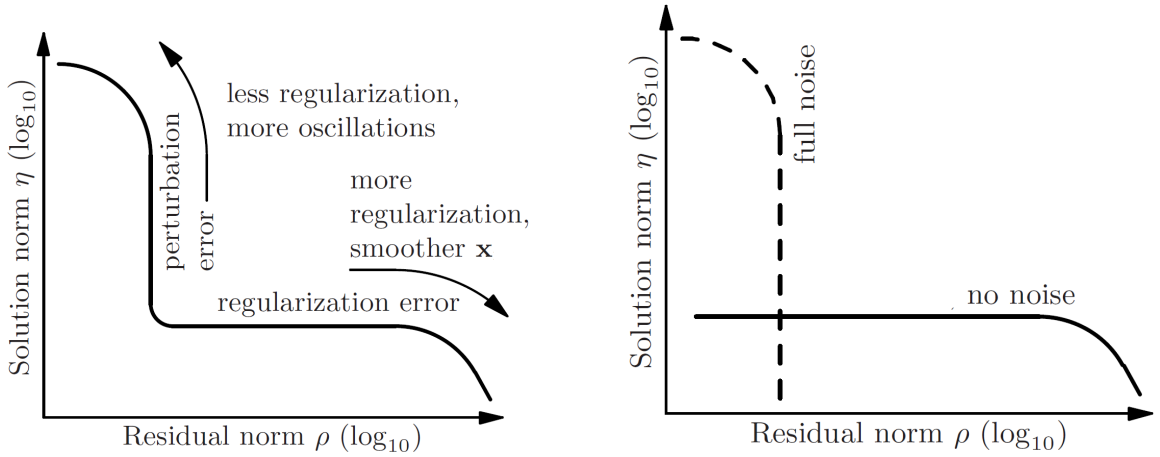

(a) Generic shape of L-curve for partially noisy $\mathbf{y} = \overline{\mathbf{y}} + \mathbf{e}_\mathbf{y}$.

(b) Limit situations for totally noisy $\mathbf{y} = \mathbf{e}_\mathbf{y}$ and a pure signal $\mathbf{y} = \overline{\mathbf{y}}$ (no noise)

Figure 3.6: Illustration of the generic L-curve form [26, 221, 222], assuming that the exact data vector $\overline{\mathbf{y}}$ satisfies the discrete Picard condition of Section 3.2.2.2.

white noise with a zero mean value.

Note that the L-curve is a continuous curve when the regularization parameter is continuous as in general Tikhonov. For regularization methods with a discrete parameter, such as in TSVD, iterative and statistical approaches, the L-curve reduces to a collection of discrete points.

3.4.1.2 Posterior methods of Choosing the regularization parameter

From practical standpoint, the behavior of the errors in the right-hand side is rarely known. In other words, mostly, no prior knowledge about the solution sought or the level of contamination $\mathbf{y}$ is available. Thus in general neither the norm nor the distribution of $\mathbf{e}_\mathbf{y}$ can be used as input for a parameter-choice technique. Therefore this section presents some posterior methods that are used to select the optimum regularization parameter without any prior knowledge such as the noise or solution.

***Generalised Cross-Validation method* (`GCV` function)**

The Generalised Cross-Validation (`GCV`) [223] method provides an estimate of the optimal regularisation parameter by seeking to minimise the function

$$\texttt{GCV}(\lambda) = \frac{\rho^2(\lambda)}{\left[\mathrm{Tr}\left(\mathbf{I} - \mathbf{A}\mathbf{A}^{\#}\right)\right]^2}, \tag{3.70}$$

where $\mathbf{A}^{\#} = \left(\mathbf{A}^{\mathrm{H}}\mathbf{A} + \lambda^2\mathbf{I}\right)^{-1}\mathbf{A}^{\mathrm{H}}$ is the regularized inverse of $\mathbf{A}$ and $\mathrm{Tr}(\mathbf{B})$ is the trace of some matrix $\mathbf{B}$. The function $\texttt{GCV}(\lambda)$ can be expressed as a linear combination of the prediction errors $\mathbf{y}_j - \mathbf{A}_j\mathbf{x}_\lambda^{(j)}$, where $\mathbf{x}_\lambda^{(j)}$ is the regularised solution found by leaving out the jth data point, $j = 1, \ldots, \min(m,n)$ and $\mathbf{A}_j$ is the jth row of $\mathbf{A}$. In terms of the SVD, it can be shown that

$$\texttt{GCV}(\lambda) = \frac{\left(\sum_{i=1}^{\min(m,n)} \frac{\lambda^4\alpha_i^2}{\left(\lambda^2+\sigma_i^2\right)^2}\right) + \|\mathbf{r}_\perp\|_2^2}{\left(m - \sum_{i=1}^{\min(m,n)} \frac{\sigma_i^2}{\lambda^2+\sigma_i^2}\right)^2} \tag{3.71}$$

The Robust Generalised Cross-Validation method (RGCV function)

The main drawback associated with the GCV method is that the curve $\texttt{GCV}(\lambda)$ is often very flat, with no discernible minimum [223], which is often the case for the inverse problem of acoustics. To overcome this drawback, the Robust Generalised Cross-Validation (RGCV) method was introduced [224]. The estimate of the optimal regularisation parameter λ is the one that minimises the RGCV function

$$\texttt{RGCV}(\lambda) = \{\gamma + (1-\gamma)\mu(\lambda)\}\texttt{GCV}(\lambda), \tag{3.72}$$

where $\mu(\lambda)$ is defined as

$$\mu(\lambda) = \left[\mathbf{Tr}\left(\mathbf{A}\mathbf{A}^{\#}\right)\right]^2 = \sum_{i=1}^{\min(m,n)} \frac{\sigma_i^4}{\left(\lambda^2+\sigma_i^2\right)^2}, \tag{3.73}$$

using the SVD. The function $\mu(\lambda)$ is derived from the average influence $\frac{1}{\min(m,n)} \sum_{j=1}^{\min(m,n)} \left\|\mathbf{A}\mathbf{x}_\lambda - \mathbf{A}\mathbf{x}_\lambda^{(j)}\right\|_2^2$, where $\left\|\mathbf{A}\mathbf{x}_\lambda - \mathbf{A}\mathbf{x}_\lambda^{(j)}\right\|_2^2$ is a measure of the influence of the jth data point on the regularized solution. This function has the properties that $\mu(0) = \min(m,n)$ and $\mu(\lambda) \to 0$ as $\lambda \to \infty$. A consequence of this is that $\mu(\lambda)$ penalises smaller values of λ in the minimisation problem.

Equation (3.73) also contains the so-called robustness parameter, γ, where $\gamma \in [0,1]$. It can be seen that, for values of γ near 1, the RGCV function behaves like the GCV function and that

$$\lim_{\gamma \to 0} \texttt{RGCV}(\lambda) = \mu(\lambda)\texttt{GCV}(\lambda). \tag{3.74}$$

It would appear that the RGCV method has introduced another parameter, γ, which must be estimated in order to find an optimum value of λ. The purpose of this in this thesis is to demonstrate that for a particular problem, a fixed value of γ can be chosen a priori and near optimal values of λ can be determined as a consequence.

The Zero-Crossing method (ZERO function)

The Zero-Crossing method ZERO [225, 226] seeks to find a balance between the solution norm and the residual norm by estimating the optimal regularisation parameter as a zero of the function

$$\texttt{ZERO}(\lambda) = \lambda^2\eta^2(\lambda) - \rho^2(\lambda) \tag{3.75}$$

which, in terms of the SVD, can be rewritten as

$$\texttt{ZERO}(\lambda) = \sum_{i=1}^{n} \frac{\lambda^2\alpha_i^2\left(\sigma_i^2 - \lambda^2\right)}{\left(\sigma_i^2+\lambda^2\right)^2} - \|\mathbf{r}_\perp\|_2^2 \tag{3.76}$$

It can be shown [227] that when the DPC of section 3.2.2.2 is satisfied, the function $\texttt{ZERO}(\lambda)$ has only two zeros. In this case the smaller λ is chosen as the approximation to the optimal regularisation parameter.

Point of Maximum Curvature Criteria (CURV function)

The appropriate regularisation parameter λ corresponds to the maximum curvature of the

L-shaped appearance as defined by [226, 228].
Let revisit Equation (3.28) and (3.29). One can write in functional notation

$$\rho^2(\lambda) := \|\mathbf{A}\mathbf{x}_\lambda - \mathbf{y}\|_2^2 = \sum_{i=1}^{n} \frac{\lambda^4 \alpha_i^2}{\left(\sigma_i^2+\lambda^2\right)^2} + \|\mathbf{r}_\perp\|_2^2, \tag{3.77}$$

$$\eta^2(\lambda) := \|\mathbf{x}_\lambda\|_2^2 = \sum_{i=1}^{n} \frac{\sigma_i^2 \alpha_i^2}{\left(\lambda^2+\sigma_i^2\right)^2}. \tag{3.78}$$

Hansen et al.'s [228] choice is the point on the L-curve

$$(\widehat{\rho}(\lambda), \widehat{\eta}(\lambda)) \equiv (\log(\rho(\lambda)), \log(\eta(\lambda))) \tag{3.79}$$

that has maximum curvature. Here, the curvature is defined as

$$\texttt{CURV}(\lambda) = \frac{\widehat{\rho}'(\lambda)\widehat{\eta}''(\lambda) - \widehat{\rho}''(\lambda)\widehat{\eta}'(\lambda)}{\left([\widehat{\rho}'(\lambda)]^2 + [\widehat{\eta}'(\lambda)]^2\right)^{3/2}} \tag{3.80}$$

where differentiation is with respect to $\chi = \lambda^2$. The optimum parameter $\chi_{opt} = \lambda_{opt}^2$ is obtained as the extremum on the curve $\mathcal{LLP}(\chi, \texttt{CURV}(\chi))$ that yields local maximum value of $\texttt{CURV}(\lambda)$. The operator name $\mathcal{LLP}(\chi, \mathcal{W}(\chi))$ introduced is a log-log scaled plot with $\mathcal{W}(\chi)$ on the ordinate and $\chi = \lambda^2$ as the abscissa. Where $\mathcal{W}(\chi)$ represent any cost function to be optimized.

***Minimum-Product Criterion for the Corner* (MINP function)**

This criterion proposed by Lian et al. [229] is a modification of the Regińska criterion [230] which finds the value of the optimum parameter λ_{opt} that minimizes the product $\texttt{MINP}(\lambda)$ given by

$$\begin{aligned} \texttt{MINP}(\lambda) &= \rho(\lambda)\eta(\lambda) \\ &= \|\mathbf{A}\mathbf{x}_\lambda - \mathbf{y}\|_2 \|\mathbf{x}_\lambda\|_2 \end{aligned} \tag{3.81}$$

Since $\texttt{MINP}(\lambda)$ is always positive, alternatively, one can look for the value of λ^2 that minimizes the squared product denoted as $\overline{\mathcal{P}}(\lambda)$:

$$\begin{aligned} \overline{\mathcal{P}}(\lambda) &= \rho^2(\lambda)\eta^2(\lambda) \\ &= \|\mathbf{A}\mathbf{x}_\lambda - \mathbf{y}\|_2^2 \|\mathbf{x}_\lambda\|_2^2 \end{aligned} \tag{3.82}$$

The required value of λ is obtained by differentiating $\overline{\mathcal{P}}(\lambda)$ with the respect to $\chi = \lambda^2$, and setting the derivative to zero. It follows that $\frac{d\overline{\mathcal{P}}(\lambda)}{d\chi} = 0$ when

$$\chi \sum_{i=1}^{\min(m,n)} \frac{\alpha_i^2 \left(\sigma_i^2 - \chi\right)}{\left(\chi + \sigma_i^2\right)^2} - \|\mathbf{r}_\perp\|_2^2 = 0 \tag{3.83}$$

The Equation (3.83) can be written as finding the zeros of Equation (3.76) as $\texttt{ZERO}(\chi) = 0$. Thus, the zero-crossing approach and the minimum-product corner criterion are equivalent. In most regularization problems, the difference lies in the way the optimum regularization parameter is selected. In the case of zero-crossing approach, the optimum parameter $\chi_{opt} = \lambda_{opt}^2$ can be found either from the smallest zero of $\texttt{ZERO}(\chi)$ or, equivalently as an extremum on the curve $\mathcal{LLP}(\chi, \texttt{MINP}(\chi))$ that yields a local minimum value of $\texttt{ZERO}(\chi)$. For the MINP corner criteria, the optimum parameter λ_{opt} is obtained as the extremum on the curve $\mathcal{LLP}(\chi, \texttt{MINP}(\chi))$ that yields global minimum value of $\texttt{MINP}(\chi)$.

3.4.1.3 Choosing the regularization parameter when the 'expected solution' is already known (CHA function)

Without prior information, none of the regularization methods discussed above can produced the same result as reference but they can only generate an approximate result. Thus for this reason this section is dedicated to a test technique applied to the iPTF problem using prior knowledge of the source. This technique is only applicable if prior knowledge about the source is known and as such they can only be used to evaluate the best possible solution reachable with a considered regularization technique.

This technique basically involves comparing regularized solution to the reference solution and the concept of correlation criteria is significant here. Correlation criteria seek to analyze the similarity and differences between two sets of results. Usual applications are the correlation of test and analysis results and the comparison of various analysis results. Ideally, correlation criteria should quantify the ability of two models to make the same predictions. Since, the predictions of interest for a particular model can rarely be pinpointed precisely, one has to use general qualities and select, from a list of possible criteria, the ones that can be computed and do a good enough job for the intended purpose. In other words there is no best choice for a correlation criterion unless you are very specific as to what you are trying to do with your model.

For these reasons, in this PhD work, the following criterion is considered. The criterion uses the Cosine-Hermitian Angle ($\mathcal{CHA}$) of Equation (C.9) as the correlation index. The reader is informed that correlation indices of complex vectors are comprehensively treated in Appendix C.

$$\begin{aligned} \texttt{CHA}(\lambda) &= \mathcal{CHA}(\mathbf{x}_\lambda, \overline{\mathbf{x}}) \\ &= \frac{|\langle \mathbf{x}_\lambda, \overline{\mathbf{x}} \rangle|}{\|\mathbf{x}_\lambda\|_2 \, \|\overline{\mathbf{x}}\|_2} \\ &= \sqrt{\frac{\left|\mathbf{x}_\lambda^{\mathrm{H}} \overline{\mathbf{x}}\right|^2}{\left[\mathbf{x}_\lambda^{\mathrm{H}} \mathbf{x}_\lambda\right] \left[\overline{\mathbf{x}}^{\mathrm{H}} \overline{\mathbf{x}}\right]}} \end{aligned} \tag{3.84}$$

where $\mathbf{x}_\lambda$ is the outcome from the chosen regularization technique for a λ. The optimal solution $\mathbf{x}_{\lambda_{opt}}$ is the solution that yields the maximum $\texttt{CHA}(\lambda)$ for all values of λ.

3.5 Summary and Conclusion

This chapter addressed theoretically how to handle issues of inverse problems, specifically, the iPTF problem in determining an acoustic source's particle velocity using field measurements of acoustic pressures and/or particle velocities and FEM impedance transfer matrices. This is an inverse problem since it entails estimating the acoustic source normal particle velocities (unknown cause) using acoustic field measurements (observed effects) and FEM impedance matrices (acoustic virtual cavity effect). Inverse problems, like as this one, have the general property that every arbitrary little perturbation in the system's input leads in an arbitrary huge fluctuation in the output. A simple numerical experiment is used to demonstrate the properties of discrete ill-posed issues. It was about estimating the acoustic source particle velocity of the m-iPTF at a frequency of 100Hz. It was proved that by purposely polluting the observed data with a little amount of noise, a normal inversion technique leads to a nonphysical solution that is completely dominated by noise effects. A meaningful solution can be reached by applying some type of regularization to the inversion of the impedance transfer matrix, which explicitly links the cause (input) to the observed result (output).

In this process, the singular value decomposition of the matrix proved to be a very useful tool as it provides a clear physical and mathematical understanding of the ill-conditioned behavior. Furthermore the discrete Picard condition was introduced which, if satisfied, guarantees the

existence of a physically meaningful regularized solution for a given right-hand side vector.

Various regularization methods were considered. The Regularization in general can be seen as a form of optimization process that involves the generation of several solutions from which the optimum solution should be chosen and the criteria for selecting the optimum solution (through the use of regularization parameter) are an essential requirement. Based on the level of information provided, two major classes of such strategies are addressed in this thesis study. In the absence of prior knowledge, the following criteria can be applied: `GCV`, `RGCV`, `ZERO`, `CURV` and `MINP` criteria. When prior information about the test problem is available, the `CHA` criterion is utilized.

Essentially all of these regularization techniques involve a trade-off between the error component related to amplification of the noise (perturbation error) and the error component introduced by the regularization (regularization error). The amount of regularization is determined by the regularization parameter which can be chosen with the help of the so-called L-curve plot. This graphical tool visualizes the balance between the norm of the residue and the magnitude of the regularized solution, measured according an appropriate norm.

So far, only the theoretical aspects of numerical methods for dealing with inverse problems have been provided. Chapter 4 describes how to use these approaches to solve the iPTF problems.

4

Numerical Application of the Regularization Strategies

The implementation of the various regularization strategies discussed in Chapter 3 on numerical experiments is described in this part. The primary goal of this chapter is to investigate the regularization strategies for both m-iPTF and u-iPTF problems. The usual procedure to obtain the input measurement data is to perform a real experiment using acoustic sensors such as the pU probes and/or microphones. In this study, no such physical experiment is done but rather a numerical experiment is carried out in order to control each parameter.
To evaluate the capabilities of the regularization strategies, a numerical experiment consisting of a simply supported rectangular plate excited by a point force and radiating in a semi-infinite acoustic field is set up. Three configurations are used:

- `CASE A` - **Ideal test case**: it corresponds to simulations without adding noise on transfer functions computed by ACTRAN Software. The errors only come from discretization in elements and modal truncation. In addition, at this step, the number of identification patches equals the number of field points taken in the virtual volume. As a consequence, the system of equations is neither over-determined nor under-determined. This type of system is referred to as an equal-determined system in the studies.

- `CASE B` - **Noisy environment**: in this case, additive and multiplicative noises are introduced to simulate a noisy acoustic environment. Different SNR (Signal to Noise Ratio) levels (3 dB, 10 dB, and 20 dB) are introduced into the iPTF problem and the influence of noise is evaluated. An equally-determined system is considered here.

- `CASE C` - **Under-determined configuration**: it describes a scenario in which the number of measurement field points is reduced from 600 to 60 (in accordance to the sequence [600, 480, 240, 60]). In that configuration the number of equations is lower than the number of unknowns and the system of equations is under-determined.

4.1 Presentation of the numerical experiment

The aim of this section is to mimic, through numerical simulations, the measurement of pressure $\mathbf{p}_m$ and particle velocity $\mathbf{v}_k$ as an input information for Equation (2.22) of the u-iPTF and the measurements of pressure $\mathbf{p}_k$ together with $\mathbf{p}_m$ as an input data for Equation (2.30) in the m-iPTF case. The source, shown in Figure 4.1, is chosen as a simply supported rectangular plate excited by a harmonic point force. For this numerical experiment, the baffled plate radiates in a semi-infinite free field.
The plate is 0.6 m long, 0.4 m wide, and 2 mm thick, and it is made of steel (Young's modulus $E = 2.1 \times 10^{11}$ Pa; density $\rho = 7800$ kg/m^3; Poisson's ratio $\nu = 0.3$; damping $\eta = 0.02$). The plate is excited by a unit point force located at point (0.1; 0.1) m on the frequency band [100:1000] Hz

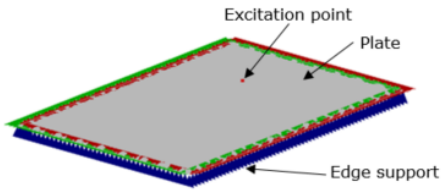

Figure 4.1: Plate model for vibration computation.

(frequency step 2 Hz).

This system is solved using a finite/infinite element (FE/IE) model with ACTRAN software. A finite acoustic volume that can be seen in Figure 4.2 is defined to discretize the acoustic nearfield and a layer of infinite elements is added on the skin of this volume to ensure Sommerfeld free field condition. A direct frequency response (DFR) with ACTRAN software was used for the calculation of the acoustic radiation. The model takes into account air damping equal to $\eta = 0.5\%$ and the infinite elements are interpolated to order 10 to ensure the convergence of the solution. An example of the radiated pressure and velocity fields is given in Figure 4.3. In Section 4.3 and 4.4, for reconstructing the velocity field of the plate, some pressures and velocities will be picked from this radiated field exactly like it would be done in a real experiment with microphones and pU probes respectively.
In addition, this numerical experiment will be used as a reference for comparing results obtained from iPTF reconstructed fields, discretized by patches.

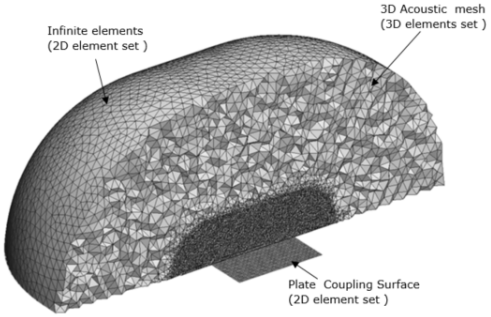

Figure 4.2: The Finite/Infinite element model of the acoustic domain for computation of acoustic radiation of the plate in free field condition.

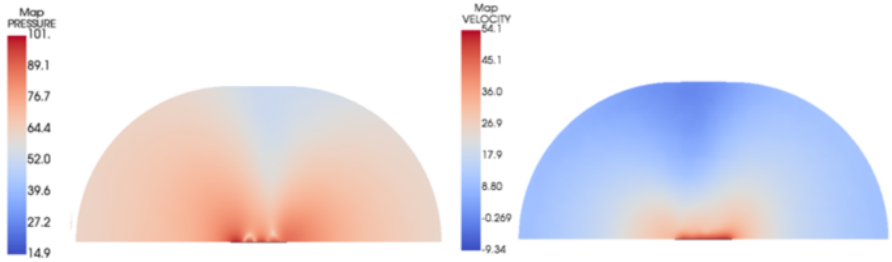

(a) (b)

Figure 4.3: A cut- section view of (a) the radiated pressure field (dB, ref: 2×10^{-5} Pa) and (b) the radiated velocity field (dB, ref: 5×10^{-8} (m/s)) at a frequency of 900Hz

4.2 Definition of the virtual volume for application of iPTF approaches

The aim of this section is to show how the acoustic impedance matrices $\mathbf{Z}_{mj}$ and $\mathbf{Z}_{mk}$ of Equation (2.22) for u-iPTF and $\mathbf{Z}_{mj}$ and $\mathbf{Y}_{mk}$ matrices of Equation (2.30) for m-iPTF are computed using a modal extraction analysis of the virtual volume with specific boundary conditions. It is important to understand that the simulation used for this numerical step for computing acoustic impedances is entirely different and independent from the numerical experiment of previous Section 4.1. Indeed, computations in Section 4.1 are performed to mimic a real experiment and give inputs to Equation (3.3). In this section, acoustic impedances involved in Equation (3.3) are obtained numerically: this is a mandatory step for applying iPTF even in case of real experiments.

As the shape of the virtual volume is completely arbitrary, a simple rectangular box surrounding the plate is chosen as can be seen in Figure 4.4. This volume is delimited by three surfaces: the virtual surface, the rigid baffle and the plate surface itself. As explained in Sections 2.1.1 and 2.1.2 and as formulated in Equation (2.11) for u-iPTF and Equation (2.14) for m-iPTF, some specific boundary conditions must be defined on this virtual volume. In the case of the u-iPTF the velocity has to be null on all the surfaces delimiting the virtual volume (uniform Neumann's boundary condition). In the case of the m-iPTF the velocity has to be null on the source surface and the baffle plane and the pressure has to be null on the virtual surface (mixed Neumann's and Dirichlet's boundary conditions). These boundary conditions are obviously not the real one but are defined for sake of mathematical resolution [180].

Due to the problem of discretization and the modal truncation, several parameters may

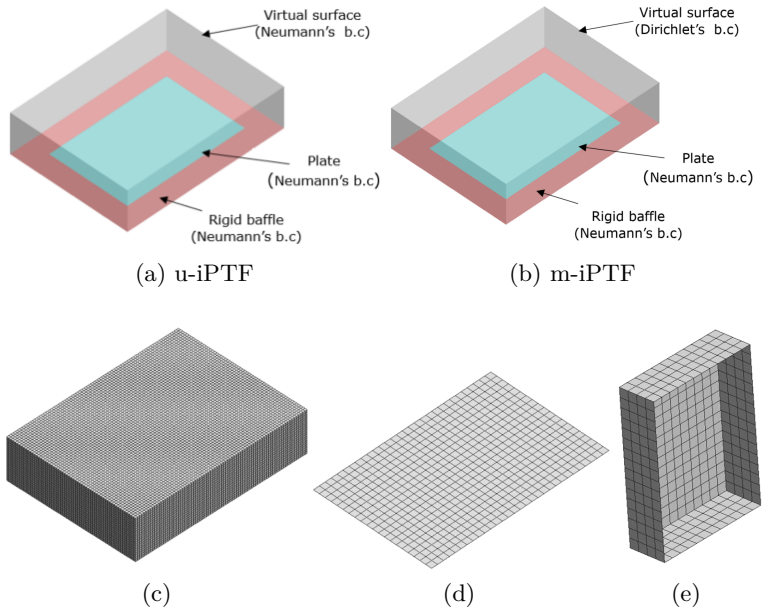

(a) u-iPTF (b) m-iPTF

(c) (d) (e)

Figure 4.4: Virtual cavity model. Definition of the surfaces delimiting the virtual acoustic cavity and the associated boundary conditions for (a) u-iPTF and (b) m-iPTF. (c) FE mesh of the virtual volume; (d) identification patch mesh of the plate; (e) "measurement" patch mesh of the virtual acoustic volume.

have an impact on the reconstruction of the source velocity field by the iPTF methods. One of such parameters is the size of the patches discretizing the virtual surface. For both m-iPTF and u-iPTF methods, the virtual surface is involved in determining the conditioning of the modal matrix $\mathbf{Z}_{mj}$ to be inverted. Forget [180] established that the identification convergence is ensured

with a maximum patch size of the virtual surface respecting the criterion $\lambda_{air}/4$ (where λ_{air} is the acoustic wavelength) at the maximum study frequency.

It is important to know that the number of field points in the virtual volume affects the determination (over-determine or under-determine) of the problem and in turn the fineness of the patch mesh used to discretize the reconstructed source field. As studied by Forget [180], at a given frequency (or the acoustic wavelength), the quality of reconstruction of the field is dependent on the number of pressure points taken in the virtual volume. Thus, a minimal number of these points are needed to ensure a good estimation of the velocity source field distribution. This minimal number N_m of points can be set using a criterion [180] linking the volume V_v of the virtual closed domain to the maximum identification frequency f:

$$N_m = \frac{V_v}{\left(\frac{\lambda_{air}}{4}\right)^3} = \frac{V_v}{\left(\frac{c}{4f}\right)^3} \tag{4.1}$$

where c is the speed of sound. This criterion should be used as a first-order indicator as it does not take into account any distribution or repartition of the chosen points.

Finally, modal truncation imposed on modal summation in Equation (2.20) of u-iPTF and Equation (2.28) of m-iPTF might also introduce reconstruction errors. The number of modes used in the computation of matrices $\mathbf{Z}_{mj}$, $\mathbf{Z}_{mk}$ and $\mathbf{Y}_{mk}$ has an influence on their rank as already noticed by Totaro et al. [231, 185]. Indeed, the rank of these matrices is driven either by the number of points inside the volume or by the number of modes used in the computation (the rank is equal to the lowest value of both). And they noticed that if the number of modes is lower than the number of measurement points taken inside the volume, the condition number suddenly highly increases. Thus, as a rule, the number of modes has to be higher than the number of measurement points. The mode extraction analysis performed in this study is carried out up to the frequency of 6500 Hz for which 2905 modes are extracted. With 600 measurement points in virtual acoustic volume, it is evident to ensure independence of linear equations of the system. It should be noted that the FE model of virtual acoustic volume of Figure 4.4 respects the standard recommendations in terms of mesh for such a calculation, namely a criterion $\lambda_{air}/6$ to 6500 Hz. The modal data (pressure) calculated at the nodes of the FE model of the acoustic volume are averaged over the plate patches and virtual surface patch models, while the nodal value (pressure) is used for the volume points. The virtual surface has been optimally discretized with a patch size of $L_{max} = 50$ mm (i.e. $L_{max} < \lambda_{air}/4$ at 1000 Hz). The virtual cavity volume is 0.8 m long, 0.6 m wide, and 0.2 m high.

4.3 `CASE A` - Ideal test case

In this section an iPTF problem which is created from an equally-determined and unperturbed system is the chosen as the test case under study. The main aim of this section is to demonstrate how the regularization techniques presented in Chapter 3 have been used to solve the above problem.

In this section, how the various regularization parameter selection criteria presented in Section 3.4.1 yield their corresponding optimum value for the both m-iPTF and u-iPTF problems is investigated. These results are essential to have a better understanding about the behaviour of how the function values of the selection-criteria vary with regularization parameter, λ^2.

4.3.1 Deterministic approaches

The deterministic approaches presented in Chapter 3 fall in three different categories:

- `Tikh` regularization techniques (zeroth-order Tikhonov approach, Section 3.3.1). The optimum regularization parameter λ^2_{opt} can be defined using different selection criteria

minimizing associated cost functions. In the following, `CURV` of Equation (3.80), `ZERO` of Equation (3.75), `GCV` of Equation (3.67), `RGCV` of Equation (3.73) and `MINP` of Equation (3.81) selection criteria will be investigated. In the following, these strategies will be referred as `Tikh_CURV`, `Tikh_ZERO`, `Tikh_GCV`, `Tikh_RGCV` and `Tikh_MINP` respectively.

- `itr` regularization techniques (Iterative approaches of Delilo, Section 3.3.2). In that case, two stopping criteria are used: `MINP` of Equation (A.2) or `ZERO` of Equation (A.3). In the following, these strategies will be referred as `Itr_MINP` and `Itr_ZERO` respectively.

- `Bay` regularization techniques (Bayesian approach, Section 3.3.3.1). In that case, the `MAP` is used to define the optimum regularization parameter as in Equation (3.45). Though it has statistical origin, `Bay_MAP` can be regarded as Tikhonov kind as it has similar formula structure. The technique is utilized for m-iPTF problem scenarios only because, unlike in the case of u-iPTF, it is much easier to formulate the noise variance using only pressure measurements (which are made up of cavity and virtual surface pressure measurements). In the following, this strategy will be referred as `Bay_MAP`.

Figures 4.5(a) and 4.5(b) present the λ^2 selection-criteria function value plot for the different deterministic regularization techniques respectively for m-iPTF and u-iPTF for the frequency of 100 Hz. The different markers on the various curves of Figure 4.5 indicate the position of optimum regularization parameter λ^2_{opt}.

Let focus first on Tikhonov approaches. One can see in Figure 4.5 that `Tikh_GCV`, `Tikh_CURV`, `Tikh_MINP` and `Tikh_ZERO` lead to approximately the same optimum regularization parameter λ^2_{opt}, and this for m-iPTF or u-iPTF. `Tikh_RGCV` indicates a higher λ^2_{opt} in both cases (even if the difference is much important for u-iPTF) leading to slightly more regularized results and so to smoother identification maps. On the contrary, `Bay_MAP` tends to indicate a lower λ^2_{opt} leading to sharper identification maps.

The iterative approaches are compared in Figures 4.5(c) and 4.5(d). At this frequency, `Itr_ZERO` convergences faster than `Itr_MINP` for m-iPTF (6 iterations vs. 20) but the opposite is observed for u-iPTF (42 iterations vs. 6). In any case, the number of iterations needed for iterative approaches is much lower than the number of loops needed to evaluate the cost functions for Tikhonov regularization (the regularization parameter scale is divided into 100 steps).

It is noticed from Figure 4.6 that the L-curve plots for both m-iPTF and u-iPTF have a L-shape as expected. This indication implies that both the m-iPTF and u-iPTF problems at 100 Hz satisfy the discrete Picard condition of Section 3.2.2.2 and as such all the λ^2 selection-criteria introduced will generate a satisfactory regularized solution. It can be noticed that the `Itr_ZERO` used on the m-iPTF problem and `Tikh_RGCV` of the u-iPTF case do not have their optimum value located exactly at the corner of their L-curve plots. As a result, their identified source velocities will be more regularized (smoother) than the L-curve solution.

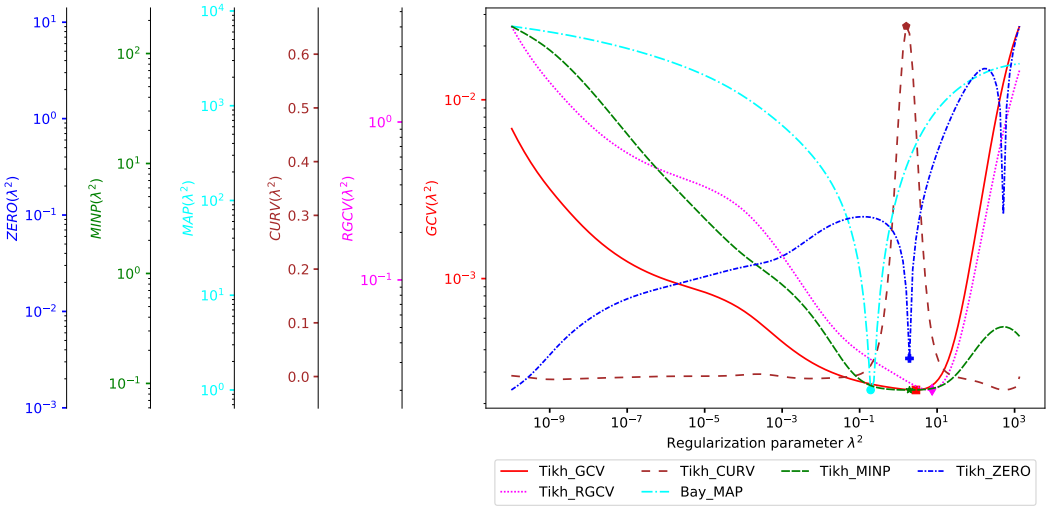

(a) m-iPTF: λ^2_{opt} selection criteria for Tikhonov regularization

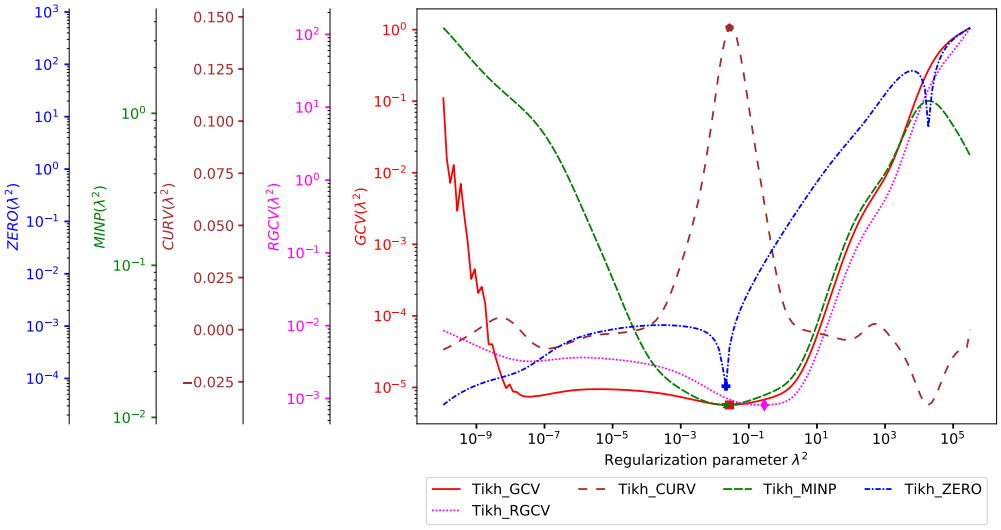

(b) u-iPTF: λ^2_{opt} selection criteria for Tikhonov regularization

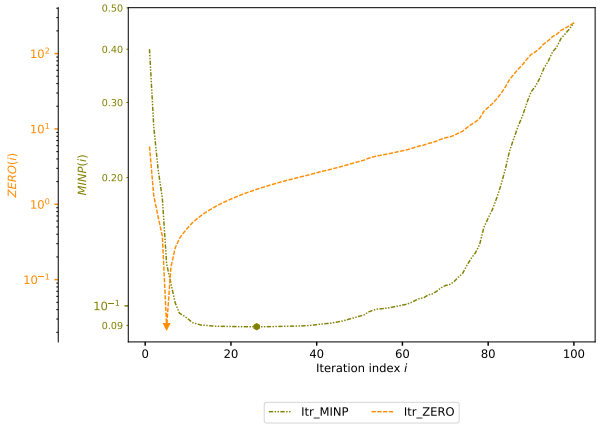

(c) m-iPTF: Iterative based λ^2_{opt} selection criteria

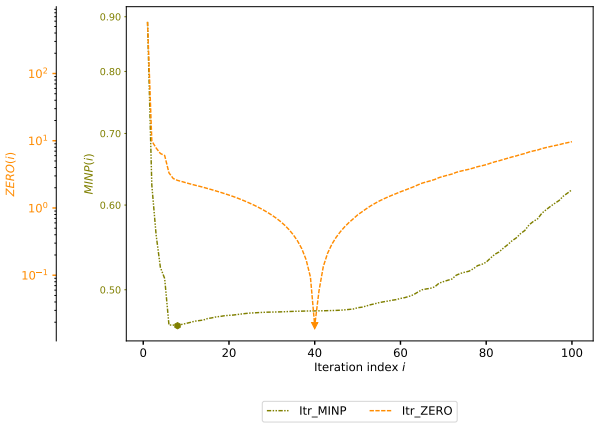

(d) u-iPTF: Iterative based λ^2_{opt} selection criteria

Figure 4.5: The λ^2 selection-criteria function value plot for the different deterministic regularization techniques for m-iPTF and u-iPTF problem carried out at 100 Hz.

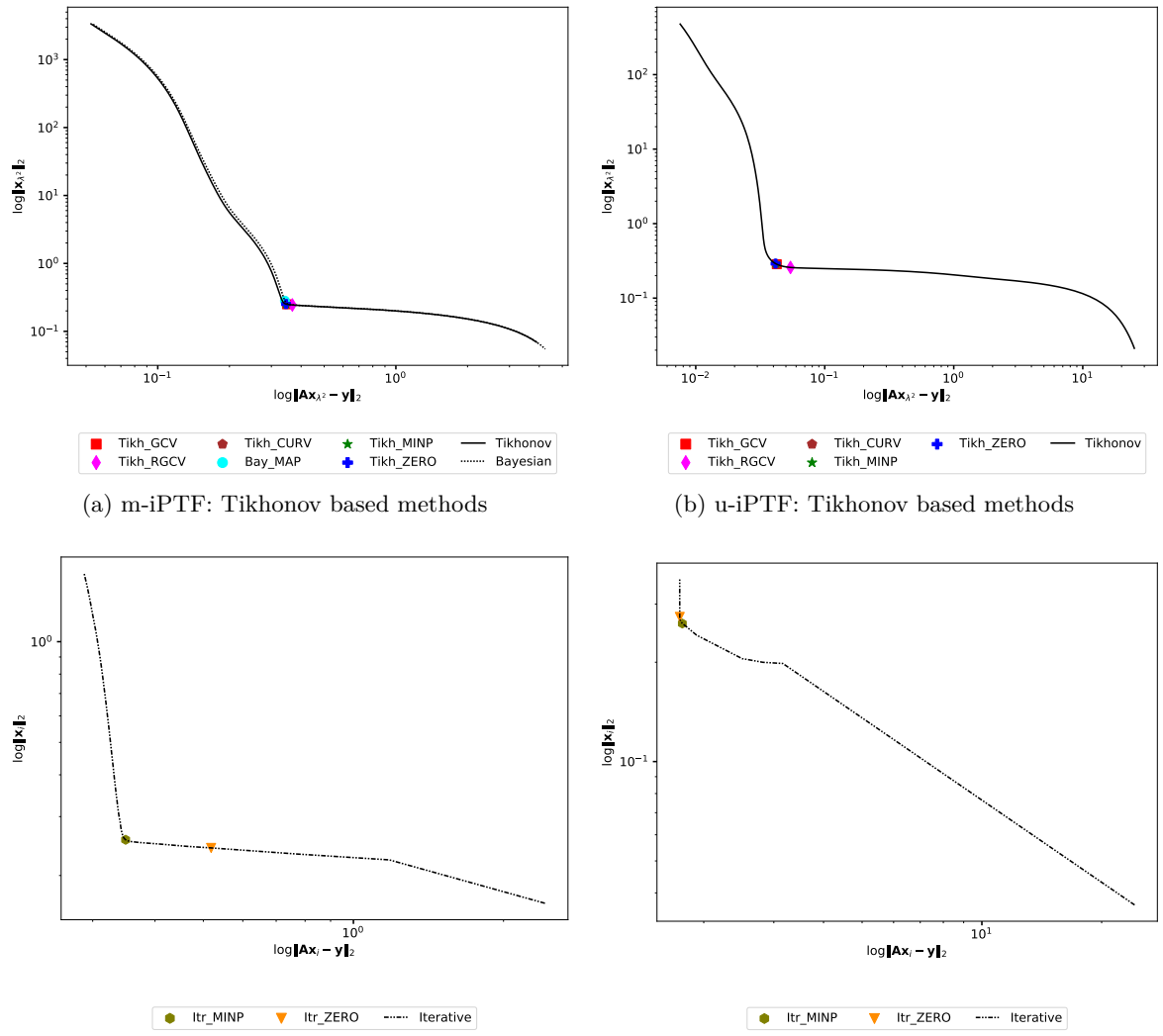

(a) m-iPTF: Tikhonov based methods

(b) u-iPTF: Tikhonov based methods

(c) m-iPTF: Iterative based methods

(d) u-iPTF: Iterative based methods

Figure 4.6: The L-curve plot for the different deterministic regularization techniques for m-iPTF and u-iPTF problem carried out at 100 Hz.

Since these plots are performed at a specific frequency of 100Hz, it is thus difficult to make a generic conclusion from a single observation. For this reason colormap representation of all the results for the frequency spectra of study is considered. The colormaps of Figure 4.7 plot the function values generated from the selection-criterion as a function of frequency and regularization parameter λ^2 for Tikhonov approaches.

To obtain good images that will reveal the some intrinsic behaviour of selection-criteria across the frequency spectrum of study, the function values of the colormaps for each frequency are normalized using the their respective L2 norm. Also the vertical dashlines on the colormaps represent the eigen-frequencies of the modes of the virtual acoustic cavity. The dotted-points in cyan color on the plots represent the optimum function values (Figure 4.7). Again for easy generation of the plot the λ^2 index was used instead of the real λ^2 values.

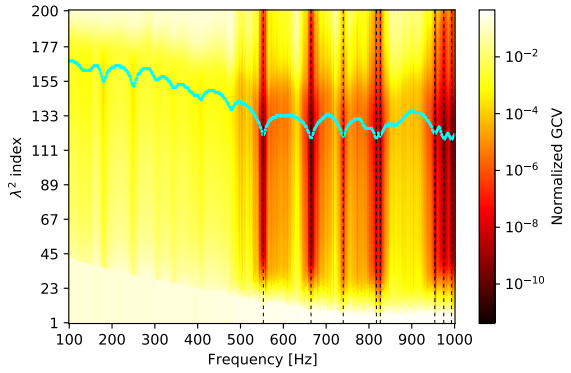

(a) m-iPTF `Tikh_GCV`

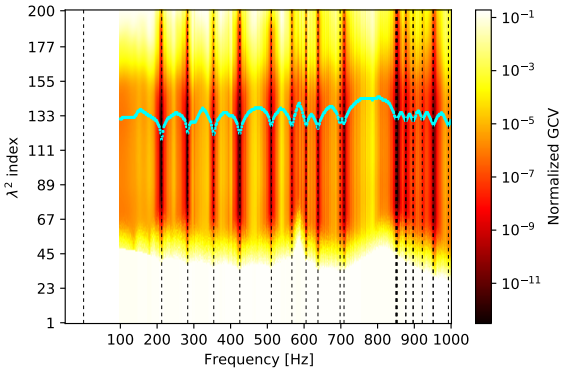

(b) u-iPTF `Tikh_GCV`

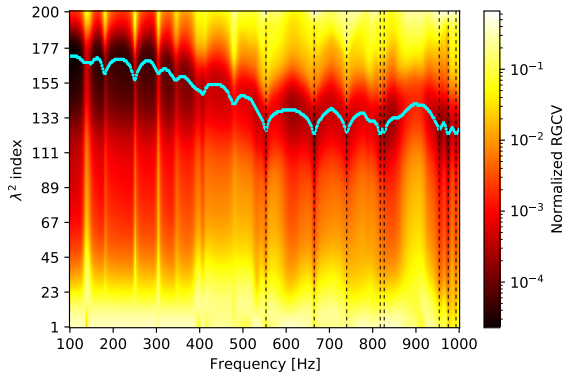

(c) m-iPTF `Tikh_RGCV`

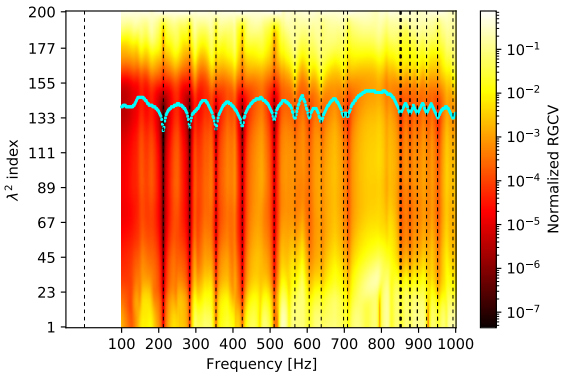

(d) u-iPTF `Tikh_RGCV`

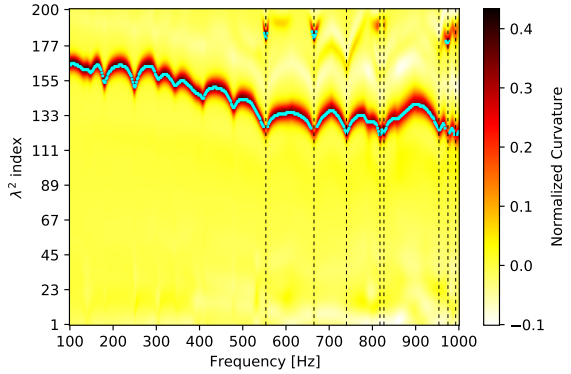

(e) m-iPTF `Tikh_CURV`

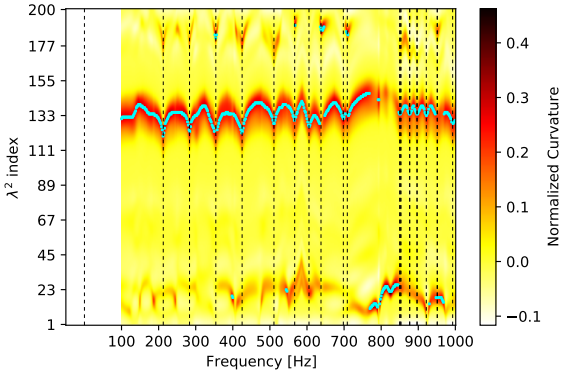

(f) u-iPTF `Tikh_CURV`

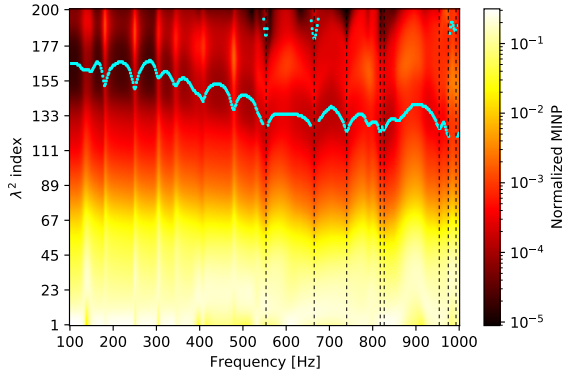

(g) m-iPTF `Tikh_MINP`

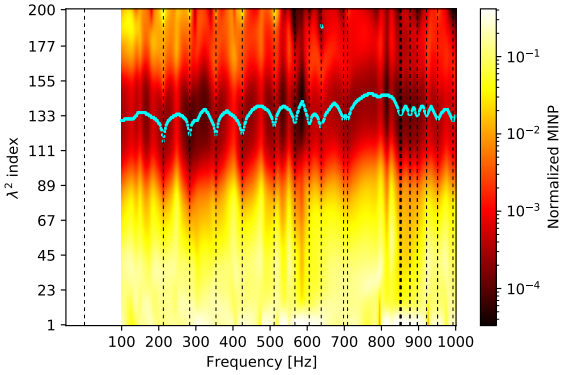

(h) u-iPTF `Tikh_MINP`

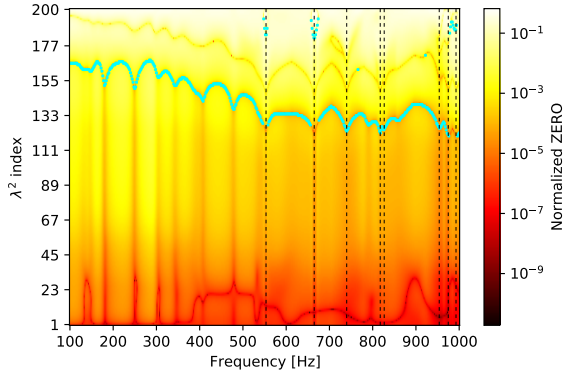

(i) m-iPTF `Tikh_ZERO`

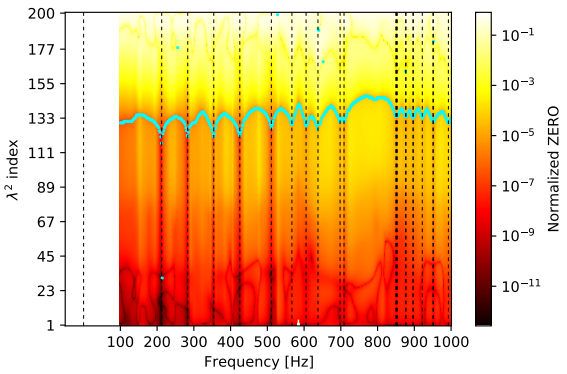

(j) u-iPTF `Tikh_ZERO`

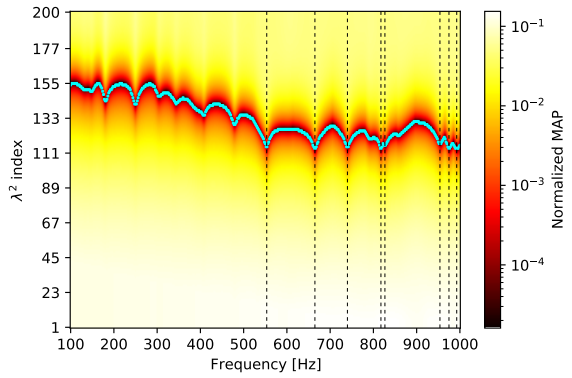

(k) m-iPTF `Bay_MAP`

Figure 4.7: Colormap plot for the various zero-order Tikhnov-based regularization parameter selection-criteria for iPTF problem as a function of frequency and regularization parameter.

It is observed from Figure 4.7 that the optimum values form a "wave-like" curve with the anti-nodes coinciding mostly with the eigen-frequencies of the virtual acoustic cavity. The use of `Tikh_CURV` reveals a behavior already noticed by Totaro et. al [185] for u-iPTF: at some frequencies, the chosen λ^2 values jumps or drops to much higher or much lower values. This is due to the fact that, at this particular frequencies the L-shape curve is rather more a W-shape curve and exhibits two corners. `Tikh_CURV` strategy applied to u-iPTF has a high level of disperse points deviating away from the wave-like curve pattern. However, applying this strategy to m-iPTF also generates this kind of artifact but it is much less pronounced as the virtual modes (which are mainly responsible of this) are less numerous. To a lesser degree, this effect appears also for `Tikh_MINP` and `Tikh_ZERO` strategies applied on m-iPTF.

`Tikh_GCV` exhibits, as explained in Chapter 3, a flattened curve on a large frequency band which makes difficult the choice of the optimal λ^2_{opt} value (it is one of its known issue). On the opposite, the `Bay_MAP` strategy (only applied to m-iPTF) shows at each frequency a cost function with a sharp peak making obvious the choice of the λ^2_{opt} value.

Figure 4.8 plots in the same graph the chosen λ^2_{opt} values as a function of frequency for each Tikhonov strategy. What was noticed for a single frequency in Figure 4.5 can be generalized on the whole frequency range: all the Tikhonov's strategies used so far lead to approximately the same λ^2_{opt} values, except `Bay_MAP` which systematically provides a lower regularization parameter leading to sharper identified maps on the whole frequency range. Conversely, the `Tikh_RGCV` strategy leads to the highest regularization parameter producing smoother identified maps. In addition, the jumps and drops already observed in Figure 4.7 are clearly visible for both iPTF approaches when using `Tikh_CURV` and `Tikh_ZERO` strategies.

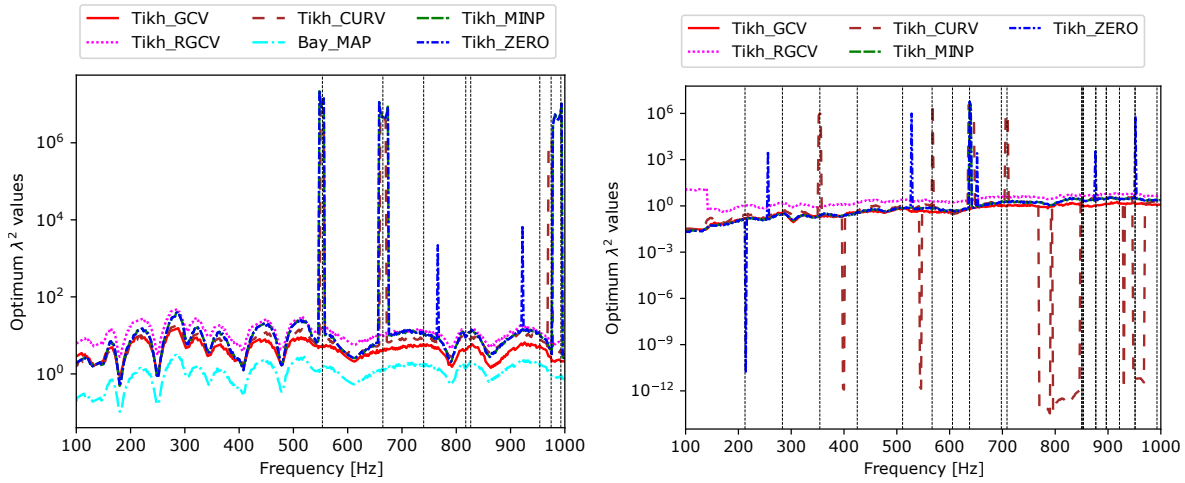

(a) m-iPTF (b) u-iPTF

Figure 4.8: Optimum regularization parameter λ^2 spectra of the deterministic regularization techniques for m-iPTF and u-iPTF method.

The condition number as defined in Equation (3.8) is a measure the instability of the impedance matrix $\mathbf{Z}_{mj}$ using the singular values. It can be observed from the condition number spectrum of Figure 4.9 that the peak values coincide with the eigen-frequencies (shown as vertical dashed lines) of the acoustic modes of the virtual cavity. This is an indication that the singular values tend to fall quickly to smaller values. Thus the higher the condition number, the more ill-posed $\mathbf{Z}_{mj}$ is. There is great link between the Figure 4.9(a) and Figure 4.8(a) for the m-iPTF case and between Figure 4.9(b) and Figure 4.8(b) the u-iPTF case. The jumps and drops observed in Figure 4.8 appear for peaks of the condition number spectra of Figure 4.9. This happens because regularizing using the Tikhonov technique, constraints are set according to Equation (3.26) which aims at the smoothness properties of the solution and thus ignoring contributions related to small singular values (according to Equation (3.30)) to yield smoother solution with a reasonable L2 norm $\|\mathbf{x}\|_2$. This validates the fact that Tikhonov regularization methods act as low-pass filters in the singular value spectrum from which the regularization parameters are generated from.

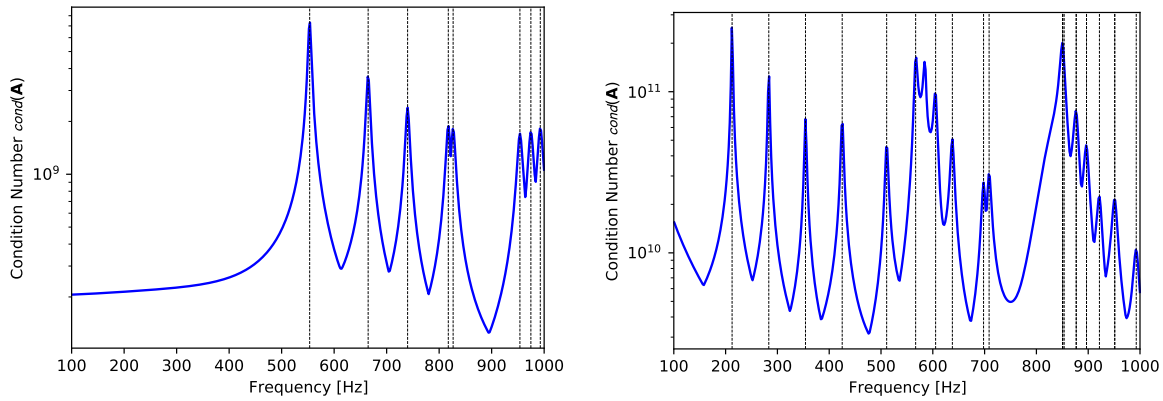

(a) m-iPTF (b) u-iPTF

Figure 4.9: Condition number spectrum of the 600×600 impedance transfer matrix $\mathbf{A}$ of Equation (3.3).

Figure 4.10 compares the number of iterations needed to reach the optimal solution for `Itr_MINP` and `Itr_ZERO` strategies as a function of frequency. From Figure 4.10, one can remark that the number of iterations increases with frequency. If, on the whole, `Itr_MINP` necessitates less iterations than `Itr_ZERO` for m-iPTF, it is the opposite for u-iPTF.

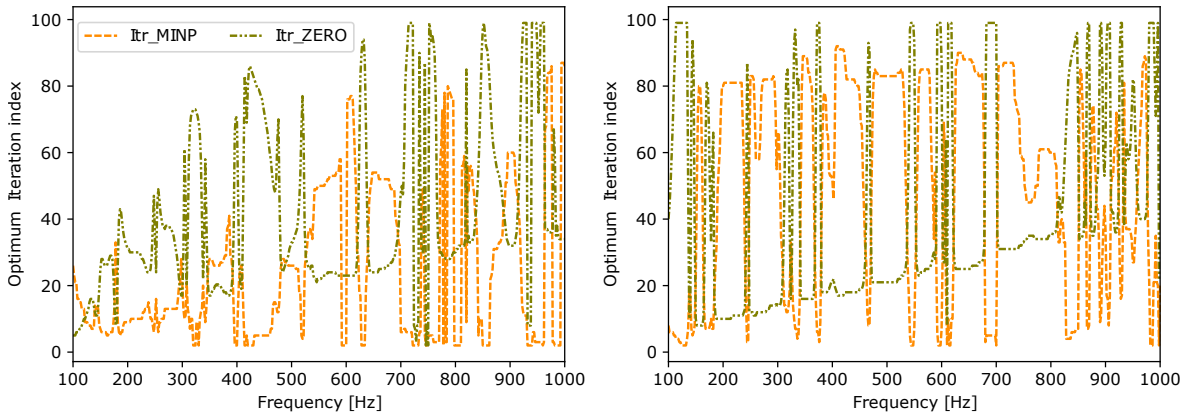

(a) m-iPTF (b) u-iPTF

Figure 4.10: Optimum iteration index spectra of the iterative regularization techniques for m-iPTF and u-iPTF method.

4.3.2 Stochastic approach

What has been presented so far are the results of functional behavioural results of the deterministic regularization approaches. At this juncture, the behavioural results of the DBKH-iPTF algorithm 1, the statistical strategies named as `Bay_MAD` and `Bay_MINP` in Section 3.3.3.2 are presented.

Just as in any other regularization strategy, the regularization parameter λ^2 values needs to be generated. The λ^2 values are generated using the Algorithm 1 which involves the stochastic sampling of the hyper-parameters γ_x^2 and γ_y^2. Figure 4.11 shows results of how this hyper-simulation is done for iPTF problem at 100 Hz. In all, a total of 200 iterative runs were performed to obtain the λ^2 samples.

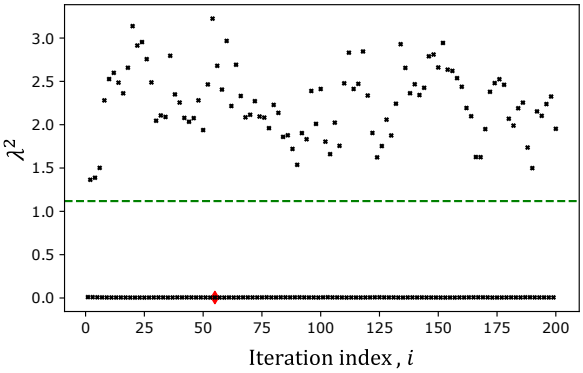

(a) m-iPTF λ^2

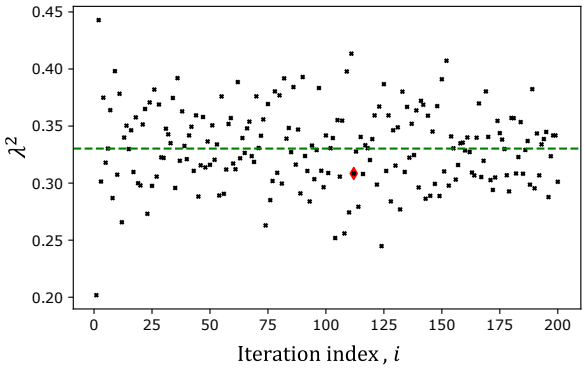

(b) u-iPTF λ^2

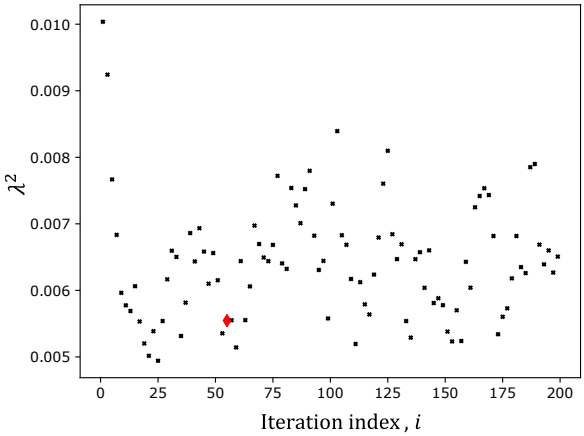

(c) m-iPTF λ^2 (zoom)

Figure 4.11: Regularization parameter λ^2 generated according to the hyper-parameter simulation of Algorithm 1 for the iPTF problem carried out 100 Hz. Green line depict the mean μ_λ according to Equation (3.62) and the red spot indicate the λ^2_{opt} computed from Equation (3.61).

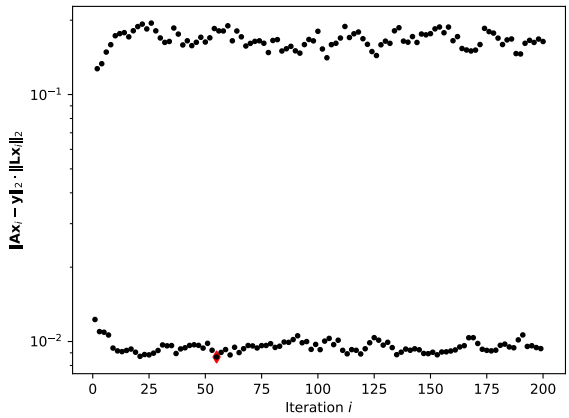

(a) m-iPTF `MINP` criterion

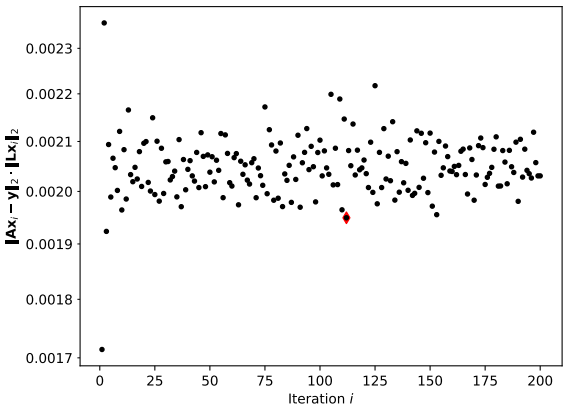

(b) u-iPTF `MINP` criterion

Figure 4.12: Results of using `Bay_MINP` of Equation (3.60) for the iPTF problem carried out 100 Hz. The red spot indicate the λ^2_{opt} computed from Equation (3.61).

As already presented, the `Bay_MINP` cost function has the same formula structure as the regular Tikhonov function and as a result a criteria for selection of the optimum regularization

parameter λ^2_{opt} is required and for this example, the `MINP` criteria is used, thus the reason for the acronym `Bay_MINP`. The other solution abbreviated as `Bay_MAD`, basically consists of finding the mean of all the sampled solutions which have their equivalent λ^2 below the μ_λ using Equation (3.62).

The green dashed horizontal lines and the red diamond-shaped marker in Figure 4.11 repre-

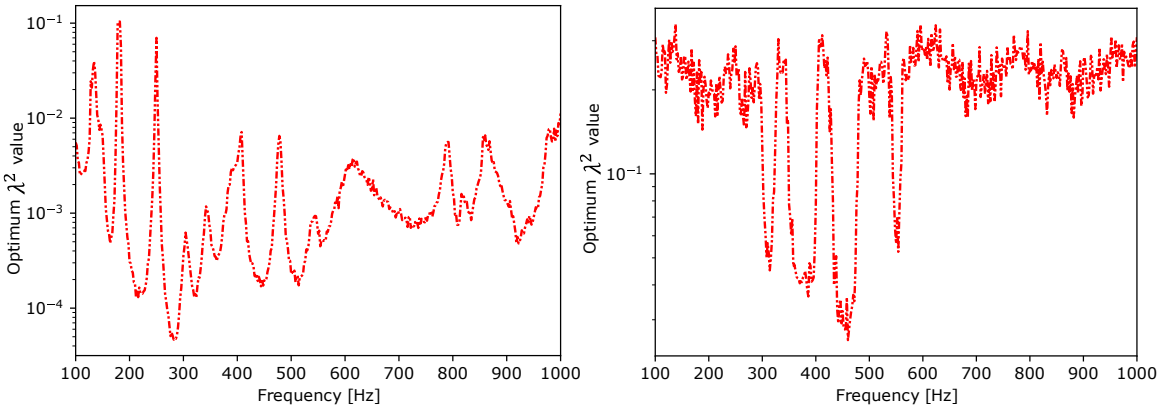

(a) m-iPTF λ^2_{opt} (b) u-iPTF λ^2_{opt}

Figure 4.13: Plots of the λ^2_{opt} regularization parameter obtained from `Bay_MINP` strategy for the frequency spectrum of study.

sent the mean and the index of the optimum solution based on the `Bay_MINP` of Equation (3.60) respectively. It is seen from the u-iPTF case of Figure 4.11(b) that the distribution patterns obtained after 200 iterative runs for the regularization parameter λ^2 is entirely different from that of the m-iPTF case of Figure 4.11(a). This disparity between these observations is linked to the inherent characteristics of their respective iPTF problem make up. The `Bay_MINP` cost function of Equation (3.60) indicated in Figures 4.12 deal with the product of the perturbation error and the regularization error. Thus, high values of `MINP` function indicate an erroneous and noisy regularized solution. The `Bay_MINP` regularization parameters λ^2_{opt} as a function of frequency are plotted in Figure 4.13. The u-iPTF of Figure 4.13(b) exhibits larger regularization parameter values than the m-iPTF case of 4.13(b). As a result, the u-iPTF with `Bay_MINP` strategy requires more filtering during the regularization process than the m-iPTF counterpart in order to reach an optimal solution.

At it this point, the numerical results describing the functional behaviour of all the regularization techniques have been presented. In next section, the results of the regularization processes is analyzed using objective metrics.

4.3.3 Objective quantification of the identified maps quality

In general, the validation involves comparison of two data sets and one/more criteria used as a means of judgment. In this thesis the two data sets used are the iPTF identification results $\mathbf{x}_{id}$ and a reference data, $\mathbf{x}_{ref}$, where variable $\mathbf{x}$ represent any acoustic indicator on the surface of the plate. The comparison criteria indices used are treated comprehensively in Appendix C. The chosen criteria indices are $\mathcal{CHA}$ of Equation (C.9), $\mathcal{CI}$ of Equation (C.12), $\mathcal{CEA}$ of Equation (C.5) and $\mathcal{SEA}$ of Equation (C.8).

4.3.3.1 Properties of the considered Reference

Firstly, the reference source data used in this work is purely numerical experiment data, which was obtained by performing a direct forward radiation analysis using the ACTRAN software. An example of corresponding retrieved acoustic information are depicted in Figure 4.14. It is

important for the reader to be informed that this forward radiation analysis performed with ACTRAN only uses nodal information from the source for computing its acoustic quantities whilst the iPTF requires elemental information in solving its inversion problem. As a result there is a conversion of nodal information to elemental information. The conversion irrespective of the numerical techniques used that is either interpolation or spatial averaging methods results in loss of information. In the following, a simple spatial averaging technique is performed to compute quantities on patches from values at nodes constituting the patches (elements). Thus the nodal acoustic information from ACTRAN is the "true" reference source we are seeking for. An example of these "true" reference is shown in Figures 4.14(a) for velocity field. However, the expected reference is the one for which the "true" reference is averaged on patches. An example of these "expected" results is shown in Figure 4.14(b). In the following, the comparison between iPTF results and a reference will be done using these "expected" results in the validation process.

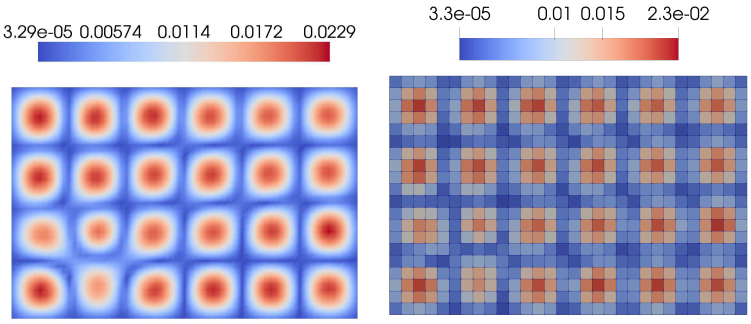

(a) ACTRAN Node Velocity (m/s) (b) Patch Velocity (m/s)

Figure 4.14: Colormaps of the velocity field obtained from ACTRAN at 1000Hz. (a): "True" reference expressed at nodes; (b): "Expected" reference expressed on patches.

4.3.3.2 Evaluation of objective correlation metrics

At this juncture, all the available information required for the validation process are available. The iPTF identified results for each of the acoustic indicators are compared with the reference using comparison metrics detailed in Appendix C. The validation process here is to check correlation between two vectors of acoustic quantities at specific frequencies across the full spatial domain of the plate. These two vectors to compare are namely; the iPTF identified vector $\mathbf{x}_{id}$ and "expected" reference computed vector $\mathbf{x}_{ref}$. The term vectors used here are basically the set of scalar values (complex or real) of the acoustic quantities carried by each patch of the discretized plate (source patches) stacked together to form 600×1 column-set.

The $\mathcal{CHA}$ is a metric for correlating two vectors. It indicates the collinearity of the two vectors. The $\mathcal{CHA}$ assumes a value between zero and unity. If the two vectors lie on the same straight line, the $\mathcal{CHA}$ value is 1 which indicates perfect correlation. If the value of $\mathcal{CHA}$ is less than 1, then the two vectors do not lie on the same straight line and indicates weak correlation. A zero value indicate no correlation, which implies that the two compared vectors are orthogonal to, or linearly independent of one another.

The $\mathcal{CHA}$ is only useful for a qualitative comparison and thus, it is incapable to detect scaling errors and discrepancies that exist between the compared vector components. The $\mathcal{CI}$ is used to detect such discrepancies between the levels of the two vectors and thus acts as form of relative error measure. The $\mathcal{CI}$ correlation measure is a more stringent type and it is unity only when the compared vectors are equally the same. It values range between 1 and -1. For instance a $\mathcal{CI}$ value of 1 indicates that the iPTF vector and the reference vector have the same values

between their matching degree of freedoms (dofs) and as such they are identical in both phase and amplitude. A $\mathcal{CI}$ value of -1 indicates that the two compaired vectors have the same values in magnitude but opposite in sign. If abs($\mathcal{CI}$) < 1, the iPTF vector and the reference vector have different values between their matching dofs that is they have different vector components. The $\mathcal{CI}$ can be used for any data type of the compared vectors, be it vectors or single scalar values of either complex or real number types.

Although $\mathcal{CI}$ offers information about the differences in the components of the two vectors compared, it does not reveal the cause origin of the difference. For example, for complex quantities, it is intriguing to know which part dominates, that is the real or the imaginary parts of the vector. And this information is not explicitly revealed by $\mathcal{CI}$ metric. The $\mathcal{CEA}$ and the $\mathcal{SEA}$ are the best known to use in this case.

The $\mathcal{CEA}$ criterion varies between -1 and 1, the absolute value indicating the amount of correlation and the sign indicating the relative phase between the acoustic indicators that are being correlated. For instance a value of -1 indicates correlation with opposite sign in their real components. A value of 1 indicates correlation with the same sign in their real components and 0 value indicates no correlation. Likewise, the $\mathcal{SEA}$ also varies between -1 and 1, its absolute value indicates the amount of orthogonality and the sign indicating the relative phase between the acoustic indicators being compared. A $\mathcal{SEA}$ value of -1 indicates orthogonality with opposite phase in their imaginary components. A value of 1 indicates orthogonality with the same phase in their imaginary components. A $\mathcal{SEA}$ value of 0 implies that the two vectors are not orthogonal to each other but parallel (collinear).

Figure 4.15 shows the metrics described above applied to the velocity fields on the surface of the plate for both iPTF methods.

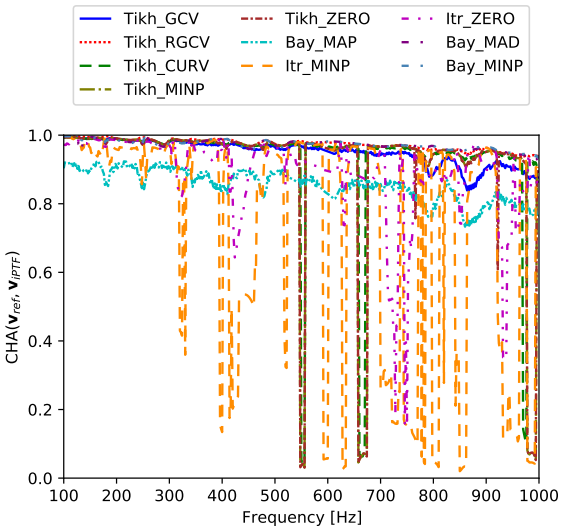

(a) m-iPTF $\mathcal{CHA}$

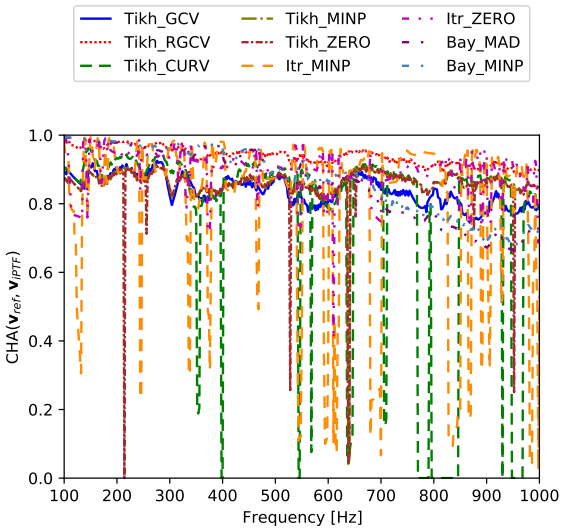

(b) u-iPTF $\mathcal{CHA}$

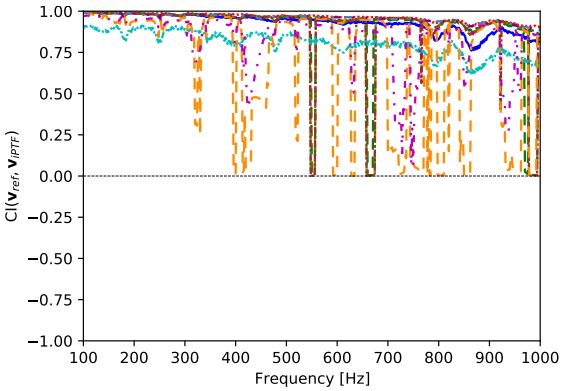

(c) m-iPTF $\mathcal{CI}$

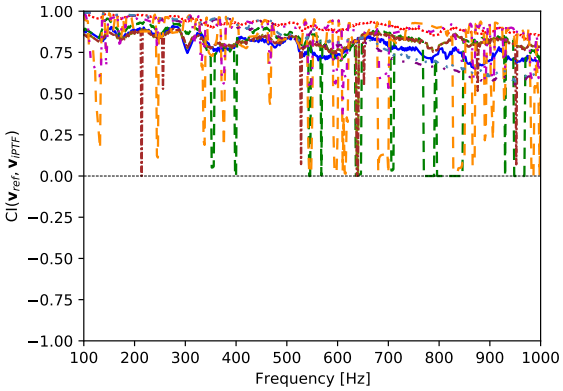

(d) u-iPTF $\mathcal{CI}$

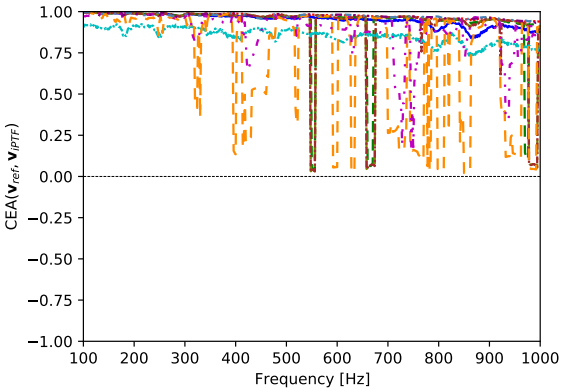

(e) m-iPTF $\mathcal{CEA}$

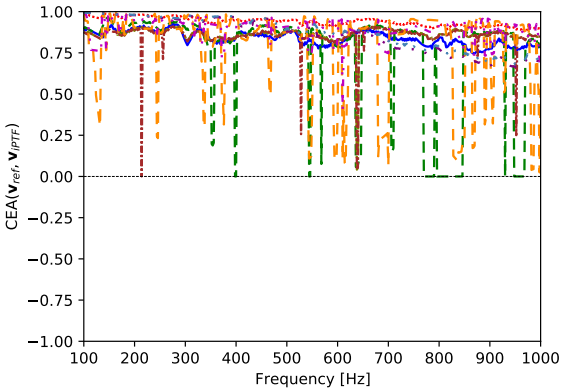

(f) u-iPTF $\mathcal{CEA}$

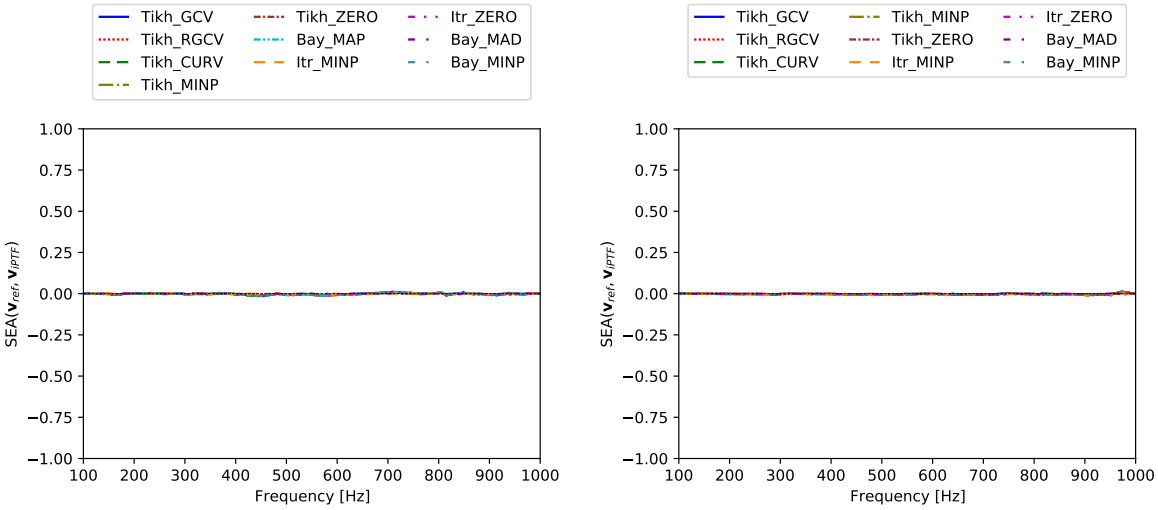

(g) m-iPTF $\mathcal{SEA}$ (h) u-iPTF $\mathcal{SEA}$

Figure 4.15: Plots of correlation metrics used in the comparison of the source velocity identified by iPTF and source velocity computed on the plate (reference) for the full frequency spectrum of study.

The results presented in Figure 4.15 exhibit some "drop-spikes" at frequencies which happens to be at eigen-frequencies of the acoustic cavity modes. These noticed "drop-spikes" manifest themselves in the $\mathcal{CI}$ plots of Figures 4.15(c) and (d) and $\mathcal{CEA}$ plots of Figures 4.15(e) and (f) for both u-iPTF and m-iPTF cases. The situation is different with $\mathcal{SEA}$ plots of Figures 4.15(g) and (h), where there are virtually no 'drop-spikes'. This implies that all the identified velocity from each of the regularization techniques have their imaginary component more strongly correlated to the reference than their corresponding real parts counterpart.
Therefore, when comparing all the available metrics one can conclude that $\mathcal{CI}$ is the most meaningful metric. Indeed, as $\mathcal{SEA}$ does not exhibit major differences between regularization approaches, $\mathcal{CEA}$ is highly comparable to $\mathcal{CI}$. Compared to $\mathcal{CHA}$, $\mathcal{CI}$ gives more information about sign and level. For all these reasons, only $\mathcal{CI}$ will be used in the following to compare identified maps to reference.

4.3.3.3 Analysis of $\mathcal{CI}$ metric

The $\mathcal{CI}$ metric is plotted as a function of frequency in Figure 4.16 for the three kinds of identified maps (velocity, pressure and intensity) for each regularization approach and for both m-iPTF and u-iPTF. The "drop-spikes" previously noticed are visible whatever the kind of maps and for both m-iPTF and u-iPTF, but only for `Tikh_ZERO`, `Tikh_MINP`, `Tikh_CURV`, `Itr_MINP` and `Itr_ZERO` regularization strategies. At these frequencies, these approaches fail to produce a good regularized solution. As pressure and intensity maps are obtained from identified velocity maps the presence of these "drop-spikes" are expected for all kinds of maps.

The "drop-spikes" phenomenon has already been observed and explained by Totaro *et. al.* [185] in case of `Tikh_CURV`. In that case, they occur at the eigen-frequencies of the virtual cavity. Depending on the chosen virtual boundary conditions, the number of eigen-frequencies changes and so the number of "drop-spikes". This is why more "drop-spikes" can be observed for u-iPTF than for m-iPTF. However, even more "drop-spikes" are visible for `Tikh_ZERO`, `Tikh_MINP`, `Itr_MINP` and `Itr_ZERO` regularization approaches. These particular frequencies are not explained by eigen-frequencies of the virtual cavity or the plate nor by a high condition number as shown in Figure 4.9. They evidence some instabilities of the iterative approaches compared to the deterministic or stochastic approaches.

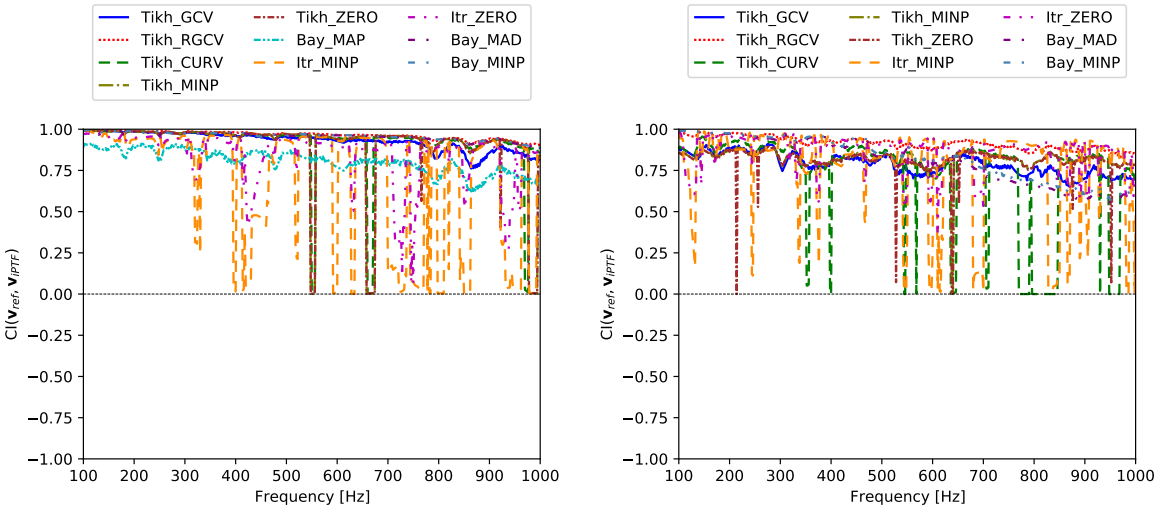

(a) m-iPTF - Velocity field

(b) u-iPTF - Velocity field

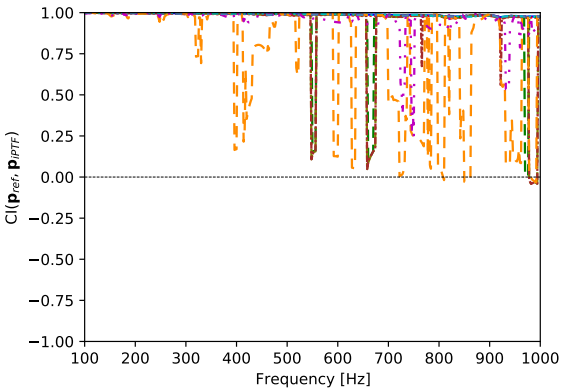

(c) m-iPTF - Pressure field

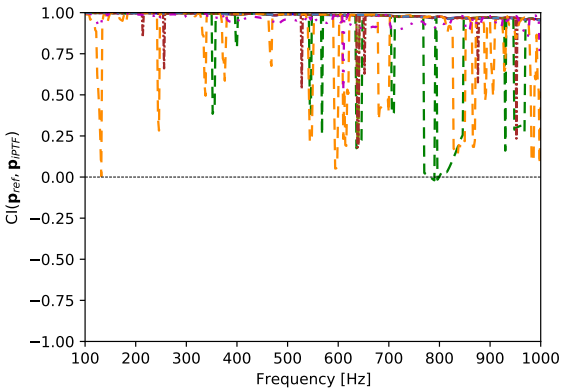

(d) u-iPTF - Pressure field

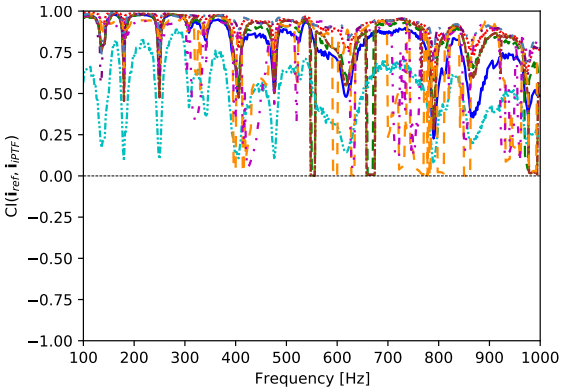

(e) m-iPTF - Intensity field

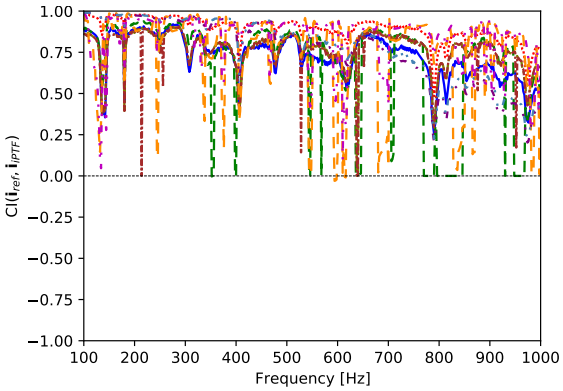

(f) u-iPTF - Intensity field

Figure 4.16: $\mathcal{CI}$ correlation metric used in the comparison of identified field (velocity, pressure or intensity) and the reference computed on the plate as a function of frequency for each regularization approach.

Figure 4.16 shows that $\mathcal{CI}$ metric slightly decreases with frequency as expected (meshing is frequency dependent). However, what is less expected is the fact that the identified pressure fields are more correlated to the reference than the velocity fields. The reason behind this observation is that these identified pressures obtained according to Equations (2.31) and (2.23) are made of two pressure vectors. The identified velocity only appears in one of them and is multiplied by the computed impedance matrix $\mathbf{Z}_{ij}$. This matrix acts as a filter that smooths the identified velocities to yield such identified pressure. The intensity maps, for their part, are the most difficult maps to retrieve. This is due to the fact that they are the last maps to be computable, from the product of the velocity and the pressure maps. In that sense, the errors committed for the velocity and the pressure maps sum up.

Lastly, it can be observed in Figure 4.16 that m-iPTF tends to have better results than u-iPTF. This is not a clear result and it depends on the regularization approach. To have a better understanding of the capabilities of the proposed regularization approaches, results of the correlation analysis performed on the u-iPTF and m-iPTF problems are summarized in Table 4.1. These results were obtained by averaging the $\mathcal{CI}$ correlation metric from the acoustic quantities over the full frequency spectrum for each regularization parameter-selection-criteria used.

Acoustic quantity	Metrics	Regularization Parameter Selection Criteria									
		Tikh _GCV	Tikh _RGCV	Tikh _CURV	Tikh _MINP	Tikh _ZERO	Bay _MAP	itr _MINP	itr _ZERO	Bay _MAD	Bay _MINP
Velocity	m-iPTF	**0.93**	**0.96**	**0.92**	**0.91**	**0.90**	0.81	0.70	0.84	**0.96**	**0.96**
Pressure	m-iPTF	**0.99**	**0.98**	**0.96**	**0.94**	**0.94**	**0.99**	0.79	**0.95**	**0.99**	**0.99**
Intensity	m-iPTF	0.79	**0.91**	0.83	0.82	0.82	0.50	0.71	0.77	**0.91**	**0.92**
Velocity	u-iPTF	0.79	**0.92**	0.72	0.82	0.81	/	0.77	0.86	0.81	0.82
Pressure	u-iPTF	**0.98**	**0.98**	0.87	**0.98**	**0.98**	/	0.88	**0.96**	**0.98**	**0.98**
Intensity	u-iPTF	0.73	0.89	0.68	0.77	0.76	/	0.76	0.84	0.76	0.78

Table 4.1: Frequency averaged $\mathcal{CI}$ correlation metric for each regularization approach and for both m-iPTF and u-iPTF. Bold font shows values higher than 0.9.

It is clear from Table 4.1 that m-iPTF globally provides better results than u-iPTF. Also, as already noticed, the pressure fields are almost perfectly retrieved whatever the regularization approach (except `Itr_MINP`) whereas the quality of the identified intensity field strongly depends on the regularization approach. Analyzing Table 4.1, three approaches stand out from others in terms of quality of their results: `Tikh_RGCV`, `Bay_MAD` and `Bay_MINP`.

Figure 4.17 and Figure 4.18 show respectively the evolution of $\mathcal{CI}$ metric as a function of frequency and examples of identified maps (for velocity, pressure or intensity) compared to the corresponding expected references at 300 Hz for the three selected regularization approaches and both m-iPTF and u-iPTF.

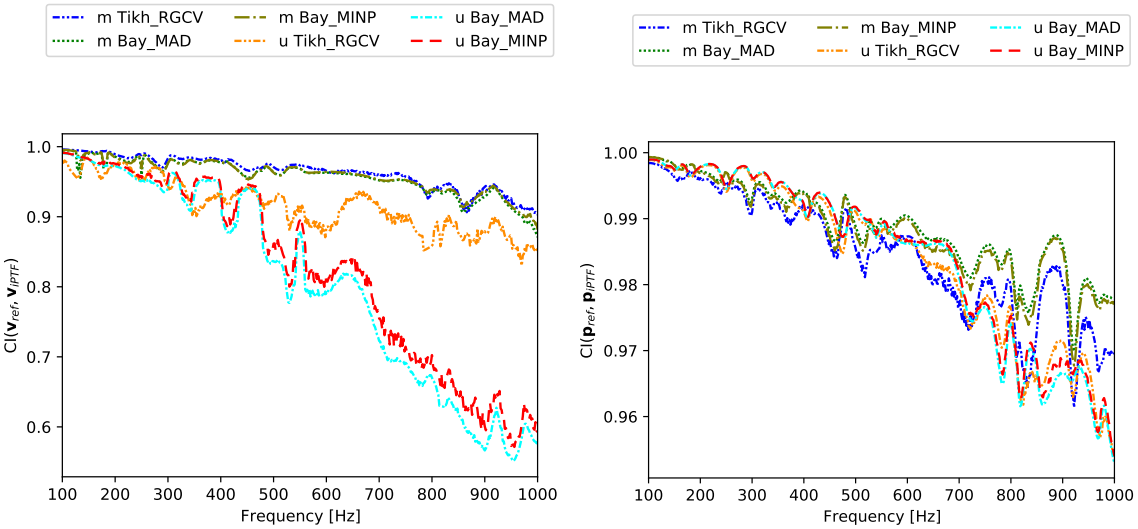

(a) Velocity field

(b) Pressure field

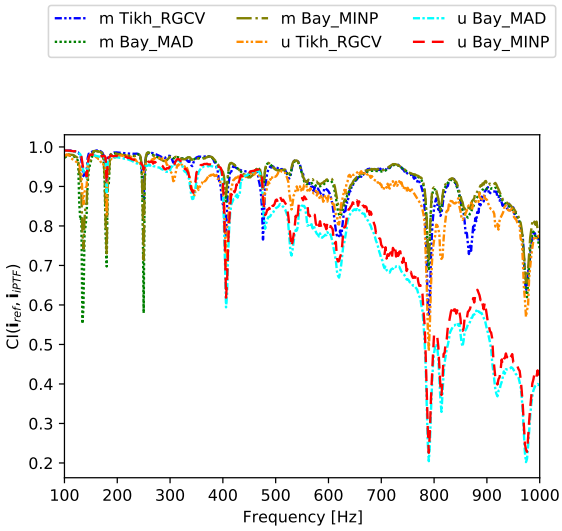

(c) Intensity field

Figure 4.17: $\mathcal{CI}$ correlation metric for the three selected regularization approaches (`Tikh_RGCV`, `Bay_MAD` and `Bay_MINP`) for both m-iPTF and u-iPTF as a function of frequency.

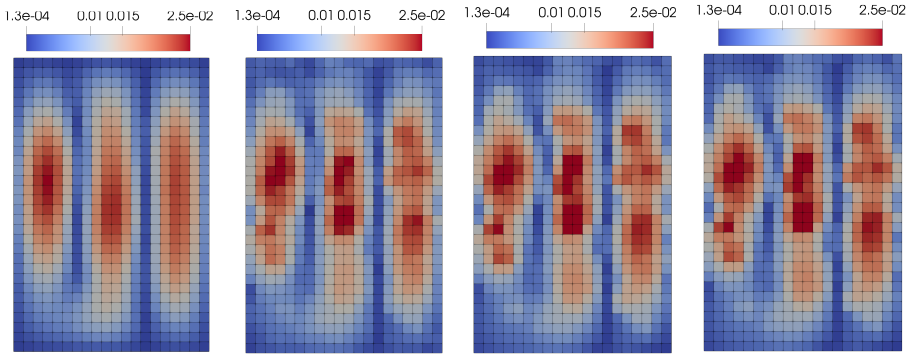

(a) Reference Velocity (m/s) (b) m-iPTF RGCV Velocity (m/s) (c) m-iPTF Bay_MINP Velocity (m/s) (d) m-iPTF Bay_MAD Velocity (m/s)

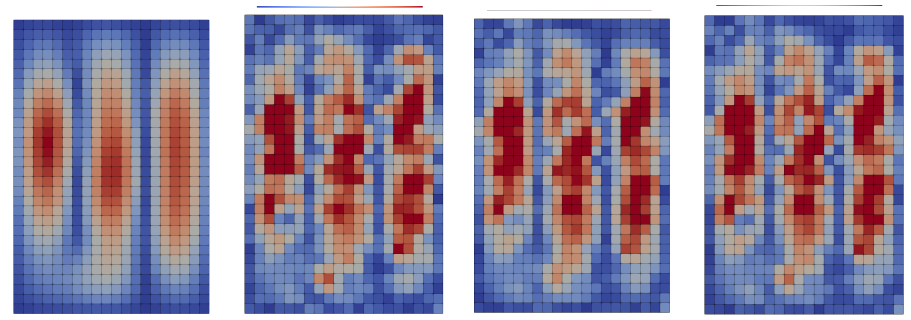

(e) Reference Velocity (m/s) (f) u-iPTF RGCV Velocity (m/s) (g) u-iPTF Bay_MINP Velocity (m/s) (h) u-iPTF Bay_MAD Velocity (m/s)

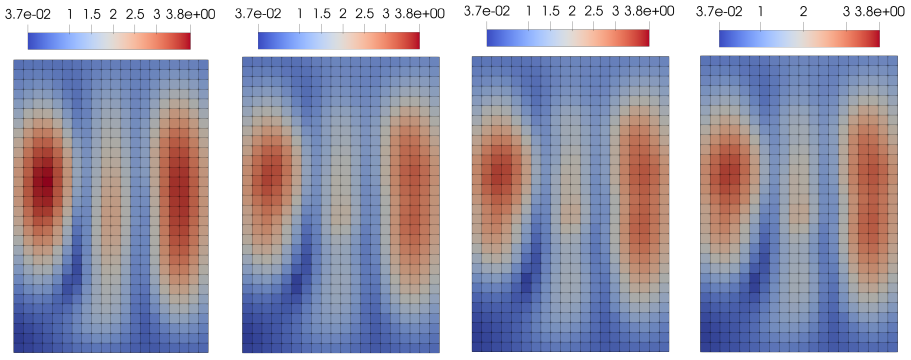

(i) Reference Pressure (Pa) (j) m-iPTF RGCV Pressure (Pa) (k) m-iPTF Bay_MINP Pressure (Pa) (l) m-iPTF Bay_MAD Pressure (Pa)

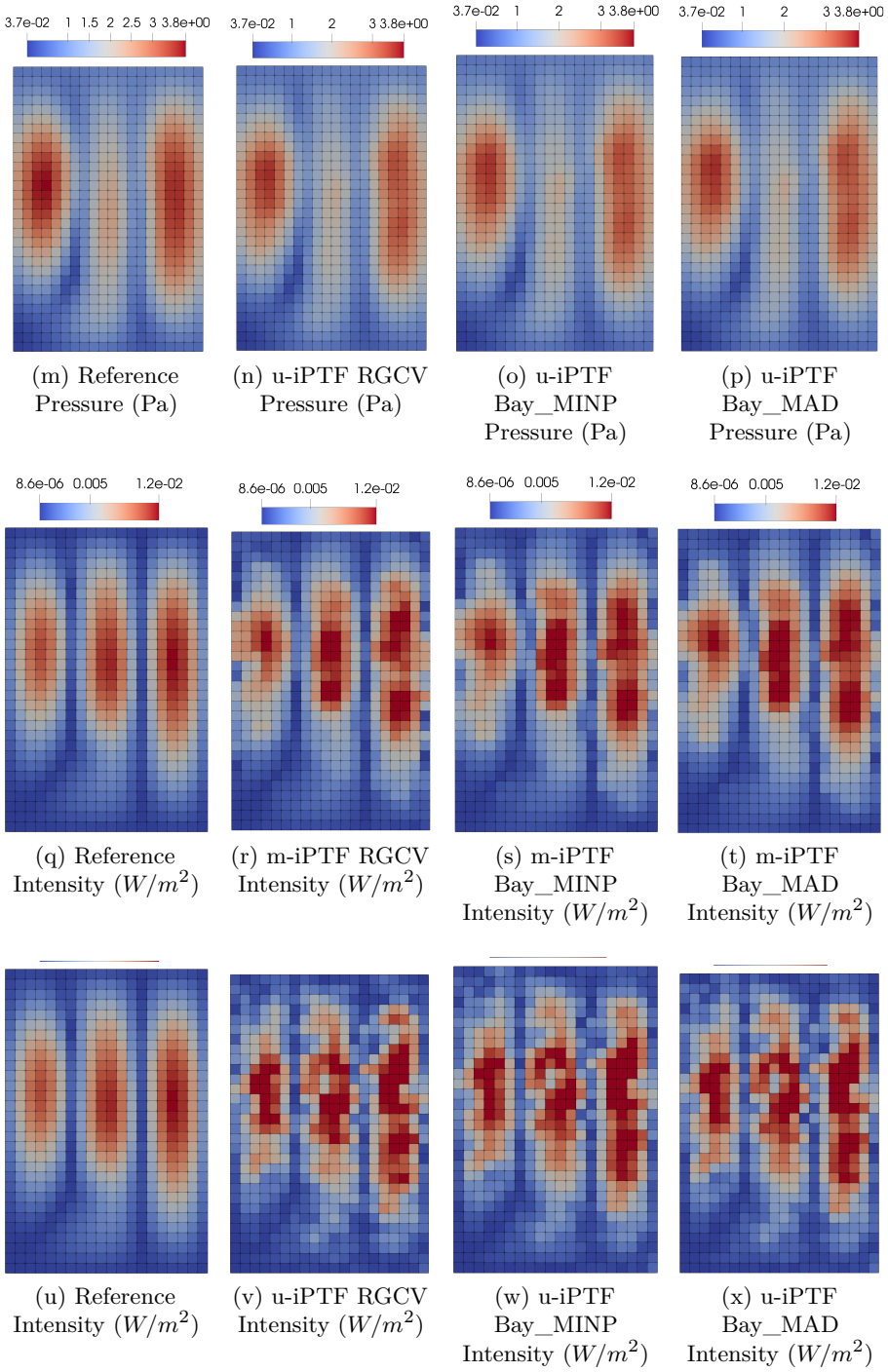

(m) Reference Pressure (Pa) (n) u-iPTF RGCV Pressure (Pa) (o) u-iPTF Bay_MINP Pressure (Pa) (p) u-iPTF Bay_MAD Pressure (Pa)

(q) Reference Intensity (W/m^2) (r) m-iPTF RGCV Intensity (W/m^2) (s) m-iPTF Bay_MINP Intensity (W/m^2) (t) m-iPTF Bay_MAD Intensity (W/m^2)

(u) Reference Intensity (W/m^2) (v) u-iPTF RGCV Intensity (W/m^2) (w) u-iPTF Bay_MINP Intensity (W/m^2) (x) u-iPTF Bay_MAD Intensity (W/m^2)

Figure 4.18: Spatial colormap distribution of local acoustic indicators identified by both m-iPTF and u-iPTF with `Tikh_RGCV` `Bay_MINP` and `Bay_MAD` at the and the reference computed result at a frequency of 300 Hz.

It can be noticed from Figure 4.18 that except for the pressure identification results, the u-iPTF identified velocity and intensity results are both noisier than the m-iPTF results. Also, the results identified with the `Tikh_RGCV` criteria are more correlated to the reference than the `Bay_MINP`, `Bay_MAD` results. This observation is also confirmed by correlation metric results displayed in Figure 4.17 and global indicators shown in Figure 4.19.

In conclusion, a thorough study of the results from the numerical validation using the

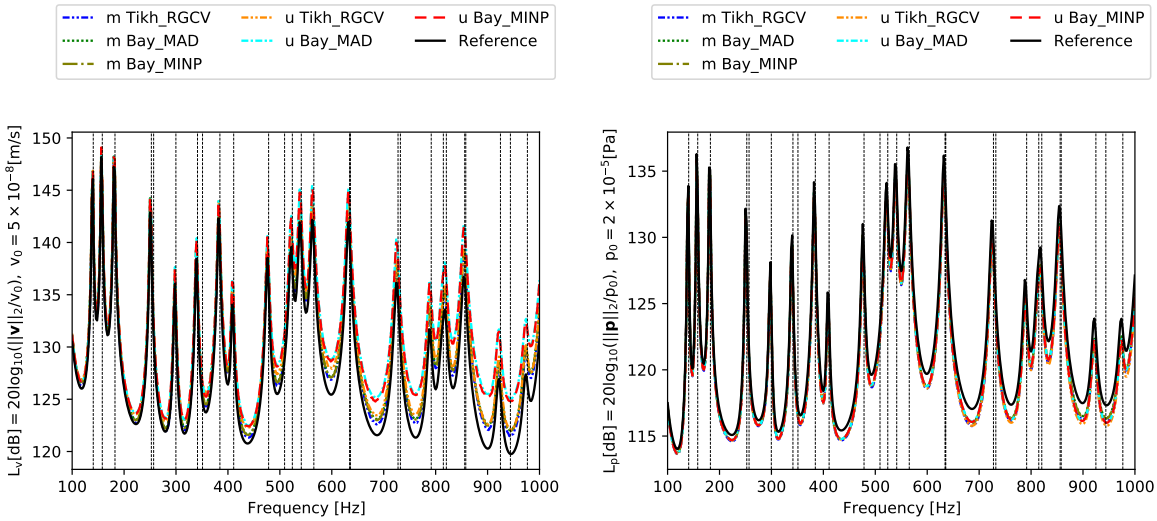

(a) Squared velocity (dB)

(b) Squared pressure (dB)

(c) Power (dB)

(d) Acoustic Efficiency

Figure 4.19: Plots of global acoustic indicators identified by m-iPTF with `Tikh_RGCV`, `Bay_MINP` and `Bay_MAD` at the and the reference computed result for the full frequency spectrum of study.

correlation metrics $\mathcal{CHA}$, $\mathcal{CEA}$, $\mathcal{CI}$ and $\mathcal{SEA}$ has revealed minor differences in the regularization selection criteria considered. The selection criteria `Tikh_RGCV`, `Bay_MINP` and `Bay_MAD` have emerged as the best strategies to be used in regularization for both m-iPTF and u-iPTF methods but m-iPTF provides systematically better results than u-iPTF. It is to be noticed that the computation involved in `Bay_MINP` and `Bay_MAD` results were highly costly. Based on these reasons the zeroth-order Tikhonov method with RGCV (`Tikh_RGCV`) as the strategy for choosing the optimum regularization parameter is selected, at this stage, as the most suitable regularization technique for the iPTF method in solving this idealistic problem case. Therefore, this approach is further explored in other realistic cases as presented in Section 4.4 and 4.5.

4.4 `CASE B` - noisy environment

In real experiments, measurements are carried out in a noisy environment characterized by a Signal-to-Noise Ratio (SNR). As for any inverse approaches, this background noise can highly affect the quality of the iPTF results. The aim of this section is to explore the use of the zeroth-order-Tikhonov-RGCV based regularization technique (`Tikh_RGCV` of Equation (3.73)) to solve a iPTF problem in presence of a disturbing noise. As in Section 4.3, no such real experiment was carried out but numerical experiment conducted. As explained in [232], the noisy measurements are computed using an additive and a multiplicative perturbation described by two zero-mean Gaussian random variables. The level of perturbations is set according to a SNR. A mathematical description of how to simulate the noise is presented in Algorithm 5. Three different situations are used in the following: good measurements (SNR=20 dB), acceptable measurements (SNR=10 dB) and poor quality measurements (SNR=3 dB).

Figure 4.20 shows an example of noisy pressure for SNR values of 3 dB, 10 dB and 20 dB respectively. The multiplicative perturbation, representing an error due to the acquisition of the signal, is computed from the pressure level measured for a particular microphone at a particular frequency. This why the multiplicative perturbation exhibits almost the same evolution than the noise-free pressure but shifted according to the SNR value. The additive perturbation, representing the background noise, is expected to have the same level, whatever the frequency or the sensor. The additive perturbation is then defined with respect to the "noise-free" median value of the quantity under interest (pressure or velocity) computed from all the sensors and all the frequencies. This is why the additive perturbation is parallel to the median value but shifted according to the SNR value. This process is repeated for all the positions of the sensors (pressure and/or velocity) used as an input for the application of the iPTF methods.

As was done in Section 4.3, the `Tikh_RGCV` behavioural process is shown using the function plots and the L-curve plot. It can be seen from the function plot of Figure 4.21 that optimum regularization parameter is located at the corner at the local minima of the `RGCV` curve as expected. Also as the noise level increases (decrease in the SNR value) the `Tikh_RGCV` curve becomes less convex and the chosen regularization parameter value increases as well.

As already mentioned, the regularization acts as a buffer system which regulates the noise in the measurement and the solution smoothness. Thus, the noisier the measurement data $\mathbf{y}$ the more the filtering (which means the higher value of regularization parameter λ^2) and vice-versa to obtain a satisfactory solution. This effect is manifested in the L-curve plot of Figure 4.21(b). The residual norm which signifies the level of noise in the $\mathbf{y}$ increases as SNR value decreases but the difference in the smoothening level of noise in the regularized solution is small.

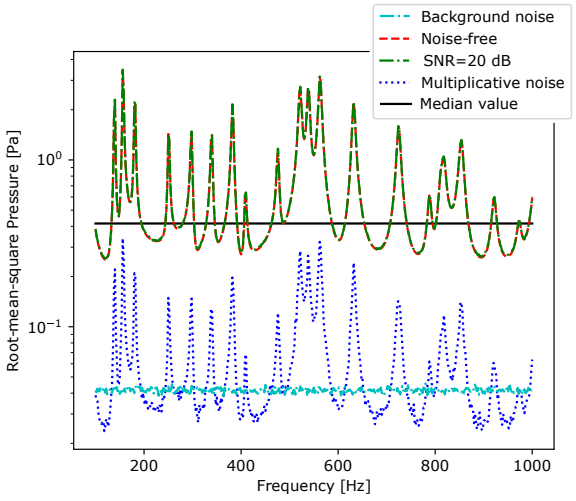

(a) SNR=20 dB: good measurements

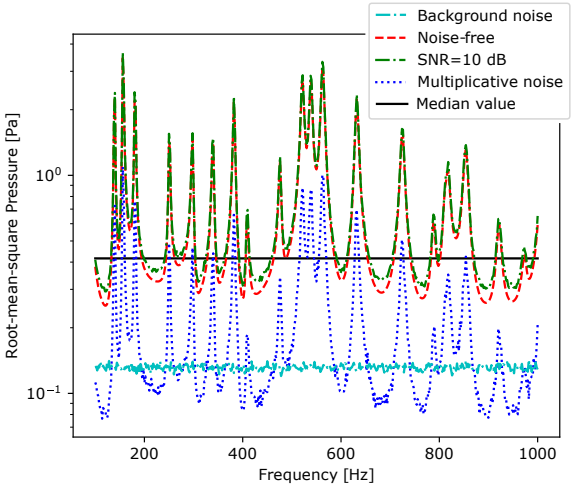

(b) SNR=10 dB: acceptable measurements

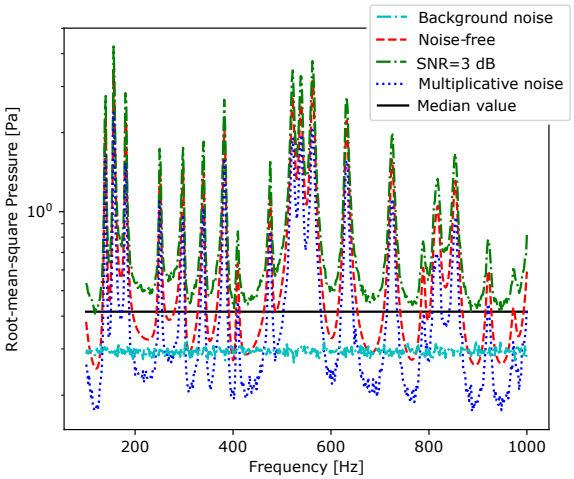

(c) SNR=3 dB: poor quality measurements

Figure 4.20: Root-mean-square (rms) spectra of the noisified acoustic measurement according to [232]

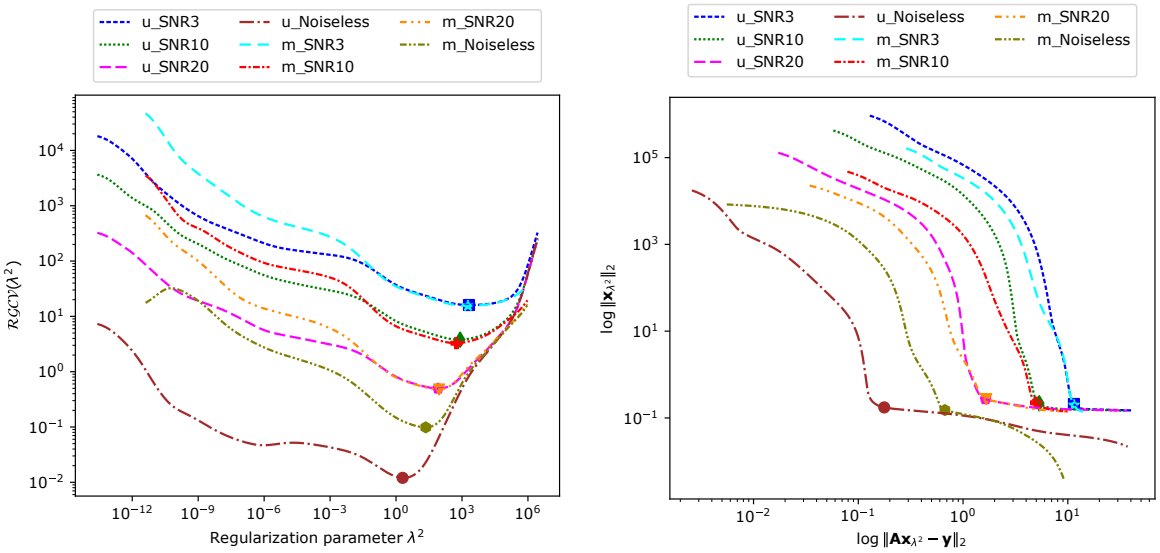

(a) Function plot (b) The L-curve plot

Figure 4.21: Process results at 500 Hz

In order to have a clear picture for the `Tikh_RGCV` function behaviour, the full frequency representation of the results is displayed in Figure 4.22.

From Figure 4.22(a) and (b) it is observed that the optimum value of λ^2 increases as the

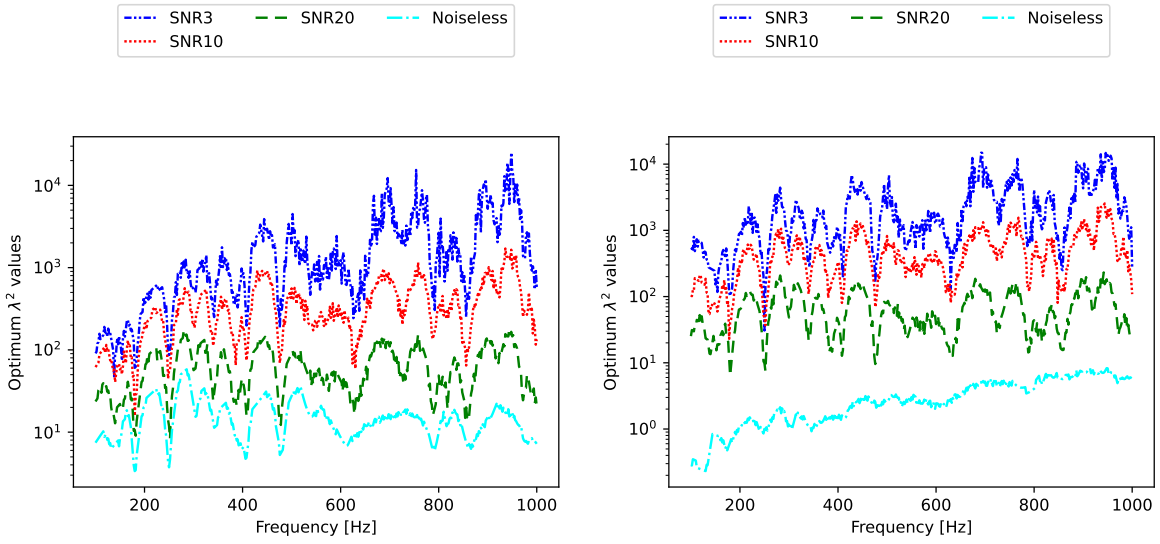

(a) m-iPTF (b) u-iPTF

Figure 4.22: Optimum regularization parameter λ^2_{opt} spectra for m-iPTF and u-iPTF method

level of noise increases (or SNR decreases) across the full frequency spectra. This is a typical of regularizing with Tikhonov technique that is the noise in the measurement $\mathbf{y}$ implies more filtering (higher values of λ^2).

It is to be noticed that the condition number spectrum as shown in Figure 4.9 is the same for all the noise configurations. The reason is that the noise was added only to the measurement data ($\widehat{\mathbf{p}}_k$, $\widehat{\mathbf{p}}_m$ and $\widehat{\mathbf{v}}_k$ of Equation (3.3)) and not to the impedance transfer matrix $\mathbf{Z}_{mj}$ of Equation (3.3) and as a result the matrix $\mathbf{A}$ of Equation (3.3) remains the same whilst $\mathbf{y}$ changes.

The quantification of the quality of the results for these different noise configurations is in-line with the validation process already introduced in Section 4.3.3. Also, the reference and the correlation metrics are the same as previously presented. The evolution of the $\mathcal{CI}$ metric as a function of frequency and for both m-iPTF and u-iPTF is shown in 4.23.

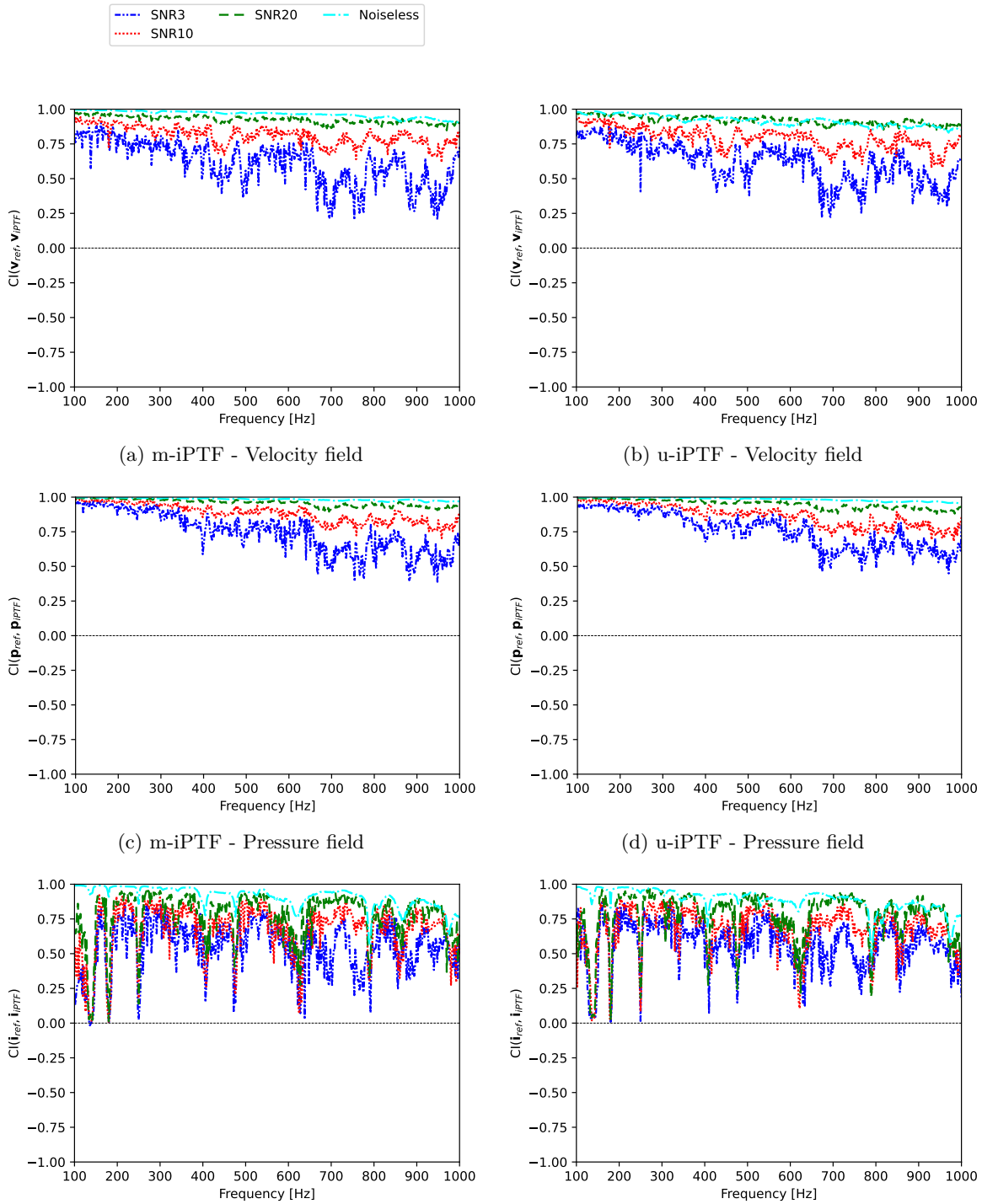

(a) m-iPTF - Velocity field

(b) u-iPTF - Velocity field

(c) m-iPTF - Pressure field

(d) u-iPTF - Pressure field

(e) m-iPTF - Intensity field

(f) u-iPTF - Intensity field

Figure 4.23: Correlation metric $\mathcal{CI}$ used in the comparison of the source fields identified by iPTF and the ones computed on the plate (reference) for different SNR values and for both m-iPTF and u-iPTF as a function of frequency.

It can be noticed from Figure 4.23 that the correlation metric $\mathcal{CI}$ using the velocity as the acoustic indicator is "noisier" and lower as the SNR level decreases. This was an expected result as the optimum regularization parameter λ^2_{opt} increases with the SNR, as shown in Figure 4.22. However, both the iPTF approaches are robust and can be used with satisfactory results with a classical SNR of 10 dB. As already observed in the previous section, the pressure field is more correlated to the reference field than the velocity field and the intensity field is the most difficult quantity to retrieve.

In terms of regularization numerics, the DPC analysis of Section 3.2.2.2 about the iPTF problem must be diagnosed. The level of satisfaction of the DPC determines the state of regularization results. So basically, what the DPC is saying is that for the `Tikh_RGCV` strategy to produce a satisfactory results for any problem, on the average the rate at which the Fourier coefficients $\left|\mathbf{u}_i^{\mathrm{H}}\mathbf{y}\right|$ decay to asymptotic value along the increasing indices i must be faster than the singular values σ_i. And also the number of σ_i involved in the satisfaction of the above condition is a measure of the posednesss of the iPTF problem. The ill-posedness level defined according to the DPC (see Section 3.2.2.2) is plotted in Figure 4.24 as a function of frequency.

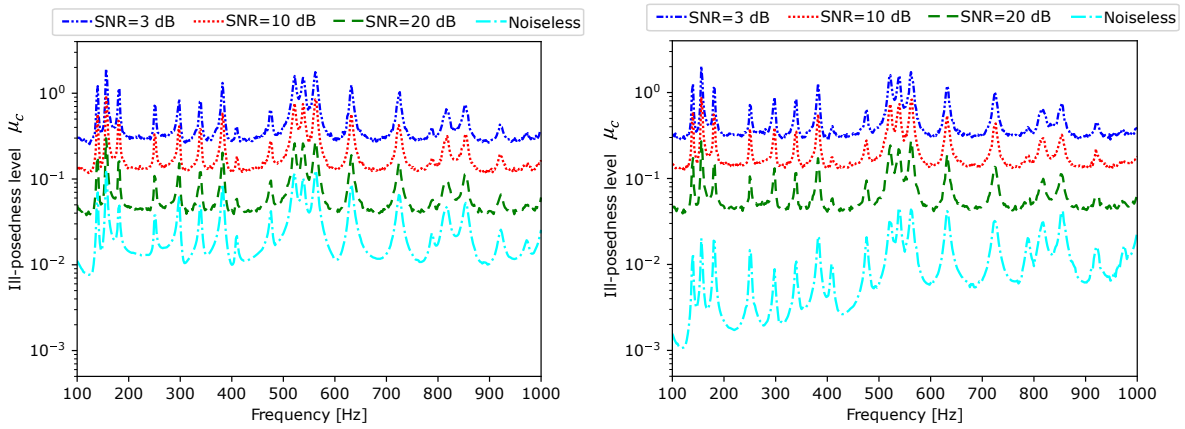

(a) m-iPTF Error in $\left|\mathbf{u}_i^{\mathrm{H}}\mathbf{y}\right|$ (b) u-iPTF Error in $\left|\mathbf{u}_i^{\mathrm{H}}\mathbf{y}\right|$

Figure 4.24: ill-posedness level μ_c as a function of frequency for the different noise configurations.

Figure 4.24(a) and (b) depict clearly that the error in $\left|\mathbf{u}_i^{\mathrm{H}}\mathbf{y}\right|$ increases as measurement data $\mathbf{y}$ becomes noisier (SNR value reduces) just as expected. It should be noted that though in the 'Noiseless' configuration contains only pure signal, the observed error is numerical in nature (a combination of discretization, modelling and approximation errors) whilst the other configurations have measurement noise in addition to these numerical errors. The ill-posedness level as shown in Figure 4.24(a) and (b) increases in accordance with the SNR values. Furthermore, the generated ill-posedness level from each of the noise configurations have their peak value occurring at the eigenfrequencies of the plate. This implies that close to the resonance frequencies of the plate the influence of the noise is highly amplified. With these observations, it can be concluded that the noisier the measurement data the more ill-posed the iPTF problem becomes and the regularized solution might be far from the reference.

The identification results for the different configurations are visually displayed in Figure 4.25 as colormaps on the spatial domain of the source along with the references.

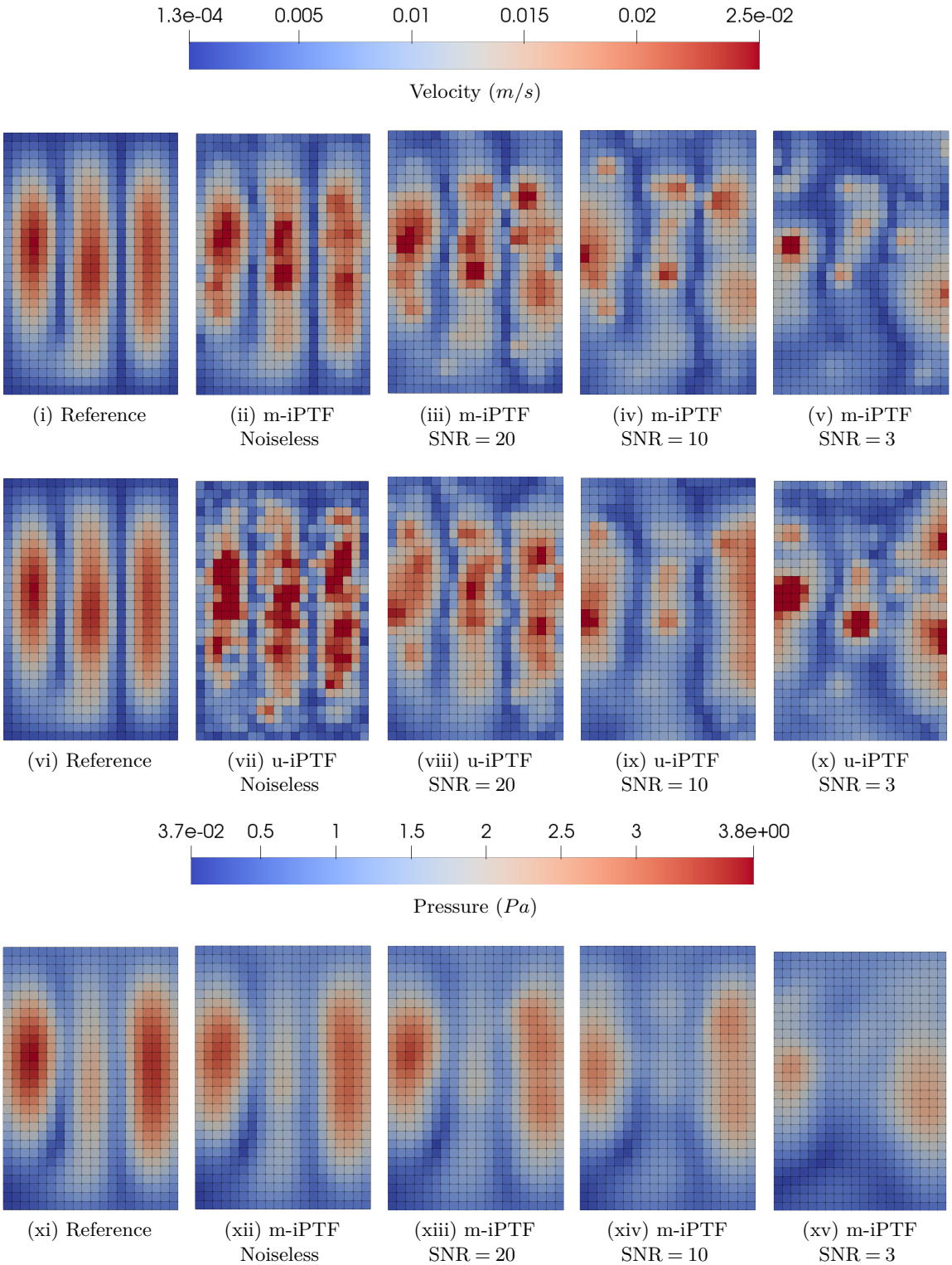

(i) Reference (ii) m-iPTF Noiseless (iii) m-iPTF SNR = 20 (iv) m-iPTF SNR = 10 (v) m-iPTF SNR = 3

(vi) Reference (vii) u-iPTF Noiseless (viii) u-iPTF SNR = 20 (ix) u-iPTF SNR = 10 (x) u-iPTF SNR = 3

(xi) Reference (xii) m-iPTF Noiseless (xiii) m-iPTF SNR = 20 (xiv) m-iPTF SNR = 10 (xv) m-iPTF SNR = 3

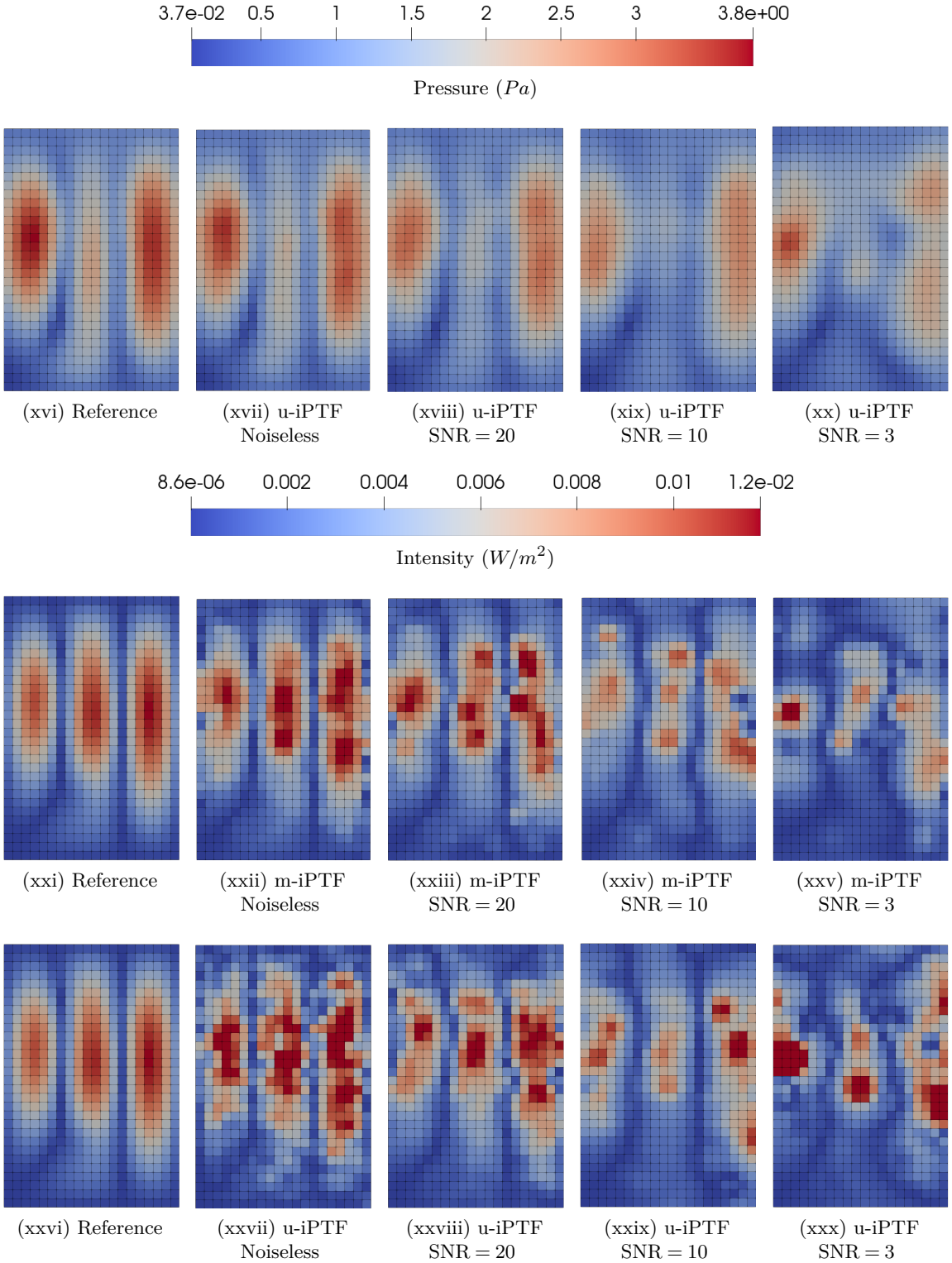

Figure 4.25: Spatial colormap distribution of local acoustic indicators identified by both m-iPTF and u-iPTF with `Tikh_RGCV` and the reference computed result at a frequency of 300 Hz for different noise configuration considered.

As the noise level is increased (from noiseless to SNR=3 dB) it can be noticed that in relation to the reference the detailed information on some region of interest of the plate is deteriorated and finally lost in the case of SNR=3 dB. Global quantities (Mean Square Velocity, Mean Square Pressure, Acoustic Power and Radiation Efficiency) for the full frequency range of study are depicted in Figure 4.26. It should be noted that the spectra from both the m-iPTF and u-iPTF

were found to be identical, hence only the m-iPTF spectra is presented.

It is observed that the global indicator aside Acoutic Power of Figure 4.26(c) revealed dif-

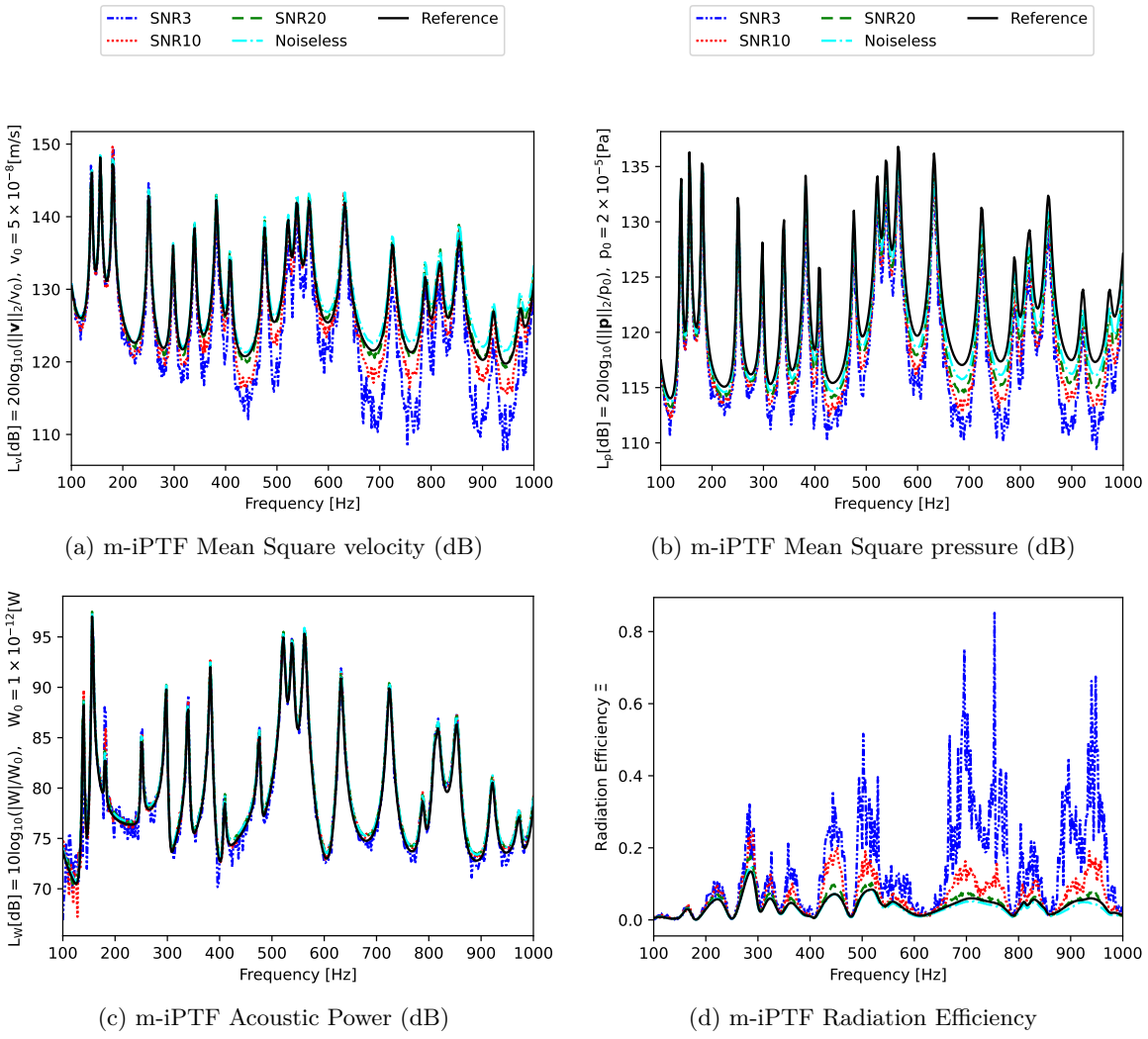

(a) m-iPTF Mean Square velocity (dB)

(b) m-iPTF Mean Square pressure (dB)

(c) m-iPTF Acoustic Power (dB)

(d) m-iPTF Radiation Efficiency

Figure 4.26: Plots of global acoustic indicators identified by m-iPTF with `Tikh_RGCV` and the reference computed result for the different noise configuration.

ferences between the reference and the noisy configurations. The estimated levels of Mean Square Velocity and Pressure are underestimated when the SNR is decreased. Conversely, the Radiation Efficiency is overestimated. However, a common SNR=10 dB leads to acceptable estimation of all the global indicators. The frequency zones where the differences are dominant of Figure 4.26(a), (b) and (d) are the same as those of ill-posedness spectra of Figure 4.24(a) and (b). This conforms exactly to what is expected, that is if the DPC condition is not fulfilled an unsatisfactory regularized result might be attained with Tikhonov technique.

In summary, the robustness nature of zeroth-order-Tikhonov-RGCV regularization (`Tikh_RGCV`) was tested using different noisy configurations. The analysis commenced with the functional behaviour of the `Tikh_RGCV` method about how it operates on noisy problems during its regularization process. The generated identified results are validated in a similar manner as in previous section using the correlation metrics. The differences in the obtained correlation results were explained using the DPC analysis. It is to be noticed that the satisfaction of DPC is paramount to the perfection level of the regularized solution. In overall, the obtained identified results for

quantifying the acoustic source are in fair agreement with the reference for the different noise configurations considered.

4.5 `CASE C` - under-determined configuration

The second realistic case study considered to check the robustness of `Tikh_RGCV` as the regularization tool for solving the iPTF problems is the under-determined problem. In these configurations the number of microphones inside the virtual cavity (referred here as field-points fp onwards) are varied in the following reduced order: 600, 480, 240 and 60. They are thus representing 100%, 80%, 40% and 10% of the number of identification patches. The numerical sets for these configurations are schematically illustrated in Figure 4.27. The rectangular wire-frame box represents the virtual cavity, the rectangular plate indicates source and the black disperse spots are the field-points.

As already presented in the previous subsections, to better understand the process involved

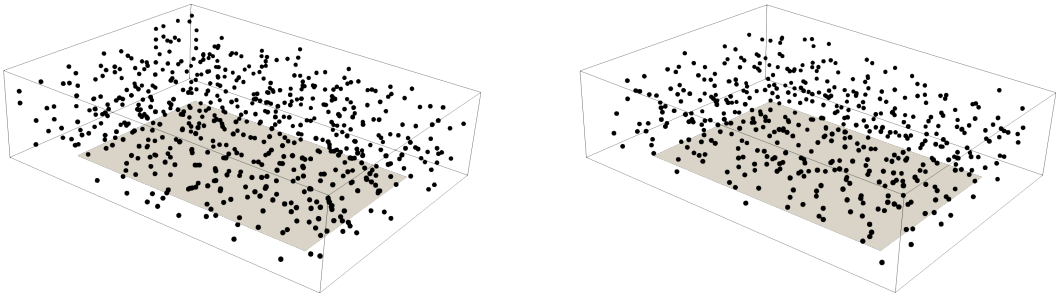

(a) $fp = 600$ (b) $fp = 480$

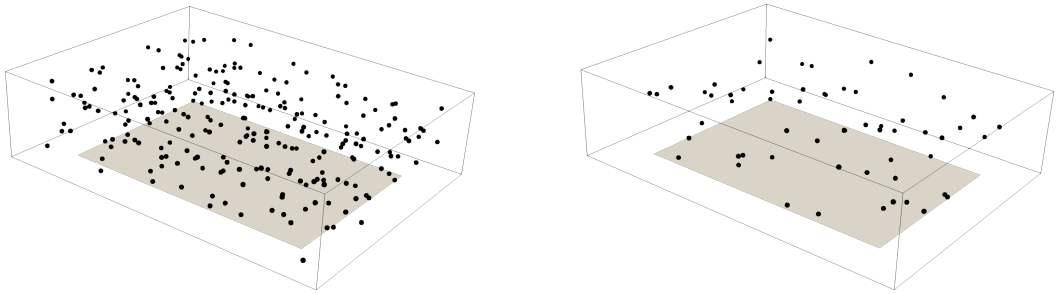

(c) $fp = 240$ (d) $fp = 60$

Figure 4.27: Settings of the different field-point configurations considered.

in `Tikh_RGCV` to arrive at its identification results, its functional behaviour needs to be known. The L-curve plot and the function plot of Figure 4.28 are example of process results of `Tikh_RGCV` applied to the different field-point configurations considered.

From Figure 4.28, the amplitude of the values in λ^2 spectrum increases as the number of field-points are decreased. This reflects exactly on the amplitude level of their singular values σ_i spectrum (as depicted in the condition number plots of Figure 4.31) which varies in accordance. It can be seen from the function plot of Figure 4.28 that optimum λ^2 is located at the corner L-curve of Figure 4.28(b) and at the local minima of the `RGCV` curve of Figure 4.28(a) as expected but there is no traceable link between the number of field points and the nature of the plots at 500 Hz.

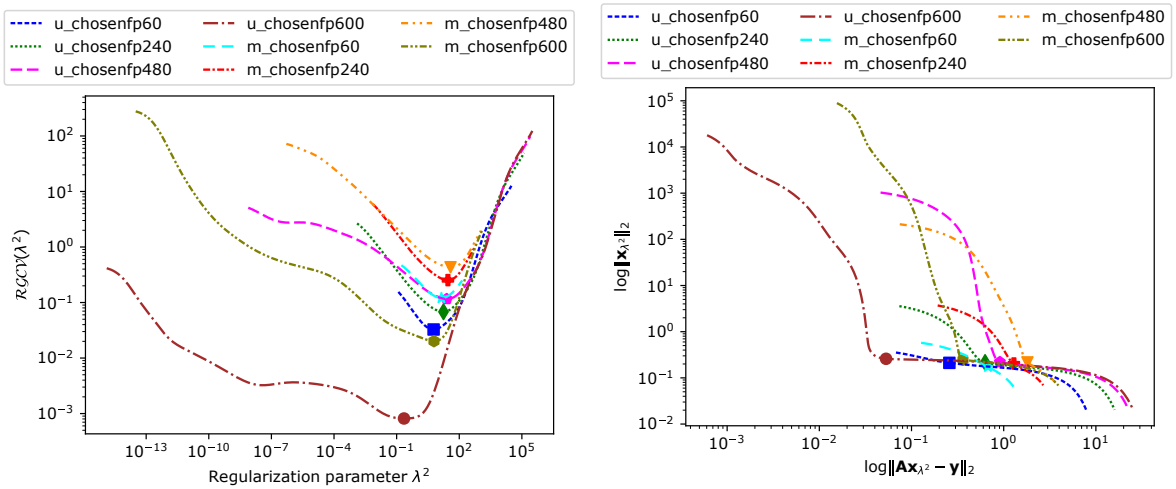

(a) Function plot (b) The L-curve plot

Figure 4.28: `Tikh_RGCV` behavioural results for the different field-point configurations at 500 Hz

A better perspective is to use a λ^2_{opt} spectra representation of the results as shown in Figure 4.29 for the full frequency range of study. The corresponding regularization parameter for both iPTF situations increases as the frequency increases, as can be observed. Also, there is a significant variance between the configuration *chosenfp*600 (equal-determined case) spectra and the others (under-determined cases). This early observation indicates that the u-iPTF and m-iPTF identified findings using `Tikh_RGCV` for the under-determined instances may be suspicious, and that additional investigation is required. However, at this point, there is currently insufficient evidence to support this claim.

The methodology used to determine the accuracy of the identified iPTF results for these

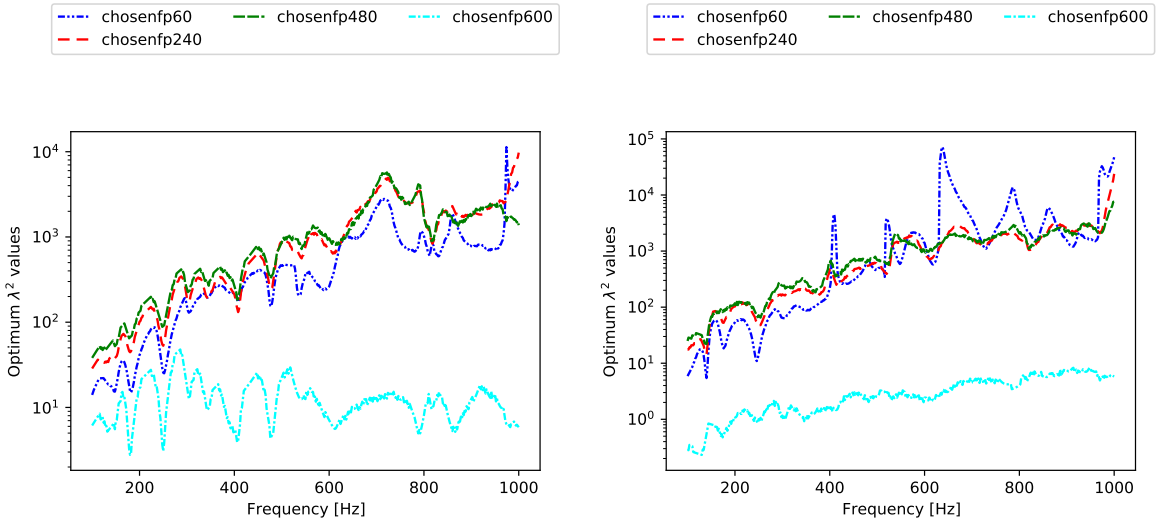

(a) m-iPTF (b) u-iPTF

Figure 4.29: Optimum regularization parameter λ^2 spectra for for the various field-point under-determined configurations using the `Tikh_RGCV` technique.

various field-point configurations follows the validation process described in Section 4.3.3. The reference and correlation measures are also the same as in the previous example. Figure 4.30 shows the initial set of numerical results.

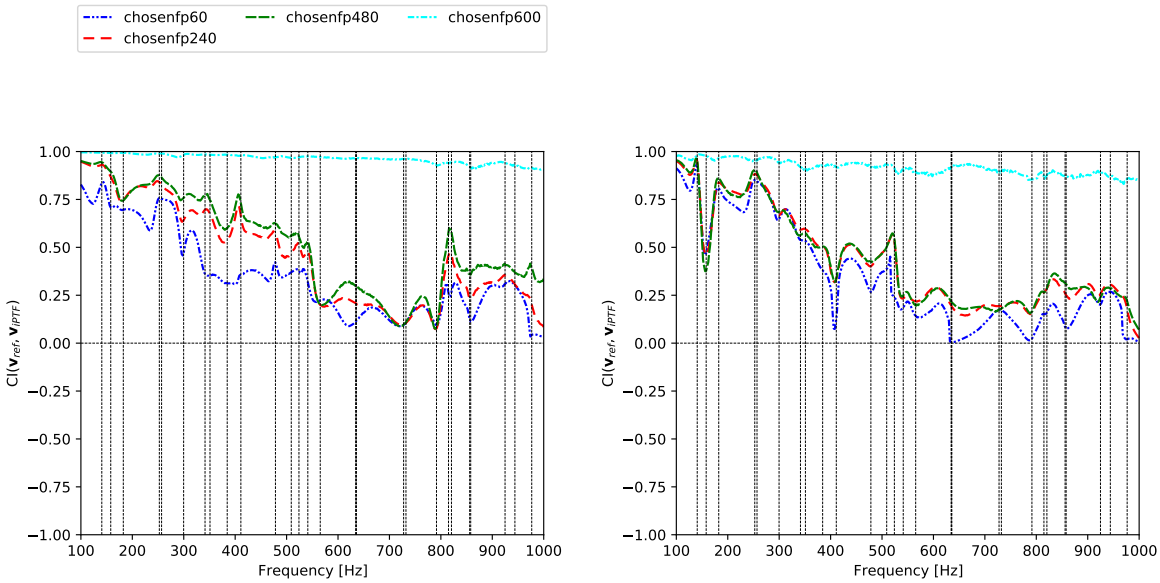

(a) m-iPTF $\mathcal{CI}$ (b) u-iPTF $\mathcal{CI}$

Figure 4.30: $\mathcal{CI}$ correlation results using the reference DFR velocity field and iPTF velocity field computed from the `Tikh_RGCV` considered for the various field-point configurations.

From Figure 4.30 in general the correlation metric values for the velocity quantity decreases along the frequency spectrum and as the number of field-points decreases. In general the identified iPTF velocity fields are poorly correlated to the reference for the under-determined cases. The causes for these observations can be better explained using the DPC analysis of Section 3.2.2.2. The first step is to examine the condition number of the transfer matrix **A** of Equation (3.4) of each of the field-point configurations as shown in Figure 4.31. It can be seen from Figure

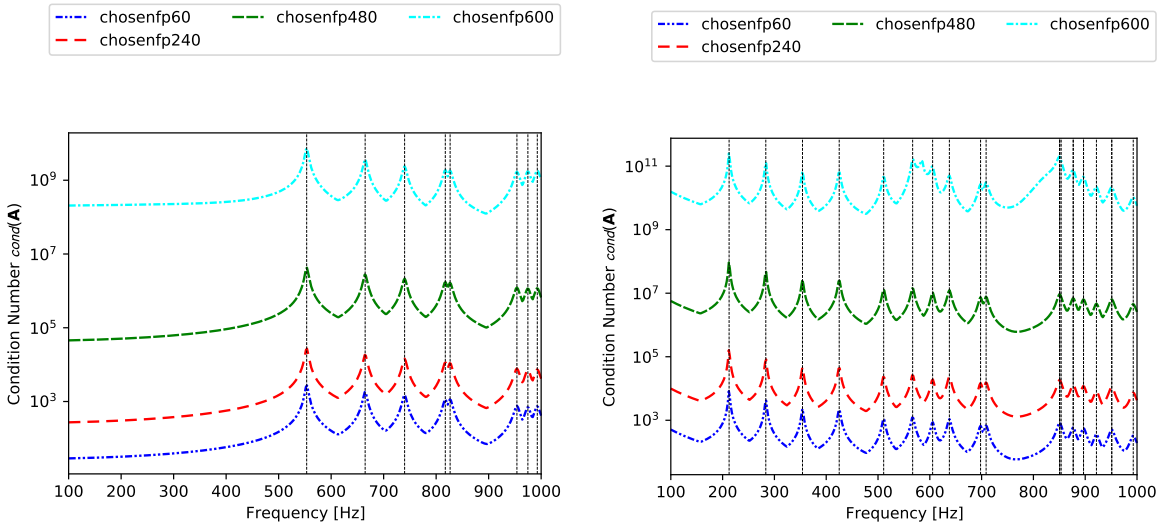

(a) m-iPTF cond($\mathbf{Z}_{mj}$) of Equation (3.2) (b) u-iPTF cond($\mathbf{Z}_{mj}$) of Equation (3.2)

Figure 4.31: Condition number spectrum of the $fp \times 600$ impedance transfer matrix **A** of Equation (3.3) for the different field-point configurations

4.31 that the more the field-points number is reduced the better the transfer matrix **A** is well conditioned. At the first glance at Figure 4.31 the observations contradict the already seen

results from Figure 4.30. Linking these results, the question that one is prompted to ask is: "Is it possible for a well conditioned matrix to produced a worse identification result than the badly conditioned one?" The answer is emphatically "Yes", this is because regularizing with Tikhonov technique takes into account two sets of data as input namely: the matrix $\mathbf{A}$ and the vector $\mathbf{y}$ of Equation (3.4). Based on this, the nature of the identification result is highly dependent both on how well $\mathbf{A}$ is conditioned and the error level in $\mathbf{y}$. This implies that for an ideal case, where the identification result is perfect, then $\mathbf{A}$ should be well-conditioned and $\mathbf{y}$ should be error-free and authentic (true representation of the phenomena). In any situation other than this, the identification results will not be as the reference. Now, that the condition nature of $\mathbf{A}$ is known, the ill-posedness level and the authenticity nature of $\mathbf{y}$ is examined, then the combined effect of $\mathbf{A}$ and $\mathbf{y}$ defines the ill-posedness nature of the iPTF problem. Thus it is the posedness nature of the iPTF problem that determines the identification results and not only the characteristics of $\mathbf{A}$ (how well condition is $\mathbf{A}$). This ill-posedness level is shown in Figure 4.32.

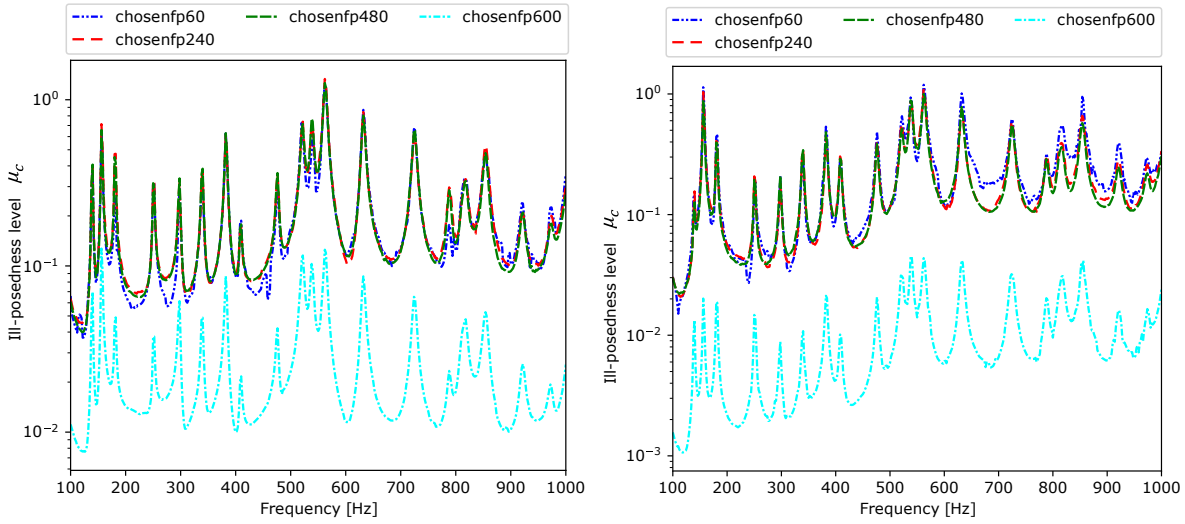

(a) m-iPTF (b) u-iPTF

Figure 4.32: Ill-posedness level μ_c as a function of frequency for the different field-point configurations.

From Figure 4.32, it can be observed that there is a clear disparity in the ill-posedness levels as the number of field-points decreases from the equally-determined level (600) to the under-determine levels (480, 240, 60). This finding indicates that when utilizing `Tikh_RGCV`, which is Tikhonov in nature, the regularized findings from the equally-determined and under-determined situations (Figures 4.32 (c) and (d)) will be far apart. Also, when just the under-determined cases are considered, the spectra are essentially the same in pattern, with a little rise in error level when the number of field points is lowered from 480 to 60. What the above observations mean practically is that, in terms of data $\mathbf{y}$, decreasing the number of field-points implies that the $\mathbf{y}$ has insufficient acoustic information to produce meaningful analysis which makes the error in $\mathbf{y}$ to be large and thus the physical relation of the underlying exact iPTF problem is not reasonable.

In Section 4.5.1, the difficulties for the `Tikh_RGCV` to generate solutions for these under-determined problems is investigated further.

4.5.1 A close examination of the under-determined case

As shown in Figure 4.30, there is a significant difference between the $\mathcal{CI}$ results of fully-determined instances, which are extremely good, and the bad results of under-determined

cases. These discrepancies, as well as the disappointing outcomes produced, have prompted more research into the under-determined circumstances, which is the subject of this section. Alternative regularization strategies are being sought as a result of these factors. The techniques under consideration include `Twomey_CHA`, `Tikh_CHA` and `Itr_CHA` (see Equation (3.84)), all of which are part of the preceding regularization technique described in Section 3.4.1.3.

It should be emphasized that using these prior regularization techniques necessitates the usage of the references that are being looked for, which is not the typical approach for solving an inverse problem. These approaches are shown here just to demonstrate that good results can still be obtained for problems that are under-determined and that difficulties main arise from the regularization strategies which often fail to provide an optimal λ^2_{opt} value. The three approaches using the $\mathcal{CHA}$ metric are used here to evaluate the inherent capacity of the considered strategy by finding the best possible solution comparing each time to the reference.

The reference ($\mathbf{v}_{ref}$) utilized in the `Tikh_CHA` and `Itr_CHA` strategies is solely used as a guide in selecting the best regularization parameter λ^2_{opt} and i_{opt}, respectively, and does not constitute part of their solution functions as shown in Equation (3.27) and Equation (A.1). The reference ($\mathbf{v}_{ref}$) is part of the objective function in the `Twomey_CHA`, as it is in Equations (3.66), and it is also used in the regularization parameter selection procedure (`CHA`). As a result, the `Twomey_CHA` findings are heavily skewed toward that specific reference indicator. The interest of using the `CHA` cost function (which performs a comparison to the reference for all the λ^2 values at each frequency) is only employed here to understand if the difficulties arising from the under-determination of the problem come from the regularization process or from the iPTF formalism itself.

Figure 4.33 depicts the behavioural results of the regularization procedure for the above-mentioned strategies. It can be seen that the associated regularization parameter value grows as the frequency increases for the `Itr_CHA` and `Tikh_CHA` approaches in all of the regularization techniques presented, as anticipated. With the exception of the completely determined case ($fp = 600$), the regularization parameter spectra increases in value as the number of field points increases in the `Tikh_CHA` technique. This pattern is identical to that exhibited in the spectra of Figure 4.29 obtained by `Tikh_RGCV`. As a consequence, it should come as no surprise that the detected results for `Tikh_CHA` and `Tikh_RGCV` are similar at some frequencies. It's worth noting that when the number of field points reduces, `Itr_CHA` takes less iterations to reach the best solution. The under-determined instances and fully determined cases are still clearly distinguished in the iteration index spectrum. This will be reflected strongly in the identification findings.

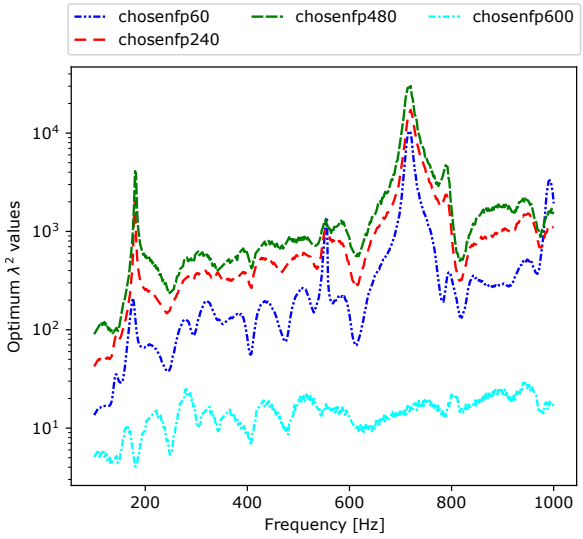

(a) m-iPTF `Tikh_CHA`

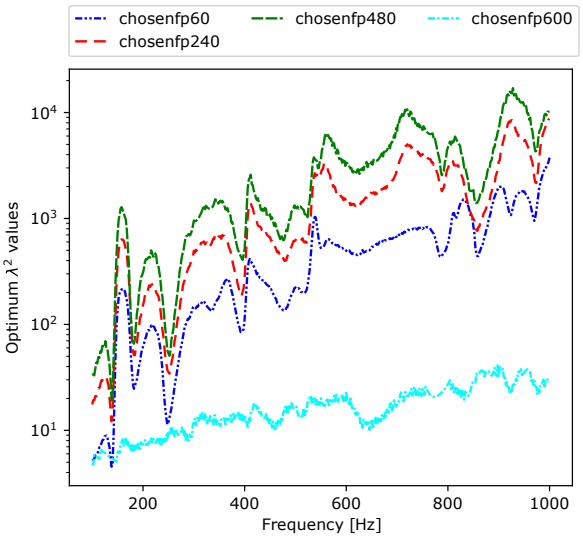

(b) u-iPTF `Tikh_CHA`

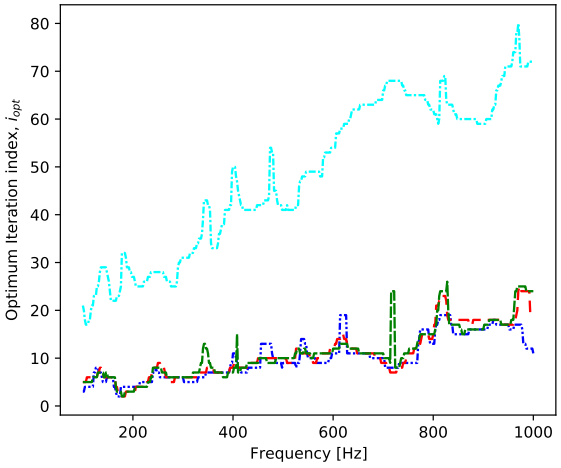

(c) m-iPTF `Itr_CHA`

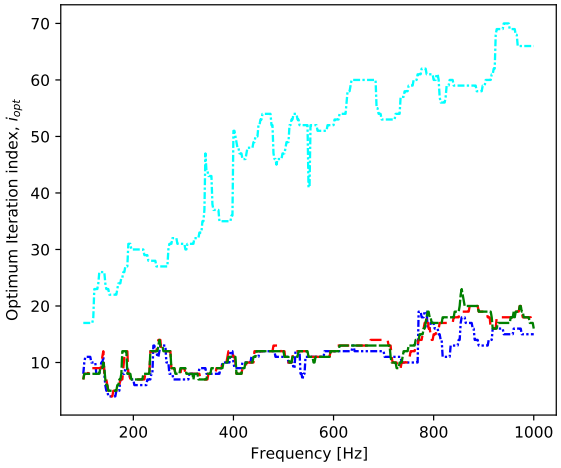

(d) u-iPTF `Itr_CHA`

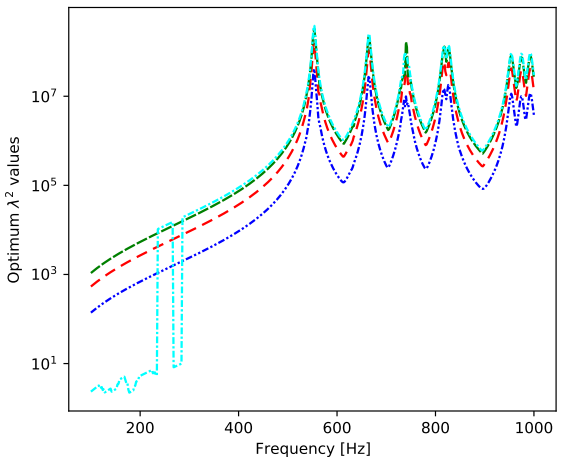

(e) m-iPTF `Twoney_CHA`

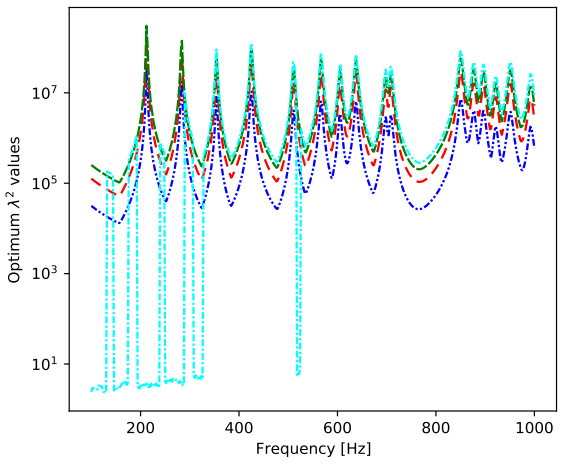

(f) u-iPTF `Twoney_CHA`

Figure 4.33: Optimum regularization parameter λ^2 spectra for the different prior regularization techniques considered for the various field-point under-determined configurations.

Surprisingly, the regularization parameter spectra in the `Twomey_CHA` strategy follow the same pattern as the condition number spectra in Figure 4.31, with peak values appearing at the virtual acoustic cavity's eigenmode frequencies. This means that the `Twomey_CHA` method is strongly dependent on the virtual cavity's eigenmodes, and that special attention should be paid to identification results that are near to the eigenmode frequencies. It's also worth noting that there's no discernible difference in spectra pattern between under-determined and fully-determined situations, as shown in the `Itr_CHA` and `Tikh_CHA` techniques.

For evaluating if the difficulties coming from the under-determination of the problem come from the regularization process or from the iPTF formalism, the $\mathcal{CI}$ metric is used to evaluate the performance of the `Tikh_RGCV` strategy already analyzed (see Figure 4.30) in regards with the best possible solution that can be reachable with `Tikh` regularization technique. This best possible solution is obtained with the `Tikh_CHA` strategy.

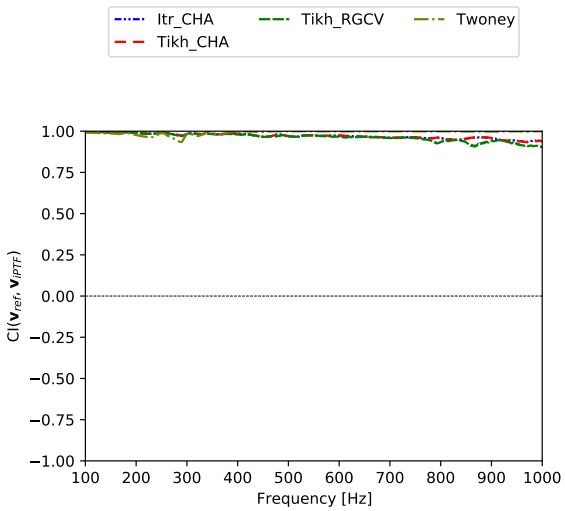

(a) m-iPTF $\mathcal{CI}$ $fp = 600$

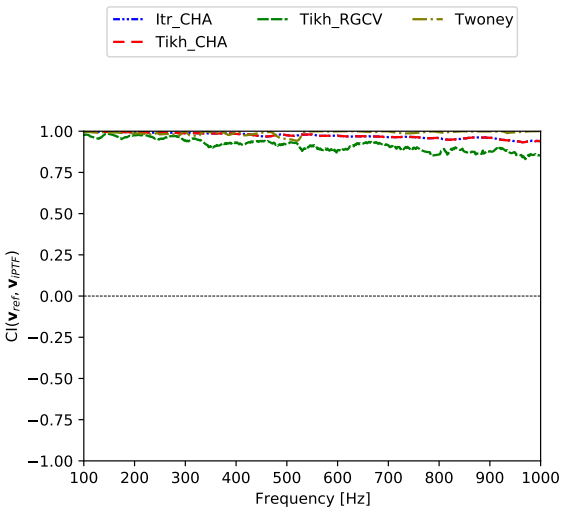

(b) u-iPTF $\mathcal{CI}$ $fp = 600$

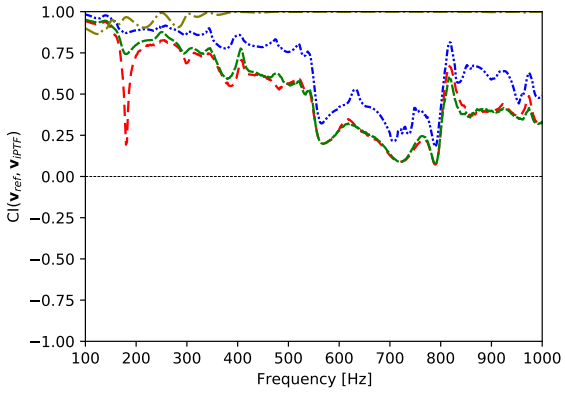

(c) m-iPTF $\mathcal{CI}$ $fp = 480$

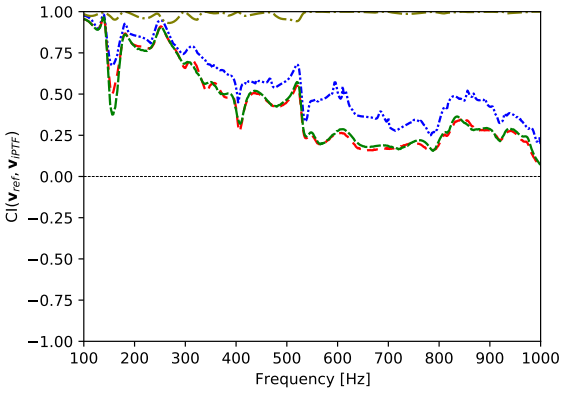

(d) u-iPTF $\mathcal{CI}$ $fp = 480$

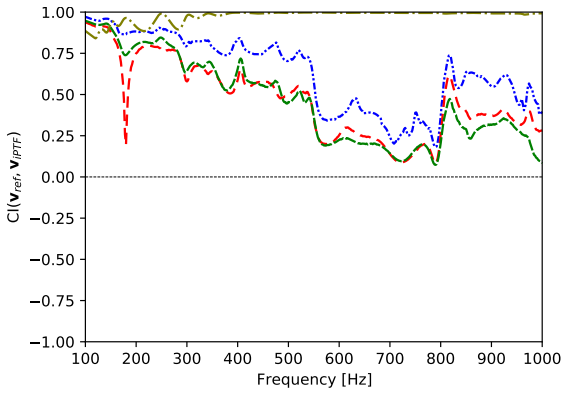

(e) m-iPTF $\mathcal{CI}$ $fp = 240$

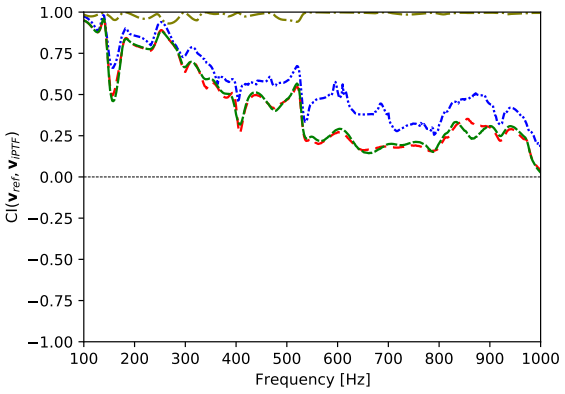

(f) u-iPTF $\mathcal{CI}$ $fp = 240$

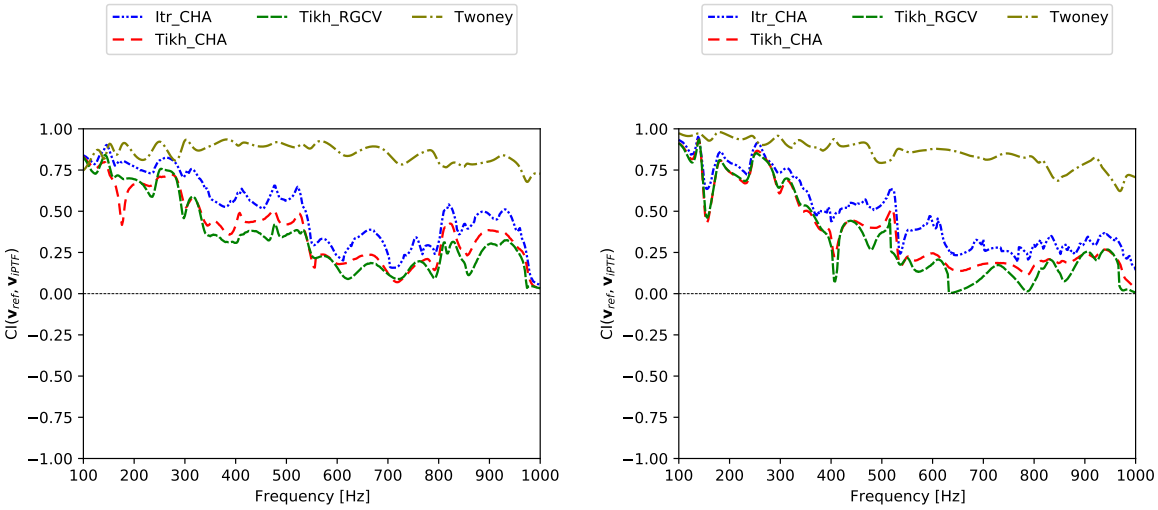

(g) m-iPTF $\mathcal{CI}$ $fp = 60$ (h) u-iPTF $\mathcal{CI}$ $fp = 60$

Figure 4.34: $\mathcal{CI}$ correlation results using the reference DFR velocity field and iPTF velocity field computed from the different regularization techniques considered for the various field-point configurations.

When comparing `Tick_RGCV` and `Tikh_CHA` in Figure 4.34, it is worth noting that the performances are really similar even if for the heavily under-determined problem ($f_p = 60$), `Tikh_CHA` exhibits slightly better reconstructions. This means that the `Tikh_RGCV` strategy leads to reconstruction fields really close to the best possible reconstruction fields that can be reachable with any `Tikh` regularization technique. Thus, the quality of the reconstruction seems to be limited here by the regularization process. This is confirmed when comparing to the results obtained by `Itr_CHA` and `Twomey_CHA`. The `Itr_CHA` provides with the best possible solution using an iterative (`Itr`) regularization technique. The performances of this strategy are identical to the `Tikh_RGCV` for the equally-determined case ($f_p = 600$) but are significantly better for under-determined cases. It is a hint that confirms that `Tikh` regularization underperfoms for under-determined problems. Finally, as can be seen in Figure 4.34, the `Twomey_CHA` strategy leads to almost perfect results even for heavily under-determined problems. This is obviously due to the fact that it necessitates the knowledge of the field one wants to retrieve as a part of its objective function. However, it also clearly demonstrates that with a perfect regularization technique, the iPTF approaches are able to handle under-determined problems.

4.6 Summary and Conclusion

This chapter's main objective was to search from a number of regularization techniques presented in Chapter 3 which is most appropriate for both m-iPTF and u-iPTF methods. The approach includes conducting numerical experiments with numerous scenarios to create set of test cases to defined the iPTF problems. The section begun with the description of the numerical experiments carried for the different test cases considered.

Two sets of different independent numerical experiments were carried out to provide input data for the both u-iPTF and m-iPTF methods. The first numerical simulation provided the acoustic field measurement data (dual pressure measurement for m-iPTF and pressure and particle velocity measurement for the u-iPTF) which is usually obtained through performing real laboratory test. This numerical experiment was achieved using the direct frequency analysis module of ACTRAN to compute the radiate acoustic field information. The second numerical

simulation was carried out to compute the matrices ($\mathbf{Z}$ and $\mathbf{Y}$) needed for application of The iPTF process. The two simulations are completely independent.

The defined iPTF problem is solved using the regularization techniques. The first test case scenario is the the idealistic case, on which all the regularization techniques (deterministic and statistical approach) were deployed. The identified results from each of the techniques are validated using a set of correlation metrics. The zeroth-order-Tikhonov-RGCV (`Tikh_RGCV`) based technique emerged as most suitable regularization technique for the iPTF methods in solving the idealistic problem case.

The `Tikh_RGCV` was further explored in two realistic cases to test for its robustness. These realistic test cases are the perturbed (noisy) and underdetermined iPTF test cases. The perturbed cases described the situation where various noise levels were added to the measurement data whereas the reduction of the number of field points in relation to the number of identification patches defines the under-determined case. The generated identified results for the realistic test case were validated in a similar manner as in idealistic test case. The differences in the obtained correlation results were explained using the DPC analysis. The acquired identified findings from the varied perturbed configurations for quantifying the acoustic source are generally in good agreement with the reference.

As a whole, for the various under-determined configurations investigated, the resulting identified findings for quantifying the acoustic source are not always in reasonable agreement with the reference. A detailed study of the validation data indicated that the `Tikh_RGCV` and Tikhonov in general are not the best appropriate techniques to apply for this rigorously under-determined issue. As a result, alternative innovative strategies, such as iteration, statistical, and sparse-based approaches, should be pursued rather than Tikhonov methods.

5

Source field reconstruction in presence of masking objects

Performing acoustic measurements in cluttered and complex environment such as the engine test-bench shown in Figure 5.1 is often challenging especially if one is interested in obtaining detailed acoustic information from a specific part. The difficulties often arise from the presence of different structures, frames or obstacles. Indeed, this kind of bench prevents classical NAH approaches to be used as:

- masking objects produce an "acoustic shadow" on microphone arrays ;
- the presence of masking objects can affect the radiated acoustic field so that the "free field" condition is far to be fulfilled ;
- such a cluttered environment makes difficult to place a necessarily large microphone array at the suitable positions ;
- it is difficult to define back-propagated plane fields on such a complicated source shape.

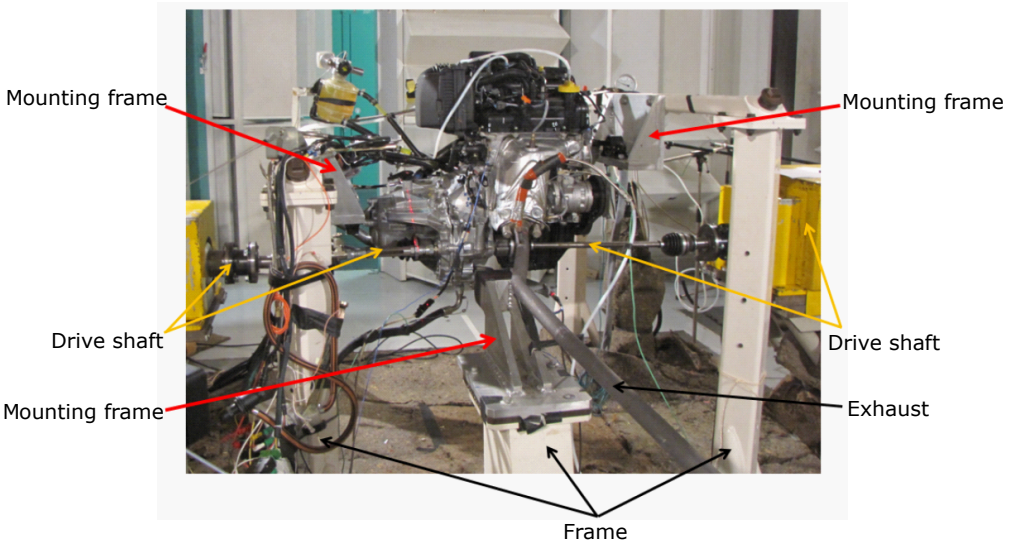

Figure 5.1: Engine test-bench with various masking structures [27].

In this chapter, how iPTF approaches can be used in this kind of situation will be explained. The concept of virtual acoustic volume around the source is the key-point that allows taking into account the presence of masking (rigid) objects. In combination with features already presented in Chapter 2, iPTF approaches become powerful tools to characterise real industrial systems or

structures.

The main aim of this chapter is to use the iPTF method in the presence of masking objects: this situation will be called "blind reconstruction" in this context. The term "blind reconstruction" used here means retrieving the acoustic properties of the source (in other words fully characterising a source) which is partially masked by an obstacle.

The chosen approach to illustrate the above problem is numerical which involves creating different configurations depicting the possible situations often encountered in real-world. As a result, parametric studies are undertaken which consist of different test case scenarios, all based on the reconstruction of the velocity field on the surface of a rectangular plate masked by a rigid parallelepiped obstacle. The first test case deals with the influence of the obstacle distance (how far or close) from the source on its identification as presented in Section 5.3. Thus the obstacle is varied for a distance of 1 cm, 5 cm, 10 cm and 15 cm from the source. The second test case as addressed in Section 5.4, deals with how widening the obstacle to increase its surface area with respect to the source area affects the identified source characteristics. The obstacle width is varied in the order of 10 cm, 30 cm and 50 cm. It should be noted that all of the text cases in sections 5.3 and 5.4 were conducted without any noise in the measurement data (noiseless equal-determined system).

In this chapter, for sake of conciseness, only the u-iPTF with the `Tikh_RGCV` regularization strategy will be used for illustrating the effect of the masking object on the quality of the reconstructed fields.

In this section, the challenging case where the source field to reconstruct is partially masked by the presence of an object is addressed. This situation is very common in real life: the system under study can be partially masked by a supporting frame or a cable or some zones of the radiated field might not be accessible due to the presence of a wall or the surface of another (non studied) part. For many methods, this challenging situation can not be considered. The aim of this section is to show that iPTF can, thanks to its formulation, treat these situations in a quite straightforward way. In fact, a masking rigid object can be treated exactly like the rigid baffle in the example of Chapter 2. In the case of the rigid baffle, no information was needed on this surface. This is due to the correspondence between the real boundary condition (rigid surface) and the virtual boundary condition (Neumann's boundary condition) on this surface. In that way, the real problem is already represented by the virtual mode shapes used in the mathematical formulation. The presence of a rigid object is treated in the same way. To do that, the virtual volume defined in Figures 2.2 and 2.3 has to be modified to take into account the shape of the object by removing the volume corresponding to the "footprint" of the object in the virtual volume. On the created surface (inside the virtual volume), a Neumann's boundary condition is imposed. As a consequence, to respect the correspondence between boundary conditions, the real object has to be perfectly rigid and not moving. This is the main assumption of the proposed approach.

5.1 Presentation of the numerical experiment

In the example presented in Figure 5.2, the masking object is considered to be a parallelepiped. It is 70 cm long and 1 cm thick. Its width will vary between 10 and 50 cm (10 cm, 30 cm and 50 cm). This object is longer than the plate and the distance to the plate will vary between 1 cm and 15 cm (1 cm, 5 cm, 10 cm and 15 cm).

Compared to the process described in section 4.1, the difference lies in the fact that the "footprint" of the rigid masking object is taken into account in the FE/IE model for the direct computation and as such the radiated acoustic field is highly modified by the presence of the masking object as can be seen in Figure 5.3. This new field will be used as an input for Equation (3.3).

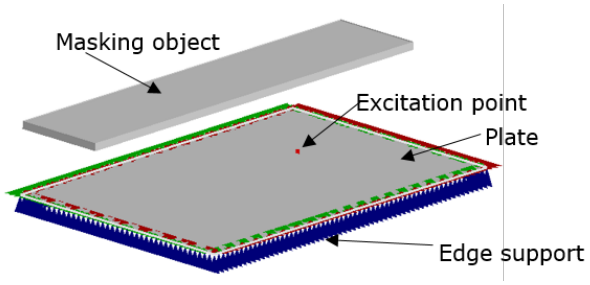

Figure 5.2: Model plate for vibration computation in the presence of masking object

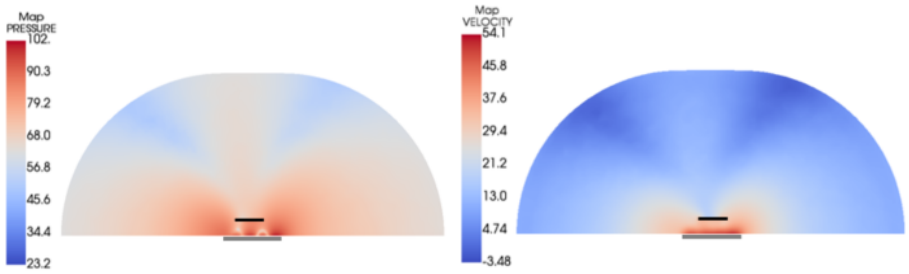

(a) (b)

Figure 5.3: A cut- section view of the acoustic radiation from the excited plate in the presence of masking object positioned 10 cm away from the plate at 900 Hz. (a) The radiated pressure field (dB, ref: 2×10^{-5} Pa) and (b) the radiated velocity field (dB, ref: 5×10^{-8} (m/s)).

5.2 Definition of the virtual volume and acoustic impedance computation

Compared to section 4.2, the virtual volume is modified to take into account the footprint of the masking object as presented in Figure 5.4(a) and Figure 5.4(b). A Neumann's boundary condition is considered on this internal surface. In this example, the masking object is completely included in the virtual volume: it is not mandatory. The masking object could be partially in and partially out the virtual volume. And as a result, only the part in the virtual volume will affect the iPTF modelling. In that case, there is no need to model the rest of the masking object: it will be taken into account by the measurement of the radiated field. Compared to case presented in section 4.2, the size of the matrices remains unchanged. Indeed, as one knows that the velocity field is null on the surface of the masking object, there is no need to discretize it into new patches. As the consequence, the number of measurement points remains unchanged too.

5.3 Test case I: Influence of masking object distance from the source

This section is the first part of the configuration examination for the blind reconstruction parametric investigation, as previously stated. The masking object is set at a specified distance away from the vibrating plate (source surface) for numerical investigations, as shown in Figure 5.5. The distances considered for numerical studies are 0 cm, 1 cm, 5 cm, 10 cm, and 15 cm. For simplicity sake, the letters ″d″ and ″w″ used here indicate the distance to the source and the width of the masking object, respectively. As a result, numerical studies for the set-ups d0cm_w0cm, d1cm_w15cm, d5cm_w15cm, d10cm_w15cm and d15cm_w15cm were carried out. The set-up d0cm_w0cm represents a scenario in which there is no masking object present, whereas d1cm_w15cm, d5cm_w15cm, d10cm_w15cm and d15cm_w15cm denote instances in

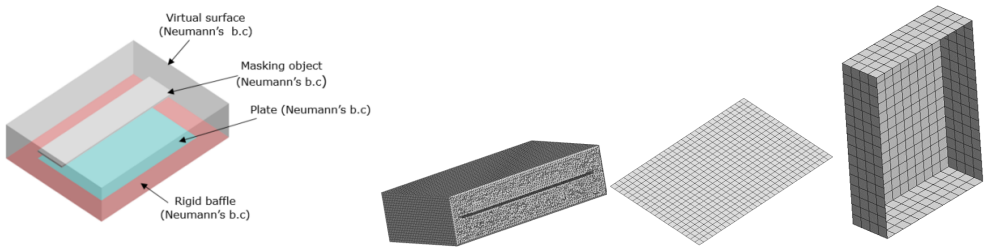

(a) (b) (c) (d)

Figure 5.4: Virtual cavity model. (a) Definition of the surfaces delimiting the virtual acoustic cavity and the associated boundary conditions (b) Mesh model of the virtual acoustic volume. Only the virtual surface and the plate surface are divided into patches, (c) source patches and (d) virtual patches.

which there is a 15 cm wide masking object positioned at a distance of 1 cm, 5 cm, 10 cm, and 15 cm away from the source surface.

Each image of Figure 5.5 consists of 3D XYZ view and upper left cornered 2D YZ schematic

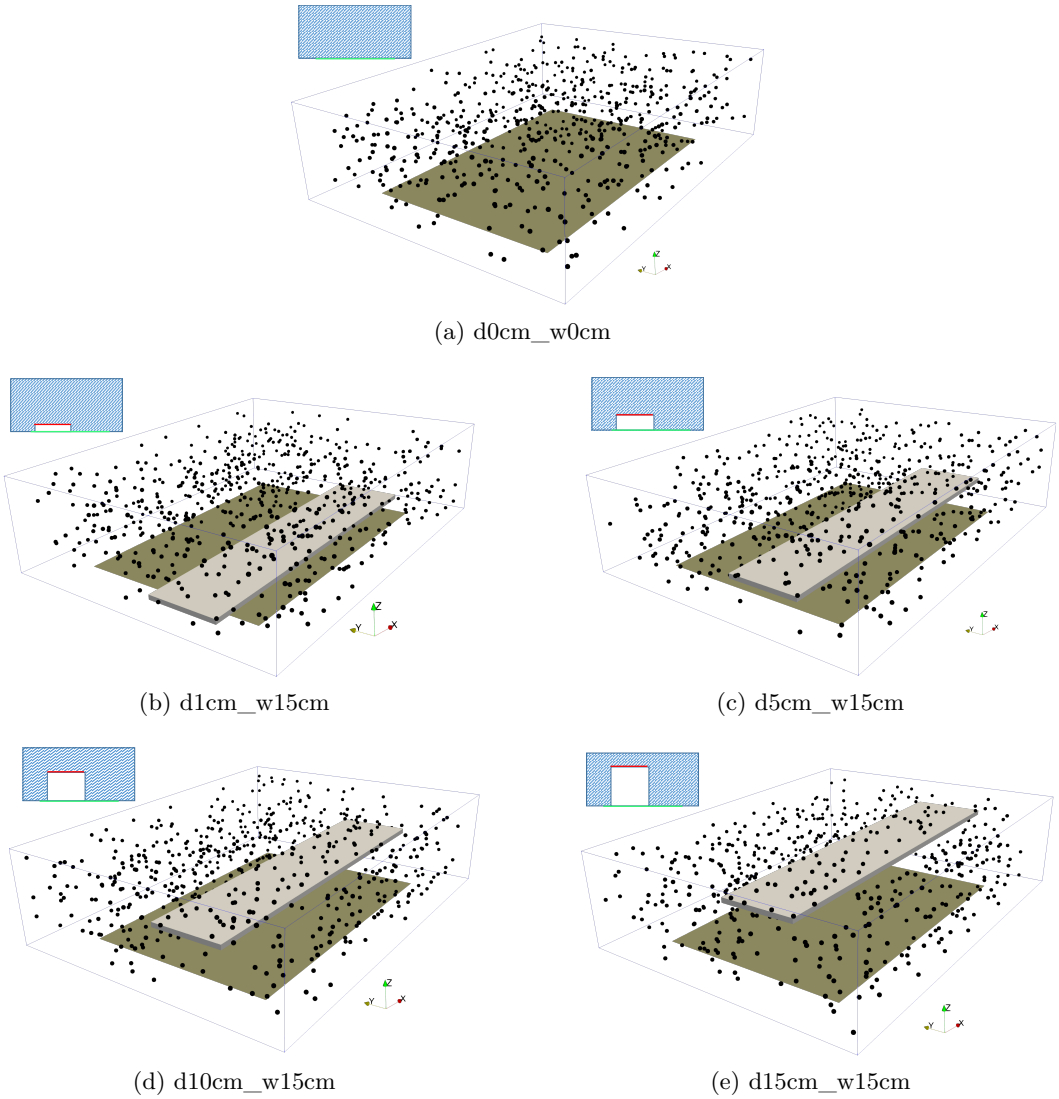

(a) d0cm_w0cm

(b) d1cm_w15cm

(c) d5cm_w15cm

(d) d10cm_w15cm

(e) d15cm_w15cm

Figure 5.5: Geometric model of the different set-ups.

view. In the 3D XYZ view, the blue rectangular wire-framed box represents the virtual cavity, the black disperse spots are the field-points (positions of the measurement sensors) whereas the olive and gray rectangular plates indicate source and masking object respectively. In the 2D YZ schematic view, the blue shaded area: measurement zone, white shaded zone: no-measurement zone, red bar: masking object, green bar: plate. It is to be noted that in all the cases shown in Figure 5.5, no measurement sensors were located between the masking object and the plate (the masked-zone).

The procedures used to determine the authenticity of the identified iPTF results for the various test set-ups is consistent with the validation process described in section 4.3.3. In addition, the reference and correlation measures are the same as before. The objective here is to compare the source fields (velocity, pressure and intensity) identified in the presence of the masking object to those obtained without masking object. It is here expected to have a good correlation if the source fields are not affected by the presence of the object. However, two different choices are possible for placing sensors in the virtual volume:

- choice 1: no microphone position is chosen in the masked zone, that is to say in between the masking object and the plate.
- choice 2: some microphones are located in the masked zone.

For both choices, the total number of microphones is constant (600). Choice 1 is obviously the most convenient choice for experiment as it does not need to place microphones in a hard to reach area. However, it is still important to evaluate if adding some microphones in the masked zone could increase significantly the quality of the results.

Figure 5.6 presents the correlation metric $\mathcal{CI}$ for the velocity (5.6a, 5.6b), pressure (5.6c, 5.6d) and intensity (5.6e, 5.6f) fields. For each correlation analysis, the difference between choice 1 and 2 is presented to evaluate if there is a gain adding microphones in the masked zone.
Figure 5.6 permits to draw some conclusions:

- correlation metric values higher than 0.75 for all the test set-ups (except d1cm_w15cm) demonstrate that even in the presence of masking objects, the iPTF approach is able to reconstruct the field behind the object. The masking object here is neither small nor far from the plate and the quality of the reconstruction is still acceptable.
- the presence of microphones in the masked zone slightly increases the correlation metric values but it is not as significant as expected. However, the number of microphones in this masked zone is not negligible (7%, 8.8%, 11.3%, 16.2% respectively for cases d1cm_w15cm, d5cm_w15cm, d10cm_w15cm and d15cm_w15cm). Considering the difficulty to put some microphones in the masked zone, the gain is too small to worth it. This is a good news when considering experimental measurements.
- the identified intensity fields are more difficult to reconstruct accurately as they are the product between the pressure and the velocity fields and so any inaccuracies in the velocity and/or pressure are magnified throughout the multiplication process. However, the produced correlation values are still acceptable even if the quality of the results decreases with the proximity of the masking object and with frequency.
- case d1cm_w15cm exhibits some falls of the correlation metric values at the eigen-frequencies of the structural modes of the plate. This is because, at these frequencies, the acoustic fluid trapped in the masked zone creates a strong structure-fluid coupling when the masking object gets closer to the source surface producing a two-way sided effect, in which the fluid and plate vibrations influence each other. As a result, for these particular frequencies and for a such small distance (1 cm) between the masking object and the plate, the comparison of the results to the case without obstacle is meaningless as the vibratory field has changed. This point has to be kept in mind in the following results.

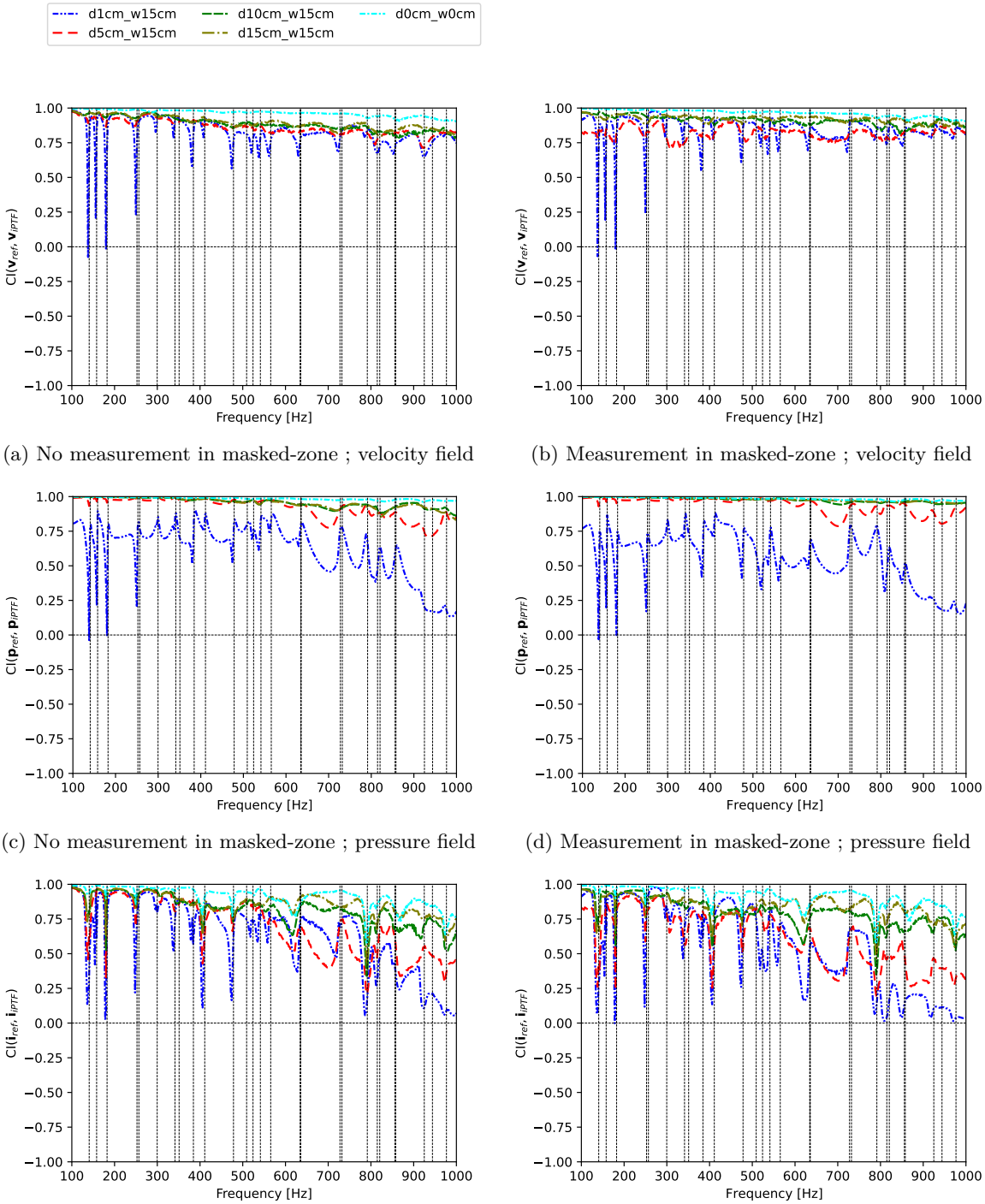

(a) No measurement in masked-zone ; velocity field

(b) Measurement in masked-zone ; velocity field

(c) No measurement in masked-zone ; pressure field

(d) Measurement in masked-zone ; pressure field

(e) No measurement in masked-zone ; intensity field

(f) Measurement in masked-zone ; intensity field

Figure 5.6: Plots of $\mathcal{CI}$ correlation metric used in the comparison of the source acoustic indicators identified by iPTF and that computed on the plate (reference) for the full frequency spectrum of the different masking object distance test set-ups. The vertical lines indicate the positions of the plate eigen frequencies.

From all the results shown so far, test set-up d1cm_w15cm (and to a lesser degree d5cm_w15cm) has outlier values compared to the rest of the data. As said before, it is expected that the presence of the masking object at such a small distance modifies the vibratory fields. As a consequence, the comparison to the case with no obstacle would be meaningless. The next paragraph aims at proving that even with a strong coupling between the vibration of the structure and the sound pressure in the acoustic volume trapped between the plate and the masking object, iPTF approach can still produce reasonable results.

Figure 5.7 shows the correlation metric $\mathcal{CI}$ computed between the identified velocity fields and the d1cm_w15cm (presence of the masking object at a distance of 1cm) and d0cm_w0cm (no masking object) cases taken as a reference. It is clear that the $\mathcal{CI}$ computed with d1cm_w15cm case does not exhibit falls as it has been observed with d0cm_w0cm case. Figure 5.7 proves two things: (i) the vibratory field is modified by the presence of a too close masking object and (ii) iPTF approach is still able to reconstruct the modified field with a reasonable accuracy.

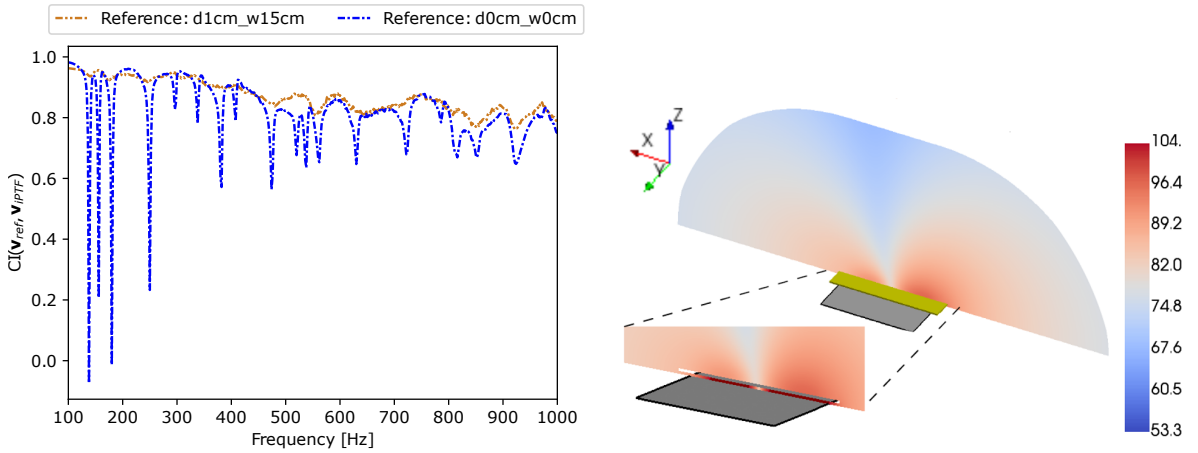

(a) (b)

Figure 5.7: (a) Correlation metric $\mathcal{CI}$ between the identified velocity fields and the d1cm_w15cm (presence of the masking object at a distance of 1cm) and d0cm_w0cm (no masking object) cases as a reference. (b) Illustration of the strong coupling between the vibratory field and the pressure field in the volume trapped between the plate and the masking object at 332 Hz.

Figures 5.8, 5.9 and 5.10 present respectively the identified velocity, pressure and intensity fields at the frequency of 332 Hz. These figures show really good comparison between identified and reference fields. The same conclusions as those observed previously still hold: (i) the presence of a masking object does not affect too much the quality of the identification, (ii) adding some microphones in the masked zone does not improve significantly the results (and can sometimes worsen them) and (iii) the increase of pressure in the trapped acoustic volume is well represented in d1cm_w15cm case (see Figure 5.9(iii)).

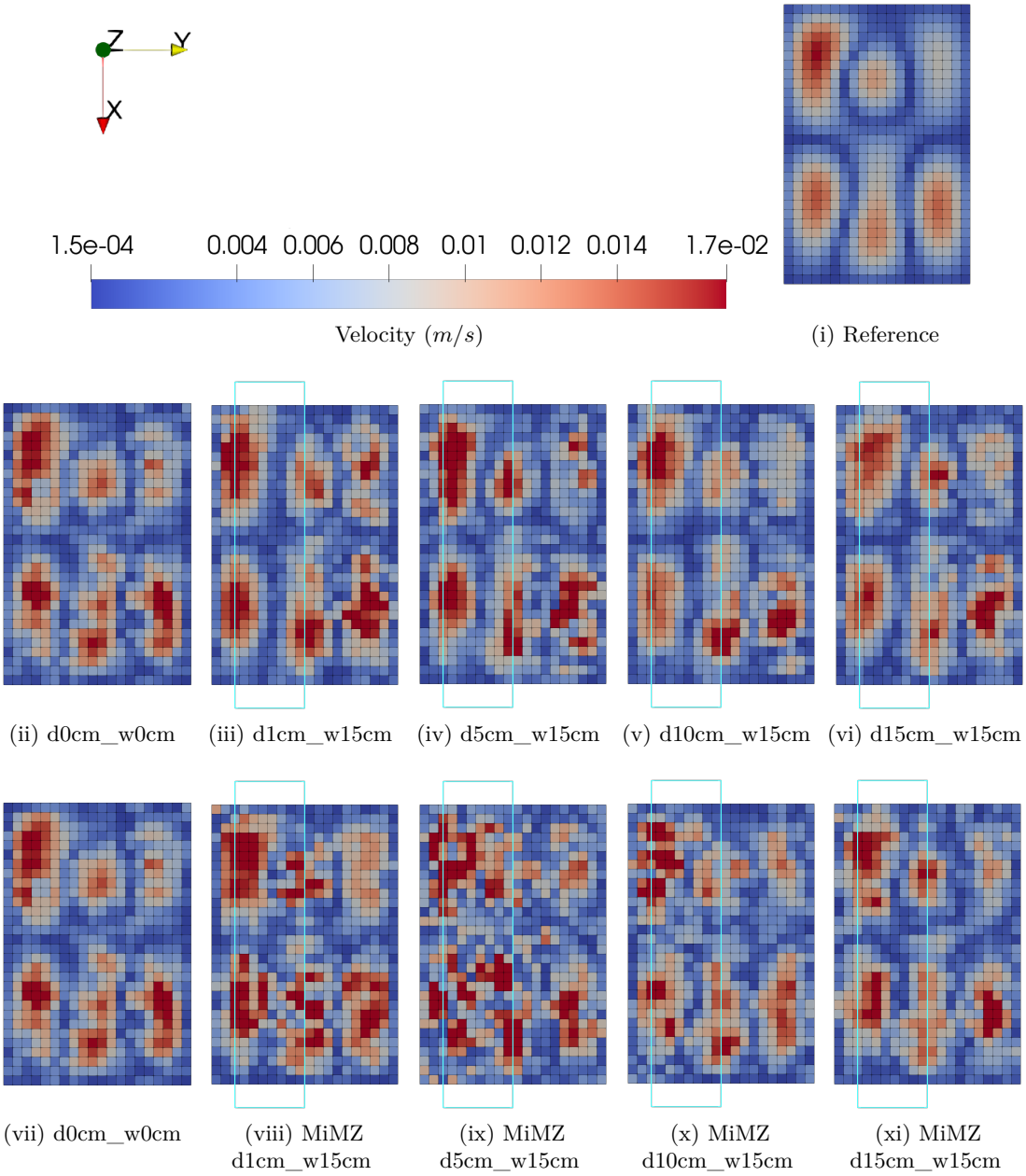

Figure 5.8: Spatial colormap of the amplitude of the acoustic velocity field on the surface of the plate identified with u-iPTF using `Tikh_RGCV` and the reference computed results at a frequency of 332 Hz for different masking object distance test set-ups. Outline position of the masking object is shown by the cyan-colored rectangle and the acronym MiMZ indicates 'Measurement in Masked-Zone'.

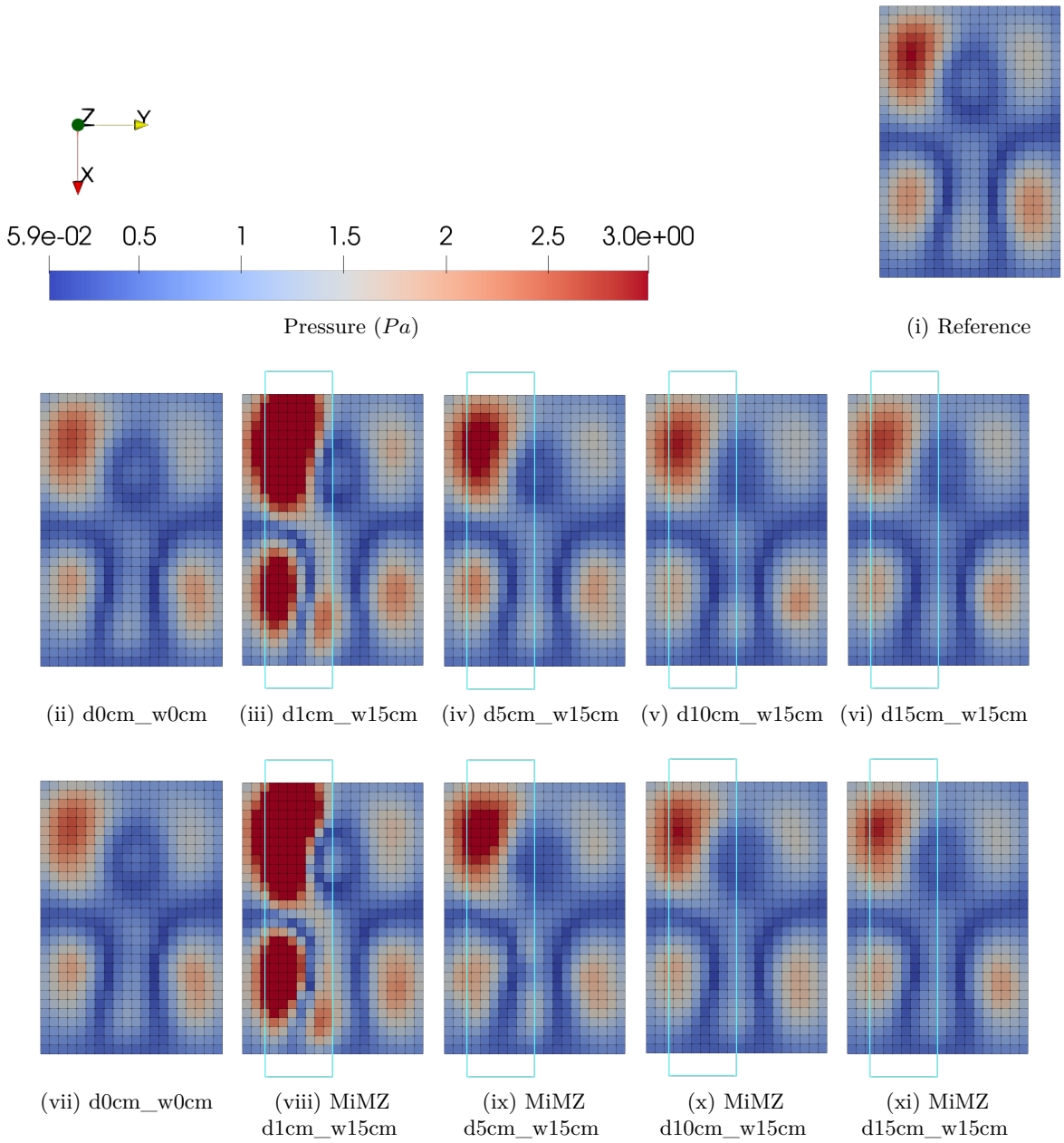

Figure 5.9: Spatial colormap of the amplitude of the acoustic pressure field on the surface of the plate identified with u-iPTF using `Tikh_RGCV` and the reference computed results at a frequency of 332 Hz for different masking object distance test set-ups. Outline position of the masking object is shown by the cyan-colored rectangle and the acronym MiMZ indicates 'Measurement in Masked-Zone'.

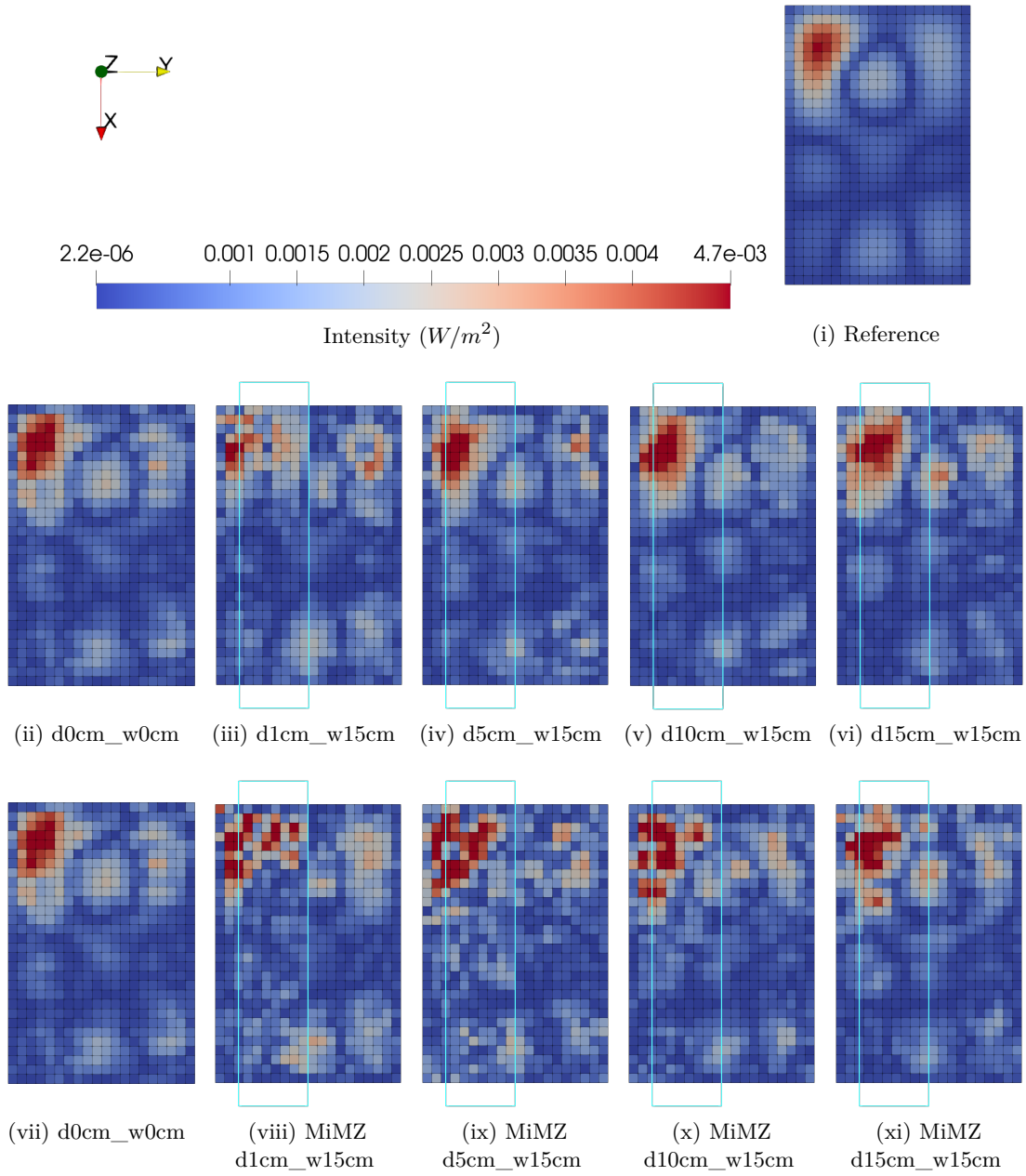

Figure 5.10: Spatial colormap of the amplitude of the acoustic intensity field on the surface of the plate identified with u-iPTF using `Tikh_RGCV` and the reference computed results at a frequency of 332 Hz for different masking object distance test set-ups. Outline position of the masking object is shown by the cyan-colored rectangle and the acronym MiMZ indicates 'Measurement in Masked-Zone'.

Figure 5.11 plots the acoustic radiated pressure and the radiation efficiency to evaluate the quality of global results as a function of frequency. The presence of the masking object at a distance of 10 cm and 15 cm from the plate does not alter the estimation of the radiated pressure and the radiation efficiency on the whole frequency band. The influence of the presence of the masking object begins to be noticeable for small distances like 1 cm or 5 cm. With such small distances, the identified intensity field is less comparable to the reference (see Figure 5.10(iii)) and so the radiated power and the radiation efficiency are more difficult to estimate. The addition of microphones in the masked zone does not change the estimation of the radiated pressure but

slightly improves the estimation of the radiation efficiency for frequencies higher than 900 Hz but again it's not a significant improvement.

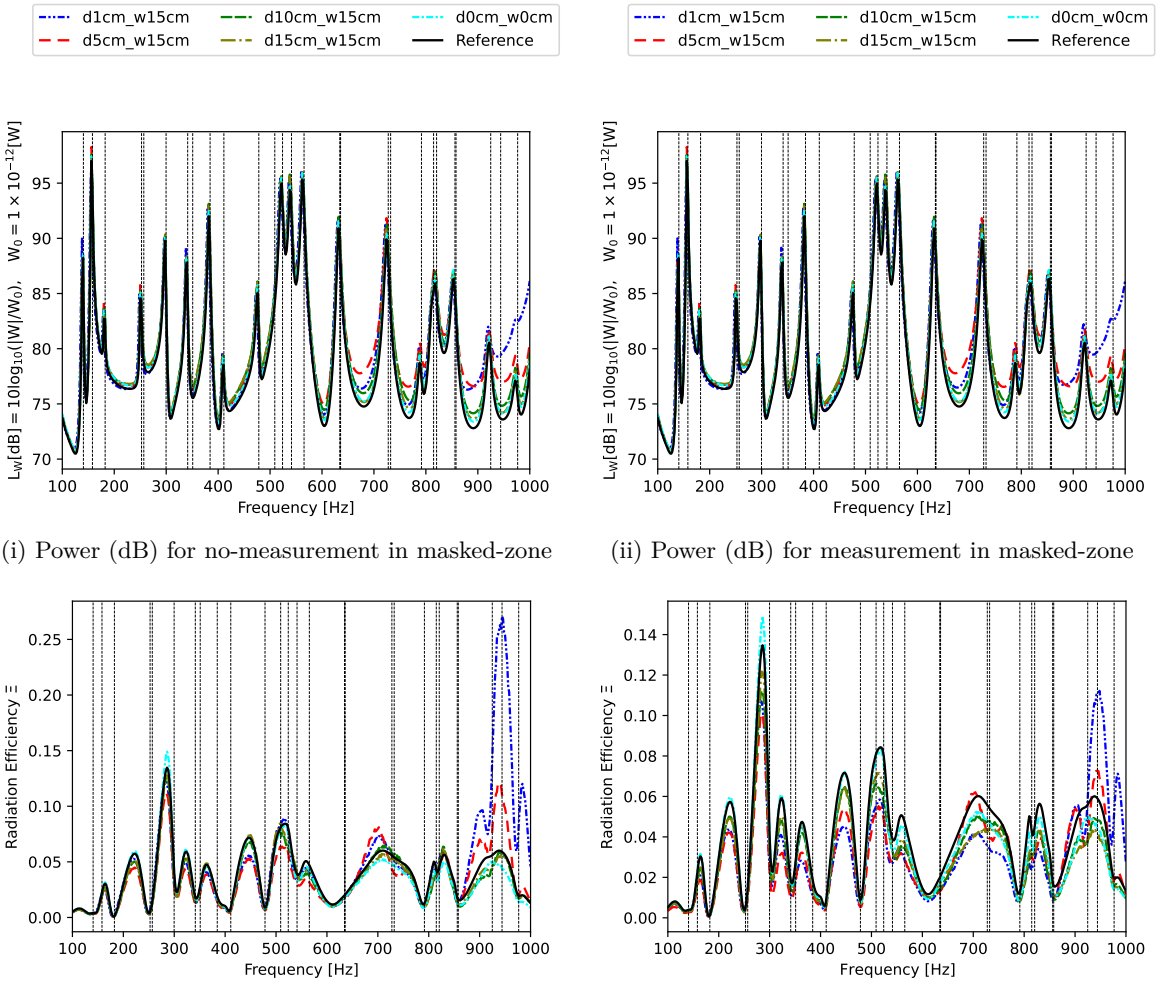

(i) Power (dB) for no-measurement in masked-zone

(ii) Power (dB) for measurement in masked-zone

(iii) Efficiency for no-measurement in masked-zone

(iv) Efficiency for measurement in masked-zone

Figure 5.11: Plots of global acoustic indicators identified by u-iPTF with `Tikh_RGCV` and the reference computed result for the different masking object distance test set-ups. The vertical lines indicate the positions of the plate eigen frequencies.

The near-field information on the source surface is the subject of all of the above-mentioned results. These source fields, especially intensity fields, are useful to locate zones responsible of the radiated sound pressure. But they can also be used as an input for computation of radiated sound. As such, the velocity field, expressed on patches can be converted on source mesh nodes and can serve as the Boundary condition (BC) in an ACTRAN DFR analysis (or any other acoustic solver). In the following, the directivity is computed using the reference vibratory fields (the ones obtained from the coupled fluid-structure case) or the identified velocity fields (without or with masking object). For the latter case, the computation is purely acoustic, imposing a velocity field on a zone of the fluid (boundary condition). If the presence of the masking object does not affect the identified fields the directivity plots should be identical to the directivity computed without masking object. Figures 5.12 and 5.13 shows respectively the directivity plots in ZX and ZY planes. In both cases, a 101-field-point semi-circular array with a radius of $r = 50$ cm and an elevated look angle θ measured from the main X-axis and Y-axis of the source plane are used to compute the directivity plots. These discrete field-points are arranged in such a way that they follow a hypothetical path on the ZX ans ZY planes in space, the centre

of which coincides with the geometrical centre of the source.

First, one has to remark that the directivity plots computed from the reference cases visible in Figure 5.12(b) and 5.13(b) are highly affected by the presence of the masking object (especially in the ZX plane). This is obviously an expected results: the presence of the masking object alter the radiated pressure field and so the directivity. Second, the directivity computed from the identified velocity fields are all similar whether the identified fields were obtained without or with the presence of the masking object. This is a powerful feature of iPTF: iPTF approach is able to "cancel" the influence of a masking object and is a tool to estimate the directivity of a source even in a non conventional acoustic environment (no anechoic chamber). The d1cm_w15cm case still presents some discrepancies (especially in the ZY plane, see Figure 5.13(c)). This is due to a too close masking object that makes difficult the reconstruction and modify the vibratory field of the plate. Finally, adding some microphones in the masked zone slightly improves the results but not in a significant manner as the results without microphones in the masked zone were already good.

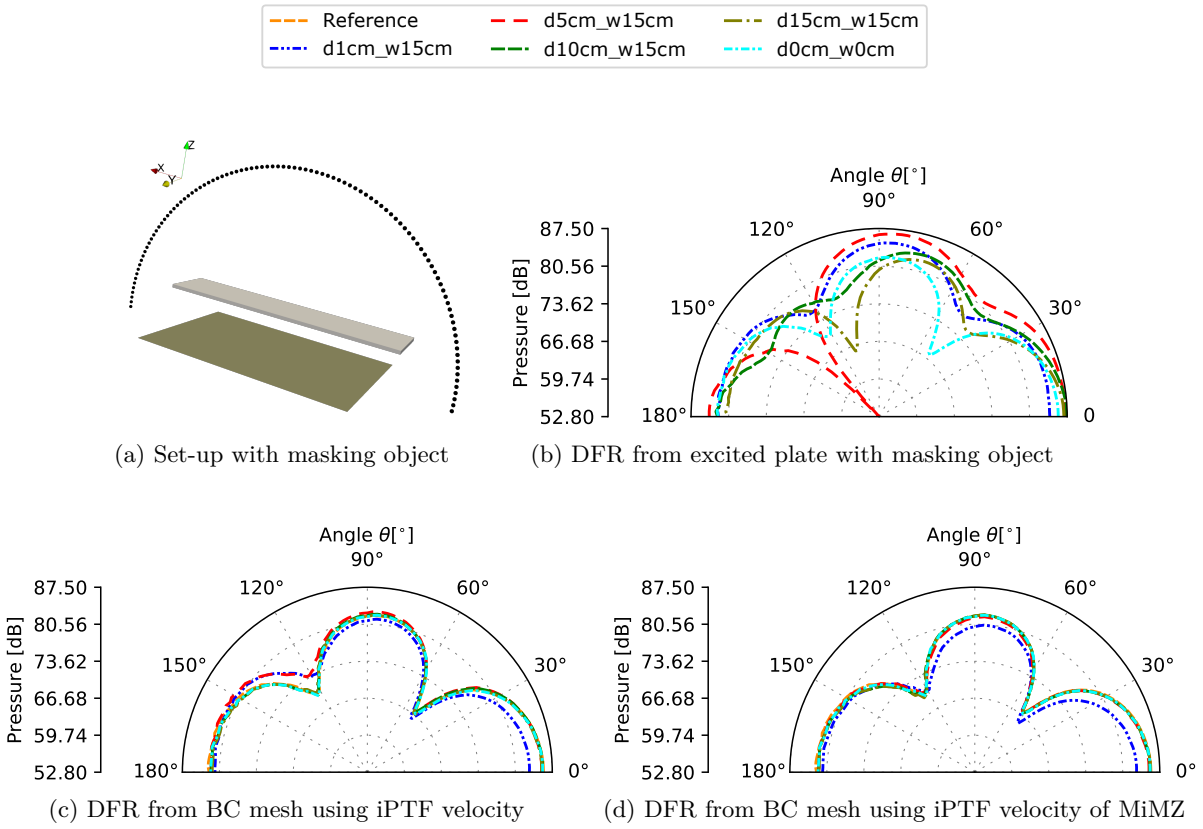

(a) Set-up with masking object

(b) DFR from excited plate with masking object

(c) DFR from BC mesh using iPTF velocity

(d) DFR from BC mesh using iPTF velocity of MiMZ

Figure 5.12: Settings and polar pressure radiation pattern of the ZX semi-circular array recorded at a frequency of 636 Hz for the different masking object distance test set-ups.

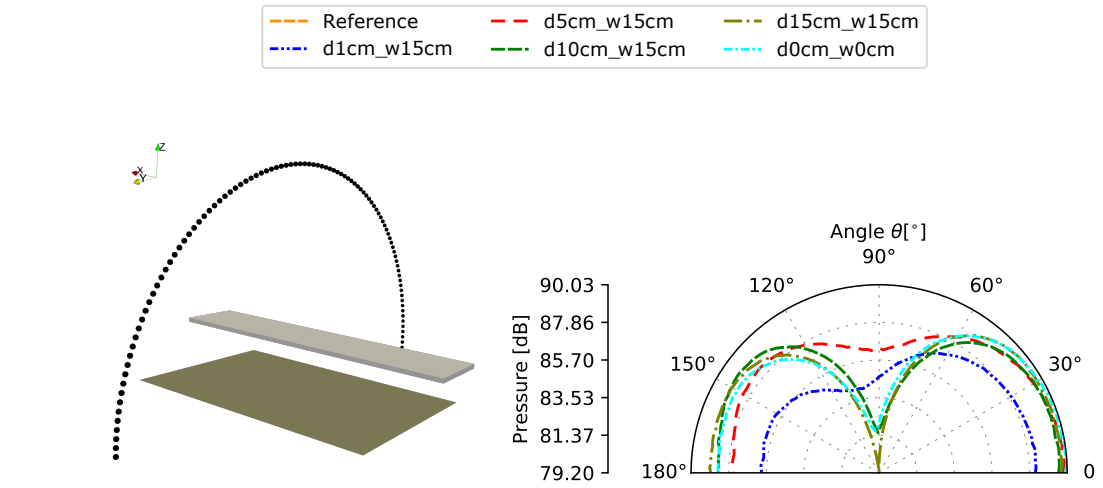

(c) Set-up with masking object

(d) DFR from excited plate with masking object

(e) DFR from BC mesh using iPTF velocity

(f) DFR from BC mesh using iPTF velocity of MiMZ

Figure 5.13: Settings and polar pressure radiation pattern of the ZY semi-circular array recorded at a frequency of 636 Hz for the different masking object distance test set-ups.

5.4 Test case II: Influence of masking object width across the source

As previously established, this section is the second phase of the configuration examination for the blind reconstruction parametric investigation. For numerical experiments, the masking object widths across the source surface are adjusted, as illustrated in Figure 5.14. The widths examined for numerical studies for a masking object location 10 cm away from the source surface are 0 cm, 15 cm, 30cm and 50 cm. The letters "d" and "w," have the same meaning as previously introduced in section 5.3, denoting the distance and width of the masking object, respectively. As a result, numerical studies for the set-ups d0cm_w0cm, d10cm_w15cm, d10cm_w30cm and d10cm_w50cm were carried out. The set-up d0cm_w0cm represents a scenario in which there is no masking object present, whereas d10cm_w15cm, d10cm_w30cm and d10cm_w50cm denote instances in which there is a masking object positioned at a distance of 10 cm away from the source surface with widths of 15 cm,30 cm, and 50 cm across the from the source surface. The masking objects d0cm_w0cm, d10cm_w15cm, d10cm_w30cm and d10cm_w50cm approximately cover 0%, 37.5%, 75% and 100% of the source surface area respectively.

Figure 5.14 shows a 3D XYZ view and a 2D YZ schematic view in the upper left corner

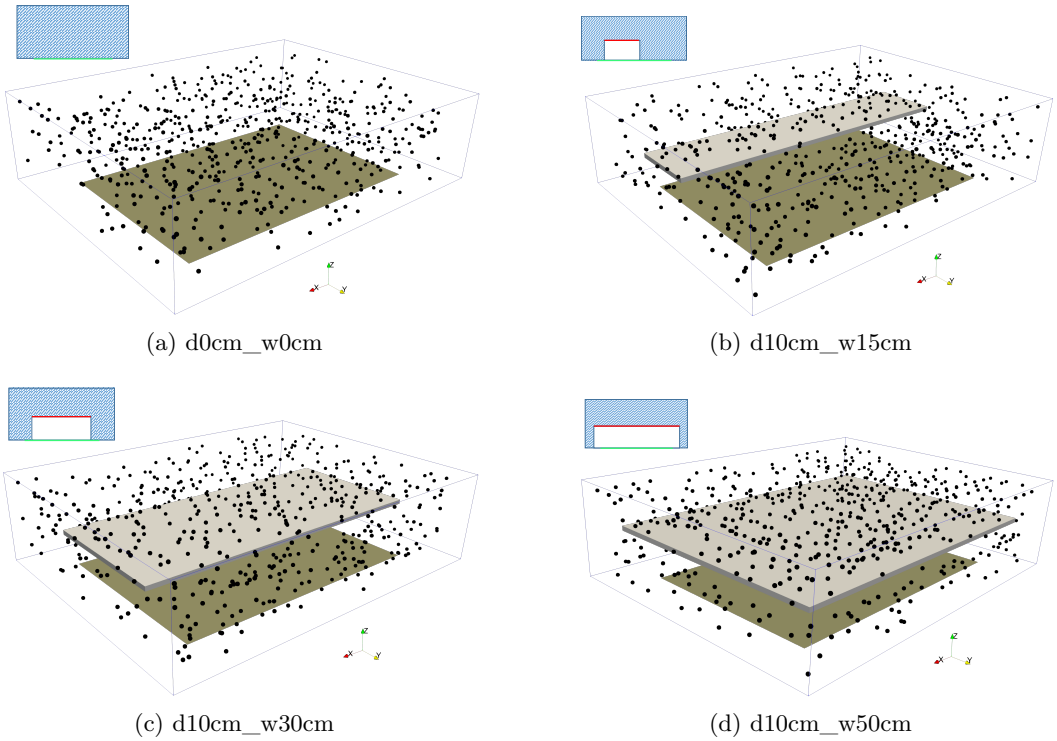

(a) d0cm_w0cm (b) d10cm_w15cm

(c) d10cm_w30cm (d) d10cm_w50cm

Figure 5.14: Geometric model of the different test set-ups with varying widths.

of each scene. The virtual cavity is represented by the blue rectangular wire-framed box in the 3D XYZ view, the field-points (positions of the measurement sensors) are represented by the black disperse spots, and the source and masking object are represented by the olive and gray rectangular plates, respectively. The blue shaded region represents the measurement zone, the white shaded area represents the no-measurement masked-zone, the red bar represents the masking barrier, and the green bar represents the plate in the 2D YZ schematic view. It's worth noting that there were no measuring sensors between the masking object and the plate in any of these circumstances but, as previously done, these cases will be compared to cases where microphones are put in the masked zone.

Figure 5.15 shows the correlation metric $\mathcal{CI}$ used to evaluate the quality of the reconstruction

as done in the previous section. For each width of the masking object, a comparison is done to the d0cm_w0cm case (no masking object) and to configurations for which microphones are also put in the masked zone.

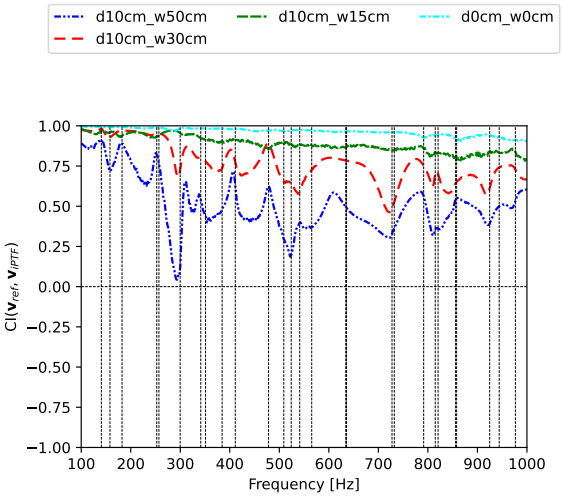

(a) No measurement in masked-zone: velocity field

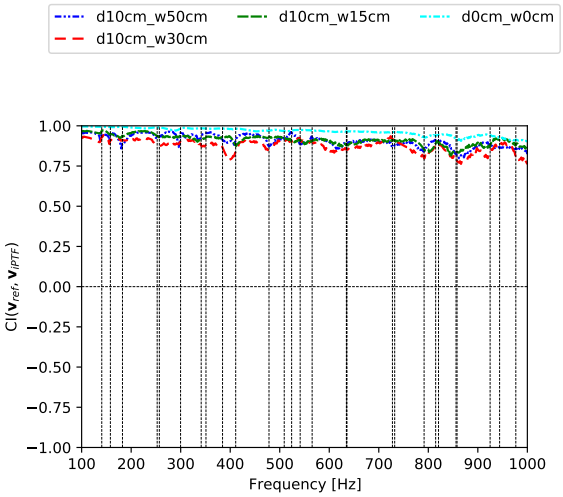

(b) Measurements in masked-zone: velocity field

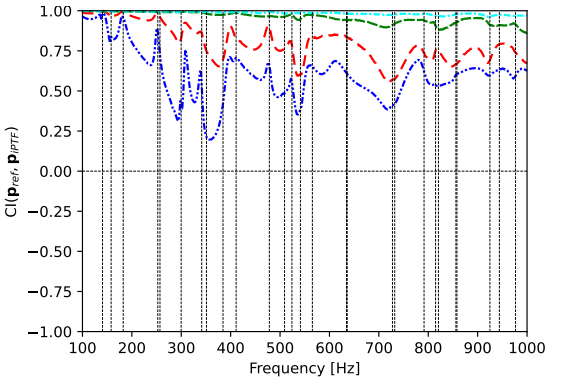

(c) No measurement in masked-zone: pressure field

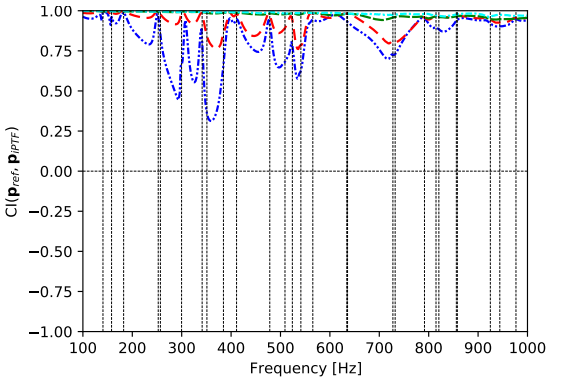

(d) Measurements in masked-zone: pressure field

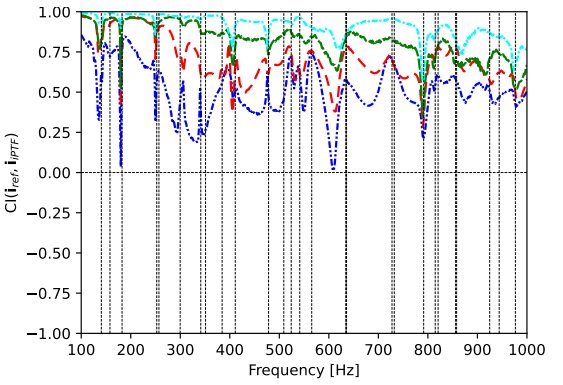

(e) No measurement in masked-zone: intensity field

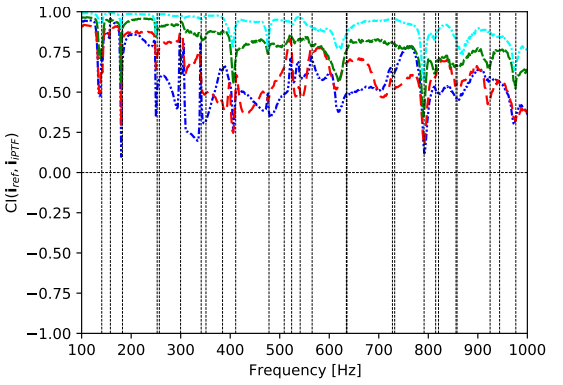

(f) Measurements in masked-zone: intensity field

Figure 5.15: Plots of $\mathcal{CI}$ correlation metric used in the comparison of the source acoustic indicators identified by iPTF and that computed on the plate (reference) for the full frequency spectrum of the different masking object width test set-ups. The vertical lines indicate the positions of the plate eigen frequencies.

It is clear from Figure 5.15 that the quality of the reconstruction worsens with the size of the masking object and so with the percentage of source surface masked by the object. On the whole frequency range, the $\mathcal{CI}$ averaged values are approximately 0.95 for the case with no masking object (0% of the source surface), 0.85 for the case with a 15 cm width object (37.5%), 0.75 with a 30 cm width object (75%) and 0.5 with a 50 cm width object (100%), and this roughly for all the field types (velocity, pressure or intensity). However, one has to remind from Figure 5.14 that all the microphones used are excluded of the masked zone. Therefore, for the extreme case of a masking object bigger than the source to identify itself, no information is captured in the vicinity of the source and most of the microphones are almost isolated from the source. But even for this extreme case, the identified maps are not meaningless as can be seen in Figures 5.16, 5.17 and 5.18. Indeed, the fields are somehow distorted, producing a low $\mathcal{CI}$ value, but the spots and the maximum values of velocity, pressure and intensity are still located in the same zones. Such interesting results were not expected when setting up this test case. This shows how iPTF approach is robust and it can be used in configurations for which no other method can be applied.

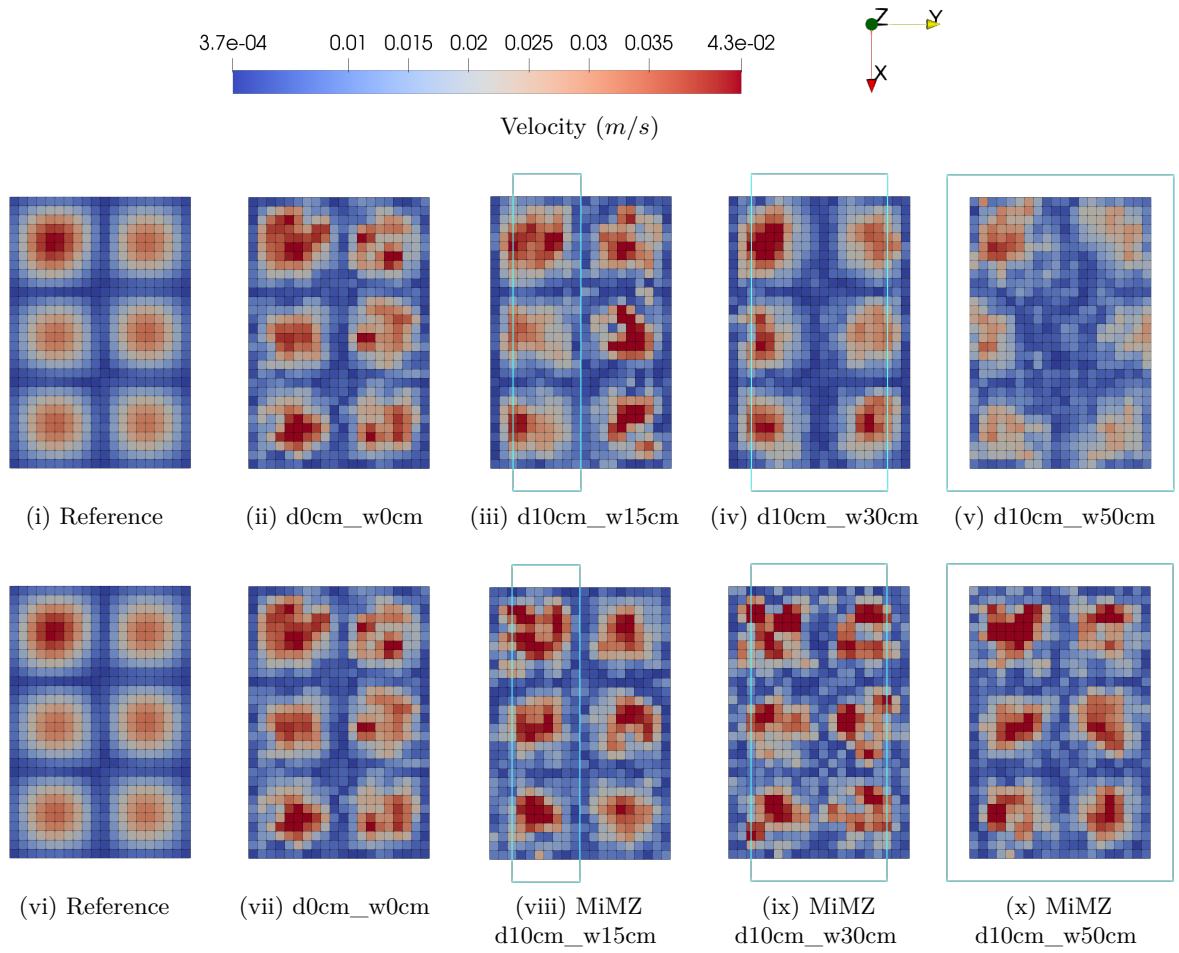

Figure 5.16: Spatial colormap distribution of the amplitude of the velocity on the surface of the source identified with u-iPTF using `Tikh_RGCV` and the reference computed results at a frequency of 332 Hz for different masking object width test set-ups. The outline position of the masking object is shown by the cyan-colored rectangle and the acronym MiMZ indicates 'Measurement in Masked-Zone'.

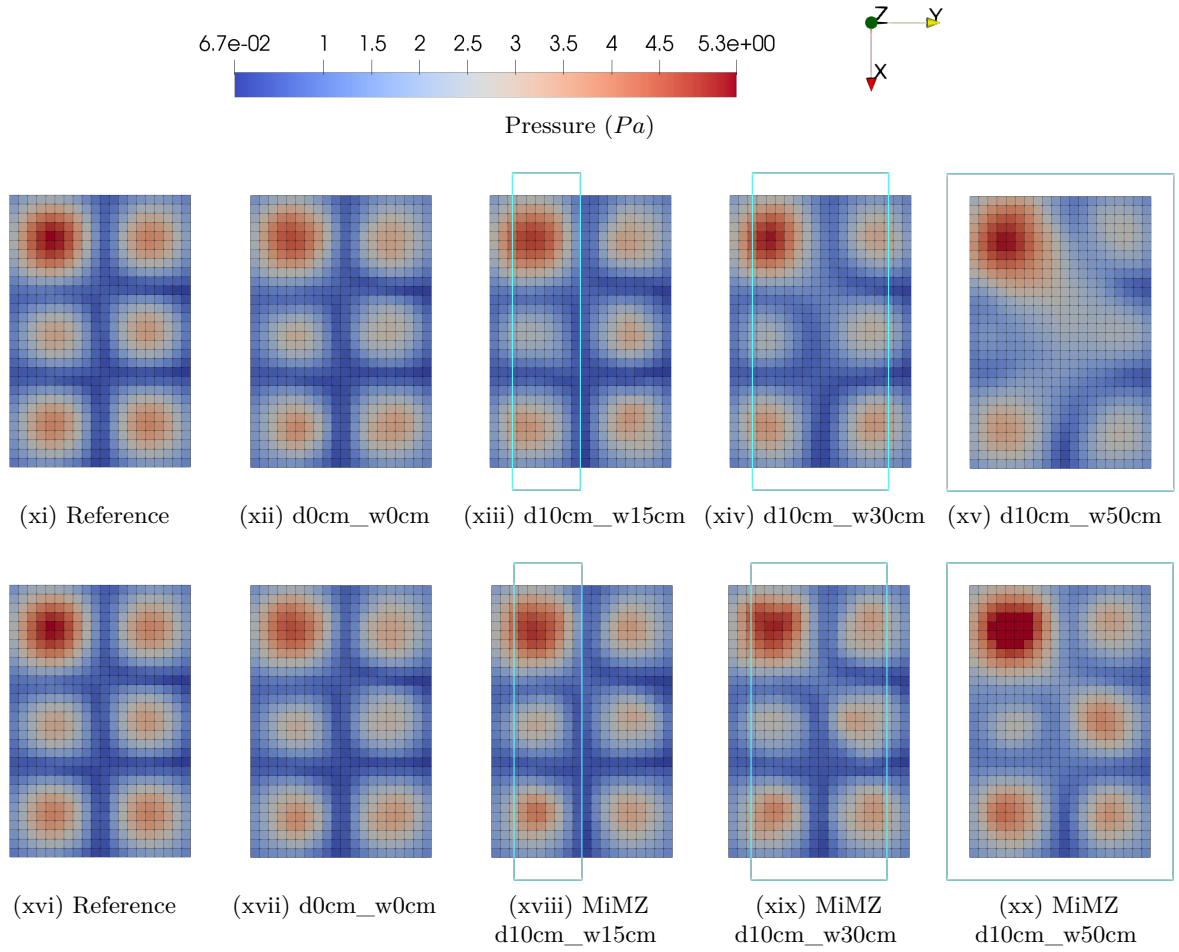

Figure 5.17: Spatial colormap distribution of the amplitude of the pressure field on the surface of the source identified with u-iPTF using `Tikh_RGCV` and the reference computed results at a frequency of 332 Hz for different masking object width test set-ups. The outline position of the masking object is shown by the cyan-colored rectangle and the acronym MiMZ indicates 'Measurement in Masked-Zone'.

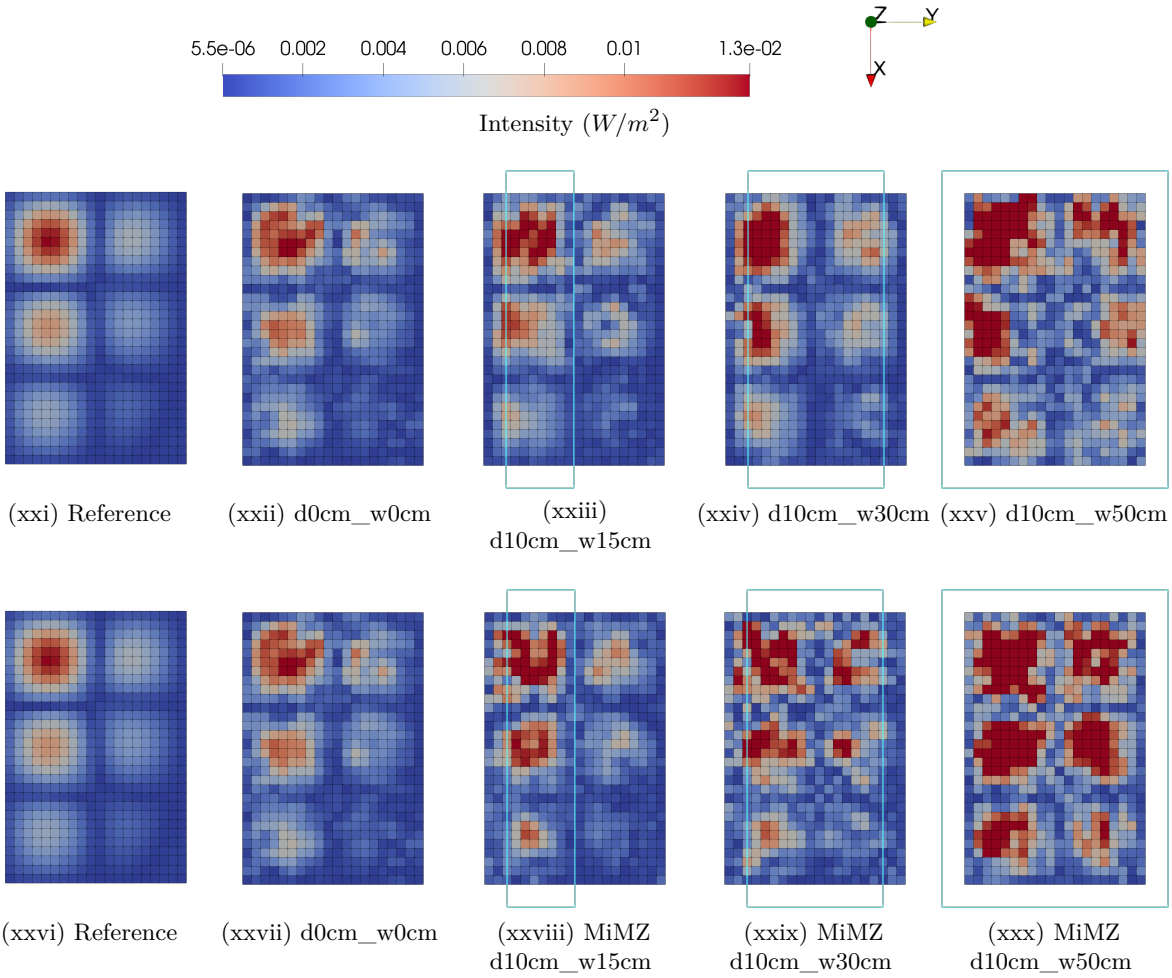

Figure 5.18: Spatial color-map distribution of the amplitude of the intensity field on the surface of the source identified with u-iPTF using `Tikh_RGCV` and the reference computed results at a frequency of 332 Hz for different masking object width test set-ups. The outline position of the masking object is shown by the cyan-colored rectangle and the acronym MiMZ indicates 'Measurement in Masked-Zone'.

Putting microphones in the masked zone clearly improves the quality of the reconstruction of the velocity fields as can be seen in Figure 5.15. This is due to the fact that these microphones are in the vicinity of the plate, in the masked zone where the two-facing-walls effect is dominant. The effect of putting microphones in the masked zone is clearly beneficial but not mandatory which paves the way to an experimental applicability of the iPTF approach even in a presence of large masking objects.

As can be seen in Figures 5.19, the main effect of the presence of the masking object is on the estimation of the radiation efficiency of the plate which is overestimated by iPTF approach. If the size of the masking object is small enough (here for 37.5% of the source surface), the effect is negligible and the radiation efficiency is well estimated. However, when the covered surface is too significant, the estimation of the radiation efficiency produces wrong results. Putting microphones in the masked zone has a significant effect on this estimation as d0cm_w0cm case is comparable to the case without obstacle on the whole frequency range. The radiated acoustic power is slightly overestimated by approximately 2-3 dB mainly for the biggest masking object that cover 100% of the source surface.

The approach for validating the identified far field pressure response is identical to that described earlier. Figures 5.20 and 5.21 present the directivity plots in ZX and ZY planes

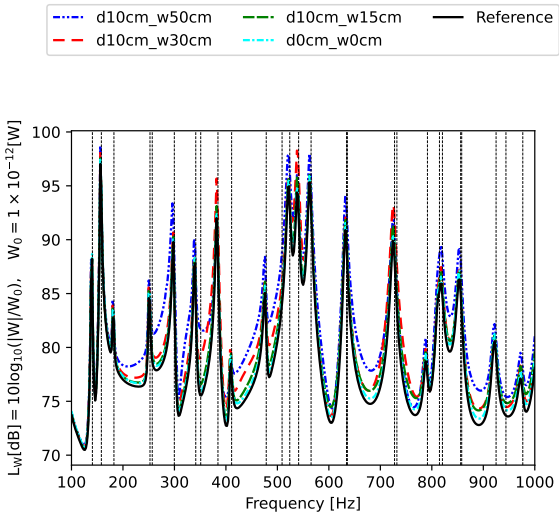

(i) Power (dB) for no-measurement in masked-zone

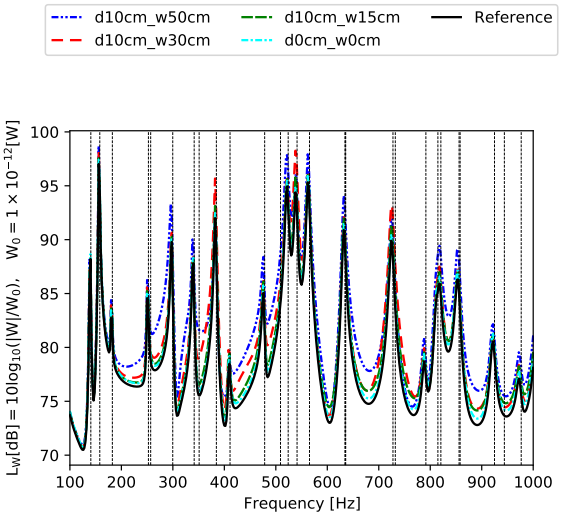

(ii) Power (dB) for measurement in masked-zone

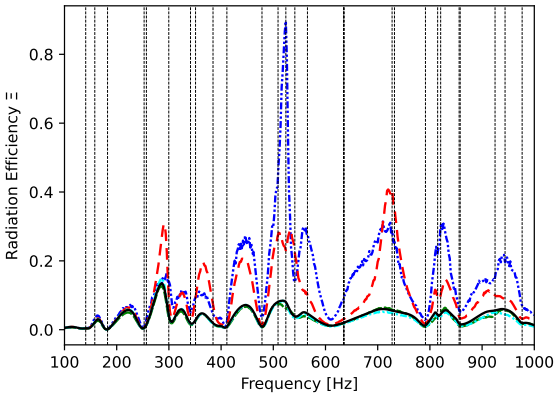

(iii) Efficiency for no-measurement in masked-zone

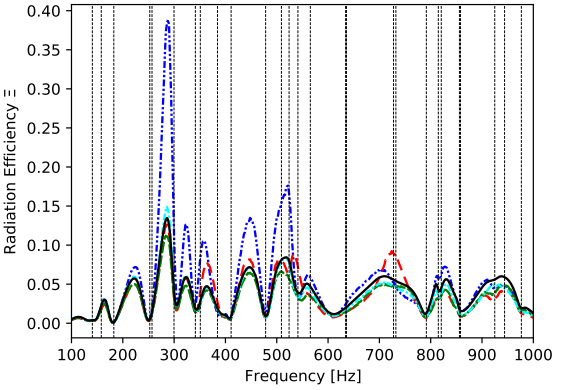

(iv) Efficiency for no-measurement in masked-zone

Figure 5.19: Plots of global acoustic indicators identified by u-iPTF with `Tikh_RGCV` and the reference computed result for the different masking object width test set-ups.

respectively, for two frequencies: 478 Hz and 1000 Hz.

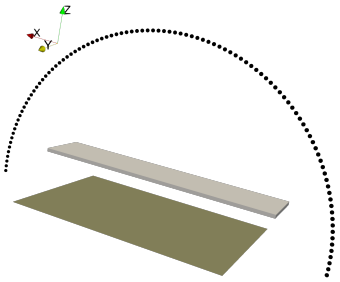

(a) Set-up of the semi-circular array

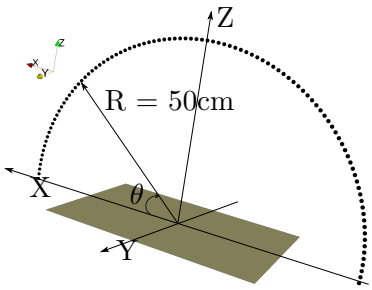

(b) Dimensions of the semi-circular array

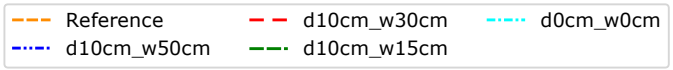

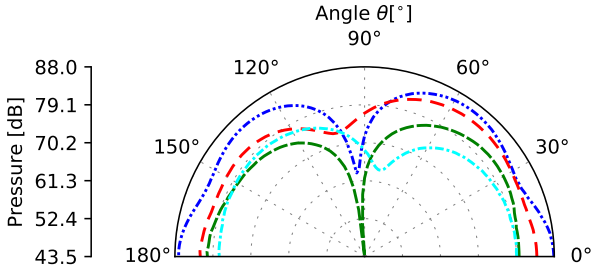

(c) DFR at 478 Hz from excited plate with masking object

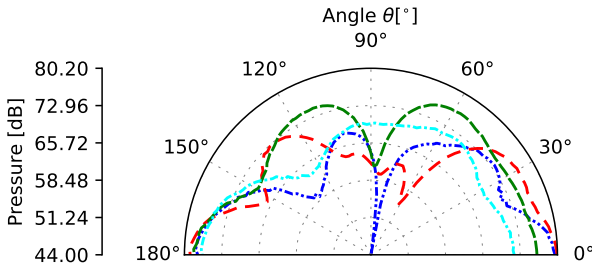

(d) DFR at 1000 Hz from excited plate with masking object

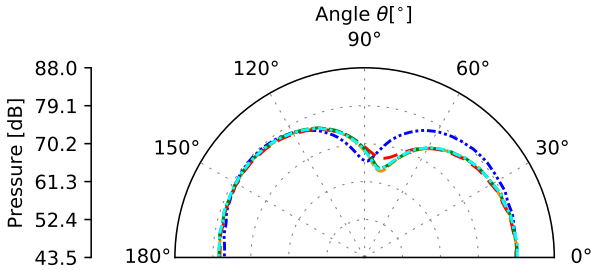

(e) DFR at 478 Hz from BC mesh using iPTF velocity

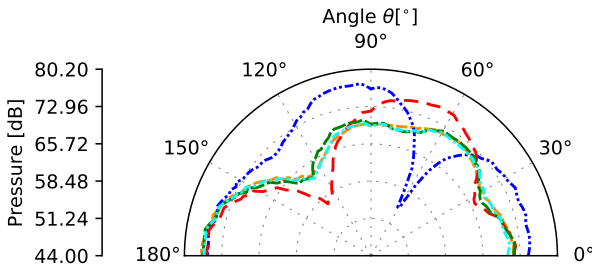

(f) DFR at 1000 Hz from BC mesh using iPTF velocity

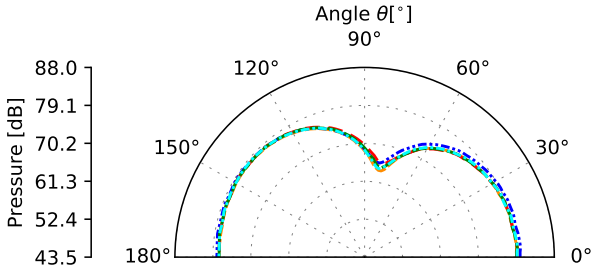

(g) DFR at 478 Hz from BC mesh using iPTF velocity of MiMZ

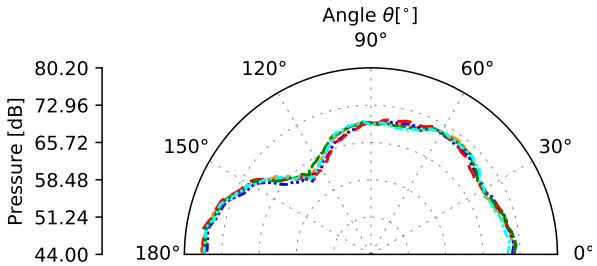

(h) DFR at 1000 Hz from BC mesh using iPTF velocity of MiMZ

Figure 5.20: Settings and polar pressure radiation pattern of the ZX semi-circular array recorded at a frequency of 478 Hz and 1000 Hz for the different masking object distance test set-ups.

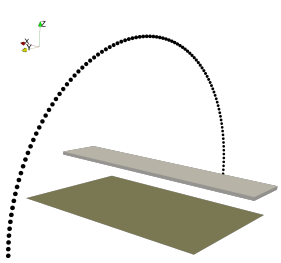

(a) Set-up of the semi-circular array

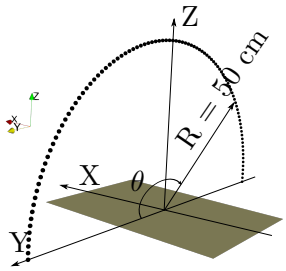

(b) Dimensions of the semi-circular array

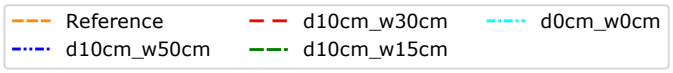

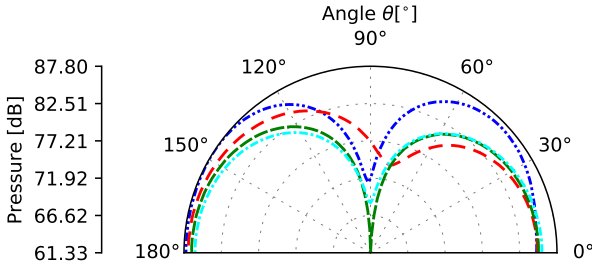

(c) DFR at 478 Hz from excited plate with masking object

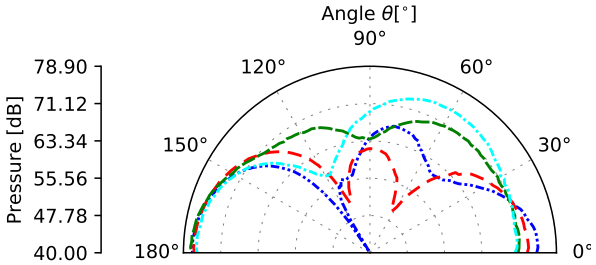

(d) DFR at 1000 Hz from excited plate with masking object

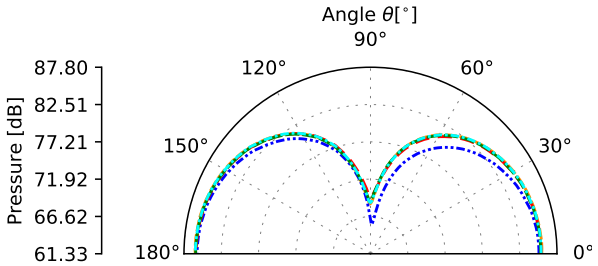

(e) DFR at 478 Hz from BC mesh using iPTF velocity

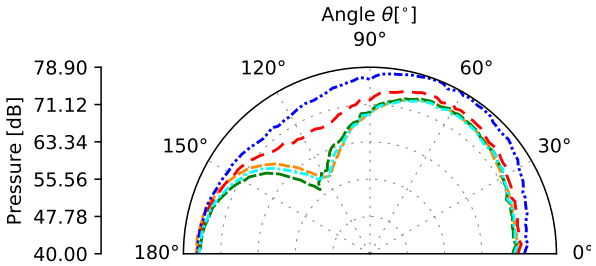

(f) DFR at 1000 Hz from BC mesh using iPTF velocity

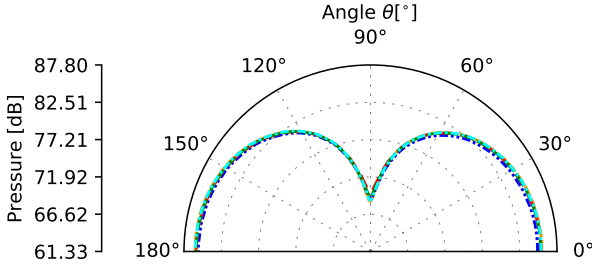

(g) DFR at 478 Hz from BC mesh using iPTF velocity of MiMZ

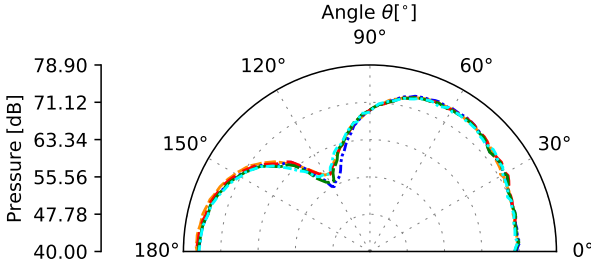

(h) DFR at 1000 Hz from BC mesh using iPTF velocity of MiMZ

Figure 5.21: Settings and polar pressure radiation pattern of the ZY semi-circular array recorded at a frequency of 478 Hz and 1000 Hz for the different masking object distance test set-ups.

Figures 5.20(c)-(d) and 5.21(c)-(d) shows the directivity plots that would be measured in the presence of the masking object in the ZX and ZY planes respectively for two frequencies: 478 Hz and 1000 Hz. The influence of the presence of the masking object clearly changes the directivity

patterns in both planes and for the two frequencies even if the effect is more pronounced at 1000 Hz. This results are compared to the directivity plots computed using the identified velocity fields as boundary conditions for a DFR analysis with masking object: the objective is here to evaluate if the iPTF approach is able to "cancel" the influence of the masking object on the estimation of the directivity plots of the source itself. When using microphones only outside the masked zone, the results are plotted in Figures 5.20(e)-(f) and 5.21(e)-(f). When using microphones everywhere in the virtual volume, the results are plotted in Figures 5.20(g)-(h) and 5.21(g)-(h). At low frequency, 478 Hz here, the results are really good, a residual effect of the presence of the masking object being only visible for the d10cm_w50cm case even if no microphone is placed in the masked zone. Again, this is a remarkable result for iPTF approach. At higher frequency, here 1000 Hz, the influence of the masking object is more pronounced and the presence of the object is not completely "canceled". To reach this "cancelling effect", one needs to put microphones in the masked zone. By doing this, the estimated directivity plots are really similar to those computed directly without masking object.

To evaluate objectively the estimation of the directivity plots on the whole frequency range, the $\mathcal{CI}$ metric is used to compute the similarity between two directivity patterns. In Figure 5.22, three different types of directivity patterns are compared to the same case: a direct computation without masking object. The three categories of directivity patterns are the following:

- directivity patterns obtained from direct computation in the presence of the masking object. These patterns are denoted direct_w15cm, direct_w30cm and direct_w50cm. For this category of patterns, the $\mathcal{CI}$ metric indicates that the directivity patterns are highly affected by the presence of the masking object, as expected. Obviously, the larger the masking object, the more different the directivity pattern compared to the case without masking object.

- directivity patterns using velocity fields identified using iPTF without microphones in the masked zone. These patterns are denoted iPTF_w0cm, iPTF_w15cm, iPTF_w30cm and iPTF_w50cm. The results plotted in Figure 5.22 for this category illustrate the "cancelling effect" of iPTF approach. For all the object widths, the $\mathcal{CI}$ metric is higher than 0.9 (except for the d10cm_w50cm above 800 Hz) showing a high similarity between the directivity patterns computed from iPTF results with a masking object and the directiviy pattern obtained with a direct computation without masking object.

- directivity patterns using velocity fields identified using iPTF with microphones in the masked zone. These patterns are denoted iPTF_MiMZ_w0cm, iPTF_MiMZ_w15cm, iPTF_MiMZ_w30cm and iPTF_MiMZ_w50cm. This category clearly shows that putting microphones in the masked zone is beneficial as the produced directivity patterns are almost identical to the one without masking object.

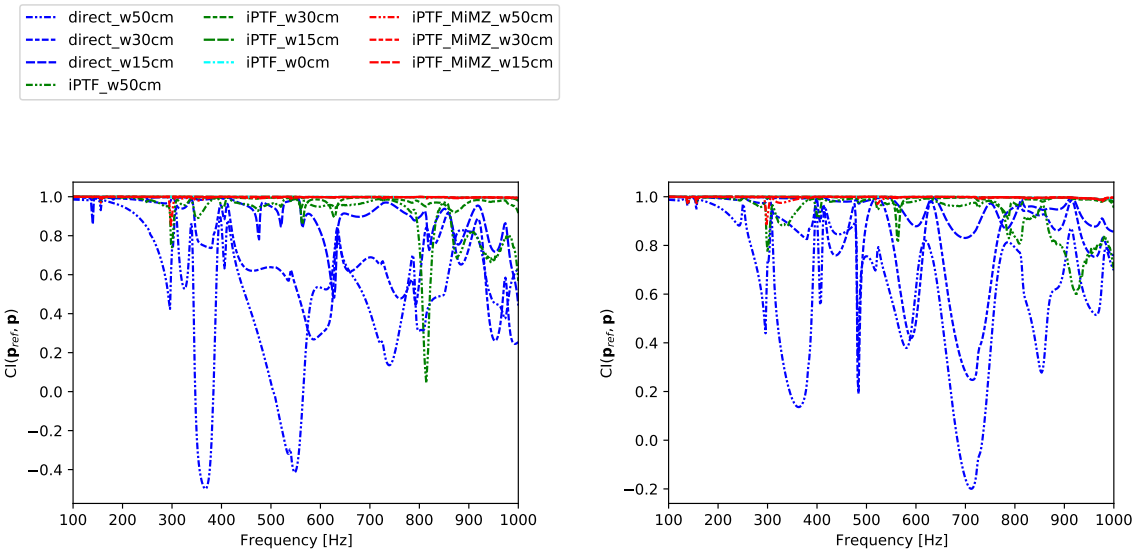

(a) $\mathcal{CI}$ of ZX-microphone array

(b) $\mathcal{CI}$ of ZY-microphone array

Figure 5.22: Evaluation of the similarities of different directivity patterns compared to the directivity pattern computed without masking object. The $\mathcal{CI}$ metric is used to evaluate the similarity on the 101 points of the semi-circular array. "direct" means that the directivity to be compared to is computed with the presence of the masking object and without the use of iPTF results. "MiMZ" means "Measurement in the masked zone".

5.5 Summary and Conclusion

The requirement to complete the overall aims of the PhD thesis work in regard to the detection and description of acoustic sources drove this investigation. One of the expectations is the blind reconstruction of sources utilizing the iPTF approach provided in this chapter. Dealing with the existence of a masking object is rather uncomplicated thanks to its formulation and the FE modelling of the virtual volume. It simply entails taking into consideration the masking obstacle's "footprint" in the virtual volume and computing the acoustic impedance matrices appropriately. This is a very useful feature for dealing with mounting frames, wires, and reflecting walls in industrial applications.

A comprehensive parametric investigation of blindly identifying an acoustic source was conducted, taking into account the effect of the masked object distance from the source and its width across the source.

The very-nearfield information and radiated far-field information are used to validate the results. The very-nearfield information on the source surface is objectively evaluated by performing a correlation analysis utilizing the $\mathcal{CI}$ metrics between the reference and identified acoustic fields. Then the directivity patterns of the radiated pressure response computed from the velocity fields identified by iPTF using data collected in the presence of the masking object were compared to those obtained from data without masking object. It was shown that both produce the same directivity patterns, indicating that iPTF is able to "cancel" the influence of a masking object.

It is critical to emphasize to the reader that the goal of these investigations is to prove that these various test set-up scenarios with the masking object present provide nearly the same identification results as when the masking object is absent. Even in severe test set-up scenarios, good correlations were achieved.

6 Industrial Application

The major goal of this chapter is to test the suggested iPTF blind reconstruction method in an experimental setting. As a result, an experimental campaign was carried out using the Siemens XiL test rig that operates a SimRod e-motor. The Simrod e-motor, as the name suggests, is an electric motor that operates on the induction principle and is often used in fully electric or hybrid electric vehicles (FEV/HEV). The induction motor has the benefit of being basic in design, resulting in a low-cost build. The Noise, Vibration, and Harshness (NVH) characteristics of an induction motor are influenced by a variety of factors, including machine size, material qualities, and electromagnetic design. In terms of ride and acoustic comforts within the car, an NVH study is crucial.

The chapter proceeds with a description of the test setup under investigation, followed by a presentation of the selected SimRod e-motor driving cycle. The application of the m-iPTF method (the choice of m-iPTF was driven by the available sensors) to reconstruct the acoustic fields on the surface of the e-motor is described afterwards. Two methods are used to verify the m-iPTF results. The first method of validation is to compare the m-iPTF findings to the Acoustic imaging results computed using the Bayesian Focusing technique [233]. The other form involves a masking object made of a wooden panel, placed near the SimRod e-motor used to evaluate the blind reconstruction with m-iPTF method.

6.1 e-Drive motor: setup description and operational conditions

The XiL test rig is shown in Figure 6.1. It consists of the SimRod e-motor, which is the part under investigation in this chapter, mounted on a coupling unit. A load is applied to the SimRod e-motor using a "load motor". The system is rigidly mounted on a heavy frame uncoupled from the rest of the workshop. The acoustic environment is not anechoic and also integrates noise generated by electric cabinets (one of them is visible in Figure 6.1).

A typical operational trajectory of the SimRod e-motor is shown in Figure 6.2. During the test, the speed is increased during 5 seconds from 0 to 2500 rpm and then is kept constant for approximately 17 seconds. During this constant speed step, the corresponding torque is in between 10 and 14 Nm. Then, the speed is decreased to 0 in 5 seconds. In all the runs, the cooling fan visible on the SimRod e-motor in Figures 6.1 and 6.3 was off (not in operation).

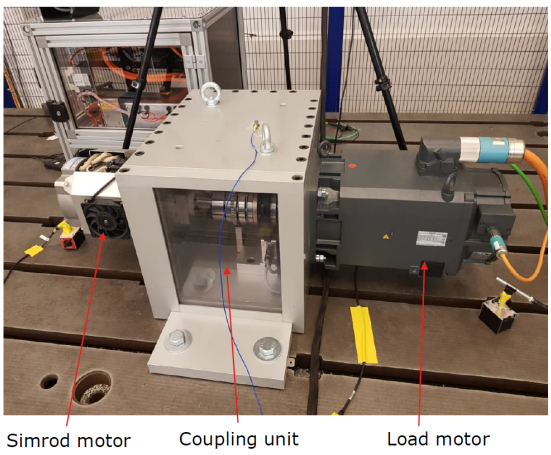

Figure 6.1: XiL test rig setup from Siemens lab.

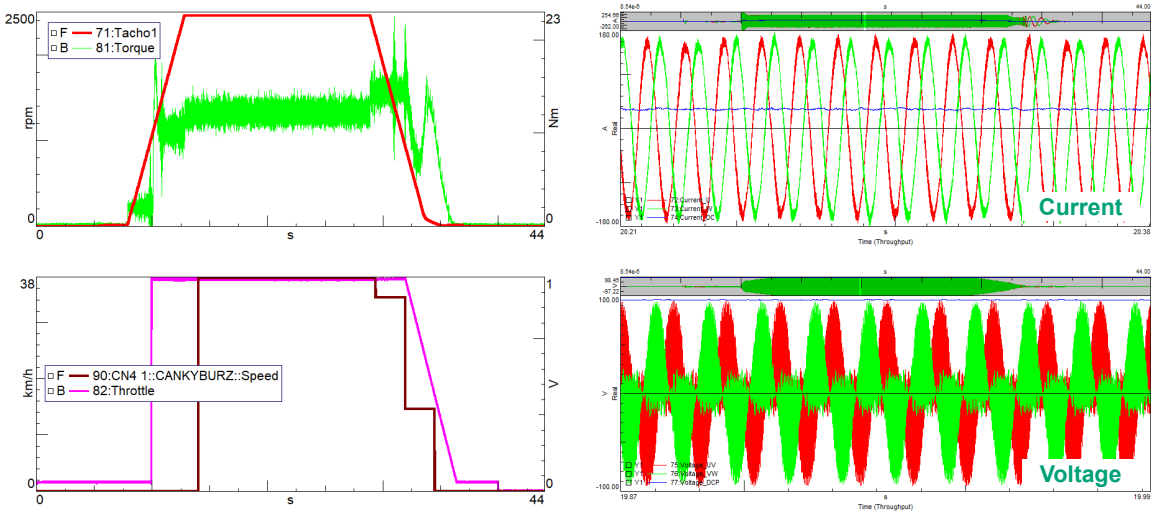

Figure 6.2: Test conditions and e-motor response

For the application of the m-iPTF approach, only the phase with a constant speed will be considered. As a results, the following operational conditions are:

- the E-drive was run in Eco-mode
- a speed of 2500 rpm was set
- a torque of 10-14 Nm was applied on the motor

6.2 Description of the application of iPTF approach

6.2.1 Definition of the virtual acoustic volume

Identification patch mesh

The aim of the present experiment is to reconstruct the acoustic fields directly on the surface of the SimRod e-motor in the [0...2000] Hz frequency range. To find a trade-off between the maximum frequency to reach and the complexity of the geometry to discretize, an average size of 30 mm has been defined for the identification patches. Therefore, 716 patches are used to discretize the surface of the SimRod e-motor as can be seen in Figure 6.3.

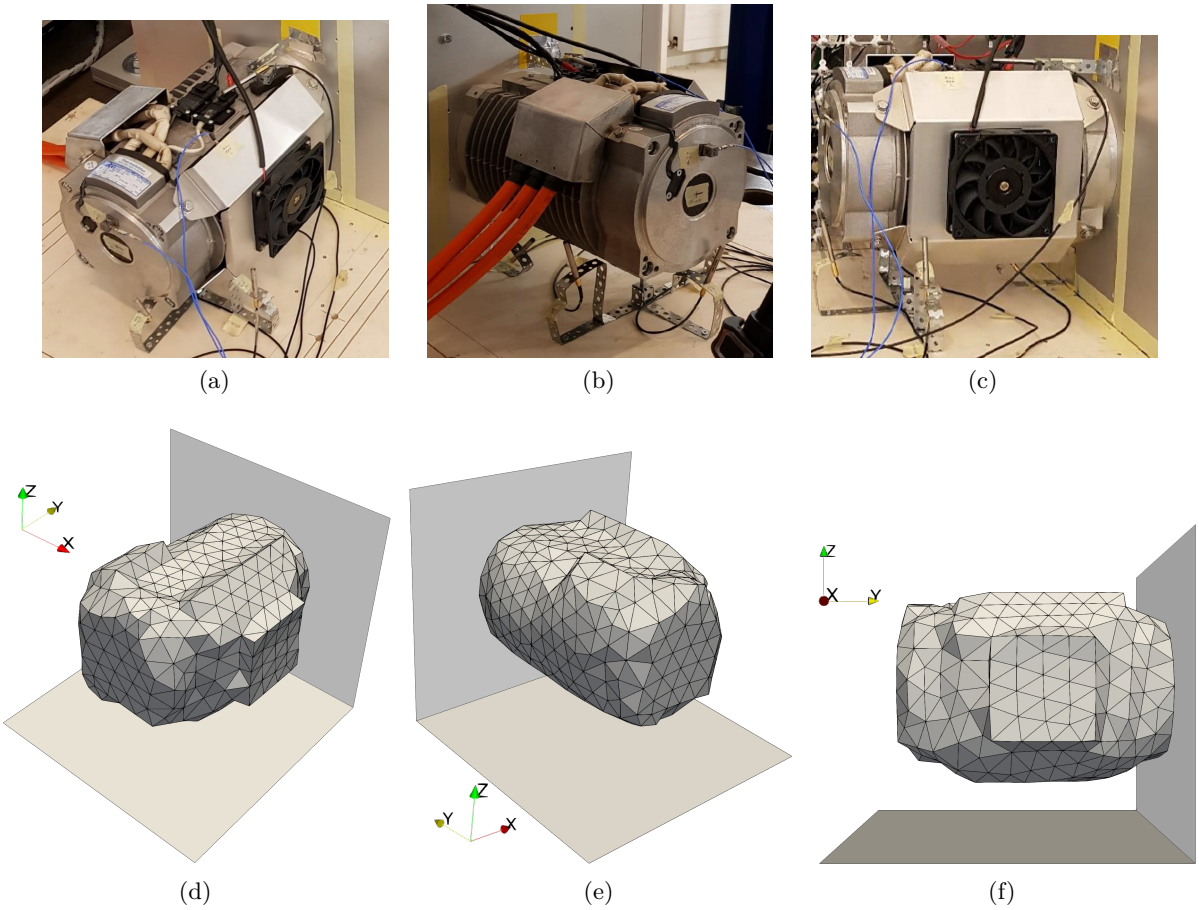

(a) (b) (c)

(d) (e) (f)

Figure 6.3: SimRod e-motor set-up representation : (a)-(c) real and (d)-(e) Identification patch mesh

Virtual surface patch mesh

The virtual surface surrounding the SimRod e-motor is composed of 4 planar measurement surfaces on the right, left, front and top sides. The four surfaces are composed by square patches of dimensions 40×40 mm as can be seen in Figure 6.4. This patch size allows applying m-iPTF up to 2 kHz with a $\lambda/4$ criterion. The left, right and front surfaces are divided into 10 (horizontal) by 9 (vertical) patches. The top surface is divided into 10 by 10 patches. The total number of patches is 370 (see Table 6.1 for FEM model description). The ground and the surface of the coupling unit will be considered as two physically rigid surfaces and as such will not be discretized into patches.

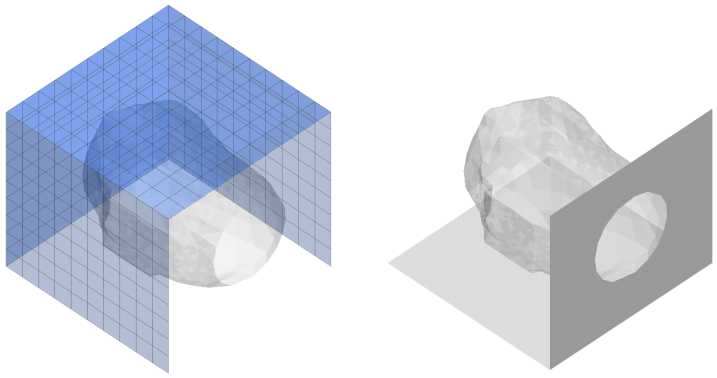

(a) (b)

Figure 6.4: Virtual surfaces delimiting the virtual acoustic volume. (a) virtual surface patch mesh and (b) rigid surfaces not discretized into patches. The transparent shape of the e-motor is drawn to see the layout of the surfaces in relation to the e-motor.

FEM parameters	**Patch model**		**Field-point model**	
	Source patches	Virtual surface patches	Cavity field-points	Virtual surface field-points
Element geometries	Triangular	Quadrangular	point	point
Mean element edge length [mm]	30.8	40	-	-
Number of nodes	363	370	694	370
Mean aspect ratio	1.2697	1	-	-
Number of elements	706	370	-	-
Interpolation	Linear	Linear	Linear	Linear

Table 6.1: FEM topology used in the computation of the modal transfer (impedance) matrices $\mathbf{Y}_{mk}$ and $\mathbf{Z}_{mk}$ of Equation (3.3).

Virtual volume mesh

The virtual volume is defined as the acoustic volume surrounded by the union of the 4 planar measurements surfaces composing the virtual surface described previously and 2 physically rigid surfaces (ground and surface of the coupling unit). The virtual volume consists then of a box with the footprint of the SimRod e-motor whose shape is described by the virtual surface patch mesh as can be seen in Figure 6.5 (see table 6.2 for FEM model description). The orange wires, visible in Figure 6.3 (b) were not taken into account in the virtual volume and, as such, their influence is assumed to be negligible.

To be able to compute natural frequencies and mode shapes of the virtual volume up to 8000 Hz, the average size of the tetrahedral elements is set to 8 mm approximately as presented in Table 6.2. Up to 8000 Hz, 2102 mode shapes are extracted for the virtual volume and will be used in Equation (3.3) to compute the impedance matrices. A total number of 694 field points is positioned inside the virtual volume (see Table 6.1). The description of their respective positions will be detailed in Section 6.2.2.

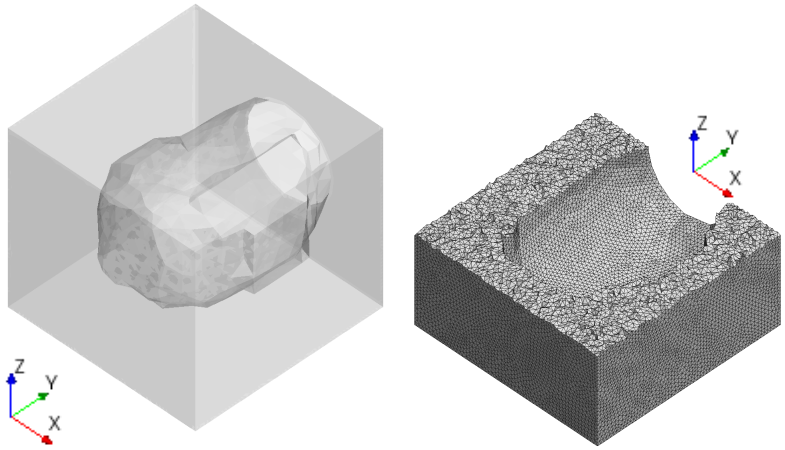

(a) Unmesh model (b) XY cut section

Figure 6.5: Virtual cavity FEM model used in the modal extraction analysis. Definition of the surfaces delimiting the virtual acoustic cavity and the associated boundary conditions (b.c)).

FEM parameters	**Virtual cavity mesh model**
Element geometries	Tetrahedral
Mean element edge length [mm]	8.3
Number of nodes	143649
Mean aspect ratio	1.6024
Number of elements	787942
Interpolation	Linear
Spatial dimension $L_x \times L_y \times L_z$ [mm]	$400 \times 400 \times 360$

Table 6.2: FEM topology used in the modal extraction analysis simulation performed with ACTRAN

6.2.2 Acoustic measurements

In this section, the choice of applying only the m-iPTF approach was driven by the fact that only microphones were available. A specific array of 5×10 microphones with a spacing of 4 cm in both directions has been designed. The array has been used to measure the acoustic pressure on the centroids of the virtual surface patches by moving it sequentially (2 positions per face). To describe the whole virtual surface, 8 positions of the array were necessary as shown in Figure 6.7. As the measurements were sequential, some fixed references were defined: 5 microphones located close to the SimRod e-motor and 2 triaxial accelerometers glued directly on the e-motor as shown in Figure 6.6.

To measure the acoustic pressure at the 694 field points inside the virtual cavity, the array was moved toward the center of the virtual volume at two different positions spaced by 2 cm. One can see the slots used to put the array in position in Figure 6.8.

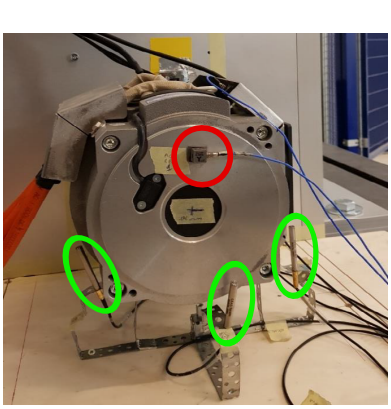

(a) Fixed Sensors: mic1, mic2, mic4 and accel1

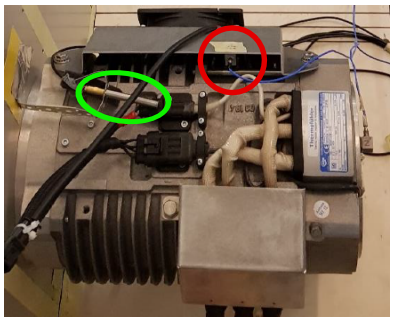

(b) Fixed Sensors: mic5 and accel2

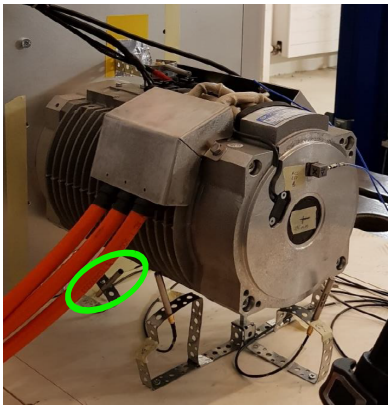

(c) Fixed Sensors: mic3

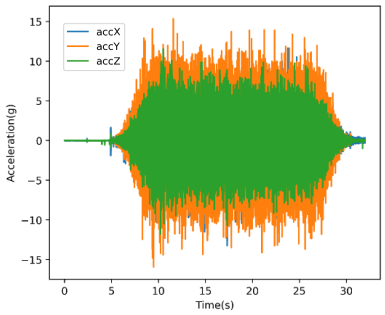

(d) Accelerometer accel1

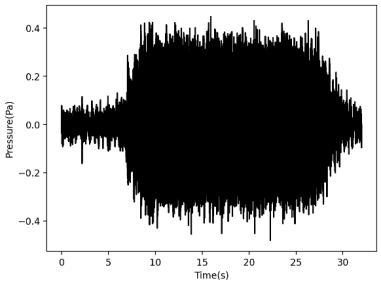

(e) Fixed microphone mic1

Figure 6.6: (a)-(c) settings of Reference sensors and (d)-(e) time domain signals for accel1 and mic1.

The signals of the sensors have been recorded during the whole run (see Figure 6.6) but only 10 seconds in the steady state were kept. The signals were recorded with a sampling frequency of 40.960 kHz. The signals acquired for the different positions of the array have been synchronized on the same event analyzing the signal of microphone as a fixed reference. The signals were then cut in 10 windows of 1 second, weighted by a Hanning window. Then a temporal-to-frequency conversion was done using a fast Fourier transform. Finally, a phase reference was chosen for all the positions of the array and the spectra were averaged. It results 370 spectra for the measurements on the virtual surface and 694 spectra for the measurements at the field points inside the volume. Each spectrum has a frequency range from 0 to 2000 Hz with a frequency

step of 0.5 Hz. An example of them (accelerometers accel1 and accel2) is plotted in Figure 6.9.

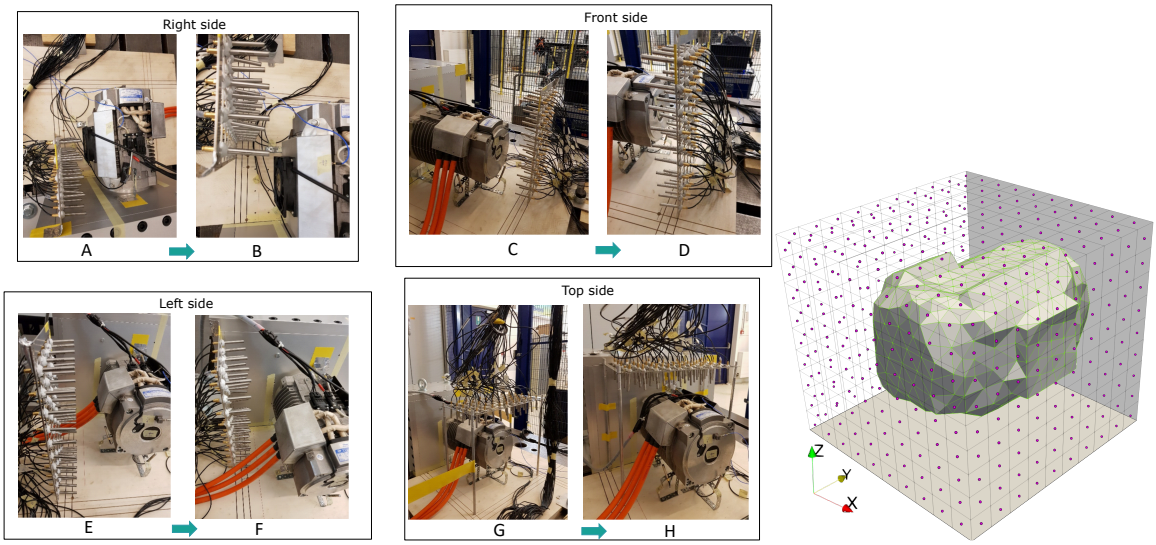

(a) (b)

Figure 6.7: (a) Steps involved in the pressure measurement on the virtual surface and (b) detail of the position of the microphones.

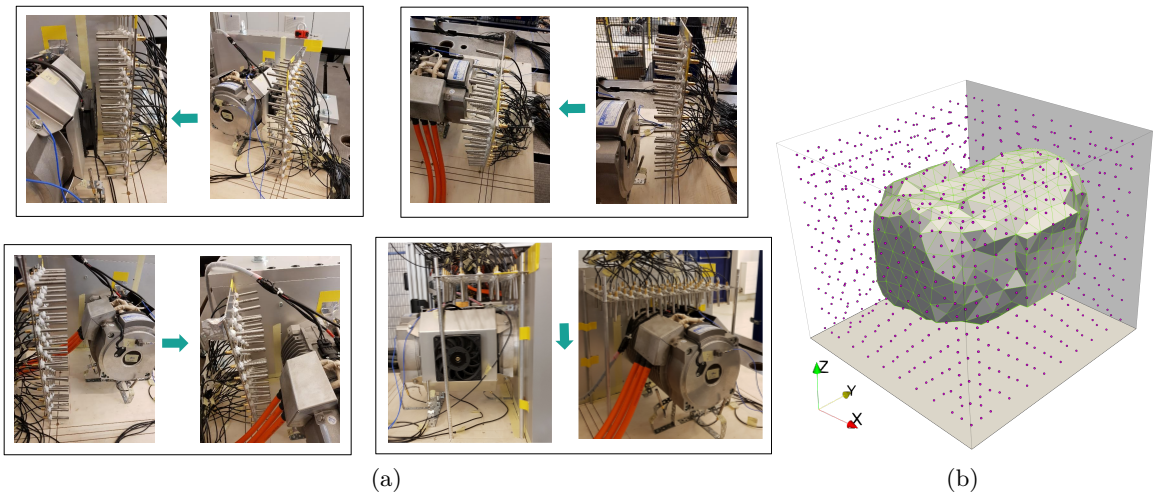

(a) (b)

Figure 6.8: (a) Steps involved in the pressure measurement inside the virtual cavity and (b) detail of the position of the microphones.

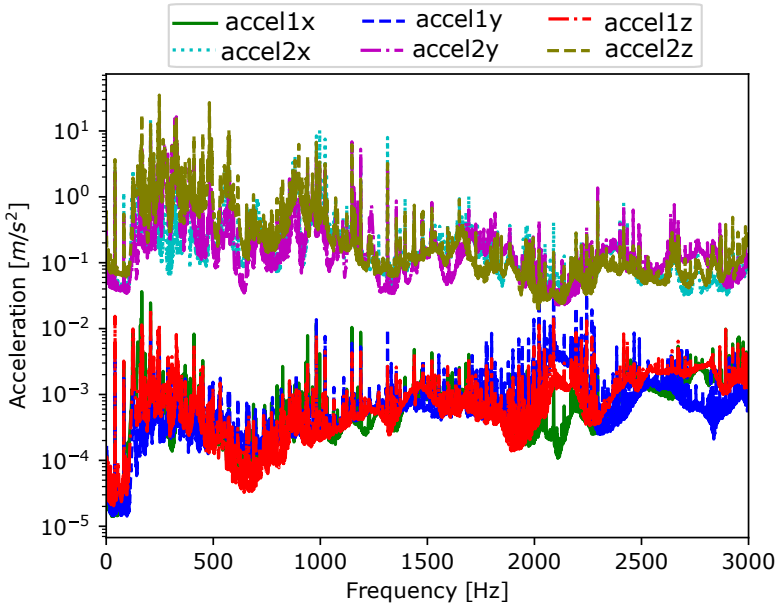

Figure 6.9: Converted acceleration spectra in frequency domain.

6.3 iPTF reconstruction without masking object and comparison to Acoustic Imaging results

At this point, the findings of the m-iPTF approach with `Itr_MINP` regularization strategy of Equation (A.2) for an obstacle-free situation are compared to the results of an Acoustic imaging method developed by Antoni [233] and marketed under the name "Bayesian Focusing approach" by MicrodB. In these noisy under-determined experimental studies, `Itr_MINP` of Equation (A.2) was chosen above `Itr_RGCV` of Equation (3.72) as the preferred regularization technique. This is due to the fact that, as stated in Section 4.5.1, `Itr_RGCV` and Tikhonov techniques in general perform poorly for under-determined systems.

The operating settings of the SimRod e-motor employed for the Bayesian methodology are the same as those stated previously for the m-iPTF method. Acoustic imaging measurements are made up of three circular microphone arrays carefully placed in three different places as shown in Figure 6.10. The objective for choosing these placements was to have a large field of view in order to capture the whole region of interest (SimRod e-motor). The array is placed at a distance of 0.3m from a "source plane". The "source plane" is a planar surface where it is assumed that the sought acoustic sources are located. The results produced by the Bayesian Focusing approach consist then in frequency averaged intensity maps back-propagated on a plane close to the source of interest. Therefore, the Bayesian Focusing approach will be used as a qualitative comparison with m-iPTF results which provides 3D mapping of the acoustic fields at one single frequency.

Figure 6.10 shows the localization maps identified by the Bayesian Focusing approach in the [570...700] Hz, [710...890] Hz and [1790...2240] Hz frequency bands. These maps are compared to the 3D mappings identified by m-iPTF approach at the frequencies 588.5 Hz, 719.5 Hz and 1992 Hz respectively. The plotted elemental power (intensity per unit patch area) fields and the color scales are defined to render the comparison easier. The so-called "dynamic range" for the Bayesian Focusing approach was set to 4 dB meaning that side-lobes and ghost images are neglected if their level is 4 dB lower than the maximum value in the map. The same "dynamic range" is set for iPTF 3D maps for sake of comparison. By analyzing Figure 6.10, some conclusions can be drawn:

- the main sources are located in the same zones for both methods. This is particularly visible for maps at 719.5 Hz and 1992 Hz. For example, the small source spot on the front

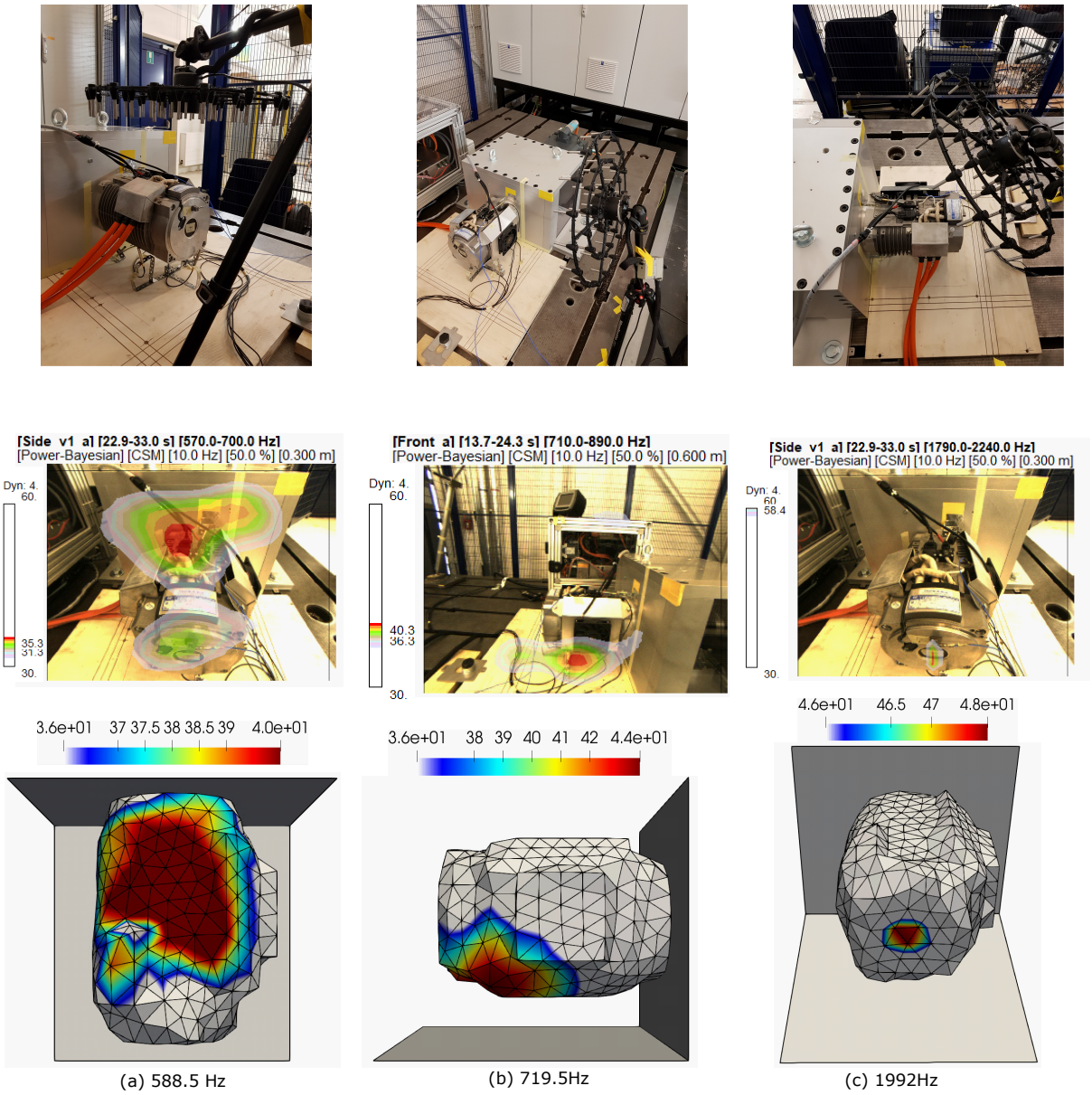

(a) 588.5 Hz (b) 719.5Hz (c) 1992Hz

Figure 6.10: Comparison of iPTF results to Bayesian Focusing results. Top: positions of the circular array for identifying maps with the Bayesian Focusing approach; Middle: maps identified with Bayesian Focusing approach. Bottom: 3D maps identified using m-iPTF and `Itr_MINP` regularization strategy.

side of the SimRod e-motor at 1992 Hz is to be located at the same position for both methods.

- the iPTF estimated levels are a little bit higher than those estimated by the Bayesian Focusing approach. This is due to the fact that in iPTF context, the values are estimated directly on the surface of the SimRod e-motor and not on a close plane as done by the Bayesian Focusing approach.

- On the surface of the SimRod motor, the iPTF displays very-nearfield power results thank to 3D mapping contrary to the Bayesian Focusing approach which only displays planar projections. This is true for most acoustic imaging techniques. The 3D maps of iPTF approach allows identifying easily which part of the system is the main source. It's more difficult using the Bayesian Focusing approach, for example at 588.5 Hz.

6.4 iPTF reconstruction in the presence of a masking object

6.4.1 Experimental and numerical setups

In the previous section, a first application of iPTF was compared to a Bayesian Focusing approach. The good comparison between these two methods is a proof of the applicability of the iPTF approach in an industrial context. Even if the rigid surfaces of the previous experiment (the ground and the surface of the coupling unit) can, per se, be considered as obstacles as they act as acoustic reflectors, they are not masking the SimRod e-motor itself. Therefore, to prove that the iPTF can be used even in the presence of a masking object, a new experiment has been designed.

This new experiment is identical to the previous one, except that a thick wooden panel has been inserted in the virtual acoustic volume. As can be seen in Figure 6.11, this thick wooden panel completely masks a part of the SimRod e-motor: almost two thirds of the side with the fan. To handle this case, the virtual acoustic volume has been modified accordingly, to take into account the footprint of the panel, see Figure 6.12. The measurements conditions were the same, except that one position of the array was not reachable any more. The corresponding field points have simply been suppressed in the iPTF process.

At this stage, one could argue that a masking object that is modifying only roughly a quarter of the pressure field is not enough to validate the approach. However, one has to keep in mind that the objective is to reconstruct the source fields directly on the 3D shape of the SimRod e-motor, including the part in between the SimRod e-motor itself and the masking object. In that zone, the source field is completely masked for all the microphones and for this reason, for some vibration patterns, the test case is, on the contrary, very challenging.

In addition, but this point is not due to the presence of the masking object, a small frequency shift has been observed between the two configurations: the characteristic peaks were not exactly the same between the two runs. This is due to the fact that the two runs were performed during two different days and the operational conditions always slightly change from one run to another, especially if there were not performed during the same day. However, this frequency shift was very small, only some Hertz up to 2000 Hz.

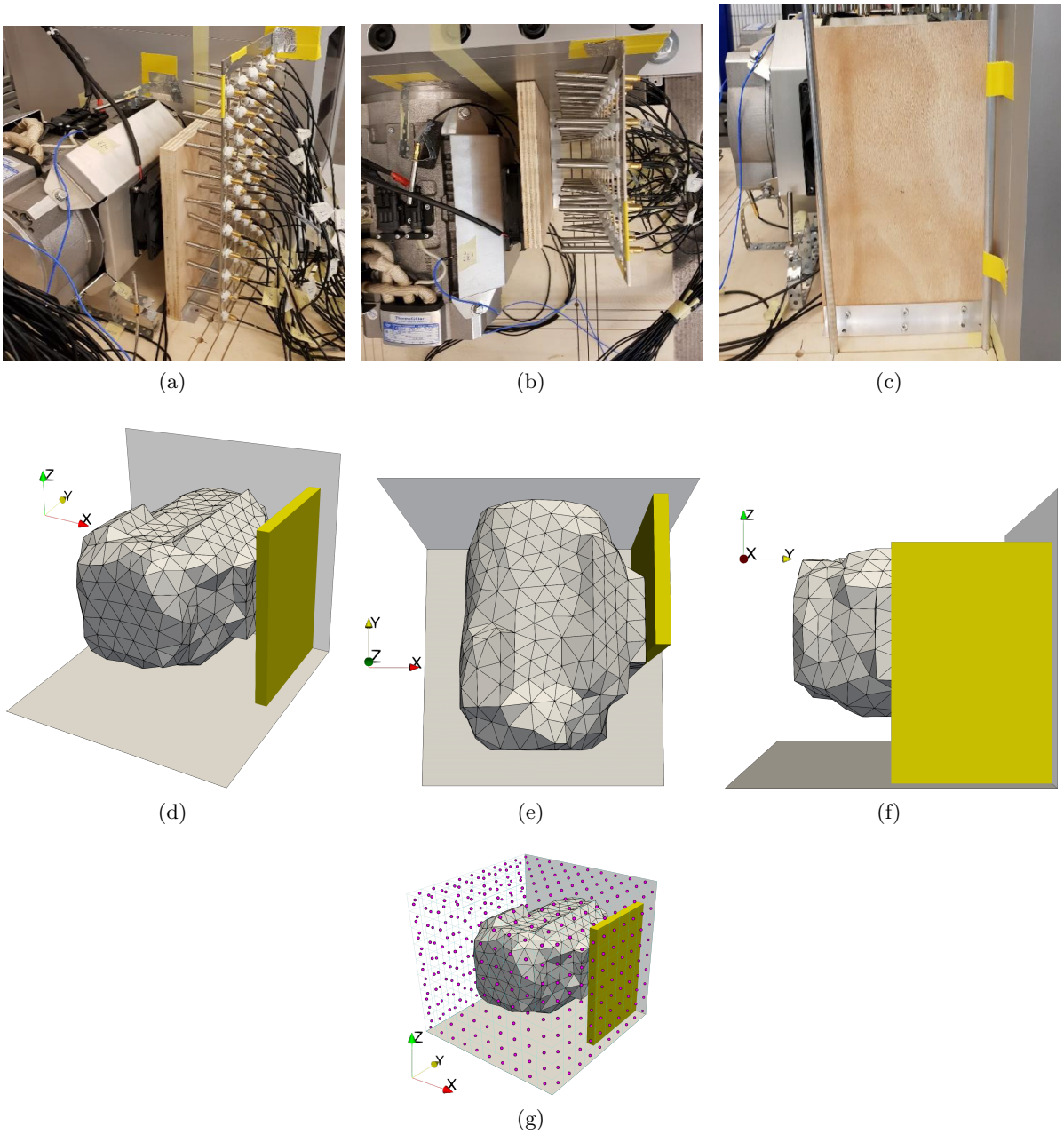

Figure 6.11: Simrod e-motor representation for set-up with obstacle: (a)-(c) real and (d)-(f) FEM model. (h): positions of the microphones on the virtual surface.

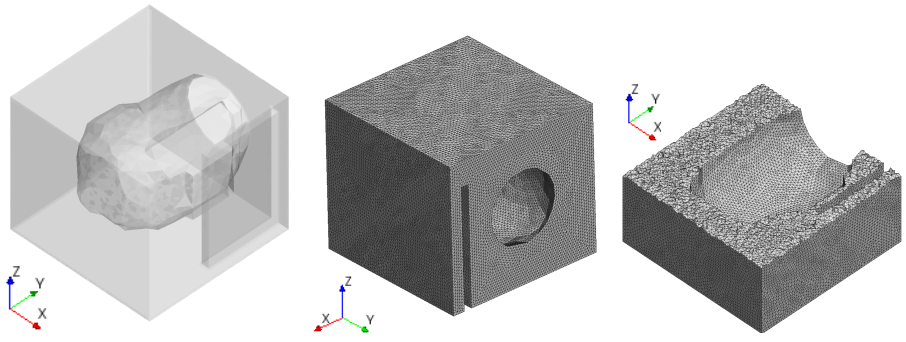

Figure 6.12: Virtual acoustic volume FEM model used in the modal extraction analysis.

6.4.2 Reconstruction and far-field results

The very-near field results represent the acoustic fields in close contact with the SimRod motors' enveloping-skin. The amplitude level of the acoustic intensity is the acoustic indicator used in the comparison. Figure 6.13 depicts intensity fields for the two configurations (with and without the presence of the masking object) evaluated at various frequencies.

It is expected that the intensity fields are not modified by the presence of the masking object.

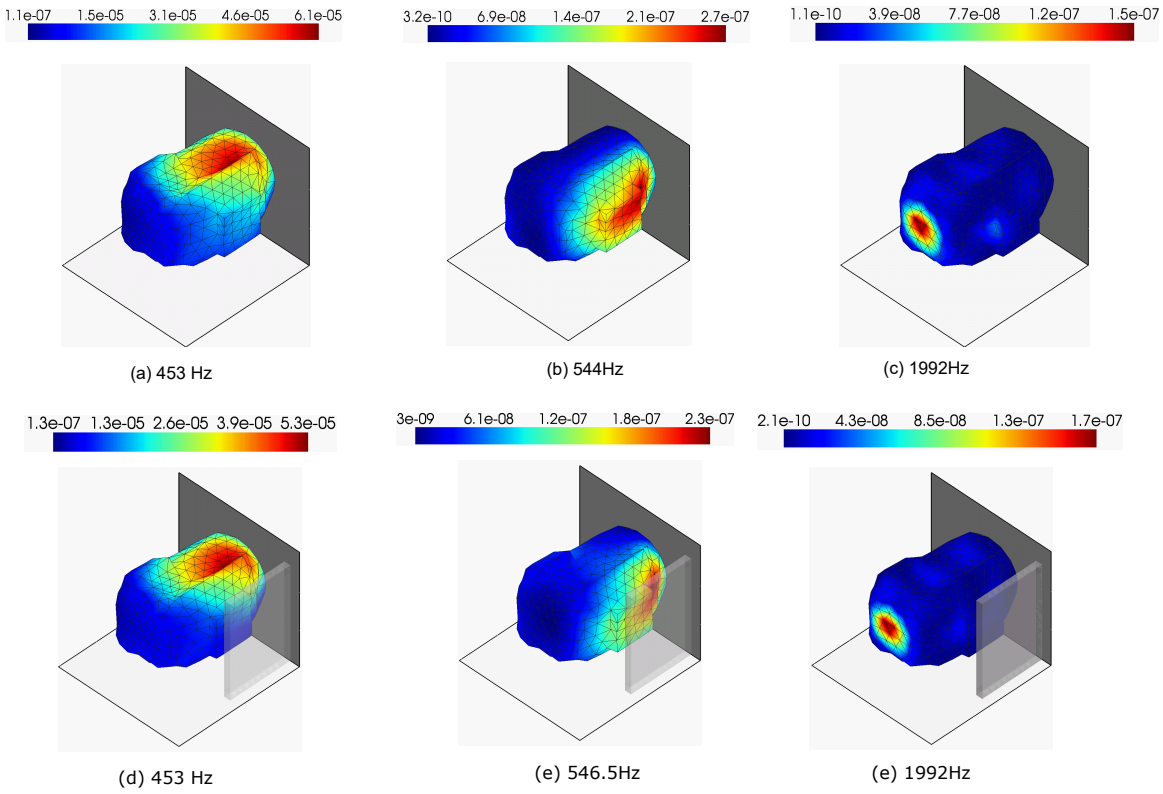

Figure 6.13: Comparison of Intensity field (W/m^2) identified with iPTF method for configuration with and without obstacle

Therefore, the intensity maps with and without masking object are supposed to be identical. The maps at 453 Hz and 1992 Hz are really similar in their distributions as well as in their levels. However, for this two frequencies, even if the masking object surely acts like an acoustic reflector, the "meaningful" pressure field might not have been modified a lot as the masking object is not actually masking these zones of the SimRod e-motor. This is not the case for frequency 544 Hz. The intensity field to be identified is mostly in front of the masking object so that almost no microphone is directly "seeing" this zone. This configuration is very challenging and, at our knowledge, no other method is able to reconstruct any field on such a masked zone. Figure 6.13(e) is proving that the iPTF approach has this powerful feature as the reconstructed field is really similar to the one obtained without masking object.

The far-field information from the two setups, with and without obstacle, is compared here. As is customary, the approach begins by translating iPTF velocity on source mesh patches to velocity fields on source mesh nodes, which serve as the Boundary condition (BC) in the subsequent ACTRAN DFR analysis. Figures 6.14 and 6.15 respectively depict the radiated pressure field in the XY-plane and the directivity diagrams in XY-plane for two diffent frequencies. Both of them are comparing the radiated fields computed from the two identified velocity fields, with and without the masking object.

As explained in Chapter 5, if the iPTF approach is able to "cancel" the influence of a masking object, the radiated pressure fields and the directivity diagrams should be the same when using

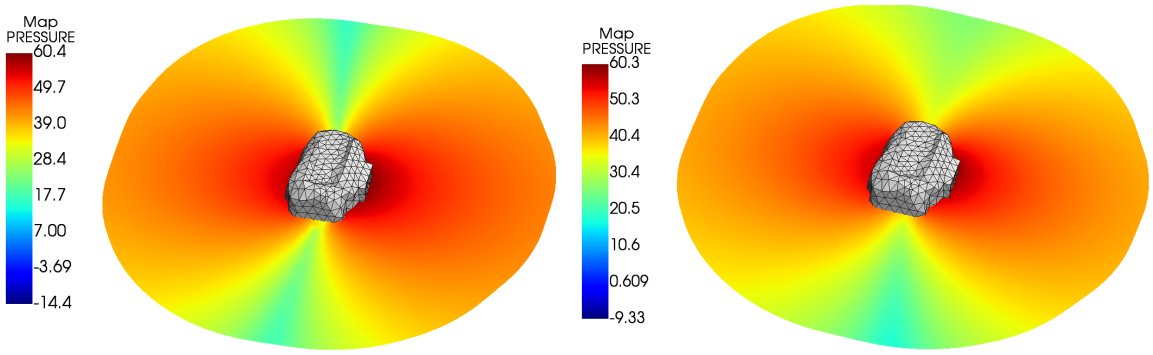

(a) 544 Hz (without masking obstacle)

(b) 546.5 Hz (with masking obstacle)

Figure 6.14: XY cutview section of the radiated pressure map for the configuration considered.

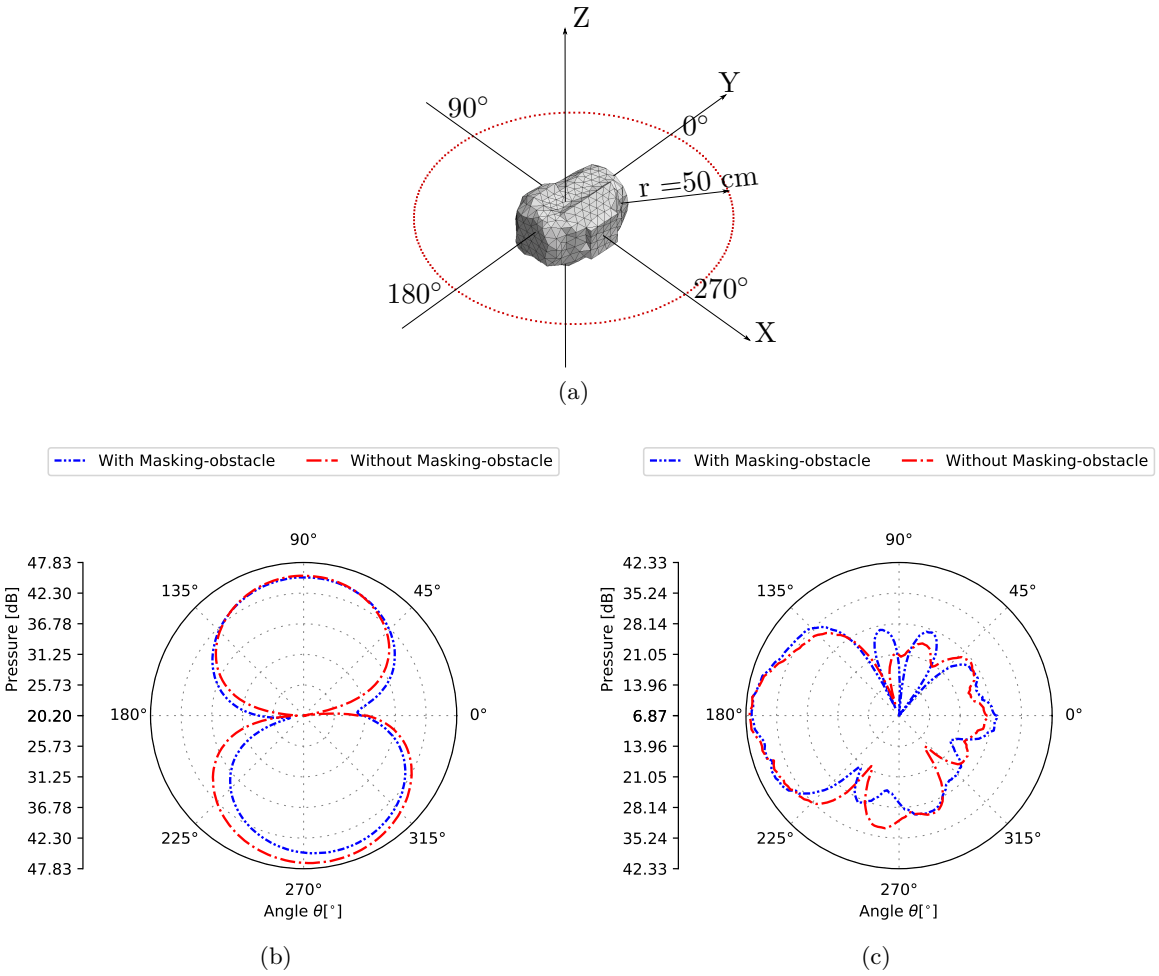

(a)

(b)

(c)

Figure 6.15: Directivity plot for 201 microphones positioned in the XY plane at 50cm from the centroid of the simrod e-motor. (a) settings ; (b) directivity diagram at 545 Hz ; (c) directivity diagram at 1992 Hz.

the velocity field identified without masking object or using the velocity field identified with the presence of the masking object. Figures 6.14 and 6.15(a) clearly show that this feature is still valid in experiment. Indeed, the radiated pressure field has a lobe directly in front of the masking object at 545 Hz. In the presence of the masking object this lobe should be highly modified: this is not the case as can be seen in Figures 6.14 and 6.15(a). This proves that iPTF approach is able to "cancel" the influence of a masking object on the radiated fields computed from the

velocity field identified with iPTF from measurements in the presence of the masking object.

To objectively evaluate this feature on the whole frequency band, the $\mathcal{CHA}$ correlation metric of Equation (C.9) is computed by comparing the directivity diagrams obtained from the two identified fields: the velocity fields with and without the masking object. The result is plotted in Figure 6.16(a). In addition, the corresponding radiated acoustic powers are compared in Figure 6.16(b).
Figure 6.16 shows a good correlation between the two computations. Figure 6.16(a) demonstrates

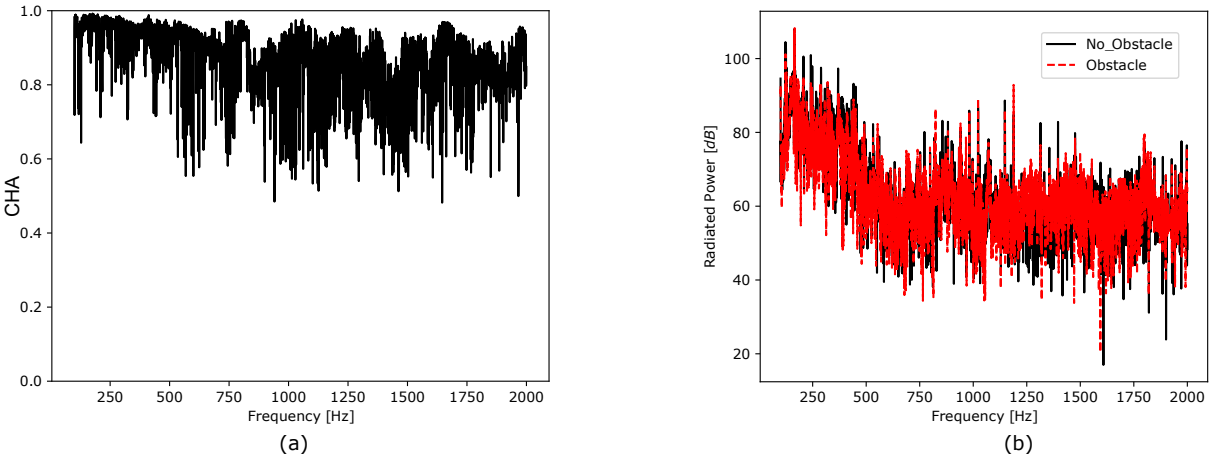

Figure 6.16: Comparison of the characterizations of the SimRod e-motor without and with the masking object. (a) $\mathcal{CHA}$ correlation metric computed by comparing the directivity diagrams obtained from the velocity fields identified from measurements with and without the presence of the masking object and (b) radiated acoustic power spectra computed from fields identified from measurements with and without the presence of the masking object.

that the directivity diagrams are highly comparable, especially at the radiated power peaks.

6.5 Summary and Conclusion

The suggested iPTF blind reconstruction method was put to the test in this chapter in an industrial setting. As a consequence, an experimental campaign was conducted utilizing the Siemens XiL test rig operating a SimRod e-motor.
This industrial application was performed with two main objectives: validating the iPTF approach in an industrial setting by comparing it to a commercial system based on the Bayesian Focusing approach and proving that the iPTF approach is able to handle the presence of a masking object. Even if subjective, the comparison to the Bayesian Focusing approach clearly shows comparable identified maps. This comparison demonstrates the applicability of the iPTF approach in an industrial context in a non anechoic acoustic environment.
In the second experiment, a masking object was put in the previously defined virtual acoustic volume. The FEM model for virtual acoustic volume has been modified accordingly. The identified maps appear to not be modified by the presence of the masking object even for zones not directly "visible" by sensors. To prove that the iPTF approach is able to "cancel" the influence of the masking object, the directivity diagrams are computed in a direct response computation using the identified velocity fields. Again, the directivity diagrams obtained from the velocity field identified from measurements without and with the masking object are similar. The results thus demonstrate that the iPTF approach is able to handle the presence of a masking object.

7 Blind Source Separation in iPTF context

The goal of this chapter is to show how to use spatial information from the iPTF perspective to separate incoherent sound sources that do not spatially overlap in frequency domain. This is useful in acoustical applications that need the identification and ranking of sound sources with various physical origins. The proposed approach, abbreviated as BSS-iPTF, follows a two-step process, the first of which is related to blind separation applied on the radiated acoustic fields and the second linked to source reconstruction with the iPTF method for each of the separated fields. The source mixture is expanded first into a linear combination of spatial basis functions, the coefficients of which are determined by back-propagating the pressures and/or velocities measured by an array of sensors to the source domain.

This results in a formulation that seems to be similar to blind source separation already published by Dong [234] but not identical. The coefficients are then blindly separated into uncorrelated latent variables, referred to as incoherent "virtual sources" in the second step. These are proven to be defined up to a rotation of any degree. Finally, a distinct set of sound sources is found by looking for the rotation that minimizes some spatial criteria such like spatial orthogonality or spatial disjointness. As a result, three separation criteria have been proposed: "decorrelation", "orthogonality" and "spatial disjointness". Moreover, the thorough derivation of the condition under which classical decorrelation (principal component analysis) can solve the problem is developed.

Numerical data is used to validate the proposed approach.

7.1 Introduction

In general, the iPTF approach can detect a radiated acoustic field based on the phenomena that cause it to exist. Separating the component contributions of the many phenomena that contribute to the total radiated acoustic field is of importance. In this case, the phenomenon is related to the various sound sources (the mechanisms that lead to the excitation). The engine noise in an automobile is a realistic industrial example. This radiating engine noise is the consequence of a complicated blend of sounds created by different sources, including combustion, injection, compression, and exhaustion. The phenomena are what we call them. Blind source separation (BSS) strategies are the class of methods for dealing with such issues.

BSS entails 'blindly' retrieving a collection of unknown signals, referred to as sources, from their observed mixes, with little to no prior knowledge of the source characteristics or mixing structure [235]. The purpose of BSS is to use a multi-sensors setup to analyze multi-sensory observations of a set of signals in a way that discloses their unique (and original) nature by incorporating the spatial and temporal variability [236]. The following particular matrix factorization may be used

to represent most linear BSS models algebraically as [237],

$$\mathbf{X} = \mathbf{A} * \mathbf{S}, \tag{7.1}$$

where $\mathbf{X}$ is the sensor matrix, $\mathbf{A}$ is the mixing matrix, '*' is the mixing operation and $\mathbf{S}$ is the source matrix. Using input data from the iPTF problem Equation (3.4) and additional source prior knowledge, the proposed algorithm BSS-iPTF tries to extract the numerous sources that make up $\mathbf{S}$ of Equation (7.1). The prior source information determines the coupling level and location of the source. The present sources are assumed to be spatially non-overlapping and uncoupled (uncorrelated).

Spatial and temporal signal information are particularly important in most BSS separation processes, as previously stated. According to Dong [234], the usual procedure to obtain these uncorrelated radiated fields is to conduct a real-world physical experiment in the time domain and then convert the time signal to its frequency counterpart using the Short-time Fourier transform (STFT) snapshot sampling technique. The current work is numerical in nature, and no physical experiment was conducted, hence access to temporal signal spectra was not possible. An alternate method of getting the mixing matrix is devised and discussed in Section 7.3.1. This entails performing a series of DFR analyses to acquire a set of uncorrelated radiated field information in the frequency domain, followed by stochastically sampling the frequency field signal using a randomization approach. In some ways, the randomizing process may be viewed as a replacement for the snapshot sampling technique used on the time signal.

It is worth noting that the BSS-iPTF algorithm can only be initiated after the mixing matrix $\mathbf{A}$ of Equation (7.1) has been obtained, therefore any other procedure that leads to the mixing matrix is completely unrelated to the BSS-iPTF technique. The BSS-iPTF technique's first steps include an inverse method that incorporates back-propagation from measurements to the source domain of interest, and hence a regularization procedure utilizing `Tikh_RGCV` technique. At this step of the process, the resulting decorrelated virtual sources do not always correspond to the genuine sources. This is because a rotation matrix is absent and must be found. Other separation criteria such as "orthogonality" and "spatial disjointness" are enforced in the search for this rotation matrix.

7.2 Theory and Concept

7.2.1 Problem statement

The starting point is the iPTF equations, as given in Equation (3.4). For the sake of simplicity, the subscript and other characters attached to the variables will be ignored, thus Equation (3.4) will be rewritten as

$$\mathbf{Z}\mathbf{v} = \hat{\mathbf{p}} \quad \text{with} \begin{cases} \hat{\mathbf{p}} = \mathbf{p} - \bar{\mathbf{Z}}\bar{\mathbf{v}} & \text{for u-iPTF} \\ \hat{\mathbf{p}} = \mathbf{p} + \bar{\mathbf{Y}}\bar{\mathbf{p}} & \text{for m-iPTF} \end{cases} \tag{7.2}$$

The aim is not only to recover the vector of velocities $\mathbf{v}$ on the source surface, but also to separate it into "independent" contributions (represented by "independent" source fields).
In order to properly define the problem, the quantities of interest are seen as random variables. Given an event ϖ in the universe Ω,

$$\mathbf{p} \;:\; \Omega \mapsto \mathbb{C}^M, \varpi \to \mathbf{p}(\varpi) \tag{7.3}$$
$$\mathbf{v} \;:\; \Omega \mapsto \mathbb{C}^N, \varpi \to \mathbf{v}(\varpi) \tag{7.4}$$
$$\bar{\mathbf{v}} \;:\; \Omega \mapsto \mathbb{C}^L, \varpi \to \bar{\mathbf{v}}(\varpi) \tag{7.5}$$
$$\bar{\mathbf{p}} \;:\; \Omega \mapsto \mathbb{C}^L, \varpi \to \bar{\mathbf{p}}(\varpi). \tag{7.6}$$

More specifically, $\mathbf{v}(\varpi)$ is assumed to be generated by K "sources", each of them being characterized by a field $\mathbf{v}_k$,

$$\mathbf{v}(\varpi) = \sum_{k=1}^{K} \mathbf{v}_k \epsilon_k(\varpi) \tag{7.7}$$

where the $\epsilon_k(\varpi)$ are zero-mean independent scalar random variables with unit variance (this is without loss of generality since any scaling factor can be absorbed in $\mathbf{v}_k$). The aim is to recover the contributions $\mathbf{v}_k$.

In the absence of other sources than the one of interest, the pressures $\mathbf{p}$ and velocities $\bar{\mathbf{v}}$ (in case of u-iPTF) or $\bar{\mathbf{p}}$ (in case of m-iPTF) are entirely due to $\mathbf{v}$. Therefore, one has

$$\mathbf{p}(\varpi) = \sum_{k=1}^{K} \mathbf{p}_k \epsilon_k(\varpi) \tag{7.8}$$

$$\bar{\mathbf{v}}(\varpi) = \sum_{k=1}^{K} \bar{\mathbf{v}}_k \epsilon_k(\varpi) \tag{7.9}$$

$$\bar{\mathbf{p}}(\varpi) = \sum_{k=1}^{K} \bar{\mathbf{p}}_k \epsilon_k(\varpi) \tag{7.10}$$

with $\epsilon_k(\varpi)$ being the same zero-mean independent scalar random variables with unit variance than the one introduced in Eq. (7.7) and with $\mathbf{p}_k$, $\bar{\mathbf{v}}_k$ and $\bar{\mathbf{p}}_k$ the contributions coming from each "source" k. These contributions must verify Eq. (7.2):

$$\mathbf{p}_k = \mathbf{Z}\mathbf{v}_k + \bar{\mathbf{Z}}\bar{\mathbf{v}}_k \quad \text{for u-iPTF,} \tag{7.11}$$

$$\mathbf{p}_k = \mathbf{Z}\mathbf{v}_k - \bar{\mathbf{Y}}\bar{\mathbf{p}}_k \quad \text{for m-iPTF .} \tag{7.12}$$

In the following, the two iPTF problems (Equation (7.2)) will be reformulated as

$$\mathbf{v}(\varpi) = \mathbf{Z}^{-1}\hat{\mathbf{p}}(\varpi) \tag{7.13}$$

with

$$\hat{\mathbf{p}}(\varpi) = \sum_{k=1}^{K} \hat{\mathbf{p}}_k \epsilon_k(\varpi) \tag{7.14}$$

Therefore, the objective is here to find the separation operator Π_k allowing to extract the contribution $\hat{\mathbf{p}}_k$ of the k^{th} sources from the measured field $\hat{\mathbf{p}}(\varpi)$

$$\hat{\mathbf{p}}_k(\varpi) = \Pi_k \hat{\mathbf{p}}(\varpi) \tag{7.15}$$

It should be noted that, the above notation $\hat{\mathbf{p}}_k(\varpi) = \hat{\mathbf{p}}_k \epsilon_k(\varpi)$. Then, the contribution of the k^{th} source of the velocity field on the surface of the structure is computed by

$$\mathbf{v}_k = \mathbf{Z}^{-1}\hat{\mathbf{p}}_k. \tag{7.16}$$

7.2.1.1 Decorrelation

A first condition to achieve the separation of independent sources is decorrelation. This suggests the form of the separation operator Π_k. From Equation (7.14) and the independence of the $\epsilon_k(\varpi)$, the correlation matrix of $\hat{\mathbf{p}}(\varpi)$ is

$$\mathbf{C}_{\hat{\mathbf{p}}\hat{\mathbf{p}}} = \mathbb{E}\{\hat{\mathbf{p}}(\varpi)\hat{\mathbf{p}}(\varpi)^H\} = \frac{1}{K}\sum_{k=1}^{K} \hat{\mathbf{p}}_k \hat{\mathbf{p}}_k^H. \tag{7.17}$$

One wants to separate sources to fulfill the two conditions of decorrelation and of conservation of "energy",

$$\mathbb{E}\{\hat{\mathbf{p}}_k(\varpi)\hat{\mathbf{p}}_l(\varpi)^H\} = 0, k \neq l \quad \Leftrightarrow \quad \Pi_k \mathbf{C}_{\hat{\mathbf{p}}\hat{\mathbf{p}}} \Pi_l = 0, k \neq l \tag{7.18}$$

$$\sum_{k=1}^{K} \mathbb{E}\{\hat{\mathbf{p}}_k(\varpi)\hat{\mathbf{p}}_k(\varpi)^H\} = \mathbf{C}_{\hat{\mathbf{p}}\hat{\mathbf{p}}} \quad \Leftrightarrow \quad \sum_{k=1}^{K} \Pi_k \mathbf{C}_{\hat{\mathbf{p}}\hat{\mathbf{p}}} \Pi_k = \mathbf{C}_{\hat{\mathbf{p}}\hat{\mathbf{p}}}. \tag{7.19}$$

In addition, since $\mathbb{E}\{\hat{\mathbf{p}}_k(\varpi)\hat{\mathbf{p}}_k(\varpi)^H\} = \hat{\mathbf{p}}_k\hat{\mathbf{p}}_k^H$ is a rank-one matrix, it comes that the separation operators Π_k necessarily has the diadic form

$$\Pi_k = \mathbf{r}_k \mathbf{w}_k^H \tag{7.20}$$

where $\mathbf{r}_k$ and $\mathbf{w}_k$ are two column vectors.

Let us now consider the eigenvalue decomposition of the correlation matrix, $\mathbf{C}_{\hat{\mathbf{p}}\hat{\mathbf{p}}} = \sum_{k=1}^{K} \mathbf{u}_k \mathbf{u}_k^H \sigma_k^2$, with $\sigma_1 \geq \sigma_2 \geq ... \geq \sigma_N \geq 0$ and $\mathbf{u}_k^H \mathbf{u}_l = \delta_{kl}$. Condition (7.18) is satisfied if $\mathbf{w}_k = \alpha_k \mathbf{u}_k$ for any non-zero scalar α_k. Without loss of generality, let us set $\alpha_k = 1/\sigma_k$ (any unknown scaling coefficient is now assigned to $\mathbf{v}_k$). Then, condition (7.19) becomes

$$\sum_{k=1}^{K} \mathbf{r}_k \mathbf{r}_k^H = \mathbf{C}_{\hat{\mathbf{p}}\hat{\mathbf{p}}}, \tag{7.21}$$

which means that the inverse of matrix $\mathbf{R} = (\mathbf{r}_1, ..., \mathbf{r}_k)$ must diagonalize $\mathbf{C}_{\hat{\mathbf{p}}\hat{\mathbf{p}}}$ to identity, i.e. $\mathbf{R}^{-1}\mathbf{C}_{\hat{\mathbf{p}}\hat{\mathbf{p}}}\mathbf{R}^{-H} = \mathbf{I}$. Therefore, one necessarily has $\mathbf{R}^{-1} = \mathbf{\Phi}^H \mathbf{\Sigma}^{-1} \mathbf{U}^H$ with $\mathbf{U} = (\mathbf{u}_1, ..., \mathbf{u}_K)$, $\mathbf{\Sigma} = \text{diag}(\sigma_1, ..., \sigma_K)$ and $\mathbf{\Phi}$ an arbitrary unitary matrix such that $\mathbf{\Phi}^H\mathbf{\Phi} = \mathbf{I}$. Finally,

$$\Pi_k = \mathbf{U}\mathbf{\Sigma}\boldsymbol{\phi}_k \sigma_k^{-1} \mathbf{u}_k^H. \tag{7.22}$$

Substituting Π_k for the above expression into Equation (7.15) then yields

$$\hat{\mathbf{p}}_k(\varpi) = \mathbf{U}\mathbf{\Sigma}\boldsymbol{\phi}_k \varepsilon_k(\varpi) \tag{7.23}$$

with $\varepsilon_k(\varpi) = \sigma_k^{-1}\mathbf{u}_k^H \hat{\mathbf{p}}(\varpi)$. It is easily checked that the variance of $\varepsilon_k(\varpi)$ is the unity. Thus, by identification with Equation (7.14), it holds that

$$\hat{\mathbf{p}}_k = \mathbf{U}\mathbf{\Sigma}\boldsymbol{\phi}_k, \tag{7.24}$$

and the decorrelated virtual sources fields are obtained from

$$\mathbf{v}_k = \mathbf{Z}^{-1}\hat{\mathbf{p}}_k = \mathbf{Z}^{-1}\mathbf{U}\mathbf{\Sigma}\boldsymbol{\phi}_k. \tag{7.25}$$

Since $\mathbf{U}$ and $\mathbf{\Sigma}$ are returned by the eigenvalue decomposition of $\mathbf{C}_{\hat{\mathbf{p}}\hat{\mathbf{p}}}$, one still has to proceed with the estimation of a "good" rotation matrix $\mathbf{\Phi}$.

Note that Equation (7.24) correctly satisfies Equation (7.17) with any unitary matrix $\mathbf{\Phi}$, even though a popular but incomplete choice is to take $\mathbf{\Phi} = \mathbf{I}$ in the so-called PCA solution. In that case, for $\mathbf{\Phi} = \mathbf{I}$, the decorrelated virtual sources can be obtained using

$$\mathbf{v}_k = \mathbf{Z}^{-1}\hat{\mathbf{p}}_k = \mathbf{Z}^{-1}\mathbf{u}_k\sigma_k. \tag{7.26}$$

7.2.1.2 Choice of a rotation matrix $\mathbf{\Phi}$

Different criteria are possible depending on the properties one wants to enforce. For instance, one may want the sources to be orthogonal on the source surface, that is

$$\mathbf{v}_k^H \mathbf{v}_l = 0 \quad \text{for any} \quad k \neq l. \tag{7.27}$$

Therefore, from Equation (7.25), $\mathbf{\Phi}$ is the unitary matrix that diagonalizes

$$\mathbf{A} = \mathbf{\Sigma}\mathbf{U}^H\mathbf{Z}^{-H}\mathbf{Z}^{-1}\mathbf{U}\mathbf{\Sigma}. \tag{7.28}$$

Another possibility is to enforce the source support sets to be disjoint on the source surface. Therefore for any diagonal matrix $\mathbf{D}$,

$$\mathbf{v}_k^H\mathbf{D}\mathbf{v}_l = 0 \quad \text{for any} \quad k \neq l. \tag{7.29}$$

Then, $\mathbf{\Phi}$ is the unitary matrix that diagonalizes

$$\mathbf{A} = \mathbf{\Sigma}\mathbf{U}^H\mathbf{Z}^{-H}\mathbf{D}\mathbf{Z}^{-1}\mathbf{U}\mathbf{\Sigma}, \tag{7.30}$$

possibly for different choices of matrix $\mathbf{D}$ [234, 238].

7.3 Numerical validation of BSS-iPTF method

In this section, a numerical experiment consisting of the radiation of two uncorrelated vibration fields is carried out in a noiseless environment. The objective here is to extract the two fields $\mathcal{S}_1$ and $\mathcal{S}_2$ from the same experiment with the BSS-iPTF method described previously as illustrated in Figure 7.1.

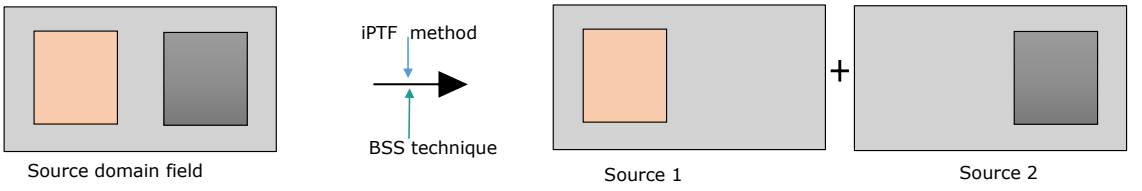

Figure 7.1: Schematic description of the iPTF-BSS objective

However, contrary to real experiments, it is not straightforward to generate an acoustic field radiated by two uncorrelated vibration fields by using numerical tools like finite element methods. As deterministic, when applying two forces at the same time in numerical simulations, they are implicitly correlated. For setting up a numerical experiment to validate the proposed BSS-iPTF method, a process to generate the acoustic radiation of uncorrelated vibration fields is explained in next section. It is important to underline here that all the procedure described in Section 7.3.1 is not necessary in the BSS-iPTF framework. It's just a way to set up a numerical experiments suitable to highlight the main results of BSS-iPTF.

7.3.1 Process to simulate the acoustic radiation of uncorrelated vibration fields

The objective here is to try to mimic an experiment consisting in two radiating disjoint plates excited each by uncorrelated point force as illustrated in Figure 7.1. In experiments, this is simply done by feeding two electrodynamic shakers with uncorrelated signals generated by two separated signal generators. In contrary, simulating this experiment with numerical tools like finite element methods is not straightforward. The process described here to generate a sound field due to two (or more) uncorrelated fields (here the vibrations of the plates) is based on the combination of two (or more) computations, each of them characterizing the acoustic field radiated by each plate, as illustrated in Figure 7.2.

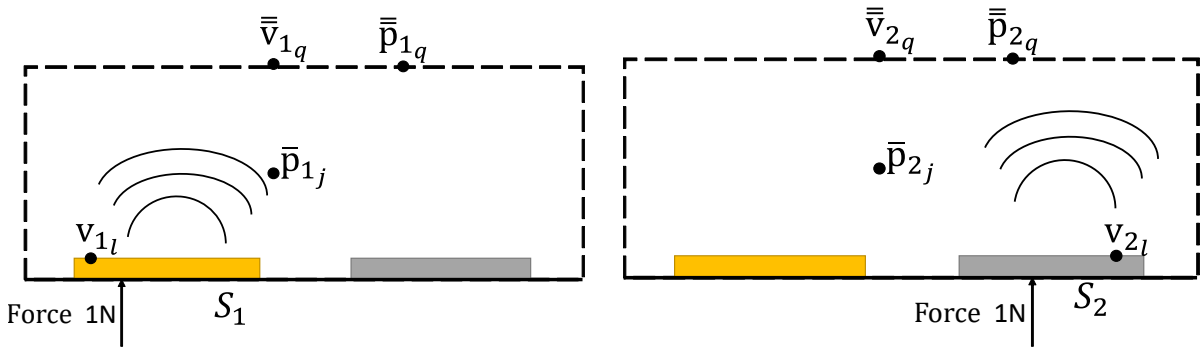

(a) Excited source 1 $\mathcal{S}_1$ (b) Excited source 2 $\mathcal{S}_2$

Figure 7.2: Schematic description of the process

In the present case described in Figure 7.2, the setup consists in two simply supported plates radiating noise in a semi-infinite free field. To enforce uncorrelation between vibration fields one needs to combine two independent Direct Frequency Response (DRF), as shown in Figures 7.2. These DFR are solved with ACTRAN software as already presented in section 4.1. The first DFR is computed by exciting $\mathcal{S}_1$ while keeping $\mathcal{S}_2$ as part of the rigid baffle floor. The second DFR is carried out by exciting $\mathcal{S}_2$ while keeping $\mathcal{S}_1$ rigid. The radiated field generated by $\mathcal{S}_1$ will be different and independent from that generated by $\mathcal{S}_2$ in these two configurations. The objective is now to combine these radiated fields in such a way that the produced field is equivalent to the one that would be due to the radiation of the two uncorrelated vibratory fields acting together. This generated field will serve in Section 7.3.2 as input data for the validation of the BSS-iPTF approach.

The mixing phase

According to iPTF formulation of Equation (3.4), we can write, for each source field $\mathcal{S}_i$ $(i=1,2)$ acting independently

$$\mathbf{Z}\mathbf{v}_i = \hat{\mathbf{p}}_i \quad \text{with} \begin{cases} \hat{\mathbf{p}}_i = \overline{\mathbf{p}}_i - \overline{\overline{\mathbf{Z}}}\overline{\overline{\mathbf{v}}}_i & \text{for u-iPTF} \\ \hat{\mathbf{p}}_i = \overline{\mathbf{p}}_i + \overline{\overline{\mathbf{Y}}}\overline{\overline{\mathbf{p}}}_i & \text{for m-iPTF} \end{cases} \tag{7.31}$$

where $\overline{\mathbf{p}}_i$, $\overline{\overline{\mathbf{p}}}_i$ and $\overline{\overline{\mathbf{v}}}_i$ are respectively vectors of pressures at points inside the virtual volume and pressures and velocities on the virtual surface as depicted in Figure 7.2.

This mixing technique involves performing several independent random realizations runs on the pressure field $\hat{\mathbf{p}}_1$ and $\hat{\mathbf{p}}_2$. The mixing process is mathematically formulated below for M realizations:

For m-iPTF we have:

$$\begin{aligned} \hat{\mathbf{p}}^1 &= \left[\overline{\mathbf{p}}_1\varepsilon_1^1 + \overline{\mathbf{p}}_2\varepsilon_2^1\right] + \overline{\overline{\mathbf{Y}}}\left[\overline{\overline{\mathbf{p}}}_1\varepsilon_1^1 + \overline{\overline{\mathbf{p}}}_2\varepsilon_2^1\right] \\ \hat{\mathbf{p}}^2 &= \left[\overline{\mathbf{p}}_1\varepsilon_1^2 + \overline{\mathbf{p}}_2\varepsilon_2^2\right] + \overline{\overline{\mathbf{Y}}}\left[\overline{\overline{\mathbf{p}}}_1\varepsilon_1^2 + \overline{\overline{\mathbf{p}}}_2\varepsilon_2^2\right] \\ &\vdots \quad \vdots \qquad\qquad \vdots \qquad\quad \vdots \qquad\qquad \vdots \\ \hat{\mathbf{p}}^M &= \left[\overline{\mathbf{p}}_1\varepsilon_1^M + \overline{\mathbf{p}}_2\varepsilon_2^M\right] + \overline{\overline{\mathbf{Y}}}\left[\overline{\overline{\mathbf{p}}}_1\varepsilon_1^M + \overline{\overline{\mathbf{p}}}_2\varepsilon_2^M\right] \end{aligned} \tag{7.32}$$

for u-iPTF we have:

$$\begin{array}{c} \hat{\mathbf{p}}^1 = \left[\overline{\mathbf{p}}_1\varepsilon_1^1 + \overline{\mathbf{p}}_2\varepsilon_2^1\right] - \overline{\overline{\mathbf{Z}}}\left[\overline{\overline{\mathbf{v}}}_1\varepsilon_1^1 + \overline{\overline{\mathbf{v}}}_2\varepsilon_2^1\right] \\ \hat{\mathbf{p}}^2 = \left[\overline{\mathbf{p}}_1\varepsilon_1^2 + \overline{\mathbf{p}}_2\varepsilon_2^2\right] - \overline{\overline{\mathbf{Z}}}\left[\overline{\overline{\mathbf{v}}}_1\varepsilon_1^2 + \overline{\overline{\mathbf{v}}}_2\varepsilon_2^2\right] \\ \vdots \quad \vdots \qquad\qquad \vdots \qquad\quad \vdots \qquad\qquad \vdots \\ \hat{\mathbf{p}}^M = \left[\overline{\mathbf{p}}_1\varepsilon_1^M + \overline{\mathbf{p}}_2\varepsilon_2^M\right] - \overline{\overline{\mathbf{Z}}}\left[\overline{\overline{\mathbf{v}}}_1\varepsilon_1^M + \overline{\overline{\mathbf{v}}}_2\varepsilon_2^M\right] \end{array} \tag{7.33}$$

where $m = 1, 2, \ldots M$ and $\varepsilon_i^m \in \mathbb{C}$ is a scalar complex number sampled from a zero means complex Gaussian distribution with unit variance with characteristics detailed in Appendix E. After several runs, a realization matrix $\mathbf{G} \in \mathbb{C}^{\mathrm{J}\times\mathrm{M}}$ is obtained and is defined as

$$\begin{aligned} \mathbf{G} &= \left[\hat{\mathbf{p}}^1, \hat{\mathbf{p}}^2 \ldots, \hat{\mathbf{p}}^M\right] \\ &= \begin{bmatrix} \hat{\mathrm{p}}_{1,1} & \hat{\mathrm{p}}_{1,2} & \cdots & \cdots & \hat{\mathrm{p}}_{1,M} \\ \hat{\mathrm{p}}_{2,1} & \hat{\mathrm{p}}_{2,2} & \cdots & \cdots & \hat{\mathrm{p}}_{2,M} \\ \vdots & \vdots & \vdots & \vdots & \vdots \\ \hat{\mathrm{p}}_{J,1} & \hat{\mathrm{p}}_{J,2} & \cdots & \cdots & \hat{\mathrm{p}}_{J,M} \end{bmatrix} \end{aligned} \tag{7.34}$$

It should be noted that the realization matrix $\mathbf{G}$ is composed of mixed pressure fields from the two uncorrelated sources $\mathcal{S}_1$ and $\mathcal{S}_2$, thus $\mathbf{G}$ can be seen as a matrix that contains uncorrelated pressure information.
The correlation matrix $\mathbf{C}_{\hat{\mathbf{p}}\hat{\mathbf{p}}} \in \mathbb{C}^{\mathrm{J}\times\mathrm{J}}$ of the realization matrix $\mathbf{G}$ which is given by

$$\begin{aligned} \mathbf{C}_{\hat{\mathbf{p}}\hat{\mathbf{p}}} &= \tfrac{1}{M}\mathbf{G}\mathbf{G}^H \\ &= \begin{bmatrix} \mathrm{c}_{1,1} & \mathrm{c}_{1,2} & \cdots & \cdots & \mathrm{c}_{1,J} \\ \mathrm{c}_{2,1} & \mathrm{c}_{2,2} & \cdots & \cdots & \mathrm{c}_{2,J} \\ \vdots & \vdots & \vdots & \vdots & \vdots \\ \mathrm{c}_{J,1} & \mathrm{c}_{J,2} & \cdots & \cdots & \mathrm{c}_{J,J} \end{bmatrix}, \end{aligned} \tag{7.35}$$

is computed then. At this step, the decorrelation process can be applied as described in Section 7.2.1.1.

7.3.2 Validation test case

As shown in Figure 7.3, each plate of the validation test case is 0.25 m long, 0.3 m wide and 2 mm thick, and is made of aluminium (Young's modulus $E = 7.0 \times 10^{10}$ Pa; density $\rho = 2400$ kg/m^3; Poisson's ratio $\nu = 0.25$). The plates, spatially disjointed at a distance of 10 cm, are excited by unit point forces (red upward arrow) located at point $(0.39; 0.05; 0)$ m and $(0.12; 0.15; 0)$ m for plate 1 and 2 respectively on the frequency band $[100 : 2000]$ Hz (frequency step 1 Hz).

The case study considered here is idealistic in the sense that performing acoustic measurements with no noise in the data is uncommon in real life. However, it is a useful case to start with in order to investigate the capabilities of the proposed BSS-iPTF approach. The results of the various steps of the BSS-iPTF procedure are described in the subsequent paragraphs.

A radiated acoustic field due to the vibration fields of plates $\mathcal{S}_1$ and $\mathcal{S}_2$ excited by uncorrelated point forces was first simulated using the process described in Section 7.3.1. Random variable simulation and signal mixing are the two fundamental aspects of the creation process. During the mixing phase (as indicated by Equations (7.32) and (7.33)), 1000 independent random realizations runs were performed to obtain a radiated acoustic field equivalent to the one that would have been measured in the presence of the two uncorrelated vibratory fields. These data (radiated pressure and/or velocity) are then used as an input for the BSS-iPTF approach.

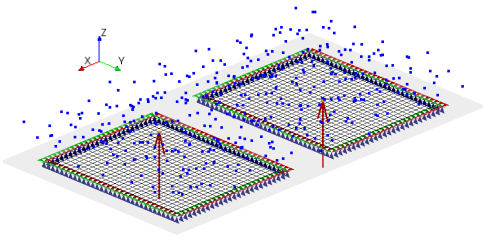

(a) Plate 1 ($\mathcal{S}_1$) and plate 2 ($\mathcal{S}_1$) are excited simultaneously with uncorrelated point forces: the radiated sound field is due to two uncorrelated vibration fields.

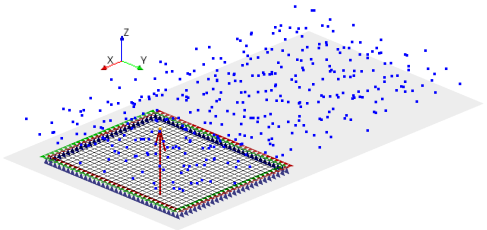

(b) Only plate 1 ($\mathcal{S}_1$) excited : the radiated sound field is due to a coherent vibration field.

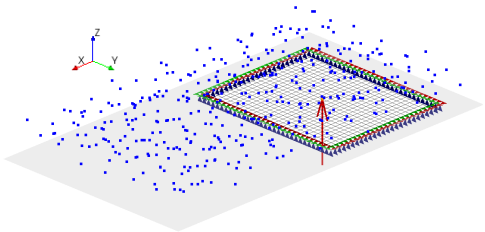

(c) Only plate 2 ($\mathcal{S}_2$) excited : the radiated sound field is due to a coherent vibration field

Figure 7.3: (a) depiction of an acoustic radiated field due to two uncorrelated vibration fields (classically done in experiments using to uncorrelated signals feeding two electrodynamic shakers). (b) and (c) are the computed independent simulations combined to mimic the pressure field depicted in (a). The randomly dispersed blues points represent a total of 390 field points.

7.3.2.1 The BSS step: blind separation of radiated acoustic fields

As explained in 7.2 As shown in Equation (7.35), the covariance matrix $\mathbf{C}_{\hat{\mathbf{p}}\hat{\mathbf{p}}} \in \mathbb{C}^{390\times390}$ is decomposed using Eigen-Value Decomposition (EVD) to generate the unitary matrix $\mathbf{U} \in \mathbb{C}^{390\times390}$ and eigenvalues matrix $\mathbf{\Sigma}^2 \in \mathbb{R}^{390\times390}$. Figure 7.4 shows the set of eigenvalues produced for the result at 816 Hz.

As can be seen in Figure 7.4, only two of the 390 eigenvalues are dominating for both u-iPTF

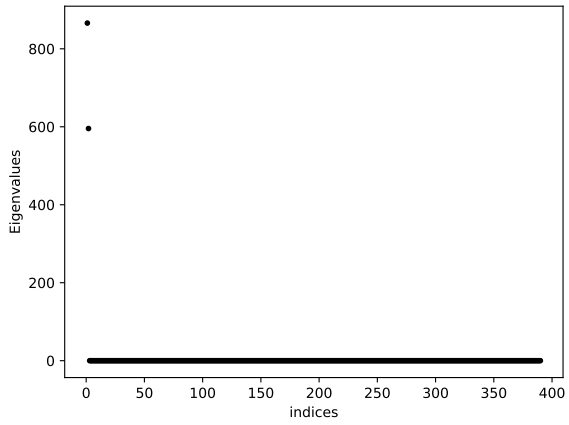

(a) m-iPTF

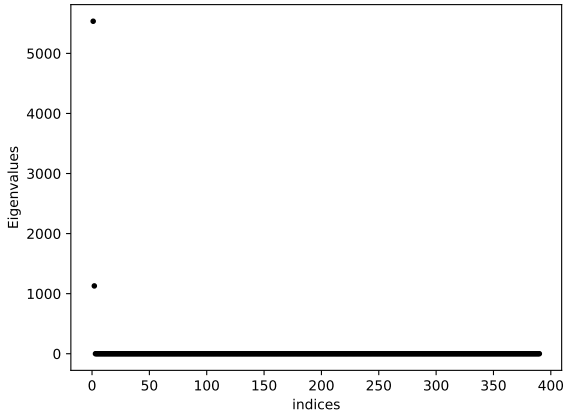

(b) u-iPTF

Figure 7.4: Plot of the 390 eigenvalues the covariance matrix $\mathbf{C}_{\hat{\mathbf{p}}\hat{\mathbf{p}}}$ obtained at 816 Hz.

and m-iPTF, indicating two possible sources.

For each frequency of study, the amplitudes of the first two higher singular values σ_1, σ_2 and

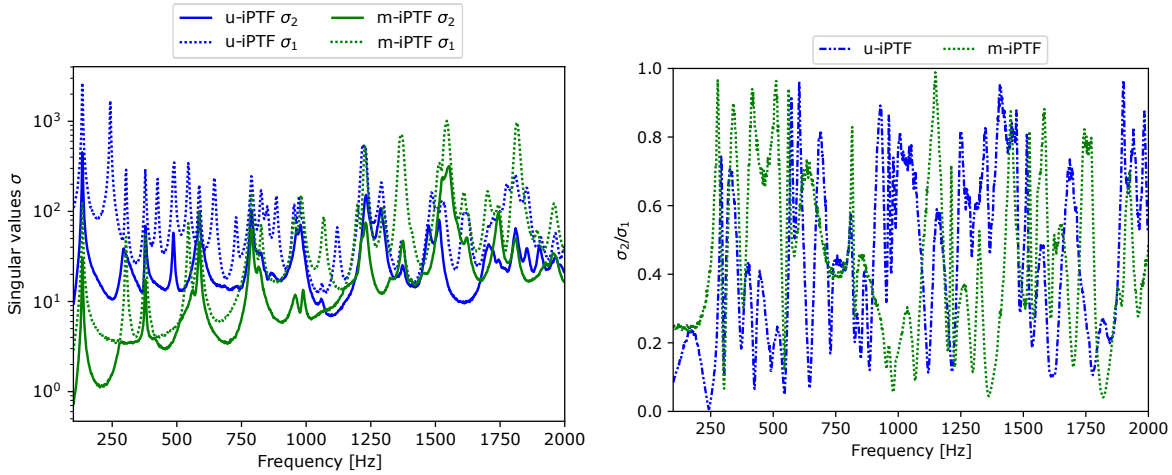

(a) σ_1, σ_2 spectra

(b) σ_2/σ_1 spectra

Figure 7.5: Spectra of the first two singular values of $\mathbf{C}_{\hat{\mathbf{p}}\hat{\mathbf{p}}}$ of Equation (7.35) (where $\sigma_1 \geq \sigma_2$) and the $\mathcal{DN}$ for m-iPTF and u-iPTF method

their corresponding ratio σ_2/σ_1 is computed and is depicted in Figure 7.5. This ratio will be referred to as "Dominance Number", $\mathcal{DN}$. A $\mathcal{DN}$ value of 0 indicates that the second source does not exist and thus only one source is present. A low $\mathcal{DN}$ basically signifies that first source is substantially dominating the second source, to the point where second source's existence is overshadowed. A $\mathcal{DN}$ value of 1 indicates that both sources are equally dominant.

Analyzing Figure 7.5(a), one can remark that two different sets of peaks appear: some peaks are at the same frequencies for both the u-iPTF and the m-iPTF methods while some other peaks have frequencies that differ from one approach to another. The first set of peaks corresponds to the plates eigenfrequencies (both plates have the same eigenfrequencies as they are identical) while the second corresponds to the virtual cavity eigenfrequencies (the boundary conditions of the virtual cavities are different from one method to another). Observing peaks for the plates eigenfrequencies was expected on σ_1 and σ_2 spectra as they are the actual sources of the radiation problem. Observing peaks for the virtual cavity eigenfrequencies was less obvious. Considering the appearance of these peaks, one could expect to obtain maps perturbed by the eigenmodes of the virtual cavity. This point will be checked later on.

7.3.2.2 How the matrices $\mathbf{\Phi}$ and $\mathbf{D}$ are computed and used

Let consider per se that for the two sources, the obtained decorrelated virtual sources $\mathbf{V}_{\text{dcl}} \in \mathbb{C}^{390\times 2}$ are given by

$$\mathbf{V}_{\text{dcl}} = [\mathbf{v}_1, \mathbf{v}_2] \tag{7.36}$$

where $\mathbf{v}_k$ with $k = 1, 2$ is defined according to Equation (7.26).

In order to use the disjointness property of Equation (7.29) to compute the virtual sources, the use of $\mathbf{D}$ is required. According to Dong et al. [238], the use of harmonic functions are recommended and as a results in this study, the sinusoidal function is used to generate $\mathbf{D}$, defined as

$$\begin{aligned} \mathrm{B} &= \left[d_i = \cos\left(\frac{10\pi i}{390}\right) \quad \text{for} \quad i = 1, \ldots, 390 \right] \\ &= [d_1, d_2 \ldots, d_{390}]\,. \end{aligned} \tag{7.37}$$

A diagonal matrix $\mathbf{D} \in \mathbb{R}^{390\times 390}$ as seen in Equation (7.29) is generated from the sequence element of B as

$$\mathbf{D} = \begin{bmatrix} d_1 & 0 & 0 & 0 \\ 0 & d_2 & 0 & 0 \\ 0 & 0 & \ddots & \vdots \\ 0 & 0 & \cdots & d_{390} \end{bmatrix} \tag{7.38}$$

Thus the $\mathbf{A} \in \mathbb{C}^{2\times 2}$ of Equation (7.30) is given by

$$\mathbf{A} = \mathbf{V}_{\text{dcl}}^{\text{H}} \mathbf{D} \mathbf{V}_{\text{dcl}} \tag{7.39}$$

performing eigen-value decomposition on $\mathbf{A}$, then the unitary rotation matrix of section 7.2.1.2 which is $\mathbf{\Phi} \in \mathbb{C}^{2\times 2}$ is computed as

$$\text{EVD}(\mathbf{A}) = \mathbf{\Phi}^{\text{H}} \mathbf{\Lambda}^2 \mathbf{\Phi} \tag{7.40}$$

where the diagonal matrix Λ^2 are the eigen-values of $\mathbf{A}$.

As a results, the virtual sources $\mathbf{V}_{\text{djt}} \in \mathbb{C}^{390\times 2}$, obtained by imposing spatial disjointness characteristics on $\mathbf{V}_{\text{dcl}}$ is given by

$$\mathbf{V}_{\text{djt}} = \mathbf{V}_{\text{dcl}} \mathbf{\Phi} \tag{7.41}$$

Similarly, by enforcing the orthogonality property on $\mathbf{V}_{\text{dcl}}$, the virtual sources $\mathbf{V}_{\text{otg}} \in \mathbb{C}^{390\times 2}$, is computed in the same way as $\mathbf{V}_{\text{djt}}$ except the diagonal matrix $\mathbf{D}$ is identity (that is $\mathbf{D} = \mathbf{I}$). The decorrelation, spatial disjointness and orthogonality properties are denoted by the subscripts "dcl", "djt" and "otg" respectively.

7.3.2.3 The iPTF step: reconstruction of velocity fields

The next stage is to reconstruct the virtual sources, which leads to an inverse problem (Equation (7.26)) to be solved from the extracted uncorrelated radiated fields. The inverse $\mathbf{Z}^{-1}$ can be computed with a variety of methods. However, due to the ill-conditioned character of $\mathbf{Z}$ and the ill-posed nature of Equation (7.26), it is preferable to employ the Tikhonov regularization approach, as detailed in section 3.3.1. As a result, the virtual source reconstruction is done with the `Tikh_RGCV`. At this step, the first virtual source with higher σ will be referred to as 'source A' (denoted as $\mathcal{S}_A$), while the second virtual source with low σ will be referred to as 'source B' (denoted as $\mathcal{S}_B$) as it is impossible to know if they actually correspond to vibratory field $\mathcal{S}_1$ or $\mathcal{S}_2$.

Figure 7.6 shows the optimal λ^2 parameter spectra, which demonstrates the functional behavior of the `Tikh_RGCV` approach. Figure 7.6 shows that the optimal λ^2 value increases as the frequency increases for both the u-iPTF and the m-iPTF, with the m-iPTF displaying some anomalies at lower frequencies. The regularization parameter λ^2 for the m-iPTF approach is also larger than for the u-iPTF equivalent. This is due to the fact that the m-iPTF problem statement (Equation (7.26)) contains more noise (instabilities and inaccuracies in its $\mathbf{Z}$ and $\hat{\mathbf{p}}_k$) than the u-PTF problem statement. As previously stated in section 4.5, the Tikhonov regularization acts as a buffer system, regulating measurement noise and solution smoothness. As a result, the noisier $\hat{\mathbf{p}}_k$ is, the more filtering is required (which means a higher value of the regularization parameter λ^2) to produce a good solution, and vice versa.

The condition number spectra for the u-iPTF has greater values in general than the m-iPTF, as seen in Figure 7.7(a). This is an indication that the impedance matrix $\mathbf{Z}$ associated to u-iPTF is more unstable and ill-conditioned than that of the m-iPTF. However, the ill-posedness level defined by the discrete Picard condition (see Section 3.2.2.2) shown in Figure 7.7(b) and (c) demonstrates the opposite: the ill-posedness level of u-iPTF is lower than that of m-iPTF. The reason for this is that the error computed is a combined effect of $\mathbf{Z}$ and $\hat{\mathbf{p}}_k$, which defines the iPTF's ill-posedness. In contrast to u-iPTF case, the anomalies in $\hat{\mathbf{p}}_k$, are so large in the m-iPTF

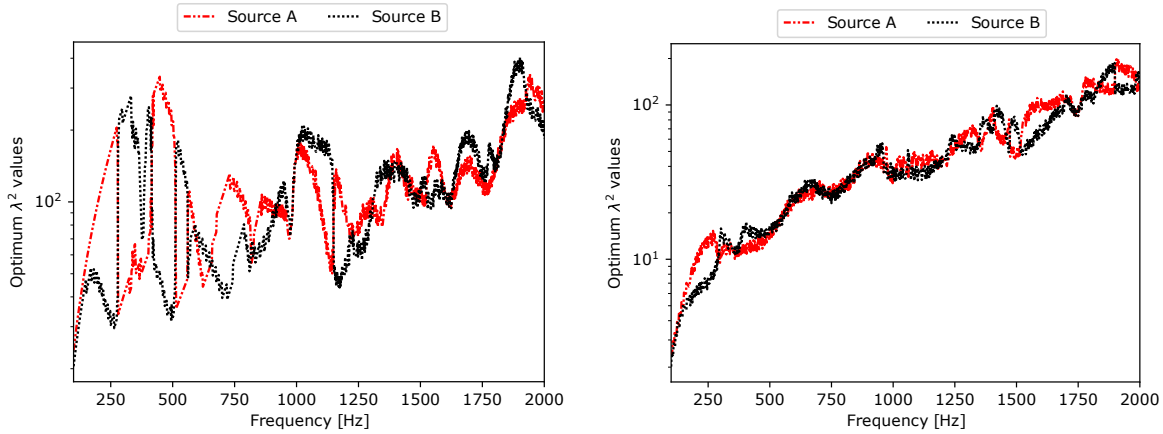

(a) m-iPTF (b) u-iPTF

Figure 7.6: Optimum regularization parameter λ^2 spectra for m-iPTF and u-iPTF method

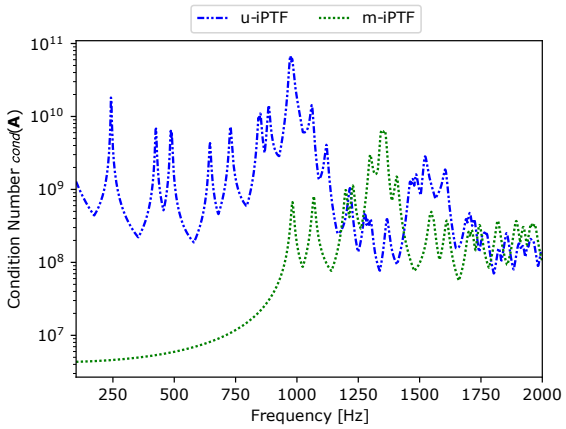

(a) Condition number spectrum of $\mathbf{Z} \in \mathbb{C}^{390\times390}$ of Equation (7.26)

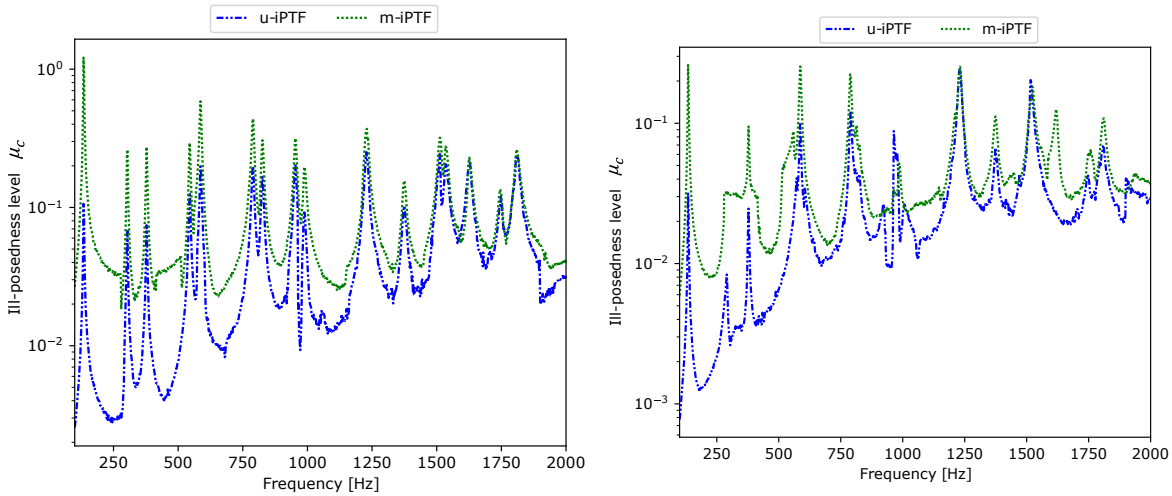

(b) Source A, $\mathcal{S}_A$ (c) Source B, $\mathcal{S}_B$

Figure 7.7: Ill-posedness level μ_c for identified fields (b) S_A and (c) S_B. The condition number spectra (a) is the same for the two sources.

case such that their combined effect with $\mathbf{Z}$ accentuates the problem's ill-posedness. The good news is that the `Tikh_RGCV` regularization is used to adjust for all of these anomalies and still produce a regularized solution that is reasonable. Figure 7.8 shows a visual representation of one such solution.

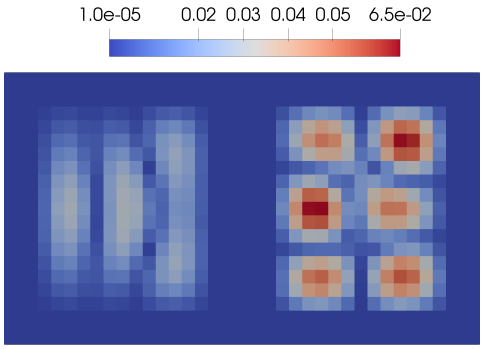

(a) Reference : $\mathcal{S}_1 + \mathcal{S}_2$

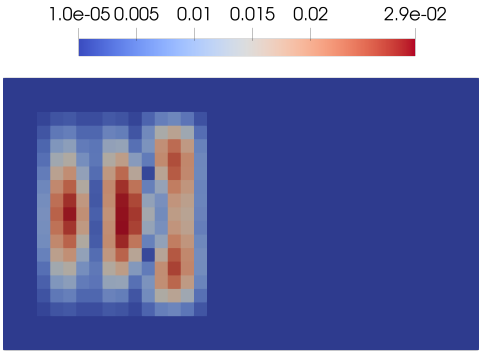

(b) Reference : $\mathcal{S}_1$

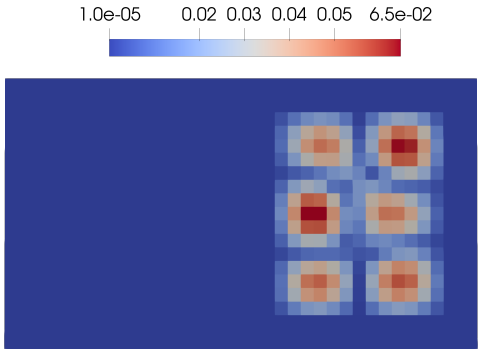

(c) Reference : $\mathcal{S}_2$

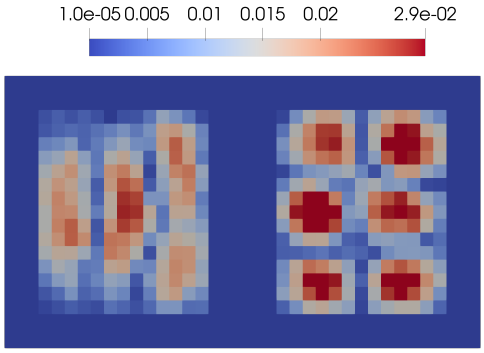

(d) m-iPTF with Decorrelation : $\mathcal{S}_B$

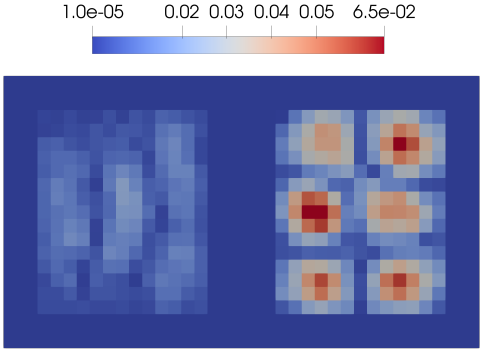

(e) m-iPTF with Decorrelation : $\mathcal{S}_A$

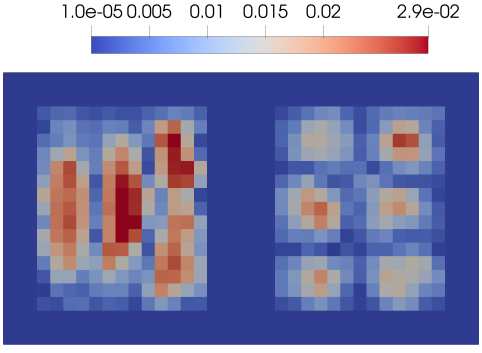

(f) u-iPTF with Decorrelation : $\mathcal{S}_B$

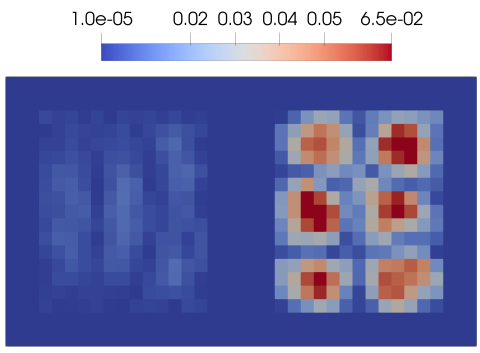

(g) u-iPTF with Decorrelation : $\mathcal{S}_A$

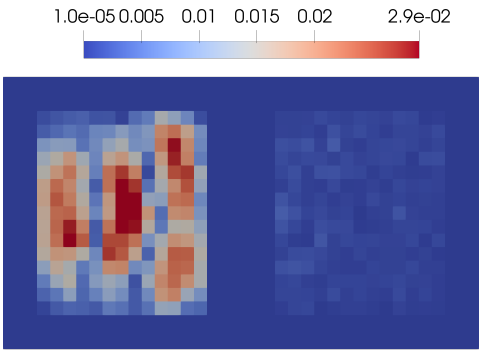

(h) m-iPTF with Orthogonality : $\mathcal{S}_B$

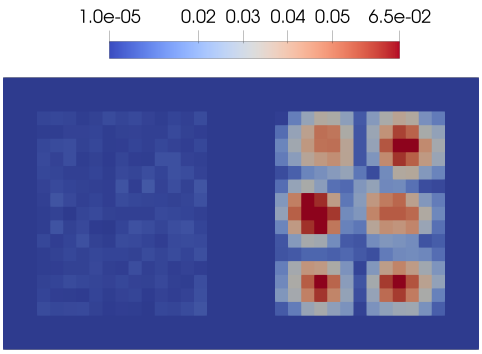

(i) m-iPTF with Orthogonality : $\mathcal{S}_A$

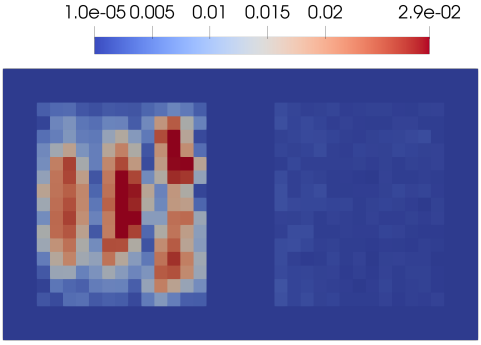

(j) u-iPTF with Orthogonality : $\mathcal{S}_B$

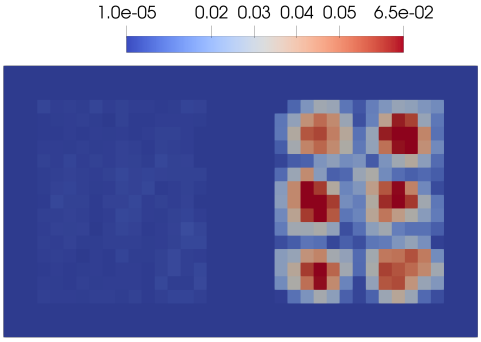

(k) u-iPTF with Orthogonality : $\mathcal{S}_A$

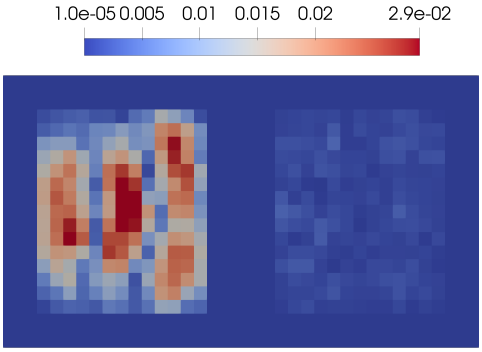

(l) m-iPTF with Spatially Disjoint : $\mathcal{S}_B$

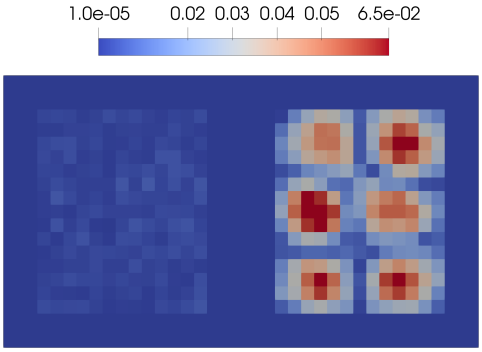

(m) m-iPTF with Spatially Disjoint : $\mathcal{S}_A$

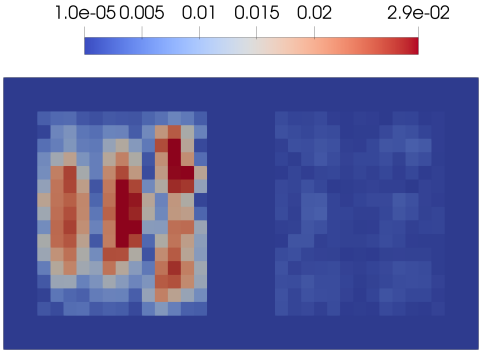

(n) u-iPTF with Spatially Disjointness : $\mathcal{S}_B$

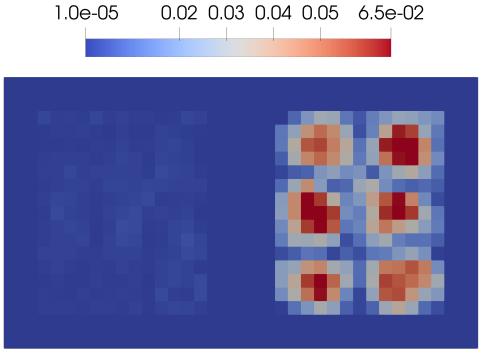

(o) u-iPTF with Spatially Disjointness : $\mathcal{S}_A$

Figure 7.8: Results of source velocity fields (m/s) at 816 Hz. (a)-(c) are the references directly computed with ACTRAN whereas (d)-(o) are identified separated source fields computed using the proposed BSS-iPTF approach.

The amplitude of the normal component of the fluid particle velocity field in direct contact

with the plate is represented by the reference results of Figure 7.8(a)-(c). When the magnitudes of $\mathcal{S}_1$ and $\mathcal{S}_2$ are compared to the magnitudes of $\mathcal{S}_1 + \mathcal{S}_2$, it is clear that $\mathcal{S}_2$ is the most dominating source. In the identification result, it is equivalent to $\mathcal{S}_A$.

The source identification patches utilized do not contain baffle floor mesh, therefore $\mathcal{S}_1$, $\mathcal{S}_2$, and their union $(\mathcal{S}_1 + \mathcal{S}_2)$ all have 390 patches. In addition, the floor baffle was not considered in the separation process. The rationale for this was to avoid the problem becoming highly under-determined, which would degrade the outcomes and make the main goal to prove impossible to achieve. It was solely included in the identification results (Figure 7.8(d)-(o)) for the sake of illustration.

It's worth noting that decorrelation alone (use of Equation (7.26)) failed to distinguish the source from its components $\mathcal{S}_A$ and $\mathcal{S}_B$. In the velocity field source $\mathcal{S}_A$ (Figure 7.8(e) and (g)), a ghost image of $\mathcal{S}_B$ was discovered, however the complete velocity field of $\mathcal{S}_A$ was detected in the velocity field that was supposed to be for $\mathcal{S}_B$ (that is Figure 7.8(d) and (f) exhibit a false call). As can be observed, separating the sources by decorrelation at 816 Hz resulted in artifacts of false calls and ghost images in the separated velocity fields. The detected artefact impact was suppressed to some extent by enforcing the orthogonality properties using Equations (7.27), and (7.28) (Figure 7.8(h) - (k)) and spatial disjoint properties with Equations (7.29) and (7.30) (Figure 7.8(l) - (o)). The suppression was more pronounced in the u-iPTF case than in the m-iPTF instance, with the u-iPTF's separated velocity field of orthogonality nature appearing as the most closely correlated results to the reference.

Again, visually comparing the identified results to the reference is a subjective method of validation that does not convey much information. As a result, an objective means is computed for the entire frequency range using the $\mathcal{CHA}$ correlation metric (see Appendix C). Figure 7.9 depicts the results of the correlation analysis.

The use of eigenvalue decomposition in the process of producing rotation matrix for the orthogonality and spatially disjointness requirements is indicated by the EVD in the legend of the plots in Figure 7.9. Figure 7.9 shows that, on average, the $\mathcal{CHA}$ spectra for the various criteria reduces as the frequency increases. The $\mathcal{CHA}$ spectra from imposing spatially disjointness condition showed anomalies at certain noticeable frequencies, but the situation was more worse for the decorrelation criteria, notably during $\mathcal{S}_B$ separation (which happens to be the less dominant source). It is clear that the worst $\mathcal{CHA}$ outcomes happened frequently when the $\mathcal{DN}$ values were very different from one iPTF method to another. When it comes to artefact phenomena (false calls and/or ghost pictures), this suggests that the criteria, particularly decorrelation, are unable to distinguish between the sources. And the artefact effect is far more obvious in the less dominant source, which happens to be $\mathcal{S}_B$, than in the very dominant source, which happens to be $\mathcal{S}_A$. The orthogonality criteria was enforced, resulting in high $\mathcal{CHA}$ values for both sources. Also, the separated sources resulting from the u-iPTF approach have higher $\mathcal{CHA}$ values on average than the m-iPTF equivalent.

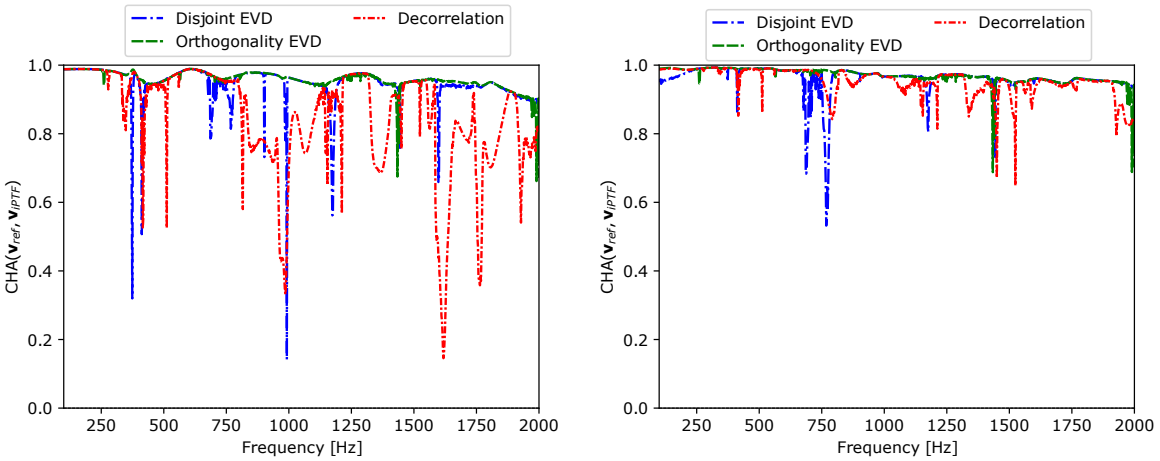

(a) m-iPTF: Source B, $\mathcal{S}_B$

(b) m-iPTF: Source A, $\mathcal{S}_A$

(c) u-iPTF: Source B, $\mathcal{S}_B$

(d) u-iPTF: Source A, $\mathcal{S}_A$

Figure 7.9: Plots of $\mathcal{CHA}$ correlation metric used in the comparison of the separated sources' velocity identified by BSS-iPTF and source velocity computed on the plate (reference) for the full frequency spectrum of study.

7.4 Summary and Conclusion

A variety of peculiarities are revealed by the blind separation of sources coupled to the iPTF technique (BSS-iPTF). One significant concern is that it incorporates a spatial component that is not included in traditional BSS. This is both a disadvantage (since it corresponds to an extra convolution over space) and a benefit (because it allows for the definition of new separation criteria). This chapter shows that enforcing the spatial disjointing or spatial orthogonality of the separated sources, two assumptions that are very plausible in many instances, leads to a unique solution to blind source separation. The search for spatially disjoint sources yielded the "spatial disjointness" criterion, whereas the search for orthogonal sources yielded the "orthogonality" criterion. BSS-iPTF's solutions are totally new and have been proven to work in numerical scenarios.

The initial phase of the BSS-iPTF technique is an inverse approach based on back-propagation from measurements to the source domain of interest, which is where regularization iPTF (`Tikh_RGCV`) comes into play. The obtained decorrelated virtual sources do not at all times coincide with the true sources at this stage of the method. The reason for this is that there is a missing rotation matrix that must be found, demonstrating that decorrelation is not a necessary requirement for separating the sources in general.

The BSS-iPTF approach appears to be promising based on the validation findings. Despite the fact that the outcomes are numerical in nature and stem from a simple academic structure, the approach will be further modified in order to be applied to complicated industrial problems in future studies. The proposed approach might be expanded to separate (partially) coherent sound sources, and also to separate sound sources emanating from rotating machinery, to name a few of the issues already noted.

8 General Conclusions and Perspectives

8.1 Conclusion

Green's identification and the idea of a virtual acoustic volume underpin the iPTF method. This closed volume is a virtual controlled zone that surrounds the source and may be arbitrarily built to provide measurement flexibility even when the source is saturated around with other structures. Green's identity is employed as a field separation method, allowing the technique to be independent of the measurement environment. The entire idea and attraction of the approach is centered on using the modal behavior of the virtual acoustic cavity as a Green's function. A choice of this sort allows one to substitute a virtual problem for the real one, avoiding any assumptions about the true nature of the field outside the virtual volume and therefore avoiding any measurement. As a corollary of its formulation and the FE modeling of the virtual volume, dealing with the existence of a masking object is rather simple. It merely includes taking into account the masking object's "footprint" in the virtual volume and accordingly calculating the acoustic impedance matrices. This is a highly significant aspect in industrial applications when dealing with mounting frames, wiring, and reflecting walls.

The PhD thesis goals were developed based on these unique characteristics of the iPTF approach. The iPTF technique is expected to be used for blind identification and blind separation of acoustic sources. All of these are aimed at identifying and characterizing acoustic sources.

Because the iPTF method is an inverse technique, it necessitates the inversion of the impedance matrix to obtain solution, necessitating extensive work in regularizing inverse issues. Thus, conceptually, how to deal with inverse difficulties were examined in the present work. The iPTF is an inverse problem because it involves calculating the acoustic source normal velocities (unknown cause) using acoustic field measurements (seen effects) and FEM impedance matrices (propagation operator). Inverse problems, just as this, have the common drawback that every arbitrarily slight disturbance in the system's input causes an arbitrary large oscillation in the output. To show the characteristics of discrete ill-posed problems, a simple numerical experiment is conducted. It was demonstrated that by purposefully contaminating the existing data with a little quantity of noise, a typical inversion procedure yields an intangible solution dominated entirely by noise effects. A reasonable solution can be found by adding some kind of regularization to the inversion of the impedance transfer matrix, which clearly connects the cause (input) to the observed outcome (output). The singular value decomposition of the matrix proved to be a very important tool in the regularization process since it gives an explicit physical and mathematical explanation of the ill-conditioned behavior. In addition, the discrete Picard condition was used, which assures the existence of a physically meaningful regularized solution for a given right-hand side vector if met. Several regularization approaches were investigated. With no prior knowledge, the technique

applied in the traditional approach can be either deterministic (Zero-Order Tikhonov, iterative CGNE-LBR) or statistical (Bayesian m-iPTF method and the proposed DBKH-iPTF method). Regularization, in broad sense, may be viewed as a type of optimization process that involves the development of numerous solutions from which the best solution should be chosen, and the criteria for picking the best solution (by the use of regularization parameters) are a must. This thesis study addresses two broad kinds of such tactics based on the degree of information offered. The following criteria can be used in the absence of prior knowledge: `GCV`, `RGCV`, `ZERO`, `CURV` and `MINP` criteria. When prior knowledge about the test problem is available, the `CHA` criteria is used. All of these regularization procedures, in essence, require a trade-off between the error component attributable to noise amplification (perturbation error) and the error component imposed by the regularization (regularization error). The quantity of regularization is dictated by the regularization parameter, which may be selected using the L-curve plot. This graphical tool depicts the equilibrium between the residue's norm and the size of the regularized solution, as determined by an acceptable norm.

The best suitable regularization approach for both m-iPTF and u-iPTF procedures was searched among the regularization techniques presented. The method entailed doing numerical experiments using a variety of situations to build a set of test cases that characterized the iPTF problems. Using regularization techniques, the described iPTF problem was addressed. The idealized situation was used as the initial test case scenario, in which all regularization approaches (deterministic and statistical) were used. A set of correlation measurements were used to validate the identified findings from each of the strategies. In handling the idealistic issue scenario, the zeroth-order-Tikhonov-RGCV (`Tikh_RGCV`) based strategy emerged as the most appropriate regularization technique for the iPTF techniques. The DBKH-iPTF approach's `Bay_MAD` and `Bay_MINP` techniques, developed specifically during the thesis work, were the next two to perform well. These two strategies were not pursued further since they are computationally costly and have been formulated to treat perturbed and/or equally-determined systems, not under-determined problem instances. The robustness of the `Tikh_RGCV` was investigated further on two realistic scenarios: perturbed (noisy) equally-determined and unperturbed under-determined iPTF test cases. The perturbed cases indicated the circumstance in which various noise levels were introduced to the measurement data, whilst the under-determined case is defined by a reduction in the number of field points with respect to the number of identification patches. The obtained identified findings for estimating the acoustic source from the various perturbed (noisy) equal-determined configurations were in excellent agreement with the reference. The scenario was completely different in the unperturbed under-determined situations, where each configuration's identified iPTF velocity field was poorly correlated to the reference. As the ratio of field points to source patches decreased, the identified velocity values were less correlated to the reference. The DPC sensitivity analysis was used to explain the disparities in the obtained correlation data. It's worth noting that DPC satisfaction is crucial to the regularized solution's degree of perfection. The `Tikh_RGCV` challenges in generating solutions for these unperturbed under-determined problems were then examined further. Prior regularization techniques such as `Twomey_CHA`, `Tikh_CHA`, and `Itr_CHA` were used in the investigation. The studies' results reveal that, `Tikh_RGCV`, and Tikhonov were not the best methods for dealing with unperturbed under-determined iPTF problems, but that by modifying the iterative technique (CGNE-LBR Algorithm), adequate and well-correlated results could be obtained.

The blind reconstruction of sources using the iPTF technique is one of the goals in this PhD thesis. The influence of the masking object distance from the source and its width across the source were considered in a detailed parametric analysis of blindly recognizing an acoustic source. The test configurations that were reviewed went through many stages of validation. Very-nearfield and radiated far-field information are used to analyze the results. The first numerical analysis

looked at how the masking object's distance from the source (how far away or close it was) influenced its identification. When the masking object was placed very close to the source, as close as 1 cm, the identified findings were overestimated, and the insertion of measurement sensors in the masked zone did not improve the results. This is due to the fact that the fluid-structure interaction in the masked zone was no longer weak, causing the vibratory field to change. The second numerical analysis investigated how widening the obstacle to increase its surface area with respect to the source region affects the identified source characteristics. Even in extreme cases when the masking item completely covers the whole surface area of the source, it was observed that a significant amount of source information could be retrieved, and that adding measurement sensors to the masked-zone improved the results. It is crucial to underline to the reader that the motivation behind this examination was to reveal that when the masking item is present, the identification results are remarkably similar to when the masking object is removed. Based on the obtained results from the studies conducted, the identified results were substantially connected to the references, and even in difficult test set-up circumstances, good correlations were attained. At this stage, an experiment was conducted on an electric motor mounted on the Siemens test rig. The capacity of iPTF to handle the presence of masking objects was proved adding a rigid thick wooden panel in between the system under study and the microphone array. The obtained results demonstrated that iPTF approach is able to "cancel" the effect of masking objects. This is quite a unique feature for source identification methods.

The "blind separation" of source fields in the iPTF architecture is another goal of the PhD thesis work. The "BSS-IPTF" approach was created as a novel concept. This strategy was validated using a numerical test case. The blind separation of sources in conjunction with the iPTF approach showed a number of oddities (BSS-iPTF). One major point of contention is that it has a spatial component that is absent from regular BSS. This is both a drawback (since it corresponds to an additional space convolution) and a benefit (because it allows for the definition of new separation criteria). This chapter demonstrates that enforcing the separated sources' spatial disjointness or spatial orthogonality, two assumptions that are quite realistic in many cases, results in a unique solution to blind source separation. The "spatial disjointness" criteria was derived from the search for spatially non-overlapping sources, while the "orthogonality" criterion was derived from the search for orthogonal sources. The BSS-iPTF strategy begins with an inverse approach based on backpropagation from measurements to the source domain of interest, which was where regularization of the iPTF with `Tikh_RGCV` entered the picture. At this level of the procedure, the acquired decorrelated virtual sources didn't always match the genuine sources. This is because there is a missing rotation matrix that must be identified, proving that decorrelation is not a condition for distinguishing the sources in general. Based on the validation results by enforcing orthogonality and spatial disjointness properties, the BSS-iPTF strategy looks to be promising.

Overall, the PhD thesis's objectives were accomplish, and the iPTF approach is enticing and has a great potential for solving most hard-knock vibroacoustic issues, not only in academia but also in industry.

8.2 Recommendations and Future works

It has been shown that the regularization methods used can have a significant impact on the quality of the results obtained from the application of the iPTF method. In most cases, deterministic approaches such as Tikhonov's approaches, associated with selection criteria for the appropriate regularization parameter, give good results. Nevertheless, they have shown their limit in cases where the problem is underdetermined. In this case, the results are mediocre even if it remains possible to exploit the identified maps. The iterative methods presented

in the thesis seem to give better quality results in this specific case. However, the stopping criterion for these methods is not always easy to obtain. Thus, it would be interesting to continue investigations on iterative methods in order to determine a relevant stopping criterion. It was also shown that Phillips-Twomey approaches, requiring the knowledge of an estimate of the expected solution (here applied using the exact expected solution for analysis and understanding purposes) could give very relevant results. It could thus be interesting to find a way to know an estimate of the solution, without knowing it a priori. To this end, one could either use an available numerical model (even if not perfectly updated) or use the maps identified in a first step using a classic Tikhonov regularization. Finally, the DBKH-iPTF regularization method developed in this thesis, although time-consuming, gives very good results. The investigation should be continued by verifying its ability to give good results in the presence of measurement noise or in the under-determined case. As far as possible, the necessary calculation times should also be reduced by using algorithms or a more suitable (compiled) programming language.

The so-called "blind reconstruction" feature of the iPTF method is very powerful and paves the way to many applications hitherto impossible with traditional source identification approaches. However, this functionality is based on the assumption of a perfectly rigid masking object, which is rarely the case in reality. If the masking object is not perfectly rigid and it vibrates then it must be considered as an additional acoustic source inside the virtual volume. The main problem in this case is that either the masking object must be discretized into an identification patch mesh like the system under study (to determine the vibrational velocity of the masking object even if it is of no interest) or the vibrational velocity of the obstacle must be known as is the case for the virtual surface (u-iPTF). In the first case, the number of identification patches increases, which will result in increasing the number of measurement points in the volume or reducing the number of patches on the surface of the system under study. In the second case, vibration measurements of all the masking objects are necessary, which seems very complicated to implement. Thus, in the case of a non-rigid masking object, it seems more appropriate to integrate it into the identification patch mesh. The unanswered question is how coarse the discretization into patches of the masking object can be.

In the same way, other configurations for which a blind reconstruction may prove necessary may exist: this would be the case of a source inside a box comprising openings or limited access or sources whose geometry includes hollow or strongly concave parts. These cases could be treated in the same way as the masking object defined in this thesis.

According to the validation results from the blind separation studies, developed BSS-iPTF approach appears to have a lot of potential. Notwithstanding the fact that the results are numerical in nature and arise from a simple academic framework, the method might be further improved in future work so that it can be applied to more complex industrial situations. To highlight a few of the challenges already envisioned, the develop method might be developed to identify (partially) coherent sound sources.

Bibliography

[1] D. Miloradović, J. Glišović, and J. Lukić, "Regulations on road vehicle noise – trends and future activities," *Mobility and Vehicle Mechanics*, vol. 43, no. 1, 2017.

[2] Science for Environment Policy (2017) Noise abatement approaches. Future Brief 17. Produced for the European Commission DG Environment by the Science Communication Unit, UWE, Bristol. Available at: `http://ec.europa.eu/science-environment-policy`.

[3] WHO, "Urban population growth." `https://www.who.int/gho/urban_health/situation_trends/urban_population_growth_text/en/`, 2017.

[4] H. M. E. Miedema and H. Vos, "Associations Between Self-Reported Sleep Disturbance and Environmental Noise Based on Reanalyses of Pooled Data From 24 Studies," *Behavioral Sleep Medicine*, vol. 5, no. 1, p. 1–20, 2007.

[5] H. R. Colten and B. M. Altevogt, "Extent and Health Consequences of Chronic Sleep Loss and Sleep Disorders," 2006.

[6] A. B. Newman, P. L. Enright, T. A. Manolio, E. F. Haponik, and P. W. Wahl, "Sleep Disturbance, Psychosocial Correlates, and Cardiovascular Disease in 5201 Older Adults: The Cardiovascular Health Study," *Journal of the American Geriatrics Society*, vol. 45, no. 1, p. 1–7, 1997.

[7] N. Kawakami, N. Takatsuka, and H. Shimizu, "Sleep Disturbance and Onset of Type 2 Diabetes," *Diabetes Care*, vol. 27, no. 1, 2003.

[8] W. Babisch, "Cardiovascular effects of noise," *Noise and Health*, vol. 13, no. 52, p. 201–204, 2011.

[9] H. Isling and B. Kruppa, "Health effects caused by noise: evidence in the literature from the past 25 years," *Noise and Health*, vol. 6, no. 22, p. 5–13, 2004.

[10] L. Goines and L. Hagler, "Noise Pollution: A Modern Plague," *Southern Medical Journal*, vol. 100, no. 3, p. 287–294, 2007.

[11] S. A. Stansfeld and M. P. Matheson, "Noise pollution: Non-auditory effects on health," *British Medical Bulletin*, vol. 68, p. 243–257, 2003.

[12] M. Sørensen, M. Hvidberg, Z. Andersen, R. Nordsborg, K. Lillelund, J. Jakobsen, A. Tjønneland, K. Overvad, and O. Raaschou-Nielsen, "Road traffic noise and stroke: a prospective cohort study," *European Heart Journal*, vol. 32, no. 6, 2011.

[13] M. Sørensen, J. Zorana, R. Nordsborg, T. Becker, A. Tjønneland, K. Overvad, and O. Raaschou-Nielsen, "Long-term exposure to road traffic noise and incident diabetes: A cohort study," *Environmental health perspectives*, vol. 121, no. 1, 2013.

[14] T. Münzel, T. Gori, W. Babisch, and M. Basner, "Cardiovascular effects of environmental noise exposure," *Eur Heart J*, vol. 35, no. 13, p. 829–836, 2014.

[15] WHO, "Burden of disease from environmental noise. quantification of healthy life years lost in europe." `https://www.euro.who.int/en/publications`, 2011.

[16] T. Bein, S. Elliot, L. Feralli, C. M., J. Meschke, E. Saemann, F. Nielsen, and W. Kropp, "Integrated solutions for noise and vibration control in vehicles," *Procedia - Social and Behavioral Sciences*, vol. 48, p. 919 – 931, 2012.

[17] "European Environment Agency Noise in Europe," 2014.

[18] E. Murphy and E. King, *Environmental Noise Pollution*. Elsevier, 2014.

[19] The SMILE Consortium (2003) Guidelines for road traffic noise abatement.

[20] G. Blokland and I. Peeters, "Final report of the Interest Group of Traffic Noise Abatement (IGNA)," 2016.

[21] EEA, "The European Environment Agency: *Evaluating 15 years of transport and environmental policy integration - TERM 2015: Transport indicators tracking progress towards environmental targets in Europe*," EEA Report No. 7/2015, Publications Office of the European Union, Luxembourg, 2015.

[22] "ISO 362:2015. Measurement of noise emitted by accelerating road vehicles."

[23] EEA, "The European Environment Agency: *Noise in Europe 2014*," EEA Report No. 10/2014, Publications Office of the European Union, Luxembourg, 2014.

[24] `https://www.h2020-pbnv2.eu/`.

[25] `https://cordis.europa.eu/project/id/721615`.

[26] R. Visser, *A Boundary Element Approach to Acoustic Radiation and Source Identification*. Phd thesis, University of Twente, Enschede, The Netherlands, 09 2004. 90-365-2051-7.

[27] S. Forget, *Reconstruction des champs acoustiques sur structure à géométrie complexe en environnement non contrôlé, hiérarchisation de sources et corrélation éléments finis : Application sur un Groupe Moto Propulseur d'automobile*. Thèse de doctorat, INSA de Lyon, Lyon, France, 2017.

[28] Sound Intensity by Brüel & Kjær, 09 1993.

[29] ISO (International Organization for Standardization) (1993) ISO 9614-1:1993: Acoustics: Determination of the Sound Power Levels of Noise Sources Using Sound Intensity. Part 1: Measurement at Discrete Points. International Organization for Standardization.

[30] ISO (International Organization for Standardization) (1996) ISO 9614-2:1993: Acoustics: Determination of the Sound Power Levels of Noise Sources Using Sound Intensity. Part 2: Measurement by Scanning. International Organization for Standardization.

[31] ISO (International Organization for Standardization) (2002b) ISO 9614- 3:2002: Acoustics: Determination of the Sound Power Levels of Noise Sources Using Sound Intensity. Part 3: Precision Method for Measurement by Scanning. International Organization for Standardization.

[32] F. Fahy and D. Thompson, *Fundamental of sound and vibration*, ch. 8. Institute for Sound and Vibration Research, 2015.

[33] F. Fahy, *Sound Intensity*. London: Spon, 2nd ed., 1995.

[34] E. C. M. Association, "Standard ECMA -160, Determination of Sound Power Levels of Computer and Business equipment using sound intensity measurements: Scanning method in controlled rooms," 12 1992.

[35] M. Crocker and J. Arenas, "Fundamentals of the direct measurement of sound intensity and practical applications," *Acoustical Physics*, vol. 49, pp. 163–175, 01 2003. 10.1134/1.1560378.

[36] G. Squicciarini, A. Putra, D. J. Thompson, X. Zhang, and M. A. Salim, "Use of a reciprocity technique to measure the radiation efficiency of a vibrating structure," *Applied Acoustics*, vol. 89, no. 1, p. 107–121, 2015.

[37] D. F. Comesana, *Scan-Based Sound Visualisation Methods Using Sound Pressure and Particle Velocity*. Phd thesis, University Of Southampton, 2009.

[38] "Microflown: A new category of sensors," 2012.

[39] J. Hald, "STSF - a unique technique for scan-based near-Field acoustics holography without restrictions on coherence," tech. rep., Bruel and Kjaer, 1989.

[40] H. S. Kwon and Y. H. Kim, "Moving frame technique for planar acoustic holography," *The Journal of the Acoustical Society of America*, vol. 103, no. 4, p. 1734–1741, 1998.

[41] S. Park and Y. H. Kim, "An improved moving frame acoustic holography for coherent bandlimited noise," *The Journal of the Acoustical Society of America*, vol. 104, no. 6, p. 3179–3189, 1998.

[42] S. Park and Y. H. Kim, "Effects of the speed of moving noise sources on the sound visualization by means of moving frame acoustic holography," *The Journal of the Acoustical Society of America*, vol. 108, no. 6, p. 2719–2728, 2000.

[43] S. H. Park and Y. H. Kim, "Visualization of pass-by noise by means of moving frame acoustic holography," *The Journal of the Acoustical Society of America*, vol. 110, no. 5, pp. 2326–2339, 2001.

[44] M. Lee and J. S. Bolton, "Scan-based near-field acoustical holography and partial field decomposition in the presence of noise and source level variation," *The Journal of the Acoustical Society of America*, vol. 119, no. 1, p. 382–393, 2006.

[45] G. Rasmussen, "Intensity: its measurement and uses," in *Sound Vibration*, vol. 23, pp. 12–21, Acoustical Publications, Incorporated, 1989.

[46] J. Lanslots, F. Deblauwe, and K. Janssens, "Selecting sound source localization techniques for industrial applications," *Sound and Vibration*, vol. 44, pp. 6–10, 06 2010.

[47] A. Koutný, *Sound Source Localization in Enclosures*. Prague: Czech Technical University, 08 2017.

[48] J. Wind, *Acoustic Source Localization, Exploring Theory and Practice*. Phd thesis,, University of Twente, Enschede, The Netherlands, 2009.

[49] D. Salvati, *Acoustic source localization using microphone arrays*. PhD thesis, University of Udine, 03 2012.

[50] C. Knapp and G. Carter, "The generalized correlation method for estimation of time delay," *IEEE Transactions on Acoustics, Speech and Signal Processing*, vol. 24, no. 4, p. 320–327, 1976.

[51] J. Benesty, "Adaptive eigenvalue decomposition algorithm for passive acoustic source localization," *Journal of the Acoustical Society of America*, vol. 107, no. 1, p. 384–391, 2000.

[52] J. Dibiase, H. Silverman, and M. Brandstein, "Robust localization in reverberant rooms," in *Microphone Arrays: Signal Processing Techniques and Applications*, pp. 3, 4, 27, 35, 36, 42, Springer, 2001.

[53] J. Chen, J. Benesty, and Y. Huang, "Robust time delay estimation exploiting redundancy among multiple microphones," *IEEE Transactions on Speech and Audio Processing*, vol. 11, no. 6, p. 549–557, 2003.

[54] J. Benesty, C. J. Chen, and Y. Huang, "Time-delay estimation via linear interpolation and cross correlation," *IEEE Transactions on Speech and Audio Processing*, vol. 12, no. 5, p. 509–519, 2004.

[55] Y. Huang and J. Benesty, "Adaptive multichannel time delay estimation based on blind system identification for acoustic source localization," in *Adaptive Signal Processing: Applications to Real-World Problems*, Springer, 2003. `https://doi.org/10.1007/978-3-662-11028-7_8`.

[56] J. Benesty, Y. Huang, and J. Chen, "Time delay estimation via minimum entropy," *IEEE Signal Processing Letters*, vol. 14, n. 3, p. 157–160, 2007.

[57] F. Wen and Q. Wan, "Robust time delay estimation for speech signals using information theory: A comparison study," *EURASIP Journal on Audio, Speech, and Music Processing*, p. 1–10, 2011.

[58] A. Lombard, Y. Zheng, H. Buchner, and W. Kellermann, "TDOA estimation for multiple sound sources in noisy and reverberant environments using broadband independent component analysis," *IEEE Transactions on Audio, Speech and Language Processing*, vol. 19, no. 6, p. 1490–1503, 2011. 3, 5.

[59] P. Stoica and J. Li, "Source localization from range-difference measurements," *IEEE Signal Processing Magazine*, vol. 23, no. 3, p. 63–66, 2006.

[60] R. O. Schmidt, "A new approach to geometry of range difference location," *IEEE Transactions on Aerospace and Electronic Systems*, vol. 8, no. 6, p. 821–835, 1972.

[61] H. C. Schau and A. Z. Robinson, "Passive source localization employing intersecting spherical surfaces from time-of-arrival differences," *IEEE Transactions on Acoustics, Speech and Signal Processing*, vol. 35, no. 8, p. 1223–1225, 1987.

[62] J. O. Smith and J. S. Abel, "Closed-form least-squares source location estimation from range difference measurements," *IEEE Transactions on Acoustics, Speech and Signal Processing*, vol. 35, no. 12, p. 1661–1669, 1987.

[63] Y. T. Chan and K. C. Ho, "A simple and efficient estimator for hyperbolic location," *IEEE Transactions on Signal Processing*, vol. 43, no. 8, p. 1905–1915, 1994.

[64] M. Brandstein, J. E. Adcock, and H. F. Silverman, "A closed-form location estimator for use with room environment microphone arrays," *IEEE Transactions on Speech and Audio Processing*, vol. 5, no. 1, p. 45–50, 1997.

[65] M. D. Gilette and H. F. Silverman, "A linear closed-form algorithm for source localization from time-differences of arrival," *IEEE Signal Processing Letters*, vol. 5, p. 1–4, 2008.

[66] W. Hahn and S. Tretter, "Optimum processing for delay-vector estimation in passive signal arrays," *IEEE Transactions on Information Theory*, vol. 19, no. 5, p. 608–614, 1973.

[67] M. Wax and T. Kailath, "Optimum localization of multiple sources by passive arrays," *IEEE Transactions on Acoustics, Speech and Signal Processing*, vol. 31, no. 5, p. 1210–1217, 1983.

[68] M. Segal, E. Weinstein, and B. R. Musicus, "Estimate-maximize algorithms for multichannel time delay and signal estimation," *IEEE Transactions on Signal Processing*, vol. 39, no. 1, p. 1–16, 1991.

[69] P. G. Georgiou and C. Kyriakakis, "Robust maximum likelihood source localization: The case for sub-gaussian versus gaussian," *IEEE Transactions on Audio, Speech, and Language Processing*, vol. 14, no. 4, p. 1470–1480, 2006.

[70] P. Aarabi, "The fusion of distributed microphone arrays for sound localization," *EURASIP Journal on Applied Signal Processing*, vol. 4, p. 338–347, 2003.

[71] M. Omologo and P. S. R. Demori, "Spoken Dialogue with Computers," *Acoustic Transduction. Academic Press*, vol. 4, p. 26, 1998.

[72] J. H. Dibiase, H. F. Silverman, and M. S. Brandstein, "Robust localization in reverberant rooms," in *Microphone Arrays: Signal Processing Techniques and Applications*, pp. 3, 4, 27, 35, 36, 42, Springer, 2001.

[73] D. B. Ward, E. A. Lehmann, and R. C. Williamson, "Particle filtering algorithms for tracking an acoustic source in a reverberant environment," *IEEE Transactions on Speech and Audio Processing*, vol. 11, no. 6, p. 826–836, 2003.

[74] P. Pertila, T. Korhonen, and A. Visa, "Measurement combination for acoustic source localization in a room environment," *EURASIP Journal on Audio, Speech, and Music Processing*, vol. 2008, p. 1–14, 2008.

[75] N. Strobel, S. Spors, and R. Rabenstein, "Joint audio-video signal processing for object localization and tracking," in *Microphone Arrays: Signal Processing Techniques and Applications*, vol. 4, p. 57, Springer, 2001.

[76] N. Strobel, S. Spors, and R. Rabenstein, "Joint audio-video object localization and tracking," *IEEE Signal Processing Magazine*, vol. 18, no. 1, p. 22–31, 2001.

[77] I. Potamitis, H. Chen, and G. Tremoulis, "Tracking of multiple moving speakers with multiple microphone arrays," *IEEE Transactions on Speech and Audio Processing*, vol. 12, no. 5, p. 520–529, 2004.

[78] U. Klee, T. Gehrig, and J. McDonough, "Kalman filters for time delay of arrival-based source localization," *EURASIP Journal on Applied Signal Processing*, vol. 2006, p. 1–15, 2006.

[79] S. Gannot and T. G. Dvorkind, "Microphone array speaker localizers using spatial-temporal information," *EURASIP Journal on Applied Signal Processing*, vol. 2006, p. 1–17, 2006.

[80] Z. Liang, X. Ma, and X. Dai, "Robust tracking of moving sound source using multiple model kalman filter," *Applied Acoustics*, vol. 69, no. 12, p. 1350–1355, 2008.

[81] C. Seguraa, A. Abad, J. Hernando, and C. Nadeu, "Multispeaker localization and tracking in intelligent environments," *Lecture Notes in Computer Science*, vol. 4625, p. 82–90, 2008.

[82] D. N. Zotkin, R. Duraiswami, and L. S. Davis, "Joint audio-visual tracking using particle filters," *EURASIP Journal on Applied Signal Processing*, vol. 11, no. 1, p. 1154–1164, 2002.

[83] J.-M. Valin, F. Michaud, and J. Rouat, "Robust localization and tracking of simultaneous moving sound sources using beamforming and particle filtering," *Robotics and Autonomous Systems*, vol. 55, no. 3, p. 216–228, 2007.

[84] F. Talantzis, A. Pnevmatikakis, and A. G. Constantinides, "Audiovisual active speaker tracking in cluttered indoors environments," *IEEE Transactions on Systems, Man, and Cybernetics, Part B: Cybernetics*, vol. 38, no. 3, p. 799–807, 2008.

[85] A. Quinlan, M. Kawamoto, Y. Matsusaka, H. Asoh, and F. Asano, "Tracking intermittently speaking multiple speakers using a particle filter," *EURASIP Journal on Audio, Speech, and Music Processing*, vol. 2009, p. 1–11, 2009.

[86] A. Levy, S. Gannot, and E. A. P. Habets, "Multiple-hypothesis extended particle filter for acoustic source localization in reverberant environments," *IEEE Transactions on Audio, Speech, and Language Processing*, vol. 19, no. 6, p. 1540–1555, 2011.

[87] J. J. Christensen and J. Hald, "Beamforming," *BK Technical Rev*, vol. 1, p. 1–31, 2004.

[88] S. Gombots and M. Kaltenbacher, "Inverse scheme for acoustic source localization in 3D," in *Euronoise 2018 - Conference Proceedings*, European Acoustics Association, 2018.

[89] H. Ding, Y. Bao, Q. Huang, C. Li, and G. Chai, "Three-dimensional localization of point acoustic sources using a planar microphone array combined with beamforming," *R. Soc. Open sci*, vol. 5, 2018. `https://doi.org/10.1098/rsos.181407`.

[90] B. D. Van Veen and K. M. Buckley, "Beamforming: a versatile approach to spatial filtering," *IEEE ASSP Mag*, vol. 5, pp. 4–24, 1988. 10.1109/53.665.

[91] M. S. Bartlett, "Smoothing periodograms from time-series with continuous spectra," *Nature*, vol. 161, p. 686–687, 1948.

[92] J. Capon, "High resolution frequency-wavenumber spectrum analysis," *Proceedings of the IEEE*, vol. 57, no. 8, p. 1408–1418, 1969.

[93] R. O. Schmidt, "Multiple emitter location and signal parameter estimation," in *Proceedings of the RADC Spectrum Estimation Workshop*, vol. 3, p. 243–258, 1979.

[94] R. O. Schmidt, "Multiple emitter location and signal parameter estimation," *IEEE Transactions on Antennas and Propagation*, vol. 34, no. 3, p. 276–280, 1986.

[95] A. Paulraj, R. Roy, and T. Kailath, "A subspace rotation approach to signal parameter estimation," *Proceedings of the IEEE*, vol. 74, no. 7, p. 1044–1046, 1986.

[96] R. Roy, A. Paulraj, and T. Kailath, "ESPRIT - a subspace rotation approach to estimation of parameters of cisoids in noise," *IEEE Transactions on Acoustics, Speech and Signal Processing*, vol. 34, no. 5, p. 1340–1342, 1986.

[97] R. Roy and T. Kailath, "ESPRIT- estimation of signal parameters via rotational invariance techniques," *IEEE Transactions on Acoustics, Speech and Signal Processing*, vol. 37, no. 7, p. 984– 995, 1989.

[98] U. Michel, *History of acoustic beamforming*. Berlin: Beamforming Conference BEBEC, 1st edn ed., 2006.

[99] C. Camier, J. Provencher, T. Padois, P. A. Gauthier, A. Berry, J. F. Blais, and R. Lapointe, "Fly-over source localization on civil aircrafts," in *19th AIAA/CEAS Aeroacoustics Conf*, Berlin, Germany: American Institute of Aeronautics and Astronautics Inc, 2013.

[100] T. Padois, C. Prax, V. Valeau, and D. Marx, "Experimental localization of an acoustic sound source in a wind-tunnel flow by using a numerical time-reversal technique," *J. Acoust. Soc. Am*, vol. 132, p. 2397–2407, 2012. 10.1121/1.4747015).

[101] C. Bahr, N. S. Zawodny, T. Yardibi, and F. Liu, "Shear layer correction validation using a nonintrusive acoustic point source," in *16th AIAA/CEAS Aeroacoustics Conf*, Stockholm, Sweden: Multi-Science Publishing Co. Ltd, 2010.

[102] M. R. Bai and J. Lee, "Industrial noise source identification by using an acoustic beamforming system," *Journal of Vibration and Acoustics*, vol. 120, p. 426–433, 1998. 10.1115/1.2893847.

[103] J. Kirkebo and A. Austeng, "Improved beamforming using curved sparse 2D arrays in ultrasound," *Ultrasonics*, vol. 46, p. 119–128, 2007. doi:10.1016/j.ultras.2007.01.001.

[104] N. Quaegebeur, T. Padois, P. A. Gauthier, and P. Masson, "Enhancement of time-domain acoustic imaging based on generalized cross-correlation and spatial weighting," *Mechanical Systems Signal Processing*, vol. 75, p. 515–524, 2016. 10.1016/j.ymssp.

[105] M. Palmese and A. Trucco, "Three-dimensional acoustic imaging by chirp zeta transform digital beamforming," *IEEE Transactions on Instrumentation and Measurement*, vol. 58, p. 2080–2086, 2009. 10.1109/TIM.2009.2015523.

[106] W. Zeng, H. Li, X. Zhu, and C. Chen, "A 2D adaptive beamforming method in sparse array," *AEU - International Journal of Electronics and Communications*, vol. 77, p. 100–104, 2017. 10.1016/j.aeue.2017.04.015.

[107] A. Koutny, O. Jiricek, J. H. Thomas, and M. Brothanek, "Source distance determination based on the spherical harmonics," *Mechanical Systems Signal Processing*, vol. 85, p. 993–1004, 2017. 10.1016/j.ymssp.

[108] T. Padois, F. Sgard, O. Doutres, and A. Berry, "Acoustic source localization using a polyhedral microphone array and an improved generalized cross-correlation technique," *Journal of Sound and Vibration*, vol. 386, p. 82–99, 2017.

[109] Z. Chu, Y. Yang, and Y. He, "Deconvolution for three-dimensional acoustic source identification based on spherical harmonics beamforming," *Journal of Sound and Vibration*, vol. 344, p. 484–502, 2015. doi:10.1016/j.jsv. 2015.01.047.

[110] Y. Yang, Z. Chu, L. Shen, and Z. Xu, "Functional delay and sum beamforming for three dimensional acoustic source identification with solid spherical arrays," *Journal of Sound and Vibration*, vol. 373, p. 340–359, 2016. 10.1016/j.jsv.2016.03.024.

[111] Z. Chu, Y. Yang, and L. Shen, "Resolution and quantification accuracy enhancement of functional delay and sum beamforming for three-dimensional acoustic source identification with solid spherical arrays," *Mechanical Systems Signal Processing*, vol. 88, p. 274–289, 2017. 10.1016/j.ymssp.

[112] Z. Zhang, S. Chen, Z. Xu, Y. He, and S. Li, "Iterative regularization method in generalized inverse beamforming," *Journal of Sound and Vibration*, vol. 396, p. 108–121, 2017. 10.1016/j.jsv.2017.02.044).

[113] S. Li, Z. Xu, Y. He, Z. Zhang, and S. Song, "Functional generalized inverse beamforming based on the double-layer microphone array applied to separate the sound sources," *Journal of Vibration and Acoustics*, vol. 138, pp. 13–21, 2016. 10.1115/1.4032305.

[114] R. Porteous, Z. Prime, C. Doolan, D. Moreau, and V. Valeau, "Three-dimensional beamforming of dipolar aeroacoustic sources," *Journal of Sound and Vibration*, vol. 355, p. 117–134, 2015. 10.1016/j.jsv.2015.06.030.

[115] A. Nehorai, K. C. Ho, and B. T. G. Tan, "Minimumnoise-variance beamformer with an electromagnetic vector sensor," *IEEE Transactions on Signal Processing*, vol. 47, p. 601–618, 1999. doi:10.1109/78.747769.

[116] A. C. Dhanantwari, "An efficient 3D beamformer implementation for real-time 4D ultrasound systems deploying planar array probes," in *IEEE ultrasonics symposium* (M. Yuhas, ed.), vol. vols 1–3, (New York, NY), p. 1421–1444, IEEE, 2004.

[117] K. Washburn, T. Frazer, and Kunio, "Correlating noise sources identified by beamforming with sound power measurements," in *SAE 2005 Noise and Vibration Conf. and Exhibition* (J., ed.), Traverse City, MI: SAE International, 2005.

[118] Z. Jin-quan, B. I. Chuan-xing, and C. Xin-zhao, "Study on array pattern and its application in noise source identification using beamforming method," *Noise Vibration and Control*, vol. 29, p. 54–58, 2009.

[119] T. Mukwevho, J. Jordaan, and G. Noel, *Advanced beamforming techniques for acoustic source localization*. New York, NY: IEEE, 2009.

[120] Z. Chu, Y. Yang, and Z. Jiang, "Study on the beamforming performance of microphones array," *Chinese Journal of Sensors and Actuators*, vol. 24, p. 665–670, 2011. 10.3969/j.issn.1004-1699.2011.05.008).

[121] G. H. Hardy, J. E. Littlewood, and G. Polya, *Inequalities*. Cambridge, UK: Cambridge University Press, 2nd edn ed., 1988.

[122] T. Padois and A. Berry, "Two and three dimensional sound source localization with beamforming and several deconvolution techniques," *Acta Acustica United with Acoustica*, vol. 103, p. 392–400, 2017. 10.3813/aaa.919069).

[123] Z. Chunping and L. Yudong, "Error analysis of the underwater imaging method using focused beamforming," *Technical Acoustics*, vol. 27, p. 18–24, 2008.

[124] R. Jia and G. Shi, "Fast direction finding algorithm for four-acoustic sensor square planar array and its error analysis," *Chinese Journal of Sensors and Actuators*, vol. 22, p. 1757–1762, 2009.

[125] M. R. Bai, J.-G. Ih, and J. Benesty, *Acoustic array systems: theory, implementation, and application*. John Wiley and Sons Singapore Pte. Ltd, 2013.

[126] E. G. Williams, J. Maynard, and E. Skudrzyk, "Sound source reconstruction using a microphone array," *Journal of Acoustical Society of America*, vol. 68, no. 4, p. 340–344, 1980.

[127] E. G. Williams, J. Maynard, and Y. Lee, "Nearfield acoustic holography: I. theory of generalized holography and the development of NAH," *Journal of Acoustical Society of America*, vol. 78, no. 4, p. 1395–1413, 1985.

[128] E. G. Williams, "Continuation of acoustic near-fields," *Journal of Acous- tical Society of America*, vol. 113, no. 3, p. 1273–1281, 2003.

[129] T. Loyau, J. C. Pascal, and P. Gaillard, "Broadband acoustic holography reconstruction from acoustic intensity measurements. i: Principle of the method," *Journal of Acoustical Society of America*, vol. 84, p. 1744–1750, 1988.

[130] M. S. Moondra and S. F. Wu, "Visualization of vehicle interior sound field using Nearfield Acoustical Holography based on the Helmholtz-Equation Least-Squares (HELS) method," *Noise Control Eng. J*, vol. 53, no. 4, 2005.

[131] E. G. Williams, J. D. Maynard, and E. Skudrzyk, "Sound source reconstruction using a microphone array," *J. Acoust. Soc. Am*, vol. 68, no. 1, p. 340–344, 1980.

[132] S. F. Wu and L. K. Natarajan, "Reconstruction Of Vibro-Acoustic Responses Of A Baffled Plate Using Helmholtz Equation Least Squares Method," in *Proceedings of the ASME 2009 International Mechanical Engineering Congress Exposition*, vol. 13201, (Lake Buena Vista, Florida, USA), 2009.

[133] E. G. Williams and J. D. Maynard, "Holographic imaging without the wavelength limit," *Physical Review Letters*, vol. 45, p. 554–557, 1980.

[134] E. G. Williams, J. D. Maynard, and E. Skudrzyk, "Sound source reconstructions using a microphone array," *Journal of the Acoustical Society of America*, vol. 68, p. 340–344, 1980.

[135] E. G. Williams, "The nearfield acoustic holography (NAH) experimental method applied to vibration and radiation in light and heavy fluids," *Computers and Structures*, vol. 65, p. 323–335, 1997.

[136] E. G. Williams and B. H. Houston, "Fast Fourier transform and singular value decomposition formulations for patch nearfield acoustical holography," *Journal of the Acoustical Society of America*, vol. 114, p. 1322–1333, 2003.

[137] J. Hald, "STSF – a unique technique for scan-based nearfield acoustic holography without restriction of coherence," *Bruel and Kjær Technical Review*, no. 1, 1989.

[138] J. Hald, "STSF – practical instrumentation and application," *Bruel and Kjær Technical Review*, no. 2, 1989.

[139] J. Hald, "Non-stationary STSF," *Bruel and Kjær Technical Review*, no. 1, 2000.

[140] E. G. Williams, *Fourier Acoustics: Sound Radiation and Nearfield Acoustical Holography*. San Diego, CA: Academic Press, 1999.

[141] M. A. Rowell and D. J. Oldham, "Determination of the directivity of a planar noise source by means of near field acoustical holography, 1: theoretical background," *Journal of Sound and Vibration*, vol. 180, p. 99–118, 1995.

[142] R. Steiner and J. Hald, "Near-field acoustical holography without the errors and limitations caused by the use of spatial dft," *Int. J. Acoust. Vib*, vol. 6, p. 83–89, 2001.

[143] F. Jacobsen and V. Jaud, "Statistically optimized near-field acoustical holography using an array of pressure-velocity probes," *Journal of Acoustical Society of America*, vol. 121, no. 3, p. 1550–1558, 2007.

[144] F. Jacobsen, V. Jaud, and C. Xinyi, "A comparison of statistically optimized near field acoustic holography using single layer pressure- velocity measurements and using double layer pressure."

[145] Z. Wang and S. F. Wu, "Helmholtz equation–least-squares method for reconstructing the acoustic pressure field," *J. Acoust. Soc. Am*, vol. 102, no. 4, p. 2020–2032, 1997.

[146] S. F. Wu, "On reconstruction of acoustic pressure fields using the Helmholtz equation–least-squares method," *J. Acoust. Soc. Am*, vol. 107, no. 5, p. 2511–2522, 2000.

[147] S. F. Wu and J. Yu, "Reconstructing interior acoustic pressure fields via Helmholtz equation–least-squares method," *J. Acoust. Soc. Am*, vol. 104, no. 4, p. 2054–2060, 1998.

[148] N. Rayess and S. F. Wu, "Experimental validations of the HELS method for reconstructing acoustic radiation from a complex vibrating structure," *J. Acoust. Soc. Am*, vol. 107, no. 6, p. 2955–2964, 2000.

[149] S. F. Wu and X. Zhao, "Combined Helmholtz equation–least squares method for reconstructing acoustic radiation from arbitrarily shaped objects," *The Journal of the Acoustical Society of America*, vol. 112, no. 1, pp. 179–188, 2002. https://doi.org/10.1121/1.1487845.

[150] M. Tournour, P. Brux, P. Mas, X. Wang, C. McCulloch, and P. Vignassa, *Inverse Numerical Acoustics of a Truck Engine*. SAE International, 2003.

[151] L. H. Chen and D. G. Schweikert, "Sound radiation from an arbitrary body," *Journal of the Acoustical Society of America*, vol. 35, p. 1626–1632, 1963.

[152] C. R. Kipp and R. J. Bernhard, "Prediction of acoustic behavior in cavities using an indirect boundary element method," *Transcations ASME, Journal of Vibration, Acoustics, Stress, and Reliability in Design*, vol. 109, p. 22–28, 1987.

[153] J.-L. Guyader, "Methods to reduce computing time in structural acoustics prediction," in *Proceedings 3rd International Congress on Air-And Structure-borne Sound and Vibration*, (Montreal, Canada), p. 5–20, 1994.

[154] G. H. Koopmann, L. Song, and J. B. Fahnline, "A method for computing acoustic fields based on the principle of wave superposition," *Journal of the Acoustical Society of America*, vol. 86, p. 2433–2438, 1989.

[155] J. B. Fahnline and G. H. Koopman, "A numerical solution for the general radiation problem based in the combined methods of superposition and singular-value decomposition," *Journal of the Acoustical Society of America*, vol. 90, p. 2808–2819, 1991.

[156] L. Song, G. H. Koopman, and J. B. Fahnline, "Active control of the acoustic radiation of a vibration structure using a superposition formulation," *Journal of the Acoustical Society of America*, vol. 89, p. 2786–2797, 1991.

[157] J. B. Mariem and M. A. Hamdi, "A new boundary finite element method for fluid-structure interaction problems," *International Journal for Numerical Methods in Engineering*, vol. 24, p. 1251–1267, 1987.

[158] G. Krishnasamy, L. W. Schmerr, T. J. Rudolphi, and F. J. Rizzo, "Hypersingular boundary integral equations: some applications in acoustic and elastic wave scattering," *Transcations ASME, Journal of Applied Mechanics*, vol. 57, p. 404–414, 1990.

[159] K. Gardner and R. J. Bernhard, "A noise source identification technique using an inverse Helmholtz integral equation method," *Trans. ASME, J. Vib. Acoust. Stress Reliab. Des*, vol. 110, p. 84–90, 1988.

[160] W. A. Veronesi and J. D. Maynard, "Digital holographic reconstruction of source with arbitrarily shaped surfaces," *J. Acoust. Soc. Am*, vol. 85, p. 588–598, 1989.

[161] M. R. Bai, "Application of BEM (boundary element method)-based acoustic holography to radiation analysis of sound sources with arbitrarily shaped geometries," *J. Acoust. Soc. Am*, vol. 92, p. 533–549, 1992.

[162] B. K. Kim and J. G. Ih, "On the reconstruction of the vibro-acoustic field over the surface enclosing an interior space using the boundary element method," *J. Acoust. Soc. Am*, vol. 100, p. 3003–3016, 1996.

[163] Z. Zhang, N. Vlahopoulos, S. T. Raveendra, T. Allen, and K. Y. Zhang, "A computational acoustic field reconstruction process based on an indirect boundary element formulation," *J. Acoust. Soc. Am*, vol. 108, p. 2167–2178, 2000.

[164] N. Valdivia and E. G. Williams, "Krylov subspace iterative methods for boundary element method based near-field acoustic holography," *J. Acoust. Soc. Am*, vol. 117, p. 711–724, 2005.

[165] J.-G. Ih, "Acoustic Holography Based on The Inverse-BEM for the Source Identification of Machinery Noise," in *14th International Congress on Sound and Vibration, ICSV14*, (Cairns ,Australia), 07 2007.

[166] H. A. Schenck, "Improved Integral Formulation for Acoustic Radiation Problems," *Journal of the Acoustical Society of America*, vol. 44, p. 41–58, 1968.

[167] A. J. Burton and G. F. Miller, "The Application of Integral Equation Methods to the Numerical Solution of Some Exterior Boundary-Value Problems," in *Proceedings of the Royal Society of London, Series A*, vol. 323, p. 201–210, 1971.

[168] D. Colton and R. Kress, *Integral Equation Methods in Scattering Theory*. John Wiley and Sons, Inc, 1983.

[169] G. H. Koopmann, L. Song, and J. B. Fahnline, "A method for computing acoustic fields based on the principle of wave superposition," *Journal of the Acoustical Society of America*, vol. 86, p. 2433–2438, 1989.

[170] L. Song, G. Koopmann, and J. B. Fahnline, "Numerical errors associated with the method of superposition for computing acoustic fields," *Journal of the Acoustical Society of America*, vol. 89, p. 2626–2633, 1991.

[171] J. B. Fahnline and G. H. Koopmann, "A numerical solution for the general radiation problem based on the combined methods of superposition and singular-value decomposition," *Journal of the Acoustical Society of America*, vol. 90, p. 2808–2819, 1991.

[172] B. Jin and Y. Zheng, "A meshless method for some inverse problems associated with the Helmholtz equation," *Computer Methods in Applied Mechanics and Engineering*, vol. 195, p. 2270–2288, 2006.

[173] I. Y. Jeon and J. G. Ih, "On the holographic reconstruction of vibroacoustic fields using equivalent sources and inverse boundary element method," *Journal of the Acoustical Society of America*, vol. 118, p. 3475–3484, 2005.

[174] N. P. Valdivia and E. G. Williams, "Study of the comparison of the methods of equivalent sources and boundary element methods for near-field acoustic holography," *Journal of the Acoustical Society of America*, vol. 120, p. 3694–3705, 2006.

[175] R. Jeans and I. C. Mathews, "The wave superposition method as a robust technique for computing acoustic fields," *Journal of the Acoustical Society of America*, vol. 92, p. 1156–1166, 1992.

[176] S. F. Wu, "Transient nearfield acoustical holography," *The Journal of the Acoustical Society of America*, vol. 136, no. 4, pp. 2171–2171, 2014. 10.1121/1.4899855.

[177] S. F. Wu, H. Lu, and M. S. Bajwa, "Reconstruction of transient acoustic radiation from a sphere," *The Journal of the Acoustical Society of America*, vol. 117, no. 4, pp. 2065–2077, 2005. 10.1121/1.1841771.

[178] M. Aucejo, N. Totaro, and J. L. Guyader, "Identification of source velocities on 3D structures in non-anechoic environments: Theoretical background and experimental validation of the inverse patch transfer functions method," *Journal of Sound and Vibration*, vol. 329, no. 18, p. 3691–3708, 2010.

[179] D. Vigoureux, N. Totaro, J. Lagneaux, and J. L. Guyader, "Inverse patch transfer functions method as a tool for source field identification," *Journal of Vibration and Acoustics*, vol. 137, no. 2, 2015.

[180] S. Forget, N. Totaro, J. L. Guyader, and M. Schaeffer, "Source fields reconstruction with 3D mapping by means of the virtual acoustic volume concept," *Journal of Sound and Vibration*, vol. 381, pp. 48–64, 2016.

[181] M. Ouisse, L. Maxit, C. Cacciolati, and J. L. Guyader, "Patch transfer functions as a tool to couple linear acoustic problems," *Journal of Vibration and Acoustics*, vol. 127, no. 5, p. 458–466, 2005.

[182] M. Aucejo, N. Totaro, and J. L. Guyader, "Identification of source velocities with Inverse Patch Transfer Functions method," in *Proceedings of ACOUSTICS08*, (Paris (France)), 2008.

[183] M. Aucejo, N. Totaro, and J. L. Guyader, "Identification of source velocities in presence of external correlated sources with the inverse patch transfer functions (IPTF) method," in *Proceedings of NOVEM 2009*, (Oxford (UK)), 2009.

[184] N. Totaro, C. Sandier, and J. L. Guyader, "Identify velocity of a complex source with iPTF method," in *Proceedings of ICSV15*, (Daejon (Korea)), 2008.

[185] N. Totaro, D. Vigoureux, Q. Leclère, J. Lagneaux, and J.-L. Guyader, "Sound fields separation and reconstruction of irregularly shaped sources," *Journal of Sound and Vibration*, vol. 336, p. 62–81, 2015.

[186] N. Totaro, S. Forget, and J. L. Guyader, "iPTF methods: How Green's identity and FEM solver can be used for acoustic inverse methods," in *Proceedings of EURONOISE 2015*, (Maastricht), 2015.

[187] M. Burger, "Lecture Notes on Inverse Problems." `https://www.uni-muenster.de/AMM/num/Vorlesungen/IP_WS07`.

[188] J. Hadamard, "Sur les problèmes aux derivées partielles et leur signification physique," *Princeton University Bulletin*, vol. 13, no. 4, p. 49–52, 1902.

[189] G. H. Golub and C. F. Loan, *Matrix Computations*. The John Hopkins University Press, second ed., 1989.

[190] P. Hansen, "Regularization tools: A Matlab package for analysis and solution of discrete ill-posed problems," *Numerical Algorithms*, vol. 6, p. 1–35, 1994.

[191] H. Golub and C. Loan, "Matrix Computations," in *Johns Hopkins Studies in the Mathematical Sciences*, Baltimore, MD: Johns Hopkins University Press, 3rd edn ed., 1996.

[192] P. C. Hansen, "The discrete Picard condition for discrete ill-posed problems," *BIT*, vol. 30, p. 658–672, 1990.

[193] P. C. Hansen, *Rank-Deficient and Discrete Ill-Posed Problems*. Philadelphia: SIAM, 2nd ed., 1998.

[194] R. Visser, "Regularization in nearfield acoustic source identification," in *Proceedings Eighth International Congress on Sound and Vibration*, (China), p. 1637–1644, Hong Kong, 2001.

[195] G. V. Borgiotti, "The power radiated by a vibrating body in an acoustic fluid and its determination from boundary measurements," *Journal of the Acoustical Society of America*, vol. 88, no. 4, p. 1884–1893, 1990.

[196] D. M. Photiadis, "The relationship of singular value decomposition to wave-vector filtering in sound radiation problems," *Journal of the Acoustical Society of America*, vol. 88, no. 2, p. 1152–1159, 1990.

[197] P. C. Hansen, "Truncated Singular Value Decomposition Solutions to Discrete Ill-Posed Problems with Ill-Determined Numerical Rank," *SIAM Journal on Scientific and Statistical Computing*, vol. 11, no. 3, pp. 503–518, 1990. 10.1137/0911028.

[198] P. Hansen, "Discrete Inverse Problems: Insight and Algorithms," *SIAM*, vol. 7, 2010. 10.1137/1.9780898718836.

[199] C. C. Tsai, Y. C. Lin, D. L. Young, and S. N. Atluri, "Investigations on the Accuracy and Condition Number for the Method of Fundamental Solutions," *Computer Modeling in Engineering & Sciences*, vol. 16, no. 2, pp. 103–114, 2006. 10.3970/cmes.2006.016.103.

[200] P. A. Nelson and S. H. Yoo, "Estimation of acoustic source strength by inverse methods: Part I, conditioning of the inverse problem," *Journal of Sound and Vibration*, vol. 233, no. 4, p. 643–668, 2000.

[201] P. A. Nelson and S. H. Yoo, "Estimation of acoustic source strength by inverse methods: Part II, experimental investigation of methods for choosing regularization parameters," *Journal of Sound and Vibration*, vol. 233, no. 4, p. 669–705, 2000.

[202] P. Hansen, *Rank-Deficient and Discrete Ill-Posed Problems: Numerical Aspects of Linear Inversion*. Philadelphia: SIAM, 1998.

[203] K. J. and E. Somersalo, "Statistical and Computational Inverse Problems," *Applied Mathematical Sciences*, vol. 160, 2005.

[204] T. A. and V. Arsenin, "Solution of Ill-posed Problems," 1977.

[205] P. Hansen, *Rank-Deficient and Discrete Ill-Posed Problems: Numerical aspects of linear inversion*. Phd thesis, Technical University of Denmark, Denmark, 1996.

[206] A. J. Pullan, L. K. Cheng, M. P. Nash, A. Ghodrati, R. MacLeod, and D. H. Brooks, "The Inverse Problem of Electrocardiography," in *Comprehensive Electrocardiology* (P. W. Macfarlane, A. van Oosterom, O. Pahlm, P. Kligfield, M. Janse, and J. Camm, eds.), (London), pp. 299–344, Springer London, 2010. `https://doi.org/10.1007/978-1-84882-046-3_9`.

[207] D. Brooks, G. Ahmad, and R. MacLeod, "Multiply constrained inverse electrocardiology: Combining temporal, multiple spatial, and iterative regularization," in *Proceedings of the IEEE Engineering in Medicine and Biology Society 16 th Annual International Conference*, p. 137–138, IEEE Computer Society, 1994.

[208] C. Ramanathan, P. Jia, R. Ghanem, D. Calvetti, and Y. Rudy, "Noninvasive electrocardiographic imaging (ECGI): application of the generalized minimal residual (GMRes) method," *Annals of Biomedical Engineering*, vol. 31, p. 981–994, September 2003.

[209] T. Delillo, T. Hrycak, and V. Isakov, "Theory and boundary element methods for near-field acoustic holography," *Journal of Computational Acoustics*, vol. 13, 03 2005. 10.1142/S0218396X05002554.

[210] J. Berger, *Statistical Decision Theory and Bayesian Analysis*. Springer, 1988.

[211] Y. Yamashita, "Theoretical studies on the inverse problem in electrocardiography and the uniqueness of the solution," *IEEE Transactions on Biomedical Engineering*, vol. 29, p. 719–725, 1982.

[212] C. Paige and M. Saunders, "LSQR: An algorithm for sparse linear equations and sparse least squares," *ACM Transactions Mathematical Software*, vol. 8, p. 43–71, 1982.

[213] J. Antoni, "A Bayesian approach to sound source reconstruction : optimal basis, regularization, and focusing," *The Journal of the Acoustical Society of America*, vol. 131, no. 4, pp. 2873–2890,, 2012.

[214] A. Pereira, Q. Leclère, and J. Antoni, "Empirical Bayesian regularization of the inverse acoustic problem," *Applied Acoustics*, vol. 97, p. 11–29, 2015.

[215] C. Robert, *The Bayesian Choice*. Springer, 2007.

[216] A. Gelman, J. B. Carlin, H. S. Stern, and D. B. Rubin, *Bayesian data analysis*. Chapman and Hall/CRC, 1995.

[217] D. Higdon, "A Primer on Space-Time Modeling from a Bayesian Perspective," 10 2006. 10.1201/9781420011050.ch6.

[218] J. Bardsley, "MCMC-Based Image Reconstruction with Uncertainty Quantification," *SIAM Journal on Scientific Computing*, vol. 34, 01 2012. 10.1137/11085760X.

[219] R. Gulrajani, "The forward and inverse problems of electrocardiography," *IEEE Engineering in Medicine and Biology Magazine*, vol. 17, no. 5, pp. 84–101, 1998. 10.1109/51.715491.

[220] S. Twomey, "On the numerical solution of Fredholm integral equations of the first kind by the inversion of the linear system produced by quadrature," *Journal of the ACM (JACM)*, vol. 10, no. 1, pp. 97–101, 1963.

[221] P. Hansen and D. O'Leary, "The use of the L-curve in the regularization of discrete ill-posed problems," *SIAM Journal on Scientific Computing*, vol. 14, pp. 1487–1503,, 1993.

[222] J. Winkler, "Tikhonov regularization in standard form for polynomial basis conversion," *Applied Mathematical Modelling*, vol. 21, p. 651–662, 1997.

[223] G. Wahba, "Practical Approximate Solutions to Linear Operator Equations When the Data are Noisy," *SIAM Journal on Numerical Analysis*, vol. 14, no. 4, pp. 651–667, 1977.

[224] M. A. Lukas, "Robust generalized cross-validation for choosing the regularization parameter," *Inverse Problems*, vol. 22, pp. 1883–1902, 2006.

[225] P. R. Johnston and R. M. Gulrajani, "A new method for regularization parameter determination in the inverse problem of electrocardiography," *IEEE Transactions on Biomedical Engineering*, vol. 44, no. 1, pp. 19–39, 1997.

[226] J. P. Barnes and P. R. Johnston, "Application of robust Generalised Cross-Validation to the inverse problem of electrocardiology," *Computers in Biology and Medicine*, vol. 69, no. 0010-4825, pp. 213–225, 2016. https://www.sciencedirect.com/science/article/pii/S0010482515004047.

[227] P. R. Johnston and R. M. Gulrajani, "An analysis of the zero-crossing method for choosing regularization parameters," *SIAM Journal on Scientific Computing*, vol. 24, no. 2, pp. 428–442, 2002.

[228] P. Hansen and D. O'Leary, "The use of the L-curve in the regularization of discrete ill-posed problems," *SIAM Journal of Scientific Computing*, vol. 14, p. 1487–1503, 1993.

[229] J. Lian, D. Yao, and B. He, "A new method for implementation of regularization in cortical potential imaging," in *Proceedings of 20th Anmu. International Conference*, p. 2155–2158, IEEE/EMBS, 1998.

[230] T. Regińska, "A regularization parameter in discrete ill-posed problems," *SIAM Journal on Scientific Computing*, vol. 17, no. 3, pp. 740–749, 1996.

[231] N. Totaro, C. Sandier, and Q. Leclère, "Source identification on a reduction gearbox using acoustical measurements in a non-anechoic environment," in *Proceedings of ICSV19*, (Vilnius (Lithuania)), 2012.

[232] Q. Leclère, "Acoustic imaging using under-determined inverse approaches: Frequency limitations and optimal regularization," *Journal of Sound and Vibration*, vol. 321, pp. 605–619, Apr. 2009.

[233] J. Antoni, "A Bayesian approach to sound source reconstruction: Optimal basis, regularization, and focusing," *Journal of the Acoustical Society of America*, vol. 131, no. 4, Part 1, pp. 2873–2890, 2012. 10.1121/1.3685484.

[234] B. Dong, *Spatial separation of sound sources*. PhD thesis, INSA de Lyon, 03 2014. `https://tel.archives-ouvertes.fr/tel-01175498/file/these.pdf`.

[235] P. Comon, "Independent component analysis: A new concept?," in *Signal Processing*, vol. 36, p. 287–314, 1994.

[236] K. Kokkinakis and P. Loizou, "Advances in Modern Blind Signal Separation Algorithms: Theory and Applications," *Synthesis Lectures on Algorithms and Software in Engineering*, vol. 2, 01 2010. 10.2200/S00258ED1V01Y201003ASE006.

[237] A. Cichocki, "Blind Signal Processing Methods for Analyzing Multichannel Brain Signals," *International Journal of Bioelectromagnetism*, vol. 6, 01 2004.

[238] B. Dong, J. Antoni, A. Pereira, and W. Kellermann, "Blind separation of incoherent and spatially disjoint sound sources," *Journal of Sound and Vibration*, vol. 383, pp. 414–445, 2016. `https://doi.org/10.1016/j.jsv.2016.07.018`.

[239] V. Thürey, "The Complex Angle in Normed Spaces," *Journal of Physics: Conference Series*, vol. 490, mar 2014. 10.1088/1742-6596/490/1/012038.

[240] K. Scharnhorst, "Angles in Complex Vector Spaces," *Acta Applicandae Mathematicae*, vol. 69, no. 1, pp. 95–103, 2001. 10.1023/a:1012692601098.

[241] A. Marsh, *Mathematics For Physics: An Illustrated Handbook*. World Scientific Publishing Company, 2017. 9789813233935.

[242] S. Trampitsch, *Complex-Valued Data Estimation: Second-Order Statistics and Widely Linear Estimators*. Phd thesis, Alpen-Adria-Universität Klagenfurt, Klagenfurt, Austria, 04 2013. 10.13140/RG.2.2.13506.30404.

A

Algorithm for the iterative approach

Algorithm 2 CGNE-LBR Algorithm. Implemented as $\mathcal{CGNELBR}$

Inputs:
$\mathbf{A} \in \mathbb{C}^{m\times n}$ and $\mathbf{y} \in \mathbb{C}^{m\times 1}$ of Equation (3.4)
$w = \left\|\mathbf{A}^{\mathrm{H}}\mathbf{y}\right\|_2 / \left\|\mathbf{A}^{\mathrm{H}}\mathbf{A}\right\|_2$ (weighting factor)
Output: $\widehat{\mathbf{x}}_{\mathrm{ZERO}} \in \mathbb{C}^{n\times 1}$ and $\widehat{\mathbf{x}}_{\mathrm{MINP}} \in \mathbb{C}^{n\times 1}$
Initialize:
$\ddot{\mathbf{A}} \leftarrow (\mathbf{A}^{\mathrm{H}}\mathbf{A}) / \left\|\mathbf{A}^{\mathrm{H}}\mathbf{A}\right\|_2$ (Normalization)
$\ddot{\mathbf{y}} \leftarrow (\mathbf{A}^{\mathrm{H}}\mathbf{y}) / \left\|\mathbf{A}^{\mathrm{H}}\mathbf{y}\right\|_2$ (Normalization)
$\mathbf{U}(:,1) \leftarrow \ddot{\mathbf{y}} / \|\ddot{\mathbf{y}}\|_2$
$\mathbf{V}(:,0) \leftarrow \mathbf{0}$
$\mathbf{B}(1,0) \leftarrow 0$
$\mathbf{X}(:,:) \leftarrow \mathbf{0}$
$\Psi(:,:) \leftarrow \mathbf{0} \in \mathbb{R}^{1\times r}$
$\mathrm{J}(:) \leftarrow \mathbf{0}, \quad \mathrm{J} \in \mathbb{R}^r$
$\mathrm{G}(:) \leftarrow \mathbf{0}, \quad \mathrm{J} \in \mathbb{R}^r$
for $i = 1, 2, \ldots, r$ **do**
$\mathbf{h} \leftarrow \ddot{\mathbf{A}}^{\mathrm{H}}\mathbf{U}(:,i) - \mathbf{B}(i,i-1) * \mathbf{V}(:,i-1)$
$\mathbf{h} \leftarrow \mathbf{h} - V(:,1:i-1)\left(\mathbf{V}(:,1:i-1)^{\mathrm{H}}\mathbf{h}\right)$ (re-orthogonalization)
$\mathbf{B}(i,i) \leftarrow \|\mathbf{h}\|_2$
$\mathbf{V}(:,i) \leftarrow \mathbf{h} / \mathbf{B}(i,i)$
$\mathbf{q} \leftarrow \ddot{\mathbf{A}}\mathbf{V}(:,i) - \mathbf{B}(i,i) * \mathbf{U}(:,i)$
$\mathbf{q} \leftarrow \mathbf{q} - \mathbf{U}(:,1:i)\left(\mathbf{U}(:,1:j)^{\mathrm{H}}\mathbf{q}\right)$ (re-orthogonalization)
$\mathbf{U}(:,i+1) \leftarrow \mathbf{q} / \mathbf{B}(i+1,i)$
$[\hat{\mathbf{U}}, \hat{\mathbf{\Sigma}}, \hat{\mathbf{V}}] \leftarrow \mathrm{SVD}(\mathbf{B}(1:i+1, 1:j))$ (the reduced SVD)
$\psi_i \leftarrow |\hat{\mathbf{U}}(1,i)| / \hat{\mathbf{\Sigma}}(i,i)$
$\Psi(1,i) \leftarrow \psi_i$

$$\mathbf{x}_i \leftarrow \|\mathbf{y}\|_2 \, \mathbf{V}(:,1:i)\hat{\mathbf{V}}\hat{\mathbf{\Sigma}}^{-1}\hat{\mathbf{U}}(1,:)^{\mathrm{H}} \tag{A.1}$$

$\mathbf{X}(:,i) \leftarrow w\mathbf{x}_i$ (De-Normalization with weighting factor)

$$\mathrm{J}(i) \leftarrow (\|w\mathbf{A}\mathbf{x}_i - \mathbf{y}\|_2) \cdot (\|\mathbf{X}(:,i)\|_2) \quad \text{(Itr\_MINP objective function value)} \tag{A.2}$$

$$\mathrm{G}(i) \leftarrow |\|w\mathbf{A}\mathbf{x}_i - \mathbf{y}\|_2 - i\|\mathbf{X}(:,i)\|_2| \quad \text{(Itr\_ZERO objective function value)} \tag{A.3}$$

end for
Estimation of $\mathbf{x}$: $\widehat{\mathbf{x}}$
`Itr_MINP` Estimation: Find $\widehat{\mathbf{x}}$ as the $\mathbf{x}_i$ in $\mathbf{X}$ that yields the minimum value in J :

$$\widehat{\mathbf{x}}_{\mathrm{MINP}} = \min_{\mathbf{x}}(\mathrm{J}), \quad \mathbf{x} \in \mathbf{X} \tag{A.4}$$

`Itr_ZERO` Estimation: Find $\widehat{\mathbf{x}}$ as the $\mathbf{x}_i$ in $\mathbf{X}$ that yields the minimum value in G :

$$\widehat{\mathbf{x}}_{\mathrm{ZERO}} = \min_{\mathbf{x}}(\mathrm{G}), \quad \mathbf{x} \in \mathbf{X} \tag{A.5}$$

B

Other Computations involved in DBKH-iPTF algorithm

Algorithm 3 Finding regularization operator from an inverse Normalized Matrix. Implemented as $\mathcal{TRM}$

1: **Inputs:**
$\mathbf{A} \in \mathbb{C}^{m\times n}$ and $\mathbf{y} \in \mathbb{C}^{m\times 1}$ of Equation (3.4)
2: Generate the normalize matrix of $\mathbf{A}$ as seen in Equation (3.33) as $\mathbf{A}^{\mathrm{H}}\mathbf{A}$
3: Check if matrix $\mathbf{A}^{\mathrm{H}}\mathbf{A}$ is symmetric positive-definite matrix
4: **if** step 3 above is True **then** :
5: Perform the Cholesky-decomposition of $\left(\mathbf{A}^{\mathrm{H}}\mathbf{A}\right)^{-1}$:

$$\left[\mathbf{A}^{\mathrm{H}}\mathbf{A}\right]^{-1} = \mathrm{chol}\left(\left[\mathbf{A}^{\mathrm{H}}\mathbf{A}\right]^{-1}\right) = \mathbf{L}\mathbf{L}^{\mathrm{H}} \tag{B.1}$$

return $\mathbf{L}^{\mathrm{H}} \in \mathbb{C}^{n\times n}$ is Upper triangular matrix.
6: **else**
7: Perform the SVD of $\mathbf{A}^{\mathrm{H}}\mathbf{A}$ considering the economy-size SVD of $\mathbf{A}$ to be $\mathbf{A} = \mathbf{U}\Sigma\mathbf{V}^{\mathrm{H}}$ in Equation (3.6) as already discussed in Section 3.2.2.1 :

$$\begin{aligned}
\left[\mathbf{A}^{\mathrm{H}}\mathbf{A}\right]^{-1} &= \mathrm{svd}\left(\left[\mathbf{A}^{\mathrm{H}}\mathbf{A}\right]^{-1}\right) \\
&= \left[\left(\mathbf{U}\Sigma\mathbf{V}^{\mathrm{H}}\right)^{\mathrm{H}}\left(\mathbf{U}\Sigma\mathbf{V}^{\mathrm{H}}\right)\right]^{-1} \\
&= \left[\mathbf{V}\mathbf{\Sigma}^{\mathrm{H}}\underbrace{\mathbf{U}^{\mathrm{H}}\mathbf{U}}_{=I}\mathbf{\Sigma}\mathbf{V}^{\mathrm{H}}\right]^{-1} \\
&= \left[\mathbf{V}\mathbf{\Sigma}^{\mathrm{H}}\mathbf{\Sigma}\mathbf{V}^{\mathrm{H}}\right]^{-1} \\
&= \mathbf{\Sigma}^{-1}\mathbf{V}\mathbf{\Sigma}^{-\mathrm{H}}\mathbf{V}^{\mathrm{H}} \\
&= \mathbf{L}\mathbf{L}^{\mathrm{H}}
\end{aligned} \tag{B.2}$$

with

$$\mathbf{L}^{\mathrm{H}} = \mathbf{\Sigma}^{-\mathrm{H}}\mathbf{V}^{\mathrm{H}} = \mathbf{\Sigma}^{-1}\mathbf{V}^{\mathrm{H}} \tag{B.3}$$

return $\mathbf{L}^{\mathrm{H}} \in \mathbb{C}^{n\times n}$.
8: **end if**

Algorithm 4 Robust statistics of estimating a univariate location. Implemented as Bay_MAD

1: **Inputs:**
Univariate complex data set $Y_k \in \mathbb{C}^n$ such that $Y_k = \{y_1, y_2 \ldots, y_n\}$
Threshold value: t
2: **Output:** $\hat{\mu}$
3: Convert Y_k to absolute values to obtain new data, $X_k \in \mathbb{R}^n$:

$$\begin{aligned} X_k &= |Y_k| \\ &= \{|y_1|, |y_2| \ldots, |y_n|\} \\ &= \{x_1, x_2 \ldots, x_n\}, \quad j = 1, \ldots, n \end{aligned} \tag{B.4}$$

4: Reshuffle X_k as univariate ordered data set $\mathrm{X_n} \in \mathbb{R}^n$ such that

$$X_n = \{x_1, x_2 \ldots, x_n\}, \quad x_1 \leqslant x_2 \leqslant \cdots \leqslant x_n, \quad i = 1, \ldots, n \tag{B.5}$$

5: Compute the median, $\underset{i=1,\ldots,n}{\text{median}}(X_n)$ as a robust estimate of the location statistic measure of X_n

$$\underset{i=1,\ldots,n}{\text{median}}(X_n) = \begin{cases} x_{\left(\frac{n+1}{2}\right)} & \text{if } n \text{ is odd} \\ \frac{1}{2}\left(x_{\left(\frac{n}{2}\right)} + x_{\left(\frac{n}{2}+1\right)}\right) & \text{if } n \text{ is even} \end{cases} \tag{B.6}$$

6: Compute the median absolute deviation (MAD) as a robust estimate of the scale statistics measure of X_k

$$\mathrm{MAD}(X_k) = 1.483 \underset{j=1,\ldots,n}{\text{median}}\left(\left|x_j - \underset{i=1,\ldots,n}{\text{median}}(X_n)\right|\right) \tag{B.7}$$

7: Compute robust score z_i for each elements in X_k as

$$z_j = \frac{1}{\mathrm{MAD}(X_k)}\left(x_j - \underset{i=1,\ldots,n}{\text{median}}(X_n)\right) \quad j = 1, \ldots, n \tag{B.8}$$

8: Generate the $Z_k \in \mathbb{R}^n$ score sequence:

$$Z_k = \{z_1, z_2 \ldots, z_n\}, \quad j = 1, \ldots, n \tag{B.9}$$

9: Select from X_k the observations that fulfil the condition below to create $X_k^* \in \mathbb{C}^m$

$$\begin{aligned} X_k^* &= \{x_j : |z_j| < t, \quad j = 1, \ldots, k\} \\ &= \{x_1, x_2 \ldots, x_m\}, \quad l = 1, \ldots, m \quad (m \leqslant k) \end{aligned} \tag{B.10}$$

10: Select from Y_k the observations that correspond to X_m^* to obtain $Y_k^* \in \mathbb{C}^m$, with $Y_k^* = \{y_1, y_2 \ldots, y_m\}$
11: Compute the arithmetic mean $\hat{\mu}$ of $\mathrm{Y_k^*}$

$$\hat{\mu} = \bar{y}_l = \frac{1}{m}\sum_{l=1}^{m} y_l \tag{B.11}$$

C

Correlation indices for complex Vectors

The introduction of an angle between two vectors $\mathbf{v}$, $\mathbf{w}$ of a (finite-dimensional) complex (Hermitian, unitary) vector space $\mathrm{V}^{\mathbb{C}}\,(\simeq \mathbb{C}_n, n \in \mathbb{N}, n \geq 2)$ is ambiguous and can be performed [239, 240]

- either directly in the complex vector space $\mathrm{V}^{\mathbb{C}}$ by relying on the Hermitian product defined in it for any pair of vectors $\mathbf{v}, \mathbf{w} \in \mathrm{V}^{\mathbb{C}}$
- by relying on the real vector space $\mathbf{V}^{\mathbb{R}}\,(\simeq \mathbb{R}^{2n})$ isometric to $\mathbf{V}^{\mathbb{C}}$

Both approaches which are not completely independent are equally justified [239, 240].

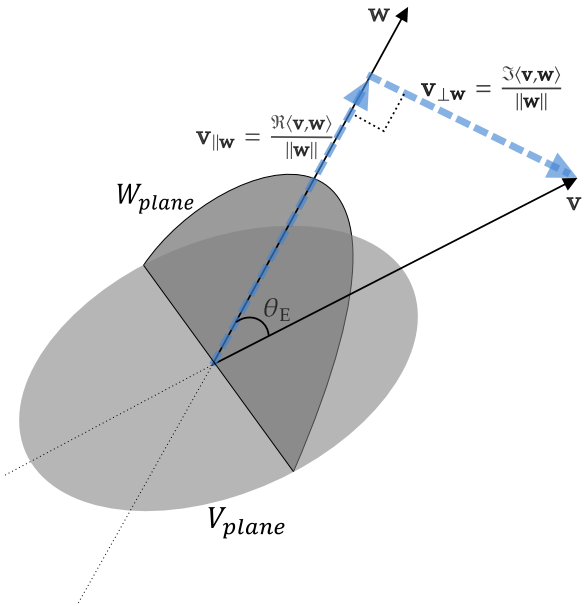

Figure C.1: Holomorphic space defined by the W_{plane} and V_{plane} planes.

Given a complex vector space $\mathrm{V}^{\mathbb{C}}$, a Hermitian form $\varphi : \mathrm{V}^{\mathbb{C}} \times \mathrm{V} \to \mathbb{C}$ is *positive* if $\varphi(\mathbf{w}, \mathbf{w}) \geq 0$ for all $\mathbf{w} \in \mathrm{V}$, *positive definite* if $\varphi(\mathbf{w}, \mathbf{w}) > 0$ for all $\mathbf{w} \neq \mathbf{0}$. A pair $\langle \mathrm{V}^{\mathbb{C}}, \varphi \rangle$ is called a *pre-Hilbert space* if φ is positive, and a *Hermitian (or unitary) space* if φ is positive definite [239, 240]. The quantity $\varphi(\mathbf{v}, \mathbf{w})$ is usually called the Hermitian inner product of $\mathbf{v}$ and$\mathbf{w}$. This will be denoted as $\langle \mathbf{v}, \mathbf{w} \rangle$.

$$\langle \mathbf{v}, \mathbf{w} \rangle = \langle (v_1, \ldots, v_n)^{\mathrm{T}}, (w_1, \ldots, w_n)^{\mathrm{T}} \rangle = \overline{v}_1 w_1 + \overline{v}_2 w_2 + \cdots + \overline{v}_n w_n \tag{C.1}$$

where $\overline{a}$ is the complex conjugate of a.
In an inner product space, the norm of a vector is defined as $\|\mathbf{v}\| \equiv \sqrt{\langle \mathbf{v}, \mathbf{v} \rangle}$. As a result a norm

on a vector space is a non-negative real function that is only nil for zero vector and satisfies the Cauchy-Schwarz inequality $|\langle \mathbf{v}, \mathbf{w} \rangle| \leq \|\mathbf{v}\|\|\mathbf{w}\|$, triangle inequality $\|\mathbf{v}+\mathbf{w}\| \leq \|\mathbf{v}\| + \|\mathbf{w}\|$ and for a constant a, $\|a\mathbf{v}\| = |a|\|\mathbf{v}\|$ [241]. This makes the space a normed vector space. Existence of a norm does not in general imply the existence of an inner product, but if a norm satisfies the parallelogram identity [241].

$$\|\mathbf{v}+\mathbf{w}\|^2 + \|\mathbf{v}-\mathbf{w}\|^2 = 2\left(\|\mathbf{v}\|^2 + \|\mathbf{w}\|^2\right), \tag{C.2}$$

an inner product can be obtained using the polarization identity [241], which for a real vector space is

$$\begin{aligned} \langle \mathbf{v}, \mathbf{w} \rangle &= \frac{1}{4}\left(\|\mathbf{v}+\mathbf{w}\|^2 - \|\mathbf{v}-\mathbf{w}\|^2\right) \\ &= \frac{1}{2}\left(\|\mathbf{v}\|^2 + \|\mathbf{w}\|^2 - \|\mathbf{v}-\mathbf{w}\|^2\right) \\ &= \frac{1}{2}\left(\|\mathbf{v}+\mathbf{w}\|^2 - \|\mathbf{v}\|^2 - \|\mathbf{w}\|^2\right) \end{aligned} \tag{C.3}$$

and for a complex vector space is

$$\langle \mathbf{v}, \mathbf{w} \rangle = \frac{1}{4}\left(\|\mathbf{v}+\mathbf{w}\|^2 - \|\mathbf{v}-\mathbf{w}\|^2 + i\|\mathbf{v}-i\mathbf{w}\|^2 - i\|\mathbf{v}+i\mathbf{w}\|^2\right). \tag{C.4}$$

In a complex vector space V, taking the real part of the cosine defines the *Euclidean angle* θ_{E} [241] (as shown in Figure C.1) such that

$$\begin{aligned} \mathcal{CEA} := \cos\theta_{\mathbb{E}} &= \frac{\Re(\langle \mathbf{v}, \mathbf{w} \rangle)}{\|\mathbf{v}\|\|\mathbf{w}\|} \\ &= \frac{\Re(\mathbf{v}^{\mathrm{H}}\mathbf{w})}{\|\mathbf{v}\|\|\mathbf{w}\|} \end{aligned} \tag{C.5}$$

where $\Re\langle \mathbf{v}, \mathbf{w} \rangle$ is the real part of Hermitian inner product, which is the angle between the vectors in the decomplexification $\mathbf{V}^{\mathbb{R}}$. This angle $\theta_{\mathbb{E}} \in [0, 2\pi]$ is a direction (or rotation) angle defined mod 2π between the directions spanned by the real unit vectors $\frac{\mathbf{v}}{\|\mathbf{v}\|}$ and $\frac{\mathbf{w}}{\|\mathbf{w}\|}$ and thus yields a real value of $\mathcal{CEA} \in [-1, 1]$.
If we decompose $\mathbf{v}$ into components parallel and orthogonal to $\mathbf{w}$, the parallel component is called the orthogonal projection of $\mathbf{v}$ onto $\mathbf{w}$ in $\mathbf{V}^{\mathbb{R}}$ is given by

$$\begin{aligned} \mathbf{v}_{\parallel \mathbf{w}} &= \frac{\Re(\langle \mathbf{v}, \mathbf{w} \rangle)}{\|\mathbf{w}\|} \\ &= \|\mathbf{v}\| \cos\theta_{\mathbb{E}}. \end{aligned} \tag{C.6}$$

The component of $\mathbf{v}$ orthogonal to $\mathbf{w}$ is given by

$$\begin{aligned} \mathbf{v}_{\perp \mathbf{w}} &= \frac{\Im(\langle \mathbf{v}, \mathbf{w} \rangle)}{\|\mathbf{w}\|} \\ &= \|\mathbf{v}\| \sin\theta_{\mathbb{E}}. \end{aligned} \tag{C.7}$$

and

$$\begin{aligned} \mathcal{SEA} := \sin\theta_{\mathbb{E}} &= \frac{\Im(\langle \mathbf{v}, \mathbf{w} \rangle)}{\|\mathbf{v}\|\|\mathbf{w}\|} \\ &= \frac{\Im(\mathbf{v}^{\mathrm{H}}\mathbf{w})}{\|\mathbf{v}\|\|\mathbf{w}\|} \end{aligned} \tag{C.8}$$

where $\mathcal{SEA} \in [-1, 1]$ and $\Im\langle \mathbf{v}, \mathbf{w} \rangle$ is the imaginary part of Hermitian inner product.
Finally, taking the modulus of the cosine defines the Hermitian angle [241], $\theta_{\mathbb{H}} \in \left[0, \frac{\pi}{2}\right]$ such that

$$\mathcal{CHA} := \cos\theta_{\mathbb{H}} = \frac{|\langle \mathbf{v}, \mathbf{w} \rangle|}{\|\mathbf{v}\|\|\mathbf{w}\|} \tag{C.9}$$

where $\mathcal{CHA} \in [0, 1]$.

The link between both angles that is $\theta_{\mathbb{E}}$ and $\theta_{\mathbb{H}}$ can be expressed as follows:

$$\begin{aligned}
\theta_{\mathbb{E}} :&= \inf_{\substack{\mathbf{v}_\theta \in \mathrm{span}\{\mathbf{v}\} \\ \mathbf{w}_\theta \in \mathrm{span}\{\mathbf{w}\}}} \cos^{-1}\left(\frac{\Re(\langle \mathbf{v}_\theta, \mathbf{w}_\theta \rangle)}{\|\mathbf{v}_\theta\|\|\mathbf{w}_\theta\|}\right) \\
&= \inf_{\substack{\theta_1 \in [0, 2\pi) \\ \theta_2 \in [0, 2\pi)}} \cos^{-1}\left(\frac{\Re(\langle e^{i\theta_1}\mathbf{v}, e^{i\theta_2}\mathbf{w} \rangle)}{\|\mathbf{v}_\theta\|\|\mathbf{w}_\theta\|}\right) \\
&= \sup_{\theta \in [0, 2\pi)} \cos^{-1}\left(\frac{\Re(e^{i\theta}\langle \mathbf{v}, \mathbf{w} \rangle)}{\|\mathbf{v}\|\|\mathbf{w}\|}\right) \\
&= \cos^{-1}\left(\frac{1}{\|\mathbf{v}\|\|\mathbf{w}\|}\Re\left(\frac{\langle \mathbf{w}, \mathbf{v} \rangle}{|\langle \mathbf{v}, \mathbf{w} \rangle|}\langle \mathbf{v}, \mathbf{w} \rangle\right)\right) \\
&= \cos^{-1}\frac{|\langle \mathbf{v}, \mathbf{w} \rangle|}{\|\mathbf{v}\|\|\mathbf{w}\|} = \theta_{\mathbb{H}}
\end{aligned} \tag{C.10}$$

where inf and sup are infimum and supremum of a set respectively.
Therefore, the Hermitian angle $\theta_{\mathbb{H}}$ between $\mathbf{v}$ and $\mathbf{w}$ can be thought of as the Euclidean angle $\theta_{\mathbb{E}}$ between the subspaces spanned by $\mathbf{v}$ and $\mathbf{w}$. Moreover, the Hermitian and Euclidean angles between two vectors $\mathbf{v}$, $\mathbf{w}$ are equal if the vectors have the same orientation in $\mathrm{V}^{\mathbb{C}}$, that is if they satisfy the condition

$$\langle \mathbf{v}, \mathbf{w} \rangle \in \mathbb{R}^+ \tag{C.11}$$

From above it can be observed that $\theta_{\mathbb{E}}$ offers both geometric and analytic meaning whilst there is no such a geometric interpretation for its Hermitian counterpart $\theta_{\mathbb{H}}$ (it has only analytic meaning).

It is intriguing for one to know the extent to which $\mathbf{v}$ is projected on $\mathbf{w}$. As a result we introduce the closeness-index which is defined with the formula

$$\begin{aligned}
\mathcal{CI} &= 1 - \frac{\|\mathbf{v} - \mathbf{w}\|^2}{\|\mathbf{v}\|^2 + \|\mathbf{w}\|^2} \\
&= \frac{\|\mathbf{v}\|^2 + \|\mathbf{w}\|^2 - \|\mathbf{v} - \mathbf{w}\|^2}{\|\mathbf{v}\|^2 + \|\mathbf{w}\|^2} \\
&= \frac{2\Re(\langle \mathbf{v}, \mathbf{w} \rangle)}{\|\mathbf{v}\|^2 + \|\mathbf{w}\|^2}
\end{aligned} \tag{C.12}$$

where $\mathcal{CI} \in [-1, 1]$.

In conclusion in order to completely compare two complex vectors $\mathbf{v}$ and $\mathbf{w}$ taking into account differences in phase and magnitude, all the above mentioned indices; $\mathcal{CHA}$, $\mathcal{CEA}$, $\mathcal{SEA}$ and $\mathcal{CI}$ should be used. For two complex vectors approximately equal, it is expected for the value of $\mathcal{CHA}(\mathbf{v}, \mathbf{w}) \simeq 1$, $\mathcal{CEA}(\mathbf{v}, \mathbf{w}) \simeq 1$, $\mathcal{SEA}(\mathbf{v}, \mathbf{w}) \simeq 0$, and $\mathcal{CI} \simeq 1$. On the contrary, if the two complex vectors are far from being equal they will generate values different from the aforementioned values.

D

Numerical Simulation of Noise for iPTF problem

Algorithm 5 Numerical simulation of Noise. Implemented as $\mathcal{NSN}$

Inputs:
$\mathbf{A} \in \mathbb{C}^{m \times n}$ where n = number of sensors and m = number of frequency
SNR value: $q \in \mathbb{R}$
Output: Noisy data $\bar{\mathbf{A}} \in \mathbb{C}^{m \times n}$
Generate zero-mean Gaussian random variables with a unit variance:

$$\mathbf{\Lambda} = \text{random.normal}(m \times n) \in \mathbb{C}^{m \times n} \tag{D.1}$$

$$\mathbf{\Delta} = \text{random.normal}(m \times n) \in \mathbb{C}^{m \times n} \tag{D.2}$$

Generate random variables uniformly distributed between 0 and 2π

$$\mathbf{\Theta} = 2\pi \times (\text{random.uniform}(m \times n)) \in \mathbb{C}^{m \times n} \tag{D.3}$$

$$\mathbf{\Phi} = 2\pi \times (\text{random.uniform}(m \times n)) \in \mathbb{C}^{m \times n} \tag{D.4}$$

compute the background noise value, $g \in \mathbb{R}$ $\mathbf{g}(:) \leftarrow \mathbf{0} \in \mathbb{C}^m$
for $i = 1, 2, \ldots, m$ **do**
    $\mathbf{g}(i) \leftarrow \mathcal{RMS}(\mathbf{A}(:, i))$, where

$$\mathcal{RMS}(\mathbf{b}) = \sqrt{\frac{1}{n}\sum_{j=1}^{n} |b_j|^2} \tag{D.5}$$

end for

$$g = \underset{i=1,\ldots,m}{\text{median}}\,(\mathbf{g}) \tag{D.6}$$

Compute the SNR factor, $\xi \in \mathbb{R}$

$$\xi = \left(\frac{1}{10}\right)^{q/20} \tag{D.7}$$

compute the multiplicative noise $\Pi \in \mathbb{C}^{m \times n}$

$$\Pi = \xi \times (\mathbf{\Lambda} \odot \exp(i\mathbf{\Theta})) \odot \mathbf{A} \tag{D.8}$$

where $\odot$ represent element-wise multiplication.
compute the Additive noise $\Upsilon \in \mathbb{C}^{m \times n}$

$$\Upsilon = \xi \times (\mathbf{\Delta} \odot \exp(i\mathbf{\Phi})) \times g \tag{D.9}$$

compute the total noise $\mathbf{E} \in \mathbb{C}^{m \times n}$

$$\mathbf{E} = \Pi + \Upsilon \tag{D.10}$$

return

$$\bar{\mathbf{A}} = \mathbf{A} + \mathbf{E} \tag{D.11}$$

E

Description of the random variable considered for generating an acoustic response due to uncorrelated source fields

All the measured signals presented in this thesis are complex in nature and for this reason the random variable to be considered should also be complex. As a result a look into the statistical behaviour of a complex random variable is presented.

A complex random variable is denoted by $\varepsilon = \varepsilon_r + j\varepsilon_i$, where ε_r and ε_i represent the real and imaginary part. As ε_r and ε_i are real-valued random variables, their statistical behavior can be completely described by a joint real probability density function (pdf). The extension to complex estimation theory requires complex pdfs. Although one calls it complex pdf, it is always a real-valued function. With it, it is possible to derive characteristics like the mean or the variance for complex-valued variables.

A complex-valued random variable ε consists of two different real-valued random variables. The equivalent real random vector $\boldsymbol{\varepsilon}_{\mathbb{R}} = \begin{bmatrix} \varepsilon_r & \varepsilon_i \end{bmatrix}^T$, where $\varepsilon_{\mathbb{R}}$ is just a different approach to look on ε.

With the above, it is possible to alter the definitions from the real to the complex case, where N$-$ dimensional random vector is complex-valued $\boldsymbol{\varepsilon} = \boldsymbol{\varepsilon}_r + j\boldsymbol{\varepsilon}_i \in \mathbb{C}^{\mathrm{N}}$. As already mentioned, the complex representation is just another way to describe the real vector $\boldsymbol{\varepsilon}_{\mathbb{R}} = \begin{bmatrix} \boldsymbol{\varepsilon}_r^{\mathrm{T}} & \boldsymbol{\varepsilon}_i^{\mathrm{T}} \end{bmatrix}^{\mathrm{T}}$.

To describe the pdf of $\boldsymbol{\varepsilon}$, it requires knowledge of the joint pdf of the real vector $p(\boldsymbol{\varepsilon}_{\mathbb{R}}) = p(\boldsymbol{\varepsilon}_r, \boldsymbol{\varepsilon}_i)$. This is given by

$$p(\boldsymbol{\varepsilon}_{\mathbb{R}}) = \frac{1}{(2\pi)^{\mathrm{N}} \det^{\frac{1}{2}}(\mathbf{C}_{\boldsymbol{\varepsilon}_{\mathbb{R}}\boldsymbol{\varepsilon}_{\mathbb{R}}})} \exp\left[-\frac{1}{2}(\boldsymbol{\varepsilon}_{\mathbb{R}} - \mu_{\boldsymbol{\varepsilon}_{\mathbb{R}}})^{\mathrm{T}} \mathbf{C}^{-1}_{\boldsymbol{\varepsilon}_{\mathbb{R}}\boldsymbol{\varepsilon}_{\mathbb{R}}} (\boldsymbol{\varepsilon}_{\mathbb{R}} - \mu_{\boldsymbol{\varepsilon}_{\mathbb{R}}})\right] \tag{E.1}$$

where for N=1, the covariance matrix takes on the form

$$\mathbf{C}_{\boldsymbol{\varepsilon}_{\mathbb{R}}\boldsymbol{\varepsilon}_{\mathbb{R}}} = \begin{bmatrix} \sigma^2_{\varepsilon_r} & \rho_{\mathbb{R}}\sqrt{\sigma^2_{\varepsilon_r}\sigma^2_{\varepsilon_i}} \\ \rho_{\mathbb{R}}\sqrt{\sigma^2_{\varepsilon_r}\sigma^2_{x_i}} & \sigma^2_{\varepsilon_i} \end{bmatrix} \in \mathbb{R}^{2\times 2} \tag{E.2}$$

which is a positive definite with the correlation coefficient defined as

$$\rho_{\mathbb{R}} = \frac{\mathrm{cov}(\varepsilon_r, \varepsilon_i)}{\sqrt{\sigma^2_{\varepsilon_r}\sigma^2_{\varepsilon_i}}} \tag{E.3}$$

Where $-1 \leq \rho_{\mathbb{R}} \leq 1 \in \mathbb{R}$ and covariance as the central moment is defined by

$$\begin{aligned} \mathrm{cov}(\varepsilon_r, \varepsilon_i) &= \mathbb{E}\left[(\varepsilon_r - \mathbb{E}(\varepsilon_r))(\varepsilon_i - \mathbb{E}(\varepsilon_i))^*\right] \\ &= \mathbb{E}\left[(\varepsilon_r - \mu_{\varepsilon_r})(\varepsilon_i - \mu_{\varepsilon_r})^*\right] \end{aligned} \tag{E.4}$$

where $\mathbb{E}(\cdot)$ is the expected value with respect to the marginal pdfs $p(\varepsilon_r)$ and $p(\varepsilon_i)$ of the real-valued random variables and the variances as $\sigma^2_{\varepsilon_r} = \text{cov}(\varepsilon_r, \varepsilon_r)$ and $\sigma^2_{\varepsilon_i} = \text{cov}(\varepsilon_i, \varepsilon_i)$.

The determinant of Equation (E.1) can now be expressed in terms of the correlation coefficient and the variances, $\det(\mathbf{C}_{\boldsymbol{\varepsilon}_\mathbb{R}\boldsymbol{\varepsilon}_\mathbb{R}}) = \sigma^2_{\varepsilon_r}\sigma^2_{\varepsilon_i}(1-\rho^2_\mathbb{R})$. The resulting bivariate pdf can be expressed as

$$p(\varepsilon) = \frac{1}{2\pi\sigma_{\varepsilon_r}\sigma_{\varepsilon_i}\sqrt{1-\rho^2_\mathbb{R}}} \exp\left[-\frac{1}{2(1-\rho^2_\mathbb{R})}\left(\frac{(\varepsilon_r-\mu_{\varepsilon_r})^2}{\sigma^2_{\varepsilon_r}} - \frac{2\rho_\mathbb{R}(\varepsilon_r-\mu_{x_r})(\varepsilon_i-\mu_{\varepsilon_i})}{\sigma_{\varepsilon_r}\sigma_{\varepsilon_i}} + \frac{(\varepsilon_i-\mu_{\varepsilon_i})^2}{\sigma_{\varepsilon_i}}\right)\right]. \tag{E.5}$$

The statistics of $\varepsilon/\boldsymbol{\varepsilon}$ are constrained now that the pdf is known. *Properness* and *circularity* [242] are the two constraints considered in this study. A complex-valued random variable ε is called proper if and only if real and imaginary parts possess the same variance and are uncorrelated, else it is improper. A complex-valued random vector/variable is called circular if and only if its pdf is rotationally invariant, that is if $\boldsymbol{\varepsilon}' = \boldsymbol{\varepsilon}\exp(j\alpha)$ have the same probability distribution for any given real phase angle α. Therefore, $\mathbb{E}(\boldsymbol{\varepsilon}) = 0$ in order that $\boldsymbol{\varepsilon}$ can be circular. Non centralized pdfs are not rotationally invariant.

Improper random variables/vectors have no bearing on the covariance matrices or the structure of the pdf. Circularity does not entail any Hermitian covariance matrix requirements. Finally, a circular complex random variable or vector is proper. This is not always the case the other way around. As a result, a proper random variable does not have to be circular. Different limitations have resulted in the relationship. While properness needs merely second-order statistics, circularity necessitates that the distribution, and hence all moments, be rotationally invariant. As a result, the distribution of a complex Gaussian random variable can be classified as proper, improper, or circular.

Considering the two sources under study, after M realizations, two sets of random variables $\boldsymbol{\varepsilon_1} = \boldsymbol{\varepsilon}_{1r} + j\boldsymbol{\varepsilon}_{1i} \in \mathbb{C}^{\text{M}\times 1}$ ($\boldsymbol{\varepsilon}_{1\mathbb{R}} = \left[\Re(\boldsymbol{\varepsilon}_{1i})^\text{T} \quad \Im(\boldsymbol{\varepsilon}_{1i})^\text{T}\right] \in \mathbb{R}^{\text{M}\times 2}$) and $\boldsymbol{\varepsilon_2} = \boldsymbol{\varepsilon}_{2r} + j\boldsymbol{\varepsilon}_{2i} \in \mathbb{C}^{\text{M}\times 1}$ ($\boldsymbol{\varepsilon}_{2\mathbb{R}} = \left[\Re(\boldsymbol{\varepsilon}_{2i})^\text{T} \quad \Im(\boldsymbol{\varepsilon}_{2i})^\text{T}\right] \in \mathbb{R}^{\text{M}\times 2}$) for source $\mathcal{S}_1$ and $\mathcal{S}_2$ respectively. These random variables must have the following behaviour:

For each source $\mathcal{S}_t$ where $t = 1, 2$

- the probability distributions $p(\Im(\boldsymbol{\varepsilon}_t))$, $p(\Re(\boldsymbol{\varepsilon}_t))$ and $p(\boldsymbol{\varepsilon_t})$ should be Gaussian in nature such that $\Re(\boldsymbol{\varepsilon}_t) \sim \mathcal{N}(0, 0.5)$, $\Im(\boldsymbol{\varepsilon}_t) \sim \mathcal{N}(0, 0.5)$ and $\boldsymbol{\varepsilon}_t \sim \mathcal{N}_c(0, 1)$. Also, the covariance matrix

$$\mathbf{C}_{\boldsymbol{\varepsilon}_{t\mathbb{R}}\boldsymbol{\varepsilon}_{t\mathbb{R}}} = \begin{bmatrix} 0.5 & 0 \\ 0 & 0.5 \end{bmatrix} \tag{E.6}$$

  which implies that the $\text{cov}(\Re(\boldsymbol{\varepsilon}_t), \Im(\boldsymbol{\varepsilon}_t)) = 0$, $\rho_{t\mathbb{R}} = 0$ and thus $\Re(\boldsymbol{\varepsilon}_t) \perp \Im(\boldsymbol{\varepsilon}_t)$

For sources $\mathcal{S}_1$ and $\mathcal{S}_2$

- the joint probability distributions $p(\Re(\boldsymbol{\varepsilon}_1), \Re(\boldsymbol{\varepsilon}_2))$ and $p(\Im(\boldsymbol{\varepsilon}_1), \Im(\boldsymbol{\varepsilon}_2))$ should be Gaussian in nature such that $[\Re(\boldsymbol{\varepsilon}_1), \Re(\boldsymbol{\varepsilon}_2)] \sim \mathcal{N}(0, 1)$ and that $[\Im(\boldsymbol{\varepsilon}_1), \Im(\boldsymbol{\varepsilon}_2)] \sim \mathcal{N}(0, 1)$ which implies that the $\text{cov}(\Re(\boldsymbol{\varepsilon}_1), \Re(\boldsymbol{\varepsilon}_2)) = 0$ and thus $\text{cov}(\Im(\boldsymbol{\varepsilon}_1), \Im(\boldsymbol{\varepsilon}_2)) = 0$. This makes $\boldsymbol{\varepsilon}_1 \perp \boldsymbol{\varepsilon}_2$.

In the nutshell, $\boldsymbol{\varepsilon}_1$ simulated should be uncorrelated to $\boldsymbol{\varepsilon}_2$ and since both have zero mean random vectors they are orthogonal as well. Which implies that $\boldsymbol{\varepsilon}_1$ is statistically independent of $\boldsymbol{\varepsilon}_2$ and their respective distribution should be circular and proper.

Figure E.1 depicts the simulation results for 1000 realization runs. The distribution of the complex random vectors obtained is Gaussian in nature according to Equation (E.4), as shown in Figure E.1, with the resultant statistics approaching the ideal situation of Equation

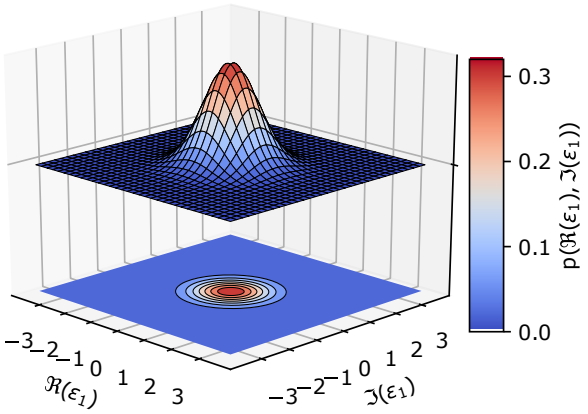

(a) $p(\Re(\varepsilon_1), \Im(\varepsilon_1))$

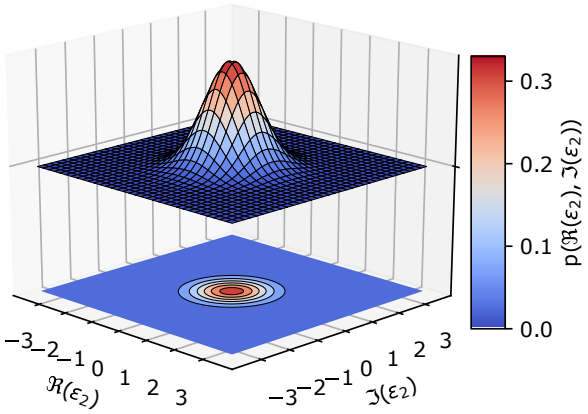

(b) $p(\Re(\varepsilon_2), \Im(\varepsilon_2))$

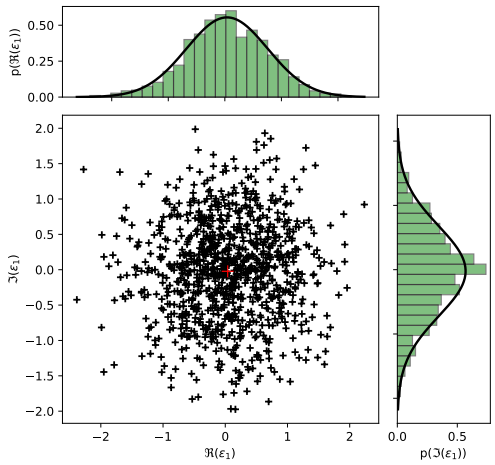

(c) $\rho = 0.0302$, $\begin{bmatrix} \Re(\varepsilon_1) \\ \Im(\varepsilon_1) \end{bmatrix} \sim \mathcal{N}\left(\begin{bmatrix} 0.0392 \\ -0.0221 \end{bmatrix}, \begin{bmatrix} 0.5175 & 0.0152 \\ 0.0152 & 0.4914 \end{bmatrix}\right)$

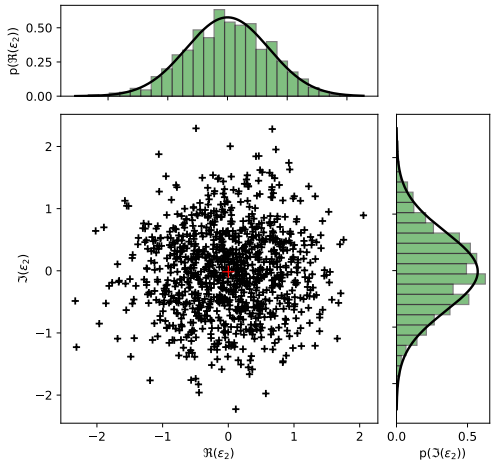

(d) $\rho = 0.0453$, $\begin{bmatrix} \Re(\varepsilon_2) \\ \Im(\varepsilon_2) \end{bmatrix} \sim \mathcal{N}\left(\begin{bmatrix} 0.0013 \\ -0.0162 \end{bmatrix}, \begin{bmatrix} 0.4795 & 0.0219 \\ 0.0219 & 0.4865 \end{bmatrix}\right)$

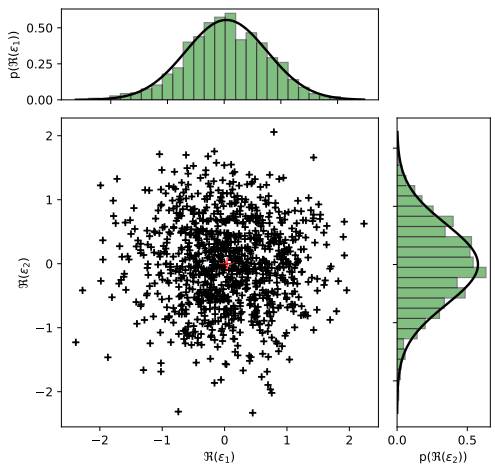

(e) $\rho = -0.0312$, $\begin{bmatrix} \Re(\varepsilon_1) \\ \Re(\varepsilon_2) \end{bmatrix} \sim \mathcal{N}\left(\begin{bmatrix} 0.0392 \\ 0.0013 \end{bmatrix}, \begin{bmatrix} 0.5175 & -0.0156 \\ -0.0156 & 0.4795 \end{bmatrix}\right)$

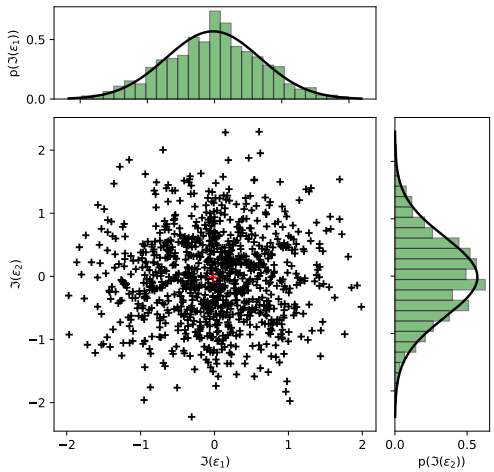

(f) $\rho = 0.0162$, $\begin{bmatrix} \Im(\varepsilon_1) \\ \Im(\varepsilon_2) \end{bmatrix} \sim \mathcal{N}\left(\begin{bmatrix} -0.0221 \\ -0.0162 \end{bmatrix}, \begin{bmatrix} 0.4914 & 0.0079 \\ 0.0079 & 0.4865 \end{bmatrix}\right)$

Figure E.1: Bivariate Gaussian distribution of the simulated complex valued random variable ε_1 and ε_2 for sources $\mathcal{S}_1$ and $\mathcal{S}_2$ respectively using 1000 realizations.

(E.5). On the whole, the estimated means (red plus sign) of the real and imaginary parts of the randomized variables are around 0.0, the variance is around 0.5, and the correlation coefficient is less than 0.05. This is an indication that the generated random variables are highly uncorrelated and independent to one another. Also, as shown in Figures E.1(a) and (a), the contour plot displays several concentric circles (far from being elliptical) centred on virtually the calculated mean values approximately $(0.0, 0.0)$. As a result, the estimated random variable created has the required characteristics of being circular, proper, and uncorrelated random complex variable, as described earlier.

FOLIO ADMINISTRATIF

THESE DE L'UNIVERSITE DE LYON OPEREE AU SEIN DE L'INSA LYON

NOM : DABANKAH

DATE de SOUTENANCE : 22/06/2022

Prénoms : Emmanuel Manu

TITRE : Source field reconstruction based on virtual acoustic volume concept: Regularization strategies and blind reconstruction and separation

NATURE : Doctorat

Numéro d'ordre : 2022LYSEI057

Ecole doctorale : MEGA (Mécanique, Energétique, Génie Civil, Acoustique)

Spécialité : Acoustique

RESUME : L'objectif du projet Européen PBNv2 (ETN GA721615, https://www.h2020-pbnv2.eu/) était de développer des approches numériques et expérimentales pour la caractérisation du bruit de passage des véhicules de nouvelle génération équipés de groupes motopropulseurs électriques ou hybrides. Le projet s'articulait autour de trois axes : les sources de bruit, les voies de passages et les sujets humains soumis au bruit.
Le travail de thèse présenté ici a permis de développer la méthode « inverse Patch Transfer Function » (iPTF) pour une caractérisation acoustique complète d'une source à géométrie complexe dans un contexte industriel acoustiquement mal maîtrisé. Le mémoire de thèse est composé de trois parties principales. La première partie porte sur une étude détaillée de méthodes de régularisation d'un problème mal posé. De nombreuses approches (Tikhonov, bayésiennes, itératives) combinées à des critères de sélection des solutions optimales sont présentées et illustrées sur un cas d'application numérique. Les sensibilités des approches au bruit perturbateur et à la sous-détermination du problème sont notamment abordées et expliquées. La seconde partie exploite le concept de volume virtuel fini pour pouvoir prendre en compte la présence d'objets masquants qui empêchent généralement d'appliquer les méthodes classiques d'holographie acoustique de champ proche. L'étude présentée démontre que la méthode iPTF est très robuste même en présence d'un objet masquant une large partie de la source (une plaque rectangulaire dans l'exemple traité) et à une faible distance. Une campagne expérimentale appliquée à un moteur électrique en fonctionnement a permis de démontrer le potentiel de l'approche. Enfin, la dernière partie développe le concept de « blind separation » (séparation à l'aveugle). Cette approche permet de décomposer les champs reconstruits en contributions provenant de différentes sources vibratoires décorrélées. Elle permet ainsi d'améliorer la compréhension des phénomènes à l'origine du bruit rayonné. Une première validation de cette approche sur une expérience numérique est proposée.

MOTS-CLÉS : Reconstruction de champs acoustiques, méthode inverse, inverse Patch Transfer Functions

Laboratoire (s) de recherche : Laboratoire Vibrations Acoustique (LVA) de l'INSA – Lyon

Directeur de thèse: TOTARO Nicolas

Président de jury : THOMAS Jean-Hugh

Composition du jury :

THOMAS, Jean-Hugh, Professeur des Universités, LAUM, Université du Maine	Rapporteur
AUCEJO, Mathieu, Maître de Conférences HDR, LMSSC, CNAM	Rapporteur
FORGET, Sandra, Docteure, Renault	Examinatrice
COLANGELI, Claudio, Docteur, Siemens	Examinateur
TOTARO, Nicolas, Professeur des Universités, INSA-Lyon	Directeur de thèse
ANTONI, Jérôme, Professeur des Universités, INSA-Lyon	Co-directeur de thèse